



AN INVESTIGATION INTO THE FEASIBILITY OF USING
A MODERN GRAVITY GRADIENT INSTRUMENT FOR
PASSIVE AIRCRAFT NAVIGATION AND TERRAIN
AVOIDANCE

THESIS

Marshall M. Rogers, Captain, USAF

AFIT/GAE/ENY/09-M16

DEPARTMENT OF THE AIR FORCE
AIR UNIVERSITY

AIR FORCE INSTITUTE OF TECHNOLOGY

Wright-Patterson Air Force Base, Ohio

APPROVED FOR PUBLIC RELEASE; DISTRIBUTION IS UNLIMITED.

The views expressed in this thesis are those of the author and do not reflect the official policy or position of the United States Air Force, Department of Defense, or the United States Government.

AFIT/GAE/ENY/09-M16

AN INVESTIGATION INTO THE FEASIBILITY OF USING A MODERN
GRAVITY GRADIENT INSTRUMENT FOR PASSIVE AIRCRAFT
NAVIGATION AND TERRAIN AVOIDANCE

THESIS

Presented to the Faculty
Department of Aeronautics and Astronautics
Graduate School of Engineering and Management
Air Force Institute of Technology
Air University
Air Education and Training Command
In Partial Fulfillment of the Requirements for the
Degree of Master of Science in Aeronautical Engineering

Marshall M. Rogers, BS
Captain, USAF

March 2009

APPROVED FOR PUBLIC RELEASE; DISTRIBUTION IS UNLIMITED.

AN INVESTIGATION INTO THE FEASIBILITY OF USING A MODERN
GRAVITY GRADIENT INSTRUMENT FOR PASSIVE AIRCRAFT
NAVIGATION AND TERRAIN AVOIDANCE

Marshall M. Rogers, BS
Captain, USAF

Approved:

/signed/

Maj Richard Huffman, PhD(Chairman)

6 March 2009

Date

/signed/

LtCol Chris Shearer, PhD (Member)

6 March 2009

Date

/signed/

Dr. Stewart DeVilbiss, PhD (Member)

6 March 2009

Date

Abstract

Over the past decade, Gravity Gradient Instruments (GGIs) - devices which measure the spatial derivatives of gravity, have improved remarkably in accuracy due to the development and refinement of a variety of accelerometer technologies. Some specialized GGIs are currently flown on aircraft for geological purposes in the mining industries and, as such, gravity gradient data is recorded in flight and detailed gradient maps are created after post mission processing. These maps, if stored in a database onboard an aircraft and combined with a GGI, form the basis for a covert navigation system using a process known as the map matching method. This system, if it could be successfully implemented, would be completely passive - impervious to conventional jamming methods and relying only on local gravity gradient measurements from an onboard sensor.

This paper entails an investigation into the feasibility of using a modern GGI on an airborne platform for covert navigation and terrain avoidance by examining GGI signal levels in different flight scenarios (low, medium, and high altitudes and velocities). Previous studies using gravity gradiometers have been accomplished with promising results (some theoretical gradiometers have been predicted to produce GPS-like navigation accuracy). However, while major improvements have been made to current airborne gravity gradient instruments, they still produce noise at least an order of magnitude too high for useful aircraft navigation purposes. This research focuses on the implementation of a new airborne GGI, currently in flight test, which has demonstrated approximately an order of magnitude better sensitivity than current airborne GGIs. To demonstrate whether or not this technology is currently feasible, a model of the GGI sensor was developed to investigate signal levels at representative flight conditions. Using the sensor model, representative aircraft trajectories were flown (simulated) over modeled gravity gradient maps to determine the utility of

flying current GGIs in the roles of terrain avoidance and navigation. The results of the GGI simulations at different altitudes, velocities, gravity gradient map resolutions and gradiometer sensitivities are presented and discussed. It was shown that the map-matching navigation system based on this new instrument has the potential to provide a marked improvement over a non-aided INS in some cases but was limited by the drop in gravity gradient strength at higher altitudes, particularly in areas of smooth terrain. It was originally hypothesized that the GGI could also be used for terrain avoidance due to the rapid signal change as rising terrain is approached. However, GGI gradient production rate and bandwidth limitations, along with the inverse nature of the terrain avoidance problem, rendered GGI aided terrain avoidance unfeasible for the time being.

Acknowledgements

I would like to express my appreciation to my thesis advisor, Maj Rich “Bart” Huffman, for suggesting this research topic. Bart, thank you for entrusting me with this work and for all of your guidance and support throughout - even during your deployment. I would also like to express my gratitude to my sponsors, Dr. Stewart DeVilbiss and Dr. Mikel Miller, from the Air Force Research Laboratory for their outstanding support in this endeavor. I am also indebted to LtCol Chris Shearer, Dr. Chris Jekeli, Mr. Steve Kenyon, Ms. Linda Sumski and LtCol Michael Veth for their valuable input.

Marshall M. Rogers

Table of Contents

	Page
Abstract	iv
Acknowledgements	vi
List of Figures	ix
List of Tables	xiii
I. Introduction	1
Background	1
Gravitational Gradient	3
A Gravitational Disturbance Gradient	6
The Gravity Gradiometer	10
An Inverse Problem	14
Problem Statement	14
Feasibility	15
Research Objectives	15
Preview	16
II. Literature Review	18
History of Gravity Gradiometry	18
Airborne Gravity Gradiometer Technology	21
Rotating Accelerometer Gravity Gradiometer	21
Superconducting Gravity Gradiometer	28
Atom Interferometer Gravity Gradiometer	36
Navigation and Terrain Avoidance via Gravity Gradiometry - Previous Works	39
III. Methodology	43
Overview	43
Gravity Gradient Maps	43
Earth Gravitational Model 1996	44
Extended Parker Method	48
Gravity Gradiometer Modeling	54
Noise Generation	54
Filtering	55
Gradiometer Model Verification	60
Navigation	61
Test Conditions	61
The Tanker Effect	64

	Page
Gradiometer Signal Metrics for Useful Navigation	68
Terrain Avoidance	71
Method 1	72
Method 2	73
IV. Results and Analysis	75
Overview	75
Model Validation	75
Aircraft Navigation Feasibility Results	81
Navigation Feasibility via Qualitative Signal Analysis	81
Navigation Feasibility via Signal Time Rate of Change Metrics	89
The Tanker Effect	93
Aircraft Terrain Avoidance Feasibility Results	95
Results Summary	102
V. Discussion	104
Research Summary	104
Challenges and Limitations	104
Significant Contributions and Insights	106
Recommendations for Future Research	108
Conclusion	109
Appendix A. Matlab [®] Code	110
Appendix B. Legendre Function Coefficients used for EGM96 Gradient Calculations	135
Appendix C. Supplementary Figures	137
Bibliography	160
Vita	165

List of Figures

Figure		Page
1	Rectangular Prism.	7
2	Hypothetical Prism Orientation and Dimensions.	8
3	Example Gravitational Disturbance Gradients.	9
4	Example Gravitational Disturbance Gradient Spectrum.	10
5	Accelerometer.	11
6	A Simple Gravity Gradiometer.	12
7	Eotvos' Torsion Balance - The First Gravity Gradiometer	18
8	Rotating Accelerometer Schematic	21
9	Single Rotating Accelerometer Disk	22
10	Bell Geospace Air-FTG	24
11	Bell Geospace Air-FTG GGI Orientation	25
12	A Magnet Levitating above a Superconductor due to the Meissner Effect	29
13	Coil and Image Coil near a Superconductor	30
14	Superconducting Accelerometer Schematic	31
15	Superconducting Gradiometer Schematic	32
16	University of Maryland SAA	34
17	University of Maryland Cryostat	34
18	ARKeX EGG	35
19	Schematic of the Stanford/JPL AI Gradiometer	37
20	Magneto-Optic Trap	37
21	Atom Interferometer	38
22	Stanford/JPL AI Gradiometer Dimensions	38
23	Richeson's Proposed Navigation System	42
24	Exaggerated Illustration of the Geoid, Ellipsoid, and Topography. .	45
25	EGM96 Geoid Undulations with respect to the WGS84 Ellipsoid. .	46

Figure		Page
26	Example Elevation Grid.	53
27	Example Butterworth Filter.	56
28	Illustration of Aliasing and the Nyquist Condition.	59
29	GGI-Aided Passive Navigation System Flowchart.	61
30	Test Tracks (note contour scale differences).	62
31	A KC-10 Offloading Fuel to an F-22 Raptor.	65
32	KC-10 Dimensions.	66
33	KC-10 Transformed into a Rectangular Prism.	67
34	Richeson's Navigation Results: 0.1Eo GGI Map-Matching System vs GPS	70
35	Terrain avoidance scenario.	72
36	World's Tallest Water Tower	73
37	Modeling the Unmodeled	74
38	Model Validation - Parker's Method vs Rigorous Rectangular Prisms.	76
39	Terrain Effect Modeling verification: Bell Geospace vs. Zhu's Nu- merical Integration vs. Parker's Method	77
40	Model Validation - Modeled Gradients vs. Air-FTG Data	78
41	Filter validation - Frequency response of a 7th order Butterworth filter with $f_c=0.2\text{Hz}$ and $f_s=1\text{Hz}$	79
42	Filter Validation - Impulse Response of a 7th Order Digital Butter- worth Filter with $f_c=0.2\text{Hz}$ and $f_s=1\text{Hz}$	79
43	GGI Noise Validation.	80
44	Low Noise GGI Signal Classification Summary (GGI1).	82
45	Noisier GGI Signal Classification Summary (GGI2).	84
46	Low Pass Filter Effect, 1200m/s, 1000m, Rough Terrain.	85
47	Signal Comparison: Excellent (GGI1) vs. Truth, 300m/s, 2500m, Rough Terrain.	86
48	Signal Comparison: Useful (GGI1) vs. Truth, 600m/s, 10000m, Smooth Terrain.	87

Figure		Page
49	Signal Comparison: Marginally Useful(GGI1) vs. Unusable(GGI2) vs. Truth, 300m/s, 10000m, Smooth Terrain.	88
50	GGI1 Signal Classification Summary - Signal Time Rate of Change Method.	90
51	Signal Comparison: Marginally Useful (GGI1) vs. Unusable (GGI2) vs. Truth, 300m/s, 10000m, Rough Terrain, Signal Rate of Change Metrics.	91
52	Signal Comparison: Unusable (GGI1 and 2) vs. Truth, 300m/s, 10000m, Smooth Terrain, Signal Rate of Change Metrics.	92
53	Signal Comparison: Ultra Low Noise GGI (0.01Eo) vs. Truth, Worst Case Scenario - 50m/s, 20000m, Smooth Terrain.	93
54	Tanker Effect, GGI1, 5000m, 150m/s.	94
55	Terrain Avoidance Scenario Summary, GGI signals, 50 m/s, No Noise.	96
56	Terrain Avoidance Scenario summary, True Gradients, 50 m/s.	98
57	Water Tower Spectrum	99
58	Water Tower Scenario, Txx vs time, 50m/s, No Noise.	100
A.1	GGI Simulink Block Diagram.	133
A.2	GGI of Justice Simulink Block Diagram.	133
A.3	Terrain Avoidance Simulink Block Diagram.	134
C.1	Runs 1-12, 1000m, GGI 1.	137
C.2	Runs 13-24, 1000m, GGI 2.	138
C.3	Runs 25-36, 2500m, GGI 1.	139
C.4	Runs 37-48, 2500m, GGI 2.	140
C.5	Runs 49-60, 5000m, GGI 1.	141
C.6	Runs 61-72, 5000m, GGI 2.	142
C.7	Runs 73-84, 10000m, GGI 1.	143
C.8	Runs 85-96, 10000m, GGI 2.	144
C.9	Runs 97-108, 20000m, GGI 1.	145
C.10	Runs 109-120, 20000m, GGI 2.	146

Figure		Page
C.11	Signal Time Rate of Change, 1000m.	147
C.12	Signal Time Rate of Change, 2500m.	148
C.13	Signal Time Rate of Change, 5000m.	149
C.14	Signal Time Rate of Change, 10000m.	150
C.15	Signal Time Rate of Change, 20000m.	151
C.16	Runs 123-124, GGI2 Tanker Effect, 5000m, 150m/s.	152
C.17	Runs 125-126, GGI1 Tanker Effect, 10000m, 150m/s.	153
C.18	Runs 127-128, GGI2 Tanker Effect, 10000m, 150m/s.	154
C.19	Terrain Avoidance Scenario, 50 m/s, 25x25x25m Block.	155
C.20	Terrain Avoidance Scenario, 50 m/s, 50x50x50m Block.	156
C.21	Terrain Avoidance Scenario, 50 m/s, 100x100x100m Block.	157
C.22	Terrain Avoidance Scenario, 50 m/s, 250x250x250m Block.	158
C.23	Terrain Avoidance Scenario, 50 m/s, 500x500x500m Block.	159

List of Tables

Table		Page
1	EGM96 Parameters	48
2	Gridded Gradient Computation Time Comparison	52
3	GGI Specifications	59
4	Along-Track Terrain Statistics	63
5	Test Matrix.	64
6	KC-10 Parameters	66
7	Richeson’s “GGI Survey” simulation parameters	69
8	0.1Eo GGI Signal Classification Metrics	71
9	Velocity vs. Minimum Wavelength, $f_c=0.2\text{Hz}$	71
10	GGI1 Signal Classification Results - Rough Terrain	81
11	GGI1 Signal Classification Results - Smooth Terrain	81
12	GGI2 Signal Classification Results - Rough Terrain	83
13	GGI2 Signal Classification Results - Smooth Terrain	83
14	Gradiometer Requirements to sense Water Tower	101
15	Predicted Gradiometer Requirements for UGM Style Terrain Avoid- ance	102

AN INVESTIGATION INTO THE FEASIBILITY OF USING A MODERN GRAVITY GRADIENT INSTRUMENT FOR PASSIVE AIRCRAFT NAVIGATION AND TERRAIN AVOIDANCE

I. Introduction

Background

The ability to precisely navigate is a critical enabler on the modern battlefield. It is essential to mission accomplishment for aircraft, land vehicles, naval vessels, and even personnel. Perhaps most importantly, in a military utility sense, is it allows fast moving (i.e. airborne) platforms to find their way to and place weapons on a target with minimum collateral damage. As they navigate, most modern military aircraft and munitions rely on some form of a Global Navigation Satellite System (GNSS) for position updates. This system, using a set of signals from independent satellites to triangulate position, is proven and provides the needed accuracy for most mission objectives. However, these satellite signals can be denied by physical blockage (i.e. inside a cave or deep underwater), jamming or by destruction of the satellites broadcasting them.

There is a significant amount of research into methods to precisely navigate in a GPS denied environment. Some of these include, but are not limited to, the use of pseudolites, terrain referenced navigation (TRN) such as Sandia Inertial Terrain Aided Navigation (SITAN), Terrain Contour Matching (TERCOM), Terrain Profile Matching (TERPROM), image based navigation, and inertial navigation systems (INS) which can be provided with position updates from the aforementioned navigation methods to correct drift errors [1,2]. Another method of aircraft navigation that has been given relatively little attention over the last 25 years is by use of a device known as a gravity gradient instrument (GGI).

A gravity gradiometer is a device that measures spatial derivatives of the earth's gravity "acceleration" vector. These spatial changes in earth's gravity are caused

by the fact that the earth is elliptical (rather than perfectly spherical), is spinning, has varying terrain features, and mass densities which are not constant. They are very small and require a great deal of sensor accuracy to properly measure. Over the past two decades, gravity gradiometers have been carried in aircraft and used with rapidly increasing success for geological surveys. The speed at which these aircraft can fly, combined with improved sampling rates and noise reduction features of modern airborne GGIs, allow surveyors to map the gravitational gradients caused by terrain and subterranean anomalies much faster than their ground based counterparts (as well as reaching areas otherwise inaccessible by land). Gravitational gradient maps are recorded, processed and used post flight to increase understanding of the earth's gravitational field and for kimberlite, oil and other valuable natural resource detection [3,4]. If received GGI signals were able to be correlated to an existing map generated by a survey (or by theory), a basis for a covert navigation system could be formed, similar to TRN, but requiring no external emissions, no susceptibility to adverse weather conditions, and a signal that is, by today's standards, virtually impossible to jam - requiring terrain to be moved to "fool" the sensor.

Before continuing, "precision navigation" must be defined as it pertains to the scope of this research. The term precision navigation is sometimes loosely thrown around when describing the accuracy of navigation systems. Centuries ago, precision navigation was a matter of arriving at the correct continent. During WWII, the Norden bombsight made "precision" high altitude bombing a reality by placing bombs within a 30m circle from an altitude of 6km (under ideal circumstances) [5]. With the advent of GPS and, more recently, differential GPS, precision navigation has, once again, been redefined with navigation errors of less than 1m. While this may seem impressive today, suppose in the future that one wants to navigate a micro UAV through a building or maybe even through an air conditioning vent! Clearly, 1m of error could be unacceptably large for that application. For this research, precision navigation refers to the level of accuracy attainable by GPS or GPS aided systems.

Gravitational Gradient

According to Wellenhoff and Moritz [6], the gravitational potential, V , of a point in a gravitational field is defined as the work done per unit mass by the pull of gravity to bring a body from infinity to that point. It is a scalar, zero order tensor function. From Newtonian potential theory, the gravitation potential at a point in a cartesian coordinate system (x, y, z) , due to an attracting mass distribution having the density function $\rho(x', y', z')$ and volume v' , is given by the following volume integral:

$$V = G \iiint_{v'} \frac{\rho}{r} dv' \quad (1)$$

where:

$r = \sqrt{(x - x')^2 + (y - y')^2 + (z - z')^2}$ and represents the distance between the element point $Q(x', y', z')$ and the computation point $P(x, y, z)$.

G is Newton's gravitational constant and is $6.6742 \cdot 10^{-11} m^3 kg^{-1} s^{-2}$

$dv' = dx' dy' dz'$ and is the volume element.

The gravitational force vector, F , is the gradient of the gravitational potential and is given by:

$$F = \nabla V = \left[\frac{\partial V}{\partial x}, \frac{\partial V}{\partial y}, \frac{\partial V}{\partial z} \right]^T \quad (2)$$

The gravitational gradient tensor, V_{ij} , is the second-order tensor of the gravitational

potential and is given by:

$$V_{ij} = \nabla F = \begin{pmatrix} \frac{\partial^2 V}{\partial x^2} & \frac{\partial^2 V}{\partial x \partial y} & \frac{\partial^2 V}{\partial x \partial z} \\ \frac{\partial^2 V}{\partial y \partial x} & \frac{\partial^2 V}{\partial y^2} & \frac{\partial^2 V}{\partial y \partial z} \\ \frac{\partial^2 V}{\partial z \partial x} & \frac{\partial^2 V}{\partial z \partial y} & \frac{\partial^2 V}{\partial z^2} \end{pmatrix} = \begin{pmatrix} V_{xx} & V_{xy} & V_{xz} \\ V_{yx} & V_{yy} & V_{yz} \\ V_{zx} & V_{zy} & V_{zz} \end{pmatrix} \quad (3)$$

The gradient is symmetric and it's trace satisfies Poisson's equation: $\nabla^2 V = -4\pi G\rho$. When the density at the computation point is zero (i.e. free air), this equation becomes Laplace's equation. Thus, by Laplace's equation, which states that the trace of the tensor must sum to zero, and symmetry, this 9 component tensor has only 5 independent components.

It should be noted that, according to Equation 1, the gravitational potential decreases linearly as r is increased. Consequently, the gravitational force and gravitational gradients attenuate as a function of r^2 and r^3 , respectively.

Note that "gravitational" phenomena have only been addressed thus far. Gravity is a more familiar term and, as it pertains to objects on the earth's surface, stems from the combination of the gravitational force vector and centrifugal force due to the earth's rotation (also a vector). These combined forces, acting on a unit mass, constitute the gravity vector, g . "Gravity" is the magnitude of vector g and carries units of acceleration. The typical value of this acceleration over the earth's surface is the familiar $9.8m/s^2$. Like gravitational potential, gravity potential, W , exists and is also a scalar, zero order tensor function. It is simply a combination of gravitational potential, V , and centrifugal potential Φ :

$$W = V + \Phi \quad (4)$$

with

$$g = \nabla W = \left[\frac{\partial W}{\partial x}, \frac{\partial W}{\partial y}, \frac{\partial W}{\partial z} \right]^T \quad (5)$$

In geophysical applications, a rotating ellipsoid of revolution is used to approximate the earth and is assumed to be an equipotential surface of a normal gravity field with potential U . The difference between the actual gravity potential, W , and the normal potential, U , is called the disturbing potential, T :

$$T = W - U \quad (6)$$

with the gravitational disturbance gradients defined as:

$$T_{ij} = \begin{pmatrix} \frac{\partial^2 T}{\partial x^2} & \frac{\partial^2 T}{\partial x \partial y} & \frac{\partial^2 T}{\partial x \partial z} \\ \frac{\partial^2 T}{\partial y \partial x} & \frac{\partial^2 T}{\partial y^2} & \frac{\partial^2 T}{\partial y \partial z} \\ \frac{\partial^2 T}{\partial z \partial x} & \frac{\partial^2 T}{\partial z \partial y} & \frac{\partial^2 T}{\partial z^2} \end{pmatrix} = \begin{pmatrix} T_{xx} & T_{xy} & T_{xz} \\ T_{yx} & T_{yy} & T_{yz} \\ T_{zx} & T_{zy} & T_{zz} \end{pmatrix} \quad (7)$$

where T_{xx} is the change of gravity in the x direction while moving a known distance in the x direction and T_{xy} is the change of gravity in the x direction while moving a known a known distance in the y direction. The remaining gradients are defined similarly.

The gravitational disturbance gradient tensor, like the gravitational gradient tensor, satisfies Laplace's equation in free air and is symmetric, thus giving it 5 independent components which carry units of $1/s^2$. Since the magnitude of the gradients is very small, units of $1/ns^2$ are commonly used. These units, known as Eotvos(EO), were named after 19th century Hungarian physicist Baron Roland von Eotvos and are not recognized by the SI system but are commonly used in the geophysics community [7]. To add physical meaning to the unit, 1 Eotvos is equivalent to the gradient of a gravitational field produced by 10 grains of sand at a distance of 1cm [8]. Since

the normal gravity potential and its gradients are known for a specified ellipsoid (i.e. WGS84), only the calculation (or estimation, as it will turn out) of T_{ij} is required. To understand how T_{ij} manifests, consider its source: Assuming the earth is approximated as an ellipsoid of revolution with a smooth surface and an assumed constant density, variations in the surface (terrain) and density contrasts within the terrain and the ellipsoid will cause variations in addition to the nominal potential and, in turn, create the gravity gradient disturbance. Some of the methods to predict these disturbance gradients will be investigated in Chapters 2 and 3. It should be noted that a GGI measures the actual gravity gradients, but the nominal gradients, U_{ij} , are known, slowly changing (spatially), and generally treated as a bias. Thus, computation of the *gravitational* disturbance gradient tensor is the more urgent focus of current research.

A Gravitational Disturbance Gradient

To gain insight into the gravitational gradient caused by a mass anomaly, an example using a simple rectangular prism of constant density, shown in Figure (1), is presented. The prism is defined by the vertices at $(x1, y1, z1)$, $(x2, y1, z1)$, $(x2, y2, z1)$, and $(x2, y2, z2)$ with the coordinate system used having axes parallel to the prism sides and the origin at point P . Beginning with Equation (1), the closed form solutions for the five gravitational disturbance gradients, observed at point P , caused by the prism can be found [9].

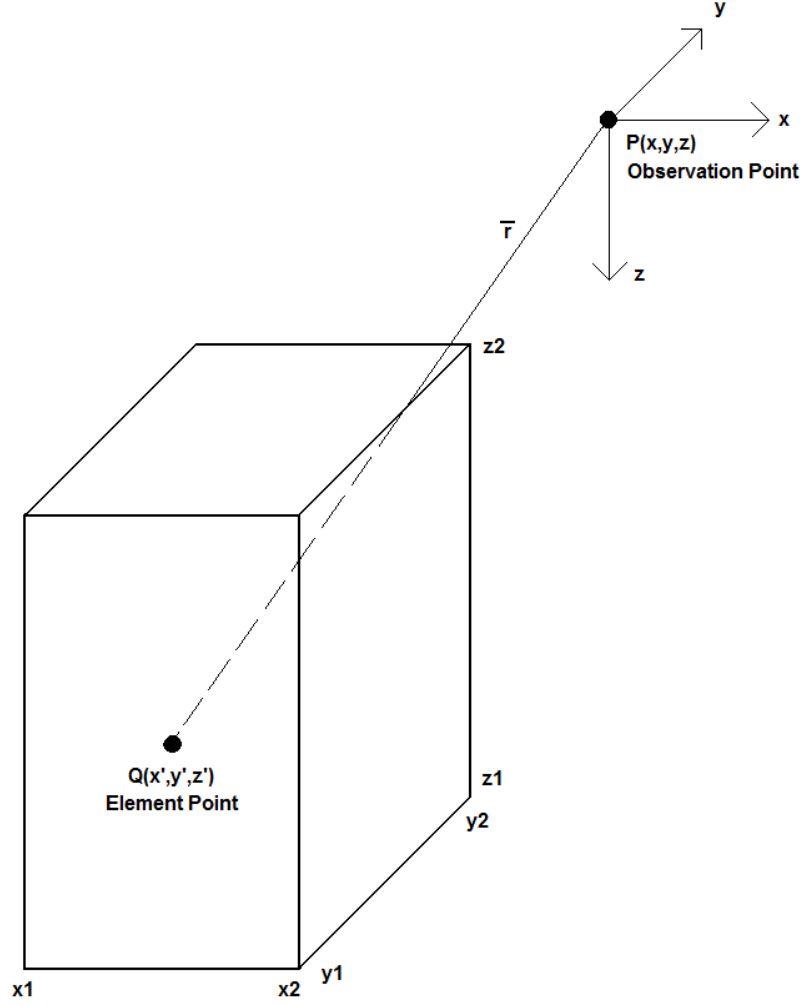


Figure 1: Rectangular Prism.

$$T_{xx} = G\Delta\rho \sum_{i=1}^2 \sum_{j=1}^2 \sum_{k=1}^2 (-1)^{i+j+k} \tan^{-1} \left(\frac{(y - y_j)(z - z_k)}{(x - x_i)r} \right) \quad (8)$$

$$T_{xy} = -G\Delta\rho \sum_{i=1}^2 \sum_{j=1}^2 \sum_{k=1}^2 (-1)^{i+j+k} \ln((z - z_k) + r) \quad (9)$$

$$T_{xz} = -G\Delta\rho \sum_{i=1}^2 \sum_{j=1}^2 \sum_{k=1}^2 (-1)^{i+j+k} \ln((y - y_j) + r) \quad (10)$$

$$T_{yy} = G\Delta\rho \sum_{i=1}^2 \sum_{j=1}^2 \sum_{k=1}^2 (-1)^{i+j+k} \tan^{-1} \left(\frac{(x - x_i)(z - z_k)}{(y - y_j)r} \right) \quad (11)$$

$$T_{yz} = -G\Delta\rho \sum_{i=1}^2 \sum_{j=1}^2 \sum_{k=1}^2 (-1)^{i+j+k} \ln((x - x_i) + r) \quad (12)$$

where:

$\Delta\rho$ is the density contrast between the element and computation point medium

$$r = \sqrt{(x - x_i)^2 + (y - y_j)^2 + (z - z_k)^2}$$

Note: The coordinate system used here and throughout this study is the North, East, Down (NED) system where positive y corresponds to North, positive x corresponds to East, and positive z corresponds to Down.

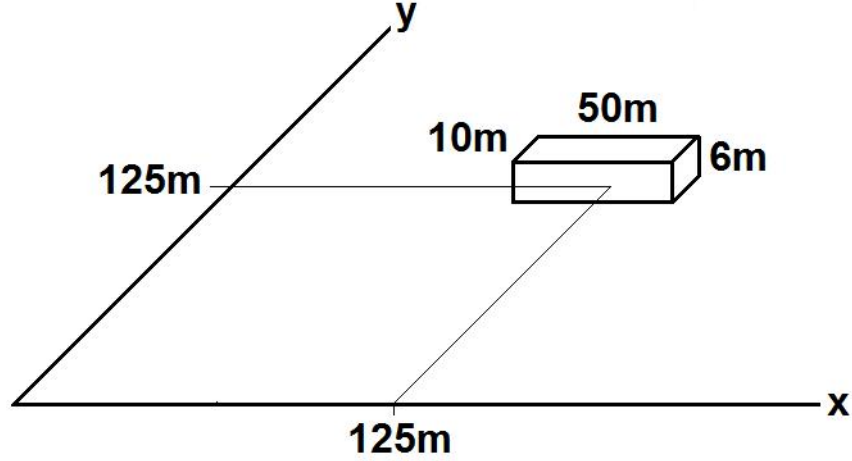


Figure 2: Hypothetical Prism Orientation and Dimensions.

Figure 2 shows the orientation and dimensions of the prism, or hypothetical brick, used to demonstrate the disturbance gradient. The brick, having a constant density of $1.5g/cm^3$, is centered on a $250m \times 250m$ grid. The gradients, shown in Figure 3, were calculated on a plane $50m$ above the center of the brick ($z=-50m$). Due to symmetry, only part of the disturbance gradient tensor is shown. The T_{xx} gradients highlight the x-axis (or east-west) edges of the brick by measuring the east-west changes in east-west gravity. Similarly, the T_{yy} gradients show the y-axis (or north-south) edges of the brick by measuring the north-south changes in north-south gravity. T_{zz} highlights the overall shape of the anomaly as it is a combination of T_{xx} and T_{yy} with a sign change. T_{xz} and T_{yz} gradient data outlines the north-south

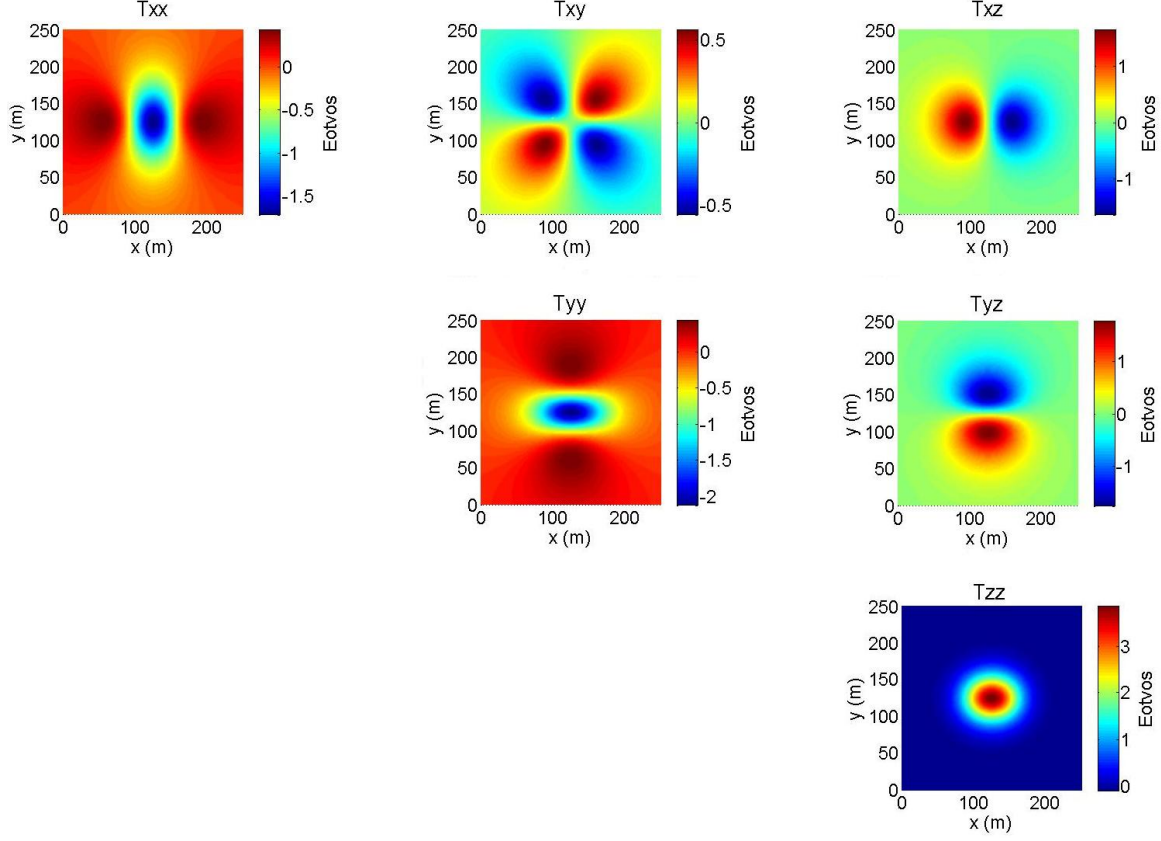


Figure 3: Example Gravitational Disturbance Gradients.

and the east-west mass anomaly axes, respectively. They also help to highlight the north-south and east-west edges. While T_{xz} , T_{yz} and T_{xy} are less intuitive, they contain unique information. If these gradient maps were stored in a database and the gradients were able to be accurately measured real-time as the grid were traversed, there is enough information for unique determination of position on the grid based on these measurements. This is the fundamental concept behind navigation via a gravity gradiometer based map matching system.

In order to better understand the frequency content of the gravitational gradients, Figure 4 shows the spatial frequency spectrum produced by the brick's gradients. These gradients can be broken into spatial frequencies because they are periodic across position in space. A basic understanding of an anomaly's signal structure will be beneficial should a filter be applied to a real-world gradiometer signal. The plot clearly

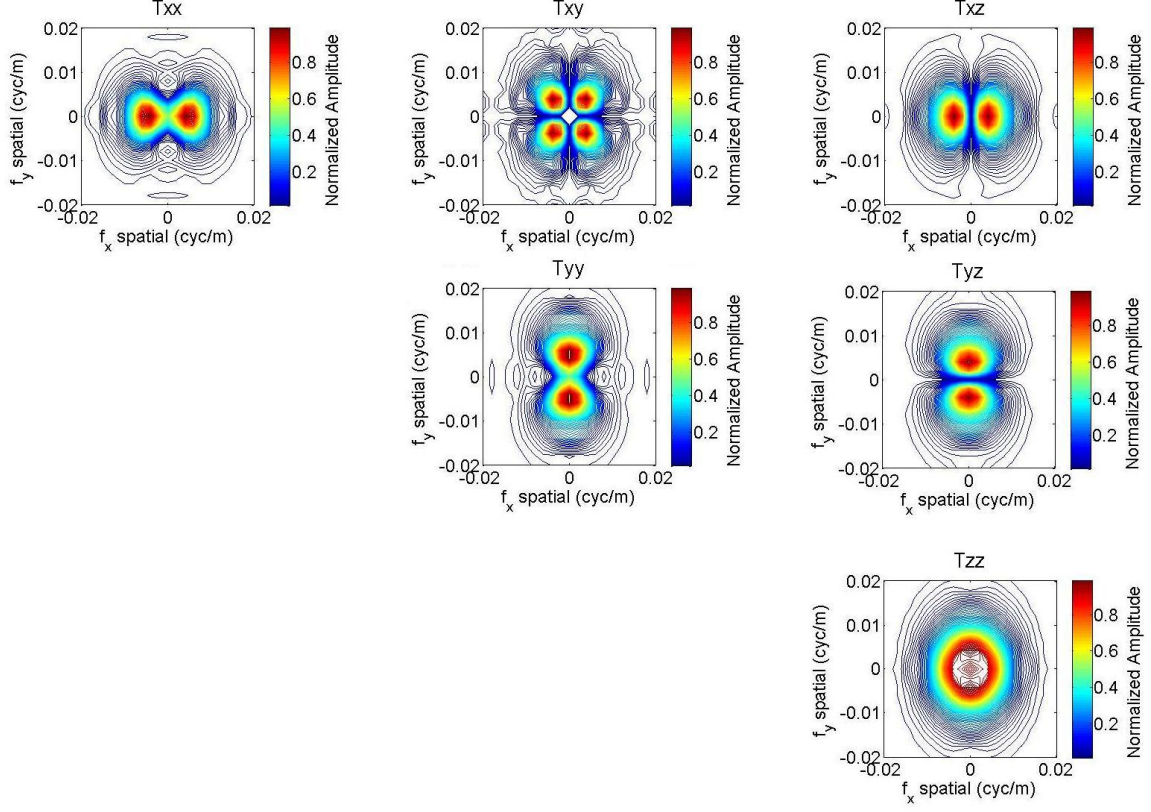


Figure 4: Example Gravitational Disturbance Gradient Spectrum.

illustrates that most of the signal from the brick is in the 0.001 to 0.01 cyc/m spatial frequency range along both axes. This corresponds to wavelengths of approximately $100 - 1000 \text{ m}$. Note that cyc/m denotes cycles (or periods) per meter and is standard nomenclature for spatial frequency.

The Gravity Gradiometer

Consider a proof mass attached to a linear spring and anchored inside a housing in a reference frame which is free from a gravitational field (see Figure 5). In this case, Newton's Second Law is simply: $m\ddot{x} = F$, where m is the mass of the proof mass, \ddot{x} is acceleration along the x axis and F is the force applied to the housing. When a specific force acts on the housing, it will accelerate with constant acceleration, a , with respect to the given reference frame. This will cause the proof mass to move

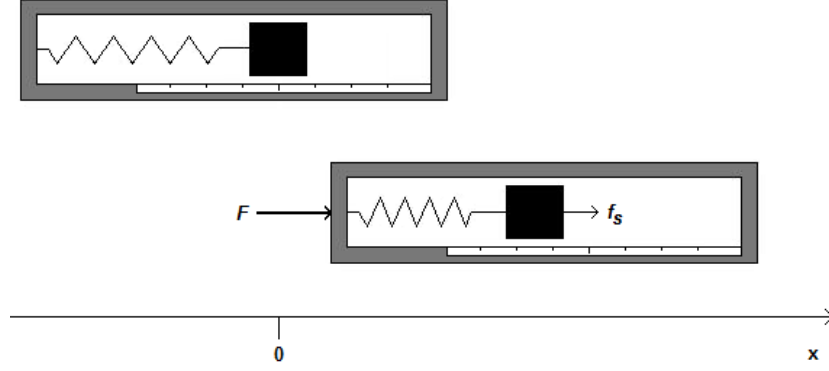


Figure 5: Accelerometer.

relative to the housing, the spring to compress, and the resultant spring force, f_s , to act on the mass. Let x_{pm} denote the position of the proof mass relative to the housing and x_h denote the position of the housing in the external reference frame. Now, the position of the proof mass in the external reference frame is $x = x_h + x_{pm}$ and its acceleration is $\ddot{x} = \ddot{x}_h + \ddot{x}_{pm}$. The spring force, given by Hooke's law, is: $f_s = -kx_{pm} = m\ddot{x}_{pm}$, where k is the spring constant. Therefore, by Newton's Second Law of Motion, the equation of motion for the proof mass is: $\ddot{x}_{pm} + \frac{k}{m}x_{pm} = -a$. Assuming initial conditions of $x_{pm}(t = 0) = 0$ and $\dot{x}_{pm}(t = 0) = 0$, the solution to the proof mass's differential equation is:

$$x_{pm}(t) = \frac{-ma}{k} \left[1 - \cos \left(t\sqrt{\frac{k}{m}} \right) \right] \quad (13)$$

Thus, the position of the proof mass relative to the housing is proportional to the applied acceleration (with proportionality constant $\frac{m}{k}$). If f_s or x can be measured, a can be found in which case this device is now an accelerometer. While this constitutes a simple example of an accelerometer, devices in use today are based on the same fundamental principles (i.e. somehow measuring the relative motion of a proof mass to solve for acceleration). Now, suppose this simple accelerometer is placed in an area where it is under the influence of a gravitational field, but no specific forces act on the housing (e.g. freefall). Newton's Second Law becomes (assuming $m_g = m_i$,

that is, inertial and gravitational mass are the same): $\ddot{x} = a + g$, where g is the gravitational acceleration vector. This gravitation vector will act to accelerate not only the housing itself, but also the proof mass and the spring. By Newton's Law of Gravitation, the gravitational acceleration of the housing and all of its components is the same (assuming the gravitational acceleration, g , is constant over the housing). Now the motion of the proof mass in the external frame becomes: $\ddot{x} = g$. Likewise, $\ddot{x}_h = g$. Thus,

$$\ddot{x} = \ddot{x}_h + \ddot{x}_{pm} \Rightarrow g = g + \ddot{x}_{pm} \Rightarrow \ddot{x}_{pm} = 0 \Rightarrow x_{pm}(t) = 0 \quad (14)$$

and there is no motion of the proof mass relative to the box. In other words, the accelerometer is accelerating in a gravitational field, but measures no acceleration! That is, an accelerometer does not directly sense the presence of a gravitational field, only specific forces resulting from applied, action or contact forces. To reiterate, accelerometers do not sense gravitational acceleration. They will, however, sense reactions from gravitational field forces. For example, if an accelerometer oriented along the “down” axis in a NED reference frame were placed on the surface of the earth, it would sense the reaction to the gravitational force provided by the earth's surface. Finally, in accordance with the principle of equivalence, the accelerometer cannot distinguish whether this reaction is a result of gravitation, rotation, or an applied force. This trait is the key behind the concept of the gravity gradiometer [10].

2 Accelerometers at a known distance apart

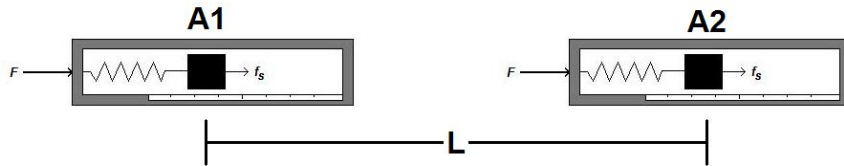


Figure 6: A Simple Gravity Gradiometer.

Suppose that an accelerometer is used in an attempt to measure gravity reaction forces. This device represents an gravimeter - a single accelerometer oriented

to measure gravity along some axis of interest. While gravimeters are very successful in measuring gravity information on fixed platforms (such as the ground), their accuracy plummets when used on a moving base platform - particularly in the airborne environment. Aircraft vibrations from engines, pumps, etc., combined with accelerations from turbulence, engine thrust changes, and maneuvers to render accurate gravity measurements difficult due to the single accelerometer's inability to distinguish between inertial and gravitational acceleration.

Now suppose that a pair of accelerometers are mounted in-line along some axis at some known distance apart, as in Figure 6. If the accelerometer readings are differenced and then divided by the length between them, a gravity gradient has been measured:

$$\text{gravity gradient} = \frac{A2 - A1}{L} \quad (15)$$

By measuring the gravity gradient, host vehicle accelerations of the first order are intrinsically rejected, thus leaving only the differential acceleration of the earth's gravity field over some unit distance [11]. It should be noted that the distance between the accelerometers is critical for gradiometer performance. If the distance is too large, the host vehicle accelerations sensed by each accelerometer may be substantially different and thus difficult to difference out. If the distance is too small, gradiometer sensitivity will be compromised. In reality, accelerometer misalignment, scale factor differences and other noise sources can corrupt the gradient measurement. In order to measure the full tensor of gravity gradients, a minimum of three accelerometer pairs are oriented along three axes. It should also be noted that the terms "gravity gradient instrument", "GGI", and "gravity gradiometer" are used interchangeably in this research.

An Inverse Problem

Suppose that the shape of the earth and the density variations within it are exactly known. With this information, a unique value of the actual potential, W , can be found. That is, the determination of the actual potential is a “direct” problem. Now suppose that the actual potential is known (perhaps by GGI measurements) and the shapes and density variations that caused it are to be calculated (i.e the “inverse” problem). It is, in fact, impossible to uniquely solve for these potential generating masses without additional information. There are an infinite number of possible combinations of mass location and density variations that could create a certain value for the potential. To determine the solution (or to better estimate it), additional information must be provided. This phenomenon may hamper GGI-based terrain avoidance performance.

Problem Statement

While a limited number of navigation performance studies using information from a gravity gradiometer have been accomplished in the past, the high error level associated with using this sensor on an aircraft rendered successful navigation mainly a function of the assumptions regarding the performance of future gradiometers. Because of these errors and the inverse problem, relatively little research into GGI based navigation and terrain avoidance is available in open literature. Since airborne gravity gradiometers have seen remarkable improvements over the past decade [12], this research aims to investigate the feasibility of using a modern GGI, which must provide *real-time* gradient measurements, in the role of passive navigation and terrain avoidance with emphasis on military type flight environments by rigorously examining simulated GGI signals at a variety of representative flight conditions and comparing them to those proven in previous works to yield navigation performance improvements. The signals will be analyzed with respect to their ability to be matched to a map. It should be noted that most of the representative flight conditions to be examined have not been previously investigated in open literature.

This research is part of the first phase of a three-phase plan. Phase one is a feasibility study where a GGI will be selected and its model developed and implemented to investigate signal levels at representative flight conditions. Phase two involves procuring a GGI and integrating it as a sensor in a navigation system. This phase will include sensor model refinements and validation and will culminate with a navigation demonstration on a land-based vehicle. The final phase involves flight-testing of the navigation system in an aircraft to demonstrate military utility and validate the overall modeling effort.

Feasibility

First and foremost, the definition of feasibility within the scope of this study must be defined. The following stipulations will apply:

- Navigation will be performed onboard an airborne aircraft.
- The gravity gradiometer will be $1m^3$ in size and weigh $450kg$, maximum.
- “Modern GGI” is defined as a gravity gradiometer projected to be available within the next 10 years.
- Passive Navigation will be based on a map-matching method and performance improvements, if any, will be measured against unaided Nav Grade IMUs.
- Terrain avoidance performance will be based on the GGI’s ability generate a signal that is useable to predict terrain impact is imminent within 1.5 seconds [13].

Research Objectives

With feasibility defined, the research objectives for this study are presented. It should be noted that sensor cost was not considered for this study. Additionally, further assumptions and limitations will be addressed in subsequent chapters.

- Investigate modern gravity gradiometers available for introduction into an aircraft.
- Select gradiometers, based on noise, bandwidth, sampling rate, size and weight, most suitable for aircraft navigation and terrain avoidance.
- Develop models of the GGI sensors deemed most usable for aircraft navigation and terrain avoidance.
- Generate gravity gradient maps that represent realistic values produced by the earth.
- Examine simulated GGI signal variations in response to factors including altitude, airspeed, terrain variation, and formation effects.
- Attempt to classify signal threshold levels for useful terrain avoidance and navigation via map-matching.
- Determine if the selected GGI meets signal threshold requirements.
- Recommend needed gradiometer improvements, if any, and appropriate ways to integrate the GGI signal into navigation (with emphasis on map-matching methods) and terrain avoidance systems.

Preview

This thesis is divided into four subsequent chapters. Chapter II presents the literature review for this research. Divided into three parts, it encompasses the history of gravity gradiometry, a review of modern airborne gravity gradiometer technology, and a review of previous gravity gradiometer based navigation and terrain avoidance research. Chapter III highlights the problem setup and methodology. It covers how gravity gradient maps were constructed, how the GGI was modeled, and the tests that were executed in order to determine navigation and terrain avoidance feasibility. Chapter IV provides the results and analysis and serves to report the findings from the feasibility study. Chapter V is a closing discussion that will conclude the thesis

with significant contributions and insights. Also, some challenges and future research recommendations will be discussed.

II. Literature Review

History of Gravity Gradiometry

Gravity gradiometry began in 1890 when Baron Roland von Eotvos, a Hungarian physicist, developed an instrument known as the torsion balance to measure the minute variations in gravity over a short distance. The torsion balance was made of a metal beam, suspended by a wire, with weights at each end (similar to a dumb-bell). If gravity varied with position along the axis the weights were placed on, the force exerted on each weight would be different, thus causing a rotational force on the beam and in turn causing the wire to twist. Eotvos measured the amount of twist to determine the gravity gradient.

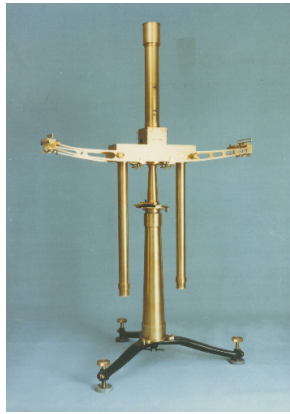


Figure 7: Eotvos' Torsion Balance - The First Gravity Gradiometer

In 1901, Hugo de Boeckh, head of the Hungarian geologic survey, convinced Eotvos to test the real-world usefulness of the torsion balance. The device was used to map the shape of a frozen lake basin, which was already well known from previous summertime measurements made from a line and sinker. The test was a resounding success - the contour map generated via the torsion balance matched the previously made maps. Eotvos and Boeckh then completed more difficult geological surveys in the region. Word of Eotvos' torsion balance success quickly spread to oil prospectors around the world - gravity gradiometry had officially been born.

After World War I, American geologists used the torsion balance in an attempt to find salt domes - mushroom shaped underground geologic structures that often have

oil and gas deposits along their sides. Since salt is less dense than most rock, it exerts a weaker gravitational force relative to the earth surrounding it. As such, gravity gradients can highlight a buried salt dome. In 1924, geologists from the Amerada Hess Corporation struck paydirt by finding a hidden salt dome via measurements made from a torsion balance. By 1935, the use of gravity gradiometry for subsurface surveys was routine - particularly in the oil business [14].

The early success of the torsion balance, however, did not secure its long term use. The instrument was fairly difficult to use in the field. In order to make a reliable measurement, geologists had to first clear a 100 meter long swath in eight directions (star pattern) from the location of the torsion balance to prevent the mass of trees and rocks from corrupting measurements. Additionally, a small building had to be erected in order to protect the instrument from wind and temperature changes. To get an idea of the sensitivity of the torsion balance, measurements could be corrupted by the large belt buckles often worn by geologists! To compound the problem, gradiometer data was often misinterpreted which led to false survey results. These issues led to the boom in the use of gravimeters, devices which measure gravity rather than the change of gravity per unit distance, for surveys. Gravimeters are inherently less sensitive than gradiometers and thus did not require extensive measurement site preparation. Furthermore, the data from gravimeters was easier to interpret. This led to increased investments in gravimeters and by the 1950s, gravimeters had replaced gradiometers in most gravity field measurement applications [4]. For the time being, the gravity gradiometer was gone but certainly not forgotten.

In the 1970s, both US and Russian navies realized that the accuracy of submarine launched ballistic missiles (SLBMs) depended greatly upon precise knowledge of gravity at the time of missile launch. Since gravimeter measurements plummet in accuracy on moving platforms, a new wave of research into gravity gradiometers was launched. [4] Around the same time, the US Air Force had abandoned gravimeter systems for airborne surveys due to the fact that kinematic accelerations overwhelmed the anomalous gravimetric signal on the aircraft in flight. By the early 1980s, Bell

Aerospace Textron had successfully developed a moving base full tensor gravity gradiometer. The instrument, developed by Ernest Metzger, was selected by the Navy (with over 400 million USD in development costs) for gravity compensation requirements of its trident submarine inertial navigation systems and by the Air Force Geophysics Laboratory (AFGL) for its region airborne gravity survey system. In the mid 1980s, part of this technology was declassified and eventually used in the 1987 Defense Mapping Agency (DMA) funded flight test of the Gravity Gradiometer Survey System (GGSS). This test, accomplished by AFGL, constituted the first airborne gravity gradiometer survey published in open literature. The GGSS consisted of Bell/Textron (now owned by Lockheed Martin) gradiometers which were installed in the back of a van along with other support equipment. Since much of the GGSS was hardwired into the van, the van was simply loaded into a C-130 Hercules aircraft for flight test. The survey was flown over southwestern Oklahoma and northern Texas and, while high in noise ($\sim 40 E_o/\sqrt{Hz}$), was able to measure low frequency effects corresponding to subterranean anomalies in the area [15]. In all, the GGSS represented an outstanding achievement that sparked a flurry of airborne gradiometer development. The speed at which aircraft can fly, as well as the ability to access remote areas of land, made much larger and quicker surveys a reality. Many oil and other valuable natural resource mining industries had renewed interest in gravity gradiometers.

Today, airborne gravity gradiometers are used mainly for geological surveys in the hunt for valuable natural resources. Companies such as Bell Geospace, ARKex, Gedex and Fugro provide airborne gravity gradient surveys to customers who desire such data. Also, geophysicists use them to better understand our planet's gravity field and overall structure. For this role, gradiometers have been installed and used with success on ships, aircraft and satellites [4, 16–18].

Airborne Gravity Gradiometer Technology

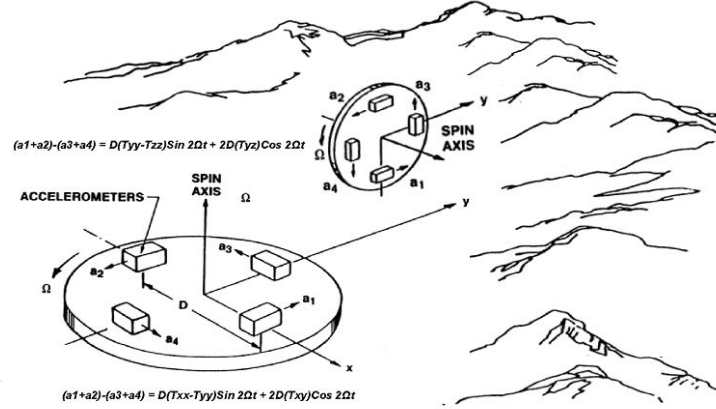


Figure 8: Rotating Accelerometer Schematic, taken from [3].

Rotating Accelerometer Gravity Gradiometer. The rotating accelerometer Gravity Gradient Instruments (GGIs) are based on the Bell Aerospace/ Textron design (now owned by Lockheed-Martin) and use, at a minimum, 2 pairs of conventional accelerometers mounted opposite of each other on a spinning disk to measure gradients in the plane of rotation (i.e. normal to the axis of spin) as shown in Figure 8. Each accelerometer consists of a mass which is pivoted (i.e. a pendulum) and a sensor that measures the offset position of the pendulum along its path of travel. Included within each accelerometer is electronic circuitry that restores the pendulum to its base position through the use of electromagnets and constrains the pendulum to minimal movements along the input axis of the accelerometer [19]. This applied electric signal represents the output of the accelerometer and serves as a measure of the acceleration of the pendulum brought on by any forces applied to the accelerometer. The measurements from each pair of accelerometers can be resolved into two gradients in the plane of the rotating disc by accounting for the distance between each accelerometer, the rate at which the disc is spinning, and the difference in the measured accelerations between each pair. In order to obtain a full gravity tensor (5 independent gradients), three rotating discs must be used since each disk can only measure 2 components of

the tensor. The tensor components measured in the external coordinate axis are then found by using the appropriate linear combination of the six GGI outputs.

The three rotating accelerometer GGI outputs are given as follows:

$$xz \text{ plane} : (A_1 + A_2) - (A_3 + A_4) = 2R_d \sin \Omega t (T_{zz} - T_{xx}) + 4R_d T_{xz} \cos 2\Omega t, \quad (16)$$

$$yz \text{ plane} : (A_1 + A_2) - (A_3 + A_4) = 2R_d \sin \Omega t (T_{zz} - T_{yy}) + 4R_d T_{yz} \cos 2\Omega t, \quad (17)$$

$$xy \text{ plane} : (A_1 + A_2) - (A_3 + A_4) = 2R_d \sin \Omega t (T_{yy} - T_{xx}) + 4R_d T_{xy} \cos 2\Omega t \quad (18)$$

More specifically, the derivation of the measured output from a single disk is presented: From the geometry of the disk and placement of the accelerometers shown

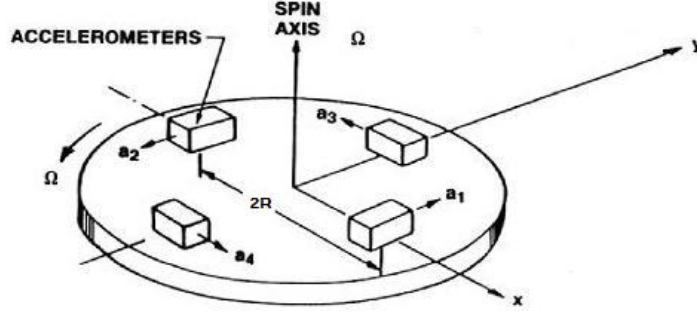


Figure 9: Single Rotating Accelerometer Disk

in Figure 9, an equation for the acceleration measured by accelerometer A_1 can be derived [11]:

$$A_1 = (a_y + T_{yx}R_d \cos \Omega t + T_{yy}R_d \sin \Omega t) \cos \Omega t - (a_x + T_{xx}R_d \cos \Omega t + T_{xy}R_d \sin \Omega t) \sin \Omega t \quad (19)$$

where a_y is the gravitational field induced acceleration at the center in the y direction, a_x is the gravitational field induced acceleration at the center in the x direction, R_d

is the distance from the center of the disk to the accelerometer, and Ω is the angular velocity of the disk about its spin axis.

Expanding Equation 19 gives:

$$\begin{aligned} A_1 = & (a_y \cos \Omega t + T_{yx} R_d \cos^2 \Omega t + T_{yy} R_d \sin \Omega t \cos \Omega t) - \\ & (a_x \sin \Omega t + T_{xx} R_d \cos \Omega t \sin \Omega t + T_{xy} R_d \sin^2 \Omega t) \end{aligned} \quad (20)$$

Recalling the following trigonometric identities: $\cos^2 \Omega = \frac{1}{2} + \frac{1}{2} \cos 2\Omega$, $\sin^2 \Omega = \frac{1}{2} - \frac{1}{2} \cos 2\Omega$, and $\sin \Omega t \cos \Omega t = \frac{1}{2} \sin 2\Omega t$ with $T_{yx} = T_{xy}$, Equation 20 gives:

$$\begin{aligned} A_1 = & a_y \cos \Omega t - a_x \sin \Omega t + T_{xy} R_d \left(\frac{1}{2} + \frac{1}{2} \cos 2\Omega t \right) + T_{yy} \frac{R_d}{2} \sin 2\Omega t - \\ & T_{xx} \frac{R_d}{2} \sin 2\Omega t - T_{xy} R_d \left(\frac{1}{2} - \frac{1}{2} \cos 2\Omega t \right) \end{aligned} \quad (21)$$

Combining like terms of Equation 21 gives:

$$A_1 = a_y \cos \Omega t - a_x \sin \Omega t + T_{xy} R_d \cos 2\Omega t + \frac{R_d}{2} \sin 2\Omega t (T_{yy} - T_{xx}) \quad (22)$$

Since the opposing accelerometer (A_2 in this case) is always π radians away from A_1 , the acceleration measured by A_2 can be derived by replacing Ωt with $\Omega t + \pi$ in Equations (1)-(4):

$$A_2 = -a_y \cos \Omega t + a_x \sin \Omega t + T_{xy} R_d \cos 2\Omega t + \frac{R_d}{2} \sin 2\Omega t (T_{yy} - T_{xx}) \quad (23)$$

Summing Equation 22 and Equation 23 gives:

$$A_1 + A_2 = 2T_{xy} R_d \cos 2\Omega t + R_d \sin 2\Omega t (T_{yy} - T_{xx}) \quad (24)$$

Replacing Ωt with $\Omega t + \frac{\pi}{2}$ and $\Omega t + \frac{3\pi}{2}$ in Equations 19-23 gives the relationship between A_3 and A_4 :

$$A_3 + A_4 = -2T_{xy} R_d \cos 2\Omega t - R_d \sin 2\Omega t (T_{yy} - T_{xx}) \quad (25)$$

Subtracting Equation 25 from Equation 24 gives the basic element of measurement from a rotating disc gravity gradient instrument:

$$(A_1 + A_2) - (A_3 + A_4) = 2R_d \sin \Omega t (T_{yy} - T_{xx}) + 4R_d T_{xy} \cos 2\Omega t \quad (26)$$

This combination signal (Equation 26), called a bandpass signal, is normally low-pass filtered and digitized, and then demodulated at $\sin 2\Omega t$ and $\cos 2\Omega t$ to obtain T_{xy} and $(T_{yy} - T_{xx})$. Also note that if the accelerometers are perfectly aligned, scale factor balanced, and linear, no angular or wheel acceleration terms appear in Equation 26. Additionally, any residual linear acceleration sensitivity will be modulated at Ω and will not appear after the demodulation at 2Ω . In essence, the perfect rotating accelerometer gradiometer, if mounted on a stabilized platform, is not sensitive to vehicle accelerations to the first order [11]. However, sensor misalignment, scale factor differences of each accelerometer, and other real-world errors create nonlinear coefficients that allow noise into the gradient measurements.



Figure 10: Bell Geospace Air-FTG, taken from [3].

The Bell Geospace Air-FTG is a 3 disc, rotating accelerometer type gradient instrument (shown in Figure 10) that was launched in 2002. It is based on Lock-

heed Martin’s 3D FTG and includes proprietary post mission processing upgrades for improved performance. Each disc is mounted such that their axes of rotation are mutually perpendicular and each make the same angle with the vertical (Figure 11). This is known as an umbrella configuration. The GGIs are also mounted on a three-gimballed stabilizing platform.

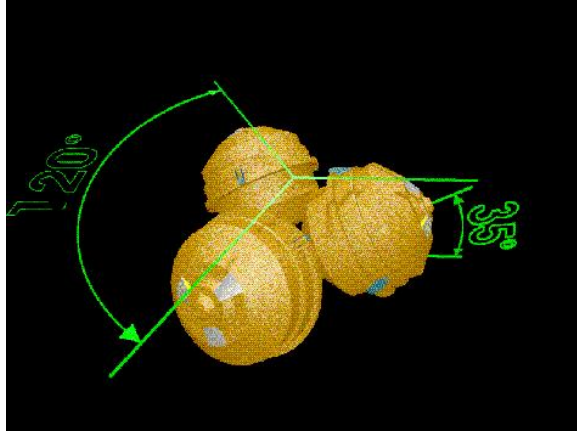


Figure 11: Bell Geospace Air-FTG, taken from [3].

To minimize bias from the orientation or movement of the instrument, the assembly of rotating discs is rotated at a constant rate (300 deg/hr) about a vertical axis. The Air-FTG is widely used in airborne gravity gradient mapping in the USA, Canada, South Africa, Botswana, Zambia, and Mali. With a weight of roughly 450kg and requiring approximately 1 cubic meter of space (with data acquisition equipment), the Air-FTG is flown primarily in the Cessna Grand Caravan - though it has been carried by zeppelins (airships) for improved stability and reduced noise [20]. The Cessna’s propeller speeds, engine noise, vibrations and other disturbances acting on or within the Air-FTG are monitored during each flight and compensated for during post-flight data processing. Since, in the real world, no instrument is perfect, there is some non-linear behavior within the gradiometer. These nonlinear coefficients can cause noise due to host vehicle accelerations and disk bearing noise within the desired bandwidth. This noise is not a direct measurement of host vehicle accelerations but instead is the various products of acceleration and the accelerometer nonlinear

coefficients. Thus, if the coefficients are known and the host vehicle accelerations are measured, the noise can be determined and eliminated. This is exactly what BellGeo's proprietary High Rate Post Mission Compensation (HRPMC) does. By recording the host vehicle accelerations and then multiplying these accelerations of the correct order to the assumed coefficients, the nonlinear coefficients are found. A numerical regression technique is then performed on each coefficient until the noise is minimized. This HRPMC technique has been proven adequate for removing noise for host vehicle accelerations of around 0.1g standard deviation. Note that two other factors that can induce measurement noise are misalignment of the combination of accelerometers within each GGI with respect to the plane of rotation and any scale factor difference between the two accelerometer pairs. Both of these issues are addressed before each survey through calibration techniques. Additionally, gravity gradient measurements are extremely sensitive to gravitational field disruptions caused by nearby masses. Such masses include the host vehicle structure and stores. Since these masses move with the host vehicle, it is critical to remove their influence from the measured data. This process is accomplished by flying a specially designed survey pattern. Airborne gradiometer surveys are always conducted in an orthogonal pattern which results in many crossing points. Data from these points is then used to remove host vehicle gravitational effects in part of a Low Rate Post Mission Compensation (LRPMC) process [21].

For relatively good resolution, surveys are typically flown using drape methods at 50-100m above the ground since the signal strength in the Air-FTG drops off with the cube of the distance to the target. The current resolution of the Air-FTG, after HRPMC and pre-flight calibration, is approximately 5 Eotvos at a gradient production rate of 1Hz with a spatial resolution of several hundred meters. Without the aforementioned processing steps, the Air-FTG noise levels are approximately 12-15Eo [3, 21]. Note that raw accelerometer data is sampled at over 100Hz but after compensation and demodulation processes, gradients are produced at 1Hz [22]. It is also noted that gradiometer noise specifications are often given in terms of a noise

spectral density (NSD) having units of E_o/\sqrt{Hz} . Furthermore, gravity gradiometer manufacturers claim zero-mean Gaussian white noise for their GGIs. These white noise characteristics are only valid over a certain range of frequencies (or bandwidth) - generally from 0 to the Nyquist rate or a low pass filter cutoff frequency [23].

The Falcon AGG is another rotating accelerometer type gravity gradiometer. The technology was jointly developed by BHP Billiton and Lockheed Martin and recently sold to Fugro NV. The Falcon was considered the first airborne gravity gradiometer - initially flying in 1997 and used for survey work in 1999. Fugro has successfully used the Falcon for airborne gravity surveys in 4 aircraft (3 Cessna Grand Caravans and 1 helicopter). This system measures only two components of the gravity tensor (T_{xz} and T_{yz}) and uses these to calculate the vertical component of the tensor, T_{zz} . The vertical gravity gradient RMS noise is around $5E_o$ after post flight processing techniques similar to those of the Bell Geospace Air-FTG. A 6th order Butterworth filter with a cutoff wavelength of $400m$ is typically used in Falcon AGG data processing [24, 25]. Assuming a survey speed of $60m/s$, this corresponds to a cutoff frequency of approximately $0.15Hz$. Dimensions and weight of the Falcon and its data acquisition equipment are similar to those of the Air-FTG.

The ARKeX FTGeX is a GGI very similar to the previously mentioned instruments. It too is based on Lockheed-Martin's 3D-FTG and is often used with ARKeX proprietary technology known as BlueQube. BlueQube involves the combination of gravity gradiometry, magnetic gradiometry, digital terrain mapping (LiDAR), and digital video to construct a complete map of the surveyed area. As with the Air-FTG and Falcon AGG, RMS noise of the FTGeX is around $5E_o$ after post-flight processing, while its size and weight are also similar [26].

While several versions of the rotating accelerometer GGIs have been presented, one final point about this type of gravity gradiometer must be made. These are the *only* type of gradiometers successfully used in airborne surveys. All other types discussed herein are either in early flight test or a laboratory setting.

Superconducting Gravity Gradiometer. Superconducting Gravity Gradiometers (SGGs) get their name from the type of accelerometer that is used in the instrument. These accelerometers rely on the Meissner effect and flux quantization to levitate a proof mass and measure the force required to hold that mass in place. Pairs of superconducting accelerometers provide gradient measurements with low noise and high resolution. They do so because superconductivity and extremely low temperatures naturally give low noise, negligible scale factor drift and mechanical stability. Superconducting circuits can also be balanced such that their responses to gravity gradients are largely independent of all linear and angular accelerations applied to the instrument. This balance stems from the ability to regulate currents in the various superconducting loops. It is because of this balance that the scale factors remain perfectly stable in time [27].

Diving deeper into the physics behind the SGG, the accelerometer itself is examined. First, a brief overview of superconductivity and the Meissner effect is presented. A superconductor is defined as an “element, inter-metallic alloy, or compound that will conduct electricity without resistance below a certain temperature” [28]. Meissner discovered that when a superconductor is placed in a weak external magnetic field, the field only penetrates the superconductor for a very short distance, after which it drops rapidly to zero. In essence, a superconductor will expel all magnetic fields (time variant and invariant). A magnet moving by a “normal” conductor induces currents in the conductor. This is the principle on which an electric generator operates. But, in a superconductor, the induced currents exactly mirror the field that would have otherwise penetrated the superconducting material - causing the magnet to be repulsed. The Meissner effect is so strong that a magnet can actually be levitated over a superconductive material, as shown in Figure 12 [29].

Flux quantization is a quantum phenomenon in which the magnetic field is quantized. This occurs in type II superconductors subjected to a magnetic field. Type II superconductors are characterized by their gradual transition from the superconducting to the normal state as temperature increases. They tend to be made

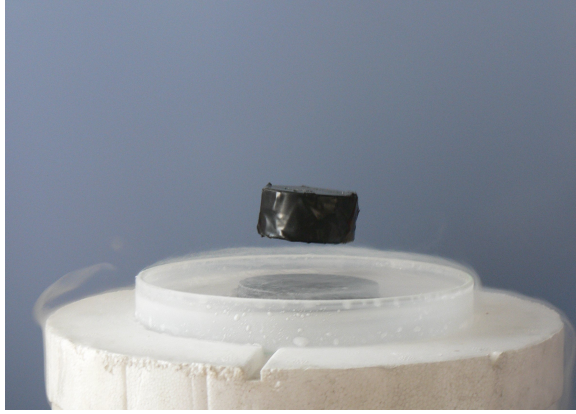


Figure 12: A Magnet Levitating above a Superconductor due to the Meissner Effect, taken from [30].

of metal alloys or complex oxide ceramics. Below a temperature dependent critical magnetic field H_{c1} , all magnetic flux is expelled according to the Meissner effect and perfect diamagnetism is observed. Up to a temperature dependent second critical field value, H_{c2} , flux penetrates in discrete units while the bulk of the material remains superconducting. Within this group of type II superconductors are high temperature superconductors. High-temperature superconductivity allows some materials to support superconductivity at temperatures above the boiling point of liquid nitrogen (approx. 77° Kelvin). As such, they offer the highest transition temperatures of all superconductors. The ability to use relatively inexpensive and easily handled liquid nitrogen as a coolant has increased the range of practical applications of superconductivity [31]. Unfortunately, this higher temperature of operation will make a system intrinsically noisier, thus high temperature superconductors are not suited for gravity gradiometer use [27]. Instead, SGs must use type II low temperature superconducting material maintained at approximately 4° Kelvin in the circuits (loops) within the accelerometers.

With superconductivity, the Meissner effect, and flux quantization now defined, an example of a superconducting accelerometer is presented. Suppose a time varying current is passed through a coil outside of a superconductor. This coil will send out a field that will induce a surface current on the superconductor. Noting that

the superconductor will expel all magnetic fields up to a material and temperature dependent critical field (i.e. the Meissner effect), this surface current will interact with the current in the coil to produce a repulsive force between the two objects. Using image theory, it can be shown that the surface current on the superconductor is equivalent to having an image of the coil within the superconductor itself. This image coil is exactly the same distance below the surface as the real coil is above it as shown in Figure 13.

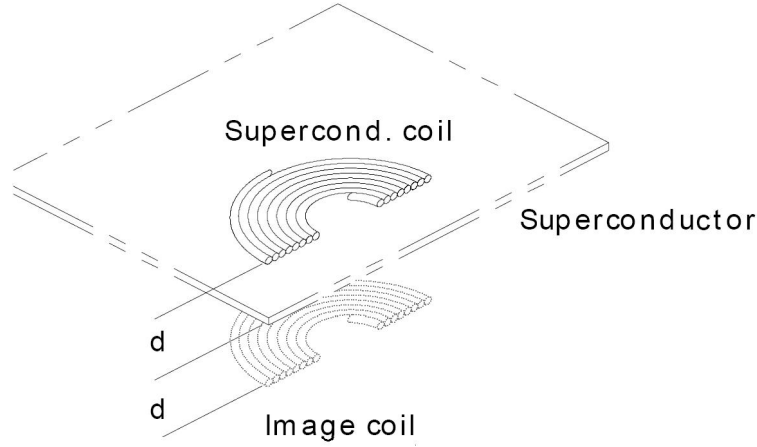


Figure 13: Coil and Image Coil near a Superconductor, taken from [32].

Now the field confined between the coil and superconductor is calculated: $B = \mu_o n_t i$, where μ_o is the permeability of the material (i.e. how susceptible it is to being magnetized), n_t is the turns per meter in the coil and i is the current in the coil. Recognizing that the total magnetic energy in the system is the field energy per unit volume times the volume of the space between the coil and superconductor:

$$\text{Magnetic Energy} = \frac{B^2}{2\mu_o} A_c d = \frac{1}{2} \mu_o n^2 A_c d i^2 \quad (27)$$

where A_c is the area of the coil and d the distance between the superconductor and the coil. Recall that:

$$\text{Magnetic Energy} = \frac{1}{2} L i^2 \quad (28)$$

where L is the inductance. Combining Equations 27 and 28 gives:

$$L = \mu_o n^2 A_c d + O(d^2) \quad (29)$$

Equation 29 shows that the inductance of the coil is proportional to its separation from the superconductor surface. Now, if the proof mass is made of superconducting material and is introduced in the vicinity of the coil, a repulsive force is present as long as current is flowing. This force is given by:

$$F = \frac{1}{2} \frac{\partial L}{\partial d} i^2 = \frac{1}{2} \mu_o n^2 A_c i^2 + O(d) \quad (30)$$

where the stiffness of this magnetic spring is determined by coil non-linearities.

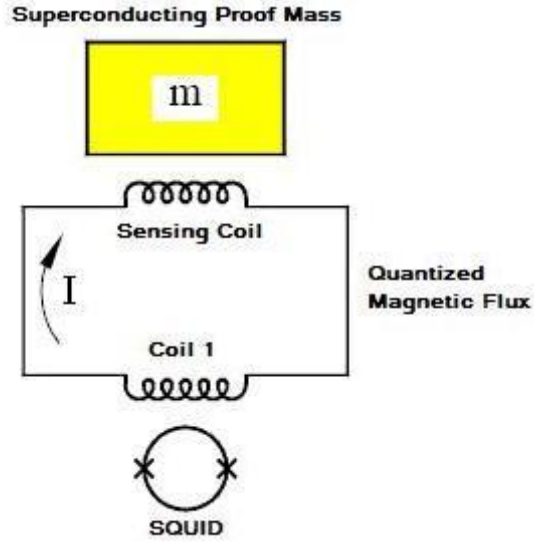


Figure 14: Superconducting Accelerometer Schematic, taken from [32].

Now a system where a closed superconducting loop levitates a superconducting proof mass (Figure 14) is constructed, noting that as the superconducting loop passes below its transition temperature, the magnetic flux in the superconducting loop remains absolutely stable (by flux quantization) and has no noise on it! Whenever the proof mass moves due to a change in acceleration, the coil inductance changes and

the current must change to preserve the original flux in the loop. This new current now exerts a different force on the proof mass in order to preserve the mass's location. This change in current is detected by a device called a SQUID. A SQUID is a Superconducting QUantum Interference Device and is the most sensitive sensor known to science. It is used to measure the changes in magnetic fields from which changes in currents can be determined. While the superconducting accelerometer is a sensor within a sensor, the SQUID's resolution of around $6.21 \times 10^{-21} \text{ Wb(Webers)}/\sqrt{\text{Hz}}$ is very accurate [33]. To put this in perspective, the SQUID can sense changes in magnetic fields approximately 16 orders of magnitude smaller than that produced by a small refrigerator magnet.

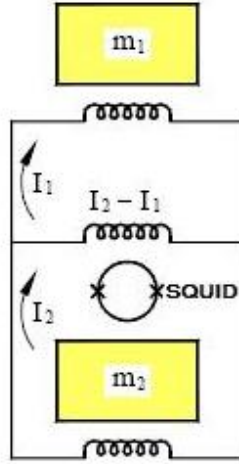


Figure 15: Superconducting Gradiometer Schematic, taken from [32].

Now that the superconducting accelerometer has been presented, the superconducting gravity gradiometer is easily shown. If two masses and two loops are used (Figure 15), differential movements in the proof masses can be detected. If both proof masses move the same distance in the same direction (downwards for example), flux quantization for each loop requires that I_1 and I_2 increase. Since these currents flow in opposite directions through the inductor next to the SQUID, they cancel each other out and the SQUID measures no change. However, if the masses move in different directions from one another (or if one moves and the other does not), I_1 and I_2 will

be different and the SQUID, because of its location, will pick up the difference in current. The current difference due to differential movement of the test masses is a direct result of a gravity gradient [32].

The first superconducting GGI was developed by Dr. Ho Jung Paik, a Univ. of Maryland professor, in conjunction with the NASA Goddard Cryogenics branch. This first version of the SGG consisted of three orthogonal pairs of superconducting accelerometers, each capable of measuring linear accelerations and the gravity gradient in all three axes. These superconducting accelerometers are made of high purity niobium (one of three Type II superconducting elements) that are kept cool in a Helium bath. Pancake coils are used to levitate the proof masses which are suspended initially by a weak spring [34].

An equivalent gravity gradient noise of $0.02 \text{ Eotvos}/\sqrt{Hz}$ has been demonstrated in a laboratory. While this is much better than rotating accelerometer GGIs, the Univ. of Maryland superconducting gravity gradient instrument (SGGI) fell short in intrinsic noise levels. The largest contributors to these noise levels were the earth's gravitational field and simulated host vehicle acceleration coupling into the gradient outputs through various mechanical errors. The instrument was also sensitive to thermal fluctuations of the helium bath, liquid helium motion and boiloff, and particle heating. Most errors could be controlled by precise design and alignment of the instrument or removed by measuring the disturbances (similar to techniques used in the rotating accelerometer GGIs). While NASA had interest in testing the SGG in space, funding was not available for such a mission [34].

Updates to the SGGI have involved making it operable in a moving base environment and include revised angular accelerometers for measuring the gradient along a single axis while using three linear accelerometers to correct for residual coupling to linear acceleration due to imperfect mass balances. This device, shown in Figure 16, is known as the UM-SAA (University of Maryland Superconducting Angular Accelerometer). To eliminate the thermal sensitivity issues, the updated SAA is cooled

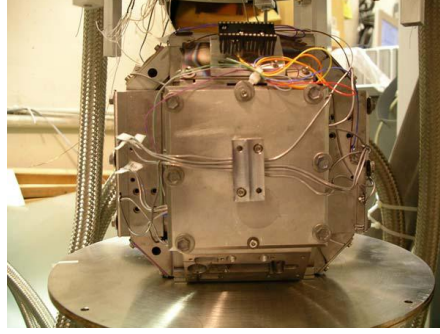


Figure 16: University of Maryland SAA, taken from [35].

by a closed cycle refrigerator based on a dual-stage pulse-tube cold-head known as a cryostat (Figure 17). The pulse-tube has no reciprocating piston in the cold-head thereby greatly reducing the harmonics of pressure pulses [35].



Figure 17: University of Maryland Cryostat, taken from [35].

The most recent University of Maryland airborne SAA has an estimated error of approximately $0.3Eo$ with a gradient production rate of $1Hz$ [35]. While bandwidth specifications are not clearly stated in open literature, Lumley et al. [32] cite “best spatial resolutions of a few hundred meters”.

The High Density Airborne Gravity Gradiometer (HD-AGG) is a another airborne superconducting GGI currently in test [36]. Created by researchers from the University of Maryland, University of Western Australia, Canadian Space Agency

and Gedex, the HD-AGG is a gradiometer designed to be carried in typical geological survey aircraft (likely the Cessna Grand Caravan) and has similar dimensions to airborne rotating accelerometer GGIs. Using licensed technology from the Canadian Space Agency, Gedex added an external disturbance isolation platform, known as the GeoMIM, to the sensor. Similar isolation platforms are found on the Space Shuttle [37]. The HD-AGG has reportedly achieved a gravity gradient error variance of less than $1Eo$ for measurements made every second -even in moderate turbulence ($1m/s^2$). Main [38] cites spatial resolutions of 60m at fixed wing survey aircraft speeds. As such, De Beers entered a strategic agreement with Gedex in 2006 for use of the HD-AGG in diamond detection [39].

Rounding out the list of superconducting GGIs currently in test is the ARKex Exploration Gravity Gradiometer (EGG). The EGG, shown in Figure 18, was developed by Dr. John Lumley at Oxford Instruments Superconductivity Ltd with assistance from ARK Geophysics Ltd (now a part of ARKeX) and was set to enter a trial deployment sometime in 2008 [26]. Though exact details of the EGG are not published, it likely uses technology from the UM-SAA and the University of Western Australia’s Orthogonal Quadrupole Responder (UWA OQR). Data from lab testing indicates similar T_{zz} error variance, noise properties, and gradient production rates as the HD-AGG [12].



Figure 18: ARKeX EGG, taken from [40].

Atom Interferometer Gravity Gradiometer. Atom Interferometer GGIs are based on quantum particle-wave duality. According to quantum mechanics, atoms behave like waves, as does light. Therefore, an interferometer (a device that shows the pattern of interference created by the superposition of two or more waves) that examines the properties of these atom-waves can be constructed. Because atoms have a finite mass, they are extremely sensitive to changes in gravity. In an Atom Interferometer accelerometer, “beams” of atoms are split into two parts via a beamsplitter and then allowed to travel a finite distance. If gravity is acting on these atoms as they travel over a certain length (i.e. the atoms are under the influence of gravity), the interferometer will pick up a phase shift that will affect the phase and/or frequency of the measurements [41].

The Stanford University Atomic Interferometer Gradiometer is a joint effort between Stanford University and the NASA Jet Propulsion Laboratory. It is currently a ground based sensor that will soon be tested as part of an all-atom, gravity-compensated inertial navigation system. The sensor will be mounted inside an RV and driven around the country to measure INS drift under realistic conditions. The gradiometer itself uses two quantum gravity accelerometers located a certain fixed distance apart (Figure 19). Inside these accelerometers, cooled Cesium atoms are condensed into a small cloud in a magneto-optic trap (MOT). The MOT, shown in Figure 20, consists of three pairs of counter-propagating laser beams along three axes centered about a non-uniform magnetic field and can collect up to 10^9 atoms [41].

After these atoms are collected, further cooling slows them to an RMS velocity of a few cm/s. The cold atoms are then launched vertically into an atomic-fountain so that the sensors have twice the available interaction time with the atoms for a given height. The atom interferometer, shown in Figure 21, is made up of Raman transitions between two hyperfine ground states with a $\frac{\pi}{2} - \pi - \frac{\pi}{2}$ pulse sequence. The first pulse creates an equal superposition of atoms in two hyperfine ground states (beam splitting). The second and third pulses redirect and recombine the atom-wave.

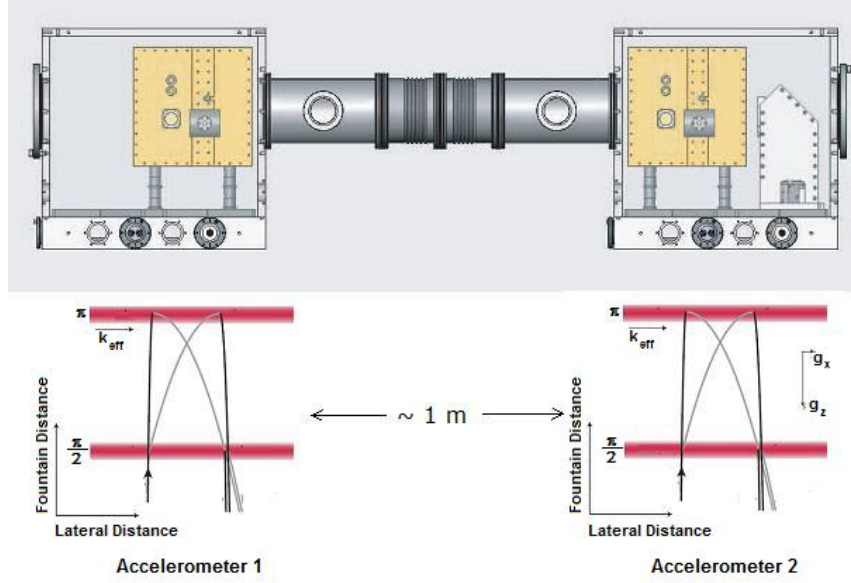


Figure 19: Schematic of the Stanford/JPL AI Gradiometer, taken from [42].

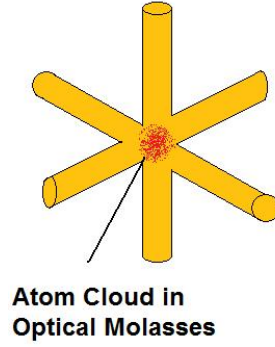


Figure 20: Magneto-Optic Trap

If gravity is acting on the atoms, their paths will be different and a phase shift will occur.

This phase shift is given by $\Delta\phi = 2k_r g T_i^2$, where T_i is the interrogation time (the time between light pulses), k_r is the Raman laser wave number and g is gravity. Gravity gradients are sensed and quantified when there is a mismatch between the readings of two fixed position accelerometers. Laboratory testing of the Stanford/JPL AI GGI has shown gravity gradient sensitivity of $10Eo/\sqrt{Hz}$, though improvements are expected [41]. It should also be noted that the gradiometer is approximately

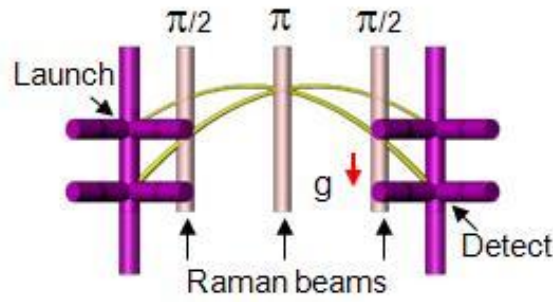


Figure 21: Atom Interferometer

1.25m tall (Figure 22) and also requires a fairly bulky array of control and laser frames, though efforts are being made to compact the system.

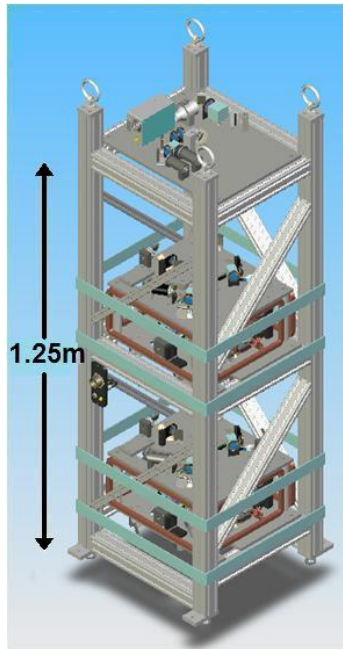


Figure 22: Stanford/JPL AI Gradiometer Dimensions

Navigation and Terrain Avoidance via Gravity Gradiometry - Previous Works

The use of GGIs as navigation aids has been investigated since the 1960s. Initial research efforts focused on real-time measurement of the gravity anomaly to provide improved unaided inertial navigation accuracy. Up until recently, there has been relatively little gravity gradiometer map-matching based aircraft navigation or terrain avoidance research published in open literature. In the mid 1970s, Metzger and Jircitano [43] presented an investigation into using gravity and gravity gradient map-matching to update an INS. Host vehicle velocities of up to approximately $250m/s$ were examined and it was found that gravity gradients provided better results due to better signal uniqueness.

In the mid 1980s, Bell Aerospace Textron began development on a system for enhanced passive submarine navigation. The system was to also provide real-time underwater terrain maps in areas where accurate terrain and obstacle data may be limited. Around that time, Affleck and Jircitano [44] proposed an INS that received position updates from a full tensor gradiometer/map-matching algorithm. The study was carried for an aircraft with a velocity of $100m/s$ and altitudes that ranged from 100-400m with promising results. A ship based navigation performance analysis was executed as well, also with encouraging results. However, very little detail about the navigation algorithm was given - likely due to the proprietary nature of the work. In 1994, Jircitano and Dosch [45] patented a Gravity Aided INS (GAINS) using a GGI and a vertical gravimeter for covert submarine navigation. Shortly thereafter, White and Jircitano patented “gradiometer based terrain estimation” [46]. The system(s) came to fruition in the mid 1990s and is known as the Lockheed-Martin Universal Gravity Module (UGM). The UGM consists of gravimeters and gravity gradiometers and implements a gravity map-matching algorithm to passively bound INS errors. It can also provide real-time underwater terrain maps based on estimation techniques applied to existing databases. In 1998, the UGM was successfully tested on the USS Memphis fast attack submarine [47]. Likely due to the covert nature of the business,

more recent information on the UGM or Jircitano's work was unable to be found in open literature.

Archibald [48] took a different map-matching approach for his PhD dissertation by using a neural network based map-matching algorithm to correlate gravity gradiometer measurements to an existing map. While his gradiometer model was relatively simple, his method matched points among large amounts of geophysical data and could be used as an acquire mode in a staged map-matching scheme.

In 1995, Gleason [23] presented a method to optimally generate gravity gradient maps and discussed the effects of gradiometer filtering in a terrain avoidance scenario as well as many other practical issues of a GGI-based map matching scheme. His work was the first found to address GGI sampling rate, gradient production rate, noise, and bandwidth in detail.

Blaylock et al. [49] then presented a terrain avoidance method using a gravity gradiometer (theoretically) on board an F-16. Likely an extension of Jircitano's work, the paper did not go into detail about an actual terrain avoidance algorithm. It did, however, present some estimated gradiometer performance requirements and various GGI signal levels as modeled obstacles were approached. Additionally, very little information was given on solving the inverse problem of calculating obstacle range from gravity gradients.

Though he did not use a map-matching algorithm, Jekeli [50] showed that future high accuracy IMUs could provide near GPS accuracy (5m error after 1 hour of dead reckoning) if the gravity error was compensated with a full tensor gravity gradiometer providing 1s updates with 0.1Eo of RMS noise. The premise is that if highly accurate accelerometers and gyroscopes are used, errors due to bias, scale factor/misalignments, platform tilt, white noise and random walk become very small relative to errors from uncompensated gravity. His research is an integral part of the DARPA Precision Inertial Navigation Systems (PINS) program. While this is arguably the more elegant and simpler approach to GGI based navigation, dead reck-

oning with this system still produced levels of position error that, over time, could hamper mission effectiveness. However, Jekeli also explains the drawbacks of matching GGI measurements to a pre-existing map. He states that worldwide map coverage, particularly in remote or mountainous areas is very limited. Also, the accuracy of gravity gradient maps is derived from major surveying efforts that are not easily augmented when improved accuracy is required. Finally, he cites the largest map-making hurdle to overcome: “the required gravitational accelerations are the horizontal components of the gravitational vector at altitude (for aircraft navigation), whereas the data typically are vertical components on the Earth’s surface (being the most easily measured)” [50]. The concerns are similar to those expressed in the early days of TRN (such as TERCOM) [2]. If the map making issues mentioned herein are solved, the following question is posed: If a gradiometer is providing INS gravity compensation and is already present within the system, why not use it to give map-matching based updates to the INS as well? This could potentially give the best of both worlds - low INS error under dead reckoning *and* the ability to correct the growing error over time.

Most recently, Richeson [51] provided an in-depth study of passive navigation via gravity gradient map- matching by developing an INS model that used an Extended Kalman Filter (EKF) to integrate gravity gradiometer and gradient map information in a position-updating algorithm. He showed that a gradiometer providing 1s updates with $0.001Eo$ of noise allowed a map-matching algorithm to meet GPS performance levels. While his research neglected terrain effects by focusing mainly on high altitude ($20km$) and high velocity ($2km/s$) scenarios seen by a hypersonic vehicle, an estimation of several important GGI signal threshold requirements, presented in Chapter 3, were deduced from his work. A schematic of Richeson’s navigation system is shown in Figure 23.

This research aims to advance knowledge and understanding of GGI-based aircraft navigation and terrain avoidance by more rigorously modeling the GGI and examining the signal itself over a wider range of flight conditions than previously studied. Note that the navigation portion of this study will focus on signal usefulness

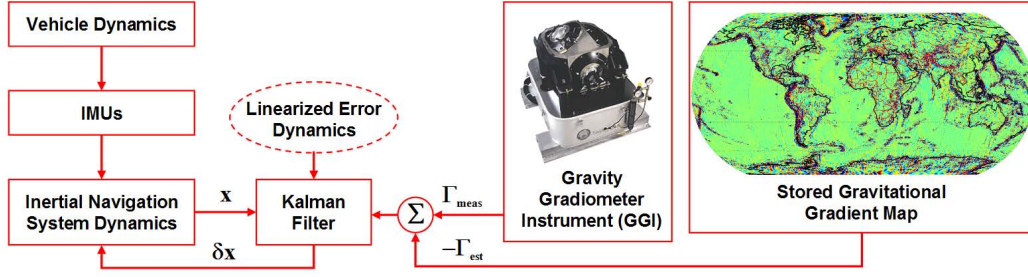


Figure 23: Richeson's Proposed Navigation System, taken from [51].

in map-matching scenarios rather than utility for INS gravity error compensation. Additionally, terrain avoidance scenarios involving a variety of hazardous obstacles will be examined in search of a useable impact warning threshold.

III. Methodology

Overview

To determine the feasibility of GGI based passive navigation and terrain avoidance, a buildup approach to simulating the GGI signal will be accomplished, followed by characterization of the signal level needed to successfully navigate or avoid terrain, and ultimately culminating in a comparison between required and achieved signal levels. First, it is desired to bound the performance metrics of GGI based navigation and terrain avoidance by simulating the GGI signal in the best and worst case scenarios. In a basic sense, these scenarios will be addressed by using areas with rapid terrain changes and areas with relatively low levels of terrain changes (i.e. mountainous versus flat terrain). A realistic representation of the earth's gravity gradients in these test areas will then be found via a combination of modeling techniques. Once acceptable maps have been generated for all test conditions, the simulated GGI signal will be determined by manipulating values from these maps with appropriate filtering and noise which mirror current or near-future GGI performance. Finally, the GGI signal, it's ability to be correlated to the original gradient maps, and ultimately, it's usefulness for navigation will be investigated qualitatively and by metrics based on previous works. A simple case study on the threshold signal levels indicating an imminent terrain collision will be accomplished as well. All work herein will be accomplished in Matlab[®] using the Microsoft Windows Vista 64 operating system on an Intel Core2Duo processor at 3GHz with 8GB of RAM. All code used in this research can be found in Appendix A.

Gravity Gradient Maps

Before the signal produced by the GGIs can be simulated, representative maps of gravitational gradients produced by the earth must be computed. The method chosen for map generation is the combination of gradients derived from the Earth Gravitational Model 1996 (EGM96) and gradients derived from a frequency domain based technique similar to the rectangular prism method shown in Chapter 1. The

EGM96 gradients will be used to account for long wavelength gravitational effects that generally correspond to anomalies well beneath the earth's visible topography while the rectangular prism-like method will be used to model terrain effects. The total gravitational gradient disturbance model used in this study is given by $T_{ij} = T_{ij_{EGM96}} + T_{ij_{Terrain}}$.

It must be stressed that these methods do not give perfect values for gravity gradients (nor do any methods at this time) but can be calculated relatively quickly and do represent realistic trends that should be seen by a GGI. It should also be noted that T_{ij} (the disturbing potential) and U_{ij} (the normal potential) can be defined differently depending on the application. For example, the oil and mining industries will often generate a terrain gradient model based on the assumption of constant terrain density and treat it as a part of U_{ij} in order to subtract it out and find density changes *within* the terrain. For navigation purposes, terrain generated gravity gradient information is a requirement. Knowledge of what corrections have been applied to map should be obtained when using gradient data from an outside source. For example, if a GGI based map-matching navigation system database were loaded with gravity gradient data that, unbeknownst to the user, had terrain effects removed, the system would be rendered useless.

Earth Gravitational Model 1996. As previously mentioned, gravitational potential outside of the attracting masses follows Laplace's equation [6]. Spherical harmonics are the angular portion of an orthogonal set of solutions to Laplace's equation (represented in spherical coordinates). This set of solutions is linear, thus the gravitational potential (or disturbing potential) may be modeled as some truncated series of spherical harmonics given below [52]:

$$T(r, \phi, \lambda) = \frac{GM}{ae} \sum_{n=2}^{N_{max}} \sum_{m=0}^n \left(\frac{a}{r}\right)^{n+1} (\overline{C}_{nm} \cos m\lambda + \overline{S}_{nm} \sin m\lambda) \overline{P}_{nm}(\cos \phi) \quad (31)$$

where r, ϕ, λ are the *geocentric* distance, latitude and logitude, respectively, GM is the product of the gravitational constant and the earth's mass, ae is the semi-major axis of the reference ellipsoid, N_{max} is the maximum degree of the spherical harmonic expansion, n, m are the degree and order, $\overline{C}_{nm}, \overline{S}_{nm}$ are the normalized geopotential coefficients and $\overline{P}_{nm}(\cos \theta)$ is the normalized associated Legendre function (Legendre functions are canonical solutions to the general Legendre differential equation that is encountered when solving Laplace's equation in spherical coordinates).

To date, there are a variety of global geopotential models which express the Earth's potential field in terms of spherical harmonic coefficients. These models are derived from satellite orbit tracking, terrestrial gravimetry, satellite altimetry, or airborne gravimetry (or a combination of these and other methods) and used to compute a gravimetric geoid [53]. The geoid (as it pertains to earth) is defined as the equipotential surface of the earth's gravity field coinciding with the mean sea level (MSL) of the oceans [54]. In very broad terms, the geoid is a mathematical figure of the earth's surface defined by gravitational measurements, as opposed to the smooth surface of a reference ellipsoid such as the WGS84 ellipsoid (see Figure 24). In other words, it is a surface which best fits the mean sea level without winds, ocean currents, or other disturbing forces. While the geoid and ellipsoid surfaces end up being similar in practice, the geoid surface varies, or undulates, approximately +85m to -106m with respect to the WGS84 reference ellipsoid and can change slightly depending on the method used to calculate the geoid.

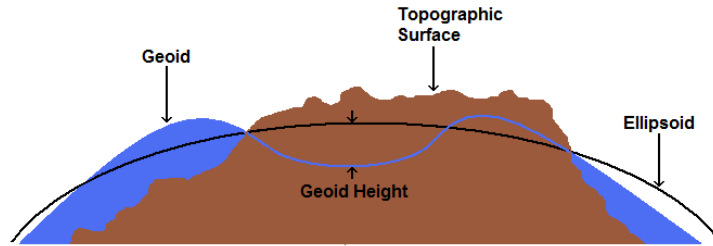


Figure 24: Exaggerated Illustration of the Geoid, Ellipsoid, and Topography.

One of the most commonly used models is EGM96. The EGM96 geopotential model is a composite solution consisting of spherical harmonic coefficients to degree and order 360 (n and m in Equation 31, respectively). EGM96 is made up of data from various contributors and completed by a joint effort between the National Imagery and Mapping Agency, NIMA (now the National Geospatial-Intelligence Agency, NGA), the NASA Goddard Space Flight Center and The Ohio State University. Some of the data sources include: gravity data from NIMA obtained by airborne surveys and other gravity collection processes, data from the GEOSAT Geodetic Mission (a US Navy satellite with a RADAR altimeter capable of measuring distances to the sea surfaces within 5cm), and data from the ERS-1 satellite [55].

The resolution of a particular model is given by $\pi R/n$ where R is the earth's average radius and n is the harmonic degree of the model. Using $R = 6371000\text{ m}$, the spatial resolution of the EGM96 model is approximately 56 km . Since the resolution of the EGM96 and rectangular prism maps often differ, a spline interpolation is often applied when fitting the EGM96 data to other grids. To better illustrate the shape of this particular geoid, EGM96 undulations for a tide-free system, with respect to the WGS84 ellipsoid, are shown in Figure 25.

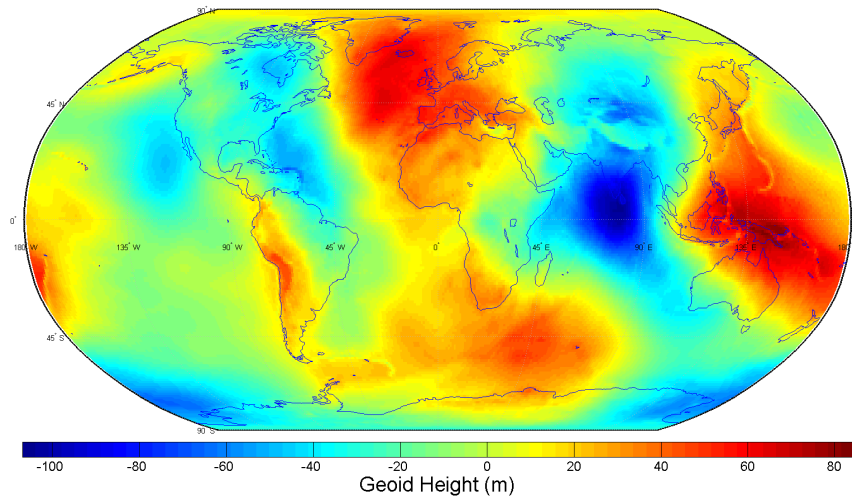


Figure 25: EGM96 Geoid Undulations with respect to the WGS84 Ellipsoid.

The five independent EGM96 gravitational disturbance gradients were calculated, using the parameters listed in Table 1, via modified freeware using the following relationships [53, 56]:

$$T_{xx_{EGM96}} = \frac{GM}{ae^3} \sum_{n=2}^{N_{max}} \sum_{m=0}^n \left(\frac{ae}{r}\right)^{n+3} (\bar{C}_{nm} \cos m\lambda + \bar{S}_{nm} \sin m\lambda) \times (a_{nm} \bar{P}_{n,m-2}(\sin\phi) + [b_{nm} - (n+1)(n+2)] \bar{P}_{nm}(\sin\phi) + c_{nm} \bar{P}_{n,m+2}(\sin\phi)), \quad (32)$$

$$T_{xy_{EGM96}} = \frac{GM}{ae^3} \sum_{n=2}^{N_{max}} \sum_{m=1}^n \left(\frac{ae}{r}\right)^{n+3} (\bar{C}_{nm} \cos m\lambda - \bar{S}_{nm} \sin m\lambda) \times (d_{nm} \bar{P}_{n-1,m-2}(\sin\phi) + g_{nm} \bar{P}_{n-1,m}(\sin\phi) + h_{nm} \bar{P}_{n-1,m+2}(\sin\phi)), \quad (33)$$

$$T_{xz_{EGM96}} = \frac{GM}{ae^3} \sum_{n=2}^{N_{max}} \sum_{m=0}^n \left(\frac{ae}{r}\right)^{n+3} (\bar{C}_{nm} \cos m\lambda + \bar{S}_{nm} \sin m\lambda) \times (\beta_{nm} \bar{P}_{n,m-1}(\sin\phi) + \psi_{nm} \bar{P}_{n,m+1}(\sin\phi)), \quad (34)$$

$$T_{yy_{EGM96}} = -\frac{GM}{ae^3} \sum_{n=2}^{N_{max}} \sum_{m=0}^n \left(\frac{ae}{r}\right)^{n+3} (\bar{C}_{nm} \cos m\lambda + \bar{S}_{nm} \sin m\lambda) \times (a_{nm} \bar{P}_{n,m-2}(\sin\phi) + b_{nm} \bar{P}_{nm}(\sin\phi) + c_{nm} \bar{P}_{n,m+2}(\sin\phi)), \quad (35)$$

$$T_{yz_{EGM96}} = \frac{GM}{ae^3} \sum_{n=2}^{N_{max}} \sum_{m=1}^n \left(\frac{ae}{r}\right)^{n+3} (\bar{C}_{nm} \cos m\lambda - \bar{S}_{nm} \sin m\lambda) \times (\mu_{nm} \bar{P}_{n-1,m-1}(\sin\phi) + \eta_{nm} \bar{P}_{n-1,m+1}(\sin\phi)), \quad (36)$$

where a , b , c , d , g , h , β , ψ , μ and η are the coefficients of the Legendre functions and are located in Appendix B. Table 1 summarizes the properties used in the EGM96 based gradient calculations.

Table 1: EGM96 Parameters

Parameter	Value
GM	$3986004.415 \times 10^8 m^3/s^2$
a	6378136.3 m
$C_{2,0}$	Tide Free
Reference Ellipsoid	WGS84

It should be noted that the newer EGM2008 model was considered for computation of the gradients due to its degree and order of 2159 (and corresponding resolution of approximately 9km) [57]. However, due to the recursive generation used for the associated Legendre functions, these functions can become unstable at higher degrees (approximately 2100). Even with algorithms that allow for better stability at high degrees, preliminary results have shown that the estimation of gravity components can take a considerable amount of time [53]. Within the scope of this investigation, the drawbacks of using the EGM2008 model outweighed the increased resolution.

Extended Parker Method. Since terrain effects make up the largest, most rapidly changing part of the bias removed GGI signal at lower altitudes [23], an approximation of these effects must be modeled to get a relatively accurate signal representation for many of the simulation test points. Nagy’s formulae (Equations 8-12) for determining gradients at a point from a single rectangular prism can be expanded to include the effects of an entire grid of rectangular prisms as follows:

$$T_{ij_{total}} = \sum_{n=1}^{NM} T_{ij,n} \quad (37)$$

where NM corresponds to the number of row and column entries on the grid. While proper use of the rectangular prism method gives good insight into the general behavior of the terrain implied gradients, it can be extremely expensive computationally

for a large grid. Parker [58] presents a fast frequency domain method of calculating the potential while Jekeli and Zhu [59] apply it to the computation of gravitational gradients.

If the surface of the geoid is approximated as a plane and a constant density contrast is assumed, the gravitation potential due to the volume mass (terrain) of height h , bounded beneath by the area A (approximated as a 0m MSL plane), can be written in a form similar to Equation 1:

$$V = G\Delta\rho \iint_A \int_0^h \frac{1}{r} dz' dA \quad (38)$$

where $h = h(x', y')$ and is the terrain height at each point.

According to 2-D Fourier transform theory, if $g(x, y)$ is a finite energy function:

$$\int_{-\infty}^{\infty} \int_{-\infty}^{\infty} (g(x, y))^2 dx dy < \infty \quad (39)$$

Then there exists a 2D continuous Fourier transform pair:

$$G(f_1, f_2) = \mathfrak{F}(g(x, y)) = \int_{-\infty}^{\infty} \int_{-\infty}^{\infty} g(x, y) \times e^{-i2\pi(f_1x+f_2y)} dx dy \quad (40)$$

$$g(x, y) = \mathfrak{F}^{-1}(G(f_1, f_2)) = \int_{-\infty}^{\infty} \int_{-\infty}^{\infty} G(f_1, f_2) \times e^{i2\pi(f_1x+f_2y)} df_1 df_2 \quad (41)$$

where f_1 and f_2 are spatial frequencies corresponding to coordinates x and y and \mathfrak{F} denotes a 2-D Fourier transform. Physically speaking, the Fourier transform is a method to break a function into oscillatory components (i.e. a frequency domain representation). The inverse Fourier transform sends the function from its frequency domain representation back into the spatial domain. This technique is particularly beneficial

because some computations (such as convolution) can be accomplished much faster in the frequency domain.

If the assumption is made that A spans from $-\infty$ to ∞ in two dimensions is made, the Fourier transform of V becomes [59]:

$$\mathfrak{F}(V) = G\Delta\rho \iint_A \int_0^h \mathfrak{F}\left(\frac{1}{r}\right) dz' dA \quad (42)$$

which, after using polar coordinates, can be expressed as:

$$\mathfrak{F}(V) = \frac{G\Delta\rho}{2\pi f^2} e^{-2\pi f z} \iint_A (e^{2\pi f h(x', y')} - 1) e^{-i2\pi(f_1 x' + f_2 y')} dA, \quad f \neq 0 \quad (43)$$

where $f = \sqrt{f_1^2 + f_2^2}$. By expanding $e^{2\pi f h(x', y')}$ in Equation 43 via a Taylor series, $\mathfrak{F}(V)$ becomes:

$$\mathfrak{F}(V) = 2\pi G\Delta\rho e^{-2\pi f z} \sum_{n=1}^{\infty} \frac{1}{n!} (2\pi f)^{n-2} \mathfrak{F}((h(x', y'))^n) \quad (44)$$

To obtain the gradients from the potential, a frequency domain relationship provided by Jekeli [60] is used:

$$\mathfrak{F}(V_{ij}) = \mu_{ij} \mathfrak{F}(V) \quad (45)$$

Recall that V was defined as the potential due to some arbitrary mass volume. If the mass volume is defined as the terrain above the geoid, Equation 45 becomes:

$$\mathfrak{F}(T_{ij_{terrain}}) = \mu_{ij} \mathfrak{F}(T_{terrain}) \quad (46)$$

where:

$$\begin{aligned}
\mu_{11} &= -(2\pi)^2 f_1^2, \quad \mu_{12} = -(2\pi)^2 f_1 f_2, \quad \mu_{13} = -i(2\pi)^2 f_1 f, \\
\mu_{22} &= -(2\pi)^2 f_2^2, \quad \mu_{23} = -i(2\pi)^2 f_2 f, \\
\mu_{33} &= (2\pi)^2 f^2
\end{aligned} \tag{47}$$

By applying an inverse Fourier transform to the frequency domain representation of T_{ij} in Equation 46, the terrain implied gravity disturbance gradients are found:

$$T_{ij_{terrain}} = 2\pi G \Delta \rho \Im^{-1} \left(\mu_{ij} e^{-2\pi f z} \sum_{n=1}^{\infty} \frac{1}{n!} (2\pi f)^{n-2} \Im((h(x', y'))^n) \right) \tag{48}$$

In practice, some assumptions regarding Equation 48 must be made. First, A is a finite area corresponding to the area of the elevation grid thus Equation 48 becomes an approximation. Also, the assumption is made that Fourier transforms of the powers of $h(x', y')$ exist. Since h is given at discrete points in the elevation grid (Figure A.1), discrete approximations of the continuous Fourier transform are used. Furthermore, a finite Taylor series expansion is also used when evaluating Equation 48. Under the assumption that $h(x', y')$ is a discrete and periodic function, the Fast Fourier Transform (FFT) can be applied:

$$T_{ij_{terrain}}(p_1, p_2) = 2\pi G \Delta \rho F F T^{-1} \left(\mu_{ij} e^{-2\pi f_{p_1, p_2} z} \sum_{n=1}^{\infty} \frac{1}{n!} (2\pi f_{p_1, p_2})^{n-2} F F T(h^n)_{p_1, p_2} \right) \tag{49}$$

where $p_1 = 0, \dots, M_1 - 1$, $p_2 = 0, \dots, M_2 - 1$, and M_1, M_2 are the total number of

samples in the x and y directions, respectively, with:

$$f_{p_1, p_2} = \sqrt{f_{1_{p_1}}^2 + f_{2_{p_2}}^2},$$

$$f_{1_{p_1}} = \frac{p_1}{\Delta x' M_1}, f_{2_{p_2}} = \frac{p_2}{\Delta y' M_2}, \text{ for } p_1 = 0, \dots, \frac{M_1}{2} - 1, p_2 = 0, \dots, \frac{M_2}{2} - 1,$$

$$f_{1_{p_1}} = \frac{p_1 - M_1}{\Delta x' M_1}, f_{2_{p_2}} = \frac{p_2 - M_2}{\Delta y' M_2}, \text{ for } p_1 = \frac{M_1}{2}, \dots, M_1 - 1, p_2 = \frac{M_2}{2}, \dots, M_2 - 1$$
(50)

where $\Delta x'$ and $\Delta y'$ are the sample intervals in the x and y directions, respectively. For a derivation of the spectral component's conjugate symmetry satisfaction requirement, refer to [59].

Unfortunately, there are three drawbacks of using the method based on Parker's work. First, the assumption of discrete and finite data causes biases in the diagonal components of the gradient tensor [61]. Second, the computation point, or gradiometer altitude, must be held constant. Furthermore, the gradiometer altitude must also be above the highest elevation in the grid. In other words, for AGL type map generation, this method will not produce reliable results and a rigorous rectangular prism method must instead be used. While the drawbacks of this method have been highlighted, the primary advantage is a rapid reduction in computation time of the gradients maps. Table 2 shows the computation times for producing full tensor gridded gravity gradient data via the rectangular prism and Parker methods. For more information regarding various map making techniques, refer to [61] and [62].

Table 2: Gridded Gradient Computation Time Comparison

Grid	Number of Points	Rectangular Prism Time	Parker's Method Time
3° x 3°, 1 arc min	32761	2640s	7s
2° x 2°, 3 arc sec	5764801	DNF*	650s

DNF=Did Not Finish - simulation was terminated after 72 hours

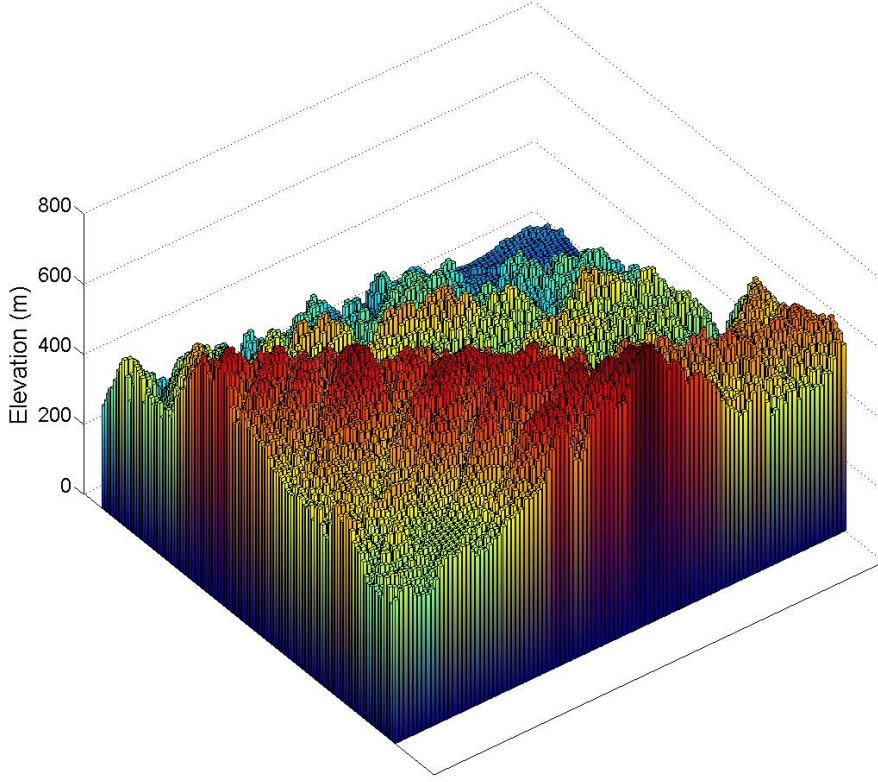


Figure 26: Example Elevation Grid.

Using 2° by 2° SRTM Digital Terrain Elevation Data (DTED) supplied by the NGA, discrete elevation grids with approximately 90 meter grid spacing (3 arc second) will be constructed. Using a flat-earth approximation, the “bottom” of the bounding plane is defined by 0 meters MSL which is assumed to be located on the EGM96 geoid surface. Consequently, the topographical surface is the terrain height of each grid cell in meters above MSL. A small sample of the discrete elements used to compute gradients due to terrain is shown in Figure A.1. For this method, a constant terrain density of $2.67g/cm^3$ is assumed. This is considered by geologists to be the average terrain density. As previously mentioned, geological surveys have shown that actual terrain mass has varying density. To mitigate this effect, the assumption that the modeled gradient maps represent truth is made for this study.

At low altitudes, much of the gradient disturbance signal is caused by the terrain in the immediate vicinity. As such, relatively small grid sizes can be used to capture

most of the terrain effects. Zhu [61] showed that at an altitude of 10m above the maximum altitude of a relatively rough grid, an area extent of a half degree was needed to achieve an accuracy of $1Eo$. However, as altitude increases, the area of influence on the signal from the terrain will increase. Be that as it may, the gradients from the terrain are also falling rapidly as the altitude increases. For this study, it is assumed that the grids are adequately sized for reliable terrain gradient results. To minimize gradient errors caused by grid edge effects, only the central-most portions of the gradient grids will be used for simulations.

Gravity Gradiometer Modeling

While gravity gradiometers designed for airborne surveys are inherently complex, the three main drivers of the signal they produce are gradient production rate, bandwidth after filtering, and noise. Because modeling the inner workings of a GGI are beyond the scope of this feasibility study (and often proprietary), the method used to simulate the signal will involve manipulation of the gradient maps. To get actual gradient values from the map, a table lookup function, based on the velocity of the GGI host vehicle that is traveling across the map, is performed at the appropriate sampling rate using Simulink®. If the location falls between grid points, a spline interpolation is used [63]. Next, appropriate noise with respect to the sensor gradient production rate will be added to the gradient maps [64]. Finally, a low pass filter with similar specifications to those used on gradiometer data will be implemented on noisy samples taken from the gradient maps to simulate methods of noise reduction. In essence, this filter will serve to reject higher frequencies, thus smoothing the signal. Two gradiometers were chosen for modeling based on the literature review in Chapter 2.

Noise Generation. As mentioned in Chapter 2, gradiometer manufacturers claim zero-mean gaussian white noise characteristics for their GGIs over a certain bandwidth. These specifications are given in terms of a noise spectral density (NSD).

The NSD is the power of noise over a given range of frequencies. Since the noise is white, the power is flat over all applicable frequencies. In order to determine the RMS value of the white noise produced by a GGI before final filtering, the following relationship is used:

$$RMS\ Noise(Eo) = \sqrt{\left(NSD \left(\frac{Eo}{\sqrt{Hz}} \right) \right)^2 \times \frac{1}{2} Gradient\ Production\ Rate(Hz)}, \quad (51)$$

where it is assumed that the gradiometer noise spectral density is valid from $0Hz$ (or “DC”) to the Nyquist frequency (defined here as $1/2$ the gradient production rate). Once the RMS value of the noise is found, it will be added to the gradient maps via the “normrnd” command in Matlab®. Since the noise is zero-mean, the RMS values are equal to the standard deviation, σ .

Filtering. No matter the type of gradiometer, all gradient signals are sent through a final low pass filter (LPF) to reduce uncompensated noise and to prevent or reduce aliasing of the signal [23, 25]. One drawback to this type of filtering is a smoothing effect on the signal. In other words, spatial resolution will be lost for the sake of noise reduction. The most commonly used LPF in GGI data noise reduction is known as a Butterworth filter [24, 25, 61] and its transfer function, H , is given by [65]:

$$|H|^2 = \frac{1}{1 + \left(\frac{f}{f_c} \right)^{2n}} \quad (52)$$

where f_c is the cutoff frequency and n is the order of the filter.

An example of a one dimensional Butterworth filter with a normalized cutoff frequency of 0.4 and varying orders is shown in Figure 27. The frequency spectrum that is allowed to pass through the filter is known as the passband while the spectrum that is cutoff is known as the stopband. On an ideal LPF, the terminal slope, or roll off,

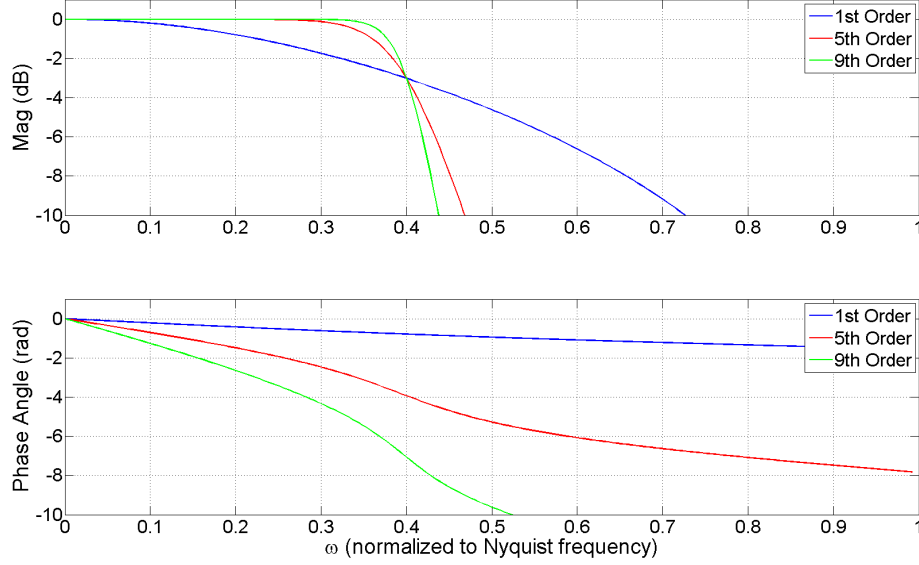


Figure 27: Example Butterworth Filter.

between the passband and stopband would be a vertical line but in practice a physical circuit cannot generate this type of response. While Butterworth filters tend to roll off more slowly than other types of low pass filters (such as the Chebyshev) they have very low ripple characteristics. Note that regardless of the filter order, the magnitude response of the Butterworth filter is always 3dB down at the cutoff frequency. Also note the non-constant relationship between frequency and phase within the passband - one of the drawbacks of the Butterworth filter.

For this research, a digital 7th order Butterworth filter (Visser, Murphy, Lane) was designed in Matlab® and applied *real-time* as the simulated gravity gradient were traversed. Real-time filter application marks a departure from the considerable post-mission processing that is done with most current GGI data. For navigation, one does not have the luxury of extensive post-flight processing - the filtered signal must be available immediately. Real time application of the Butterworth filter as signals are being sampled gives a recursive effect. That is, the filter is auto-regressive in that it relies on previously filtered samples to compute new values (i.e. feedback). With some assumptions regarding the impulse response of the filter, it can be considered to give a moving-average effect. As such, this will inevitably give the real-time filtered signal

a lag in the time domain as previous values affect the most-recent one. Additionally, the non constant phase lag of the Butterworth filter will cause a distortion in the already lagging filtered signal and may be an issue for a map-matching algorithm. The filter function of the Butterworth LPF has the following general form:

$$x'(i) = \sum_{k=0}^N a_k x(i-k) - \sum_{l=1}^N b_l x'(i-l), \quad (53)$$

where a_k and b_k are the filter coefficients, $x(i)$ is the i -th raw sample, $x'(i)$ is the i -th filtered sample, and N is the order of the filter. It is evident that for a 7th order filter, it will require raw and filtered information from the previous 7 samples. Since filtered information is unavailable when the filter is initially applied, it is assumed that the filtered samples are equal to the raw samples for the first 7 samples.

A key point when dealing with filtering on a moving platform is that sensed wavelengths are a function of *velocity*, v . The relationship between frequency (in units of Hz), f , and spatial frequency (in units of *cycles/m*), $f_{spatial}$, is given by:

$$f_{spatial} = \frac{f}{v} \quad (54)$$

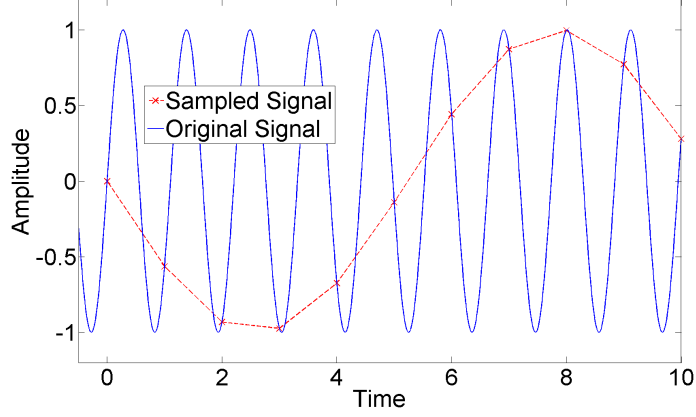
where v is the relative velocity between the sensor and the object being measured (in m/s). The corresponding wavelength, λ (in units of meters), is given by:

$$\lambda = \frac{1}{f_{spatial}} = \frac{1}{f} \times v \quad (55)$$

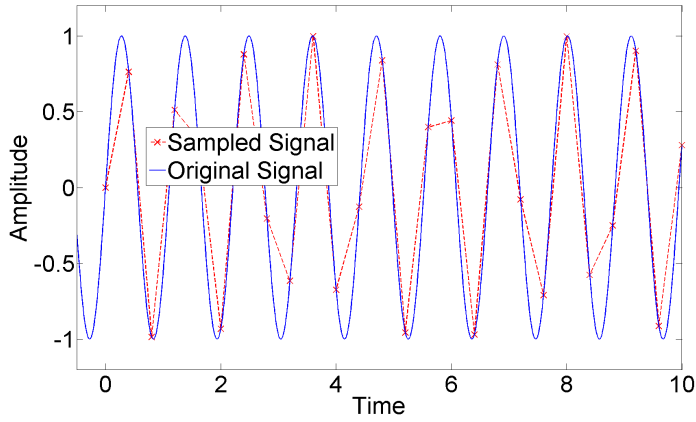
In other words, the slower the host vehicle is moving relative to the ground, the shorter the wavelength (higher frequency) that the LPF will allow to be sensed. Given a fixed cutoff frequency, this gives the most resolution and is why airborne gravity gradient surveys are generally flown as slow as safely possible. Likewise, the faster the relative velocity, the less spatial resolution (again assuming that the cutoff frequency

of the filter is held constant). To keep high resolutions at higher velocities, the obvious choice is to increase the cutoff frequency of the filter. This has two major down sides. First, the amount of noise manifesting itself into a signal is generally higher at high frequencies and can quickly render the signal useless. Second, (assuming that the measurement device is making discrete samples) if the cutoff frequency is raised to a point where it becomes close the the sampling frequency, f_s , a phenomenon known as aliasing can occur. Aliasing is the inability to distinguish different parts of the frequency spectrum of a signal due to sampling rate restrictions. It is caused by having frequency content of a signal that is $\geq \frac{1}{2}f_s$. For example (Figure 28), the function $\sin((2\pi - 0.6)t)$ has a frequency of $1Hz$. If it is sampled at $\leq 2Hz$, no unique frequency measurement can be reconstructed and the higher frequency signal can appear as, or alias to, a lower frequency. If the signal is sampled at a rate *more* than twice the maximum frequency content of the original signal, the signal can be reconstructed. This is known as the *Nyquist condition* and, in addition to noise considerations, also drives GGI filter design. In practice, it is desired to sample the signal at approximately 5 times the frequency content of the signal to better capture magnitude and energy information. It should be noted that anti-aliasing filters are applied before the signal is sampled (or before the signal is downsampled) and may be one of several filters in the sensor. Additionally, the *Nyquist frequency* is defined as one-half the sampling rate of a discrete signal sampling system. In the case of gradiometers, raw accelerometer measurements are made at very high rates, some over $100Hz$ [22]. However, after averaging, internal filtering, scale factor correction and other noise reduction techniques, useful gradient information is produced on the order of $1Hz$ [12].

In this study, it is assumed that the primary anti-aliasing filter has already been applied and the LPF used here is for signal noise reduction. Furthermore, it is assumed that host-vehicle gradient contributions are exactly known and have been removed from the signal. Table 3 summarizes the gradiometer noise and bandwidth specifications, based on the literature review in Chapter 2, used in the simulations.



(a) $f_s=1\text{Hz}$, Nyquist condition not met, aliasing present



(b) $f_s=2.5\text{Hz}$, Nyquist condition met, no aliasing

Figure 28: Illustration of Aliasing and the Nyquist Condition.

GGI1 is a lower noise sensor that represents the more optimistic end of gradiometer performance expected to be available within a decade. Likewise, GGI2 is the higher noise sensor and represents the level of performance that has already been demonstrated in tests. Subsequently, GGI1 and GGI2 may be referred to as “low noise” and “noisy” sensors, respectively.

Table 3: GGI Specifications

GGI	NSD	f_s	RMS Noise	f_c	RMS Noise after Filtering
1	$0.223E_o/\sqrt{Hz}$	$1Hz$	$0.158E_o$	$0.2Hz$	$0.1E_o$
2	$2.23E_o/\sqrt{Hz}$	$1Hz$	$1.58E_o$	$0.2Hz$	$1.0E_o$

Gradiometer Model Verification. Since no real-time filtered gravity gradiometer data is published in open literature, a build-up approach using available data will be used to validate the GGI sensor model. First, to ensure Parker’s method is implemented correctly, results from the method, using a 20th order expansion, will be validated against gradients from the summation of the rigorous calculations of each rectangular prism’s contribution to the overall gradient. These rigorous calculations are a summation of each prism’s effect calculated via Equations 8-12. A $330 \times 260km$, 1 arc minute spaced ($\sim 1.8km$) grid will be used for this comparison. The fairly large 1 arc minute spacing was chosen due to the computational expense of the rigorous rectangular prism method. As a final validation of the terrain implied gradient map making technique, results will be compared to those derived by Zhu and those calculated by Bell Geospace for a track surveyed by an Air-FTG gradiometer during a flight in 2004. Zhu’s DEM gradient data is based on a numerical integration method using a USGS provided $1^\circ \times 1^\circ$, 1 arc second elevation grid. Bell Geospace’s terrain implied gradient data is calculated from SRTM data in the area. Since actual data was unable to be obtained for the Zhu and the Bell Geospace gradient models, data from Parker’s method will be calculated along the same track, converted into the appropriate coordinate frame, plotted and superimposed over a comparison figure originally taken from Zhu [61]. Since EGM96 data will vary depending on the type of interpolation used between points, results from the overall gradient modeling effort will be compared to plots of Bell Geospace Air-FTG survey data in a manner similar to the Parker’s method validation.

For filter and noise validation, the filter’s response to a unit impulse input will first be examined and compared to expected values found using a method described by Rorabaugh [66]. According to Rorabaugh, the time at which the maximum value of a 7th order Butterworth filter’s impulse response occurs should be approximately 4 seconds if a cutoff frequency of 0.2Hz is used. Additionally, the amplitude of this peak should be approximately 0.4. To validate the noise in the signal, the mean and

standard deviation of the “normrnd” generated noise will be examined before and after filtering is applied and should match values listed in Table 3.

Navigation

To determine the feasibility of using a GGI-based map-matching navigation system, some assumptions about the system will be made in order to better classify whether the modeled GGI signal exceeds threshold requirements. It is assumed that the GGI will be used in a navigation scheme similar to those presented by Jircitano [44] and Richeson [51]. That is, an INS will be used as the primary navigator and its error will be bound by updates from a GGI signal to map matching algorithm. Figure 29 shows a schematic of a generic GGI/map matching updated INS.

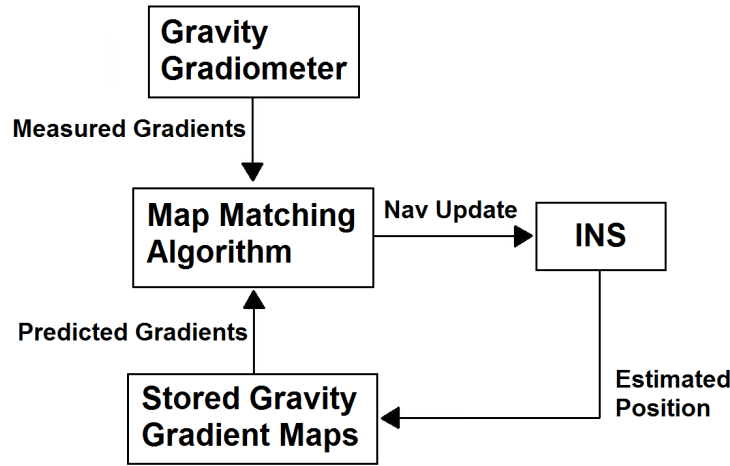
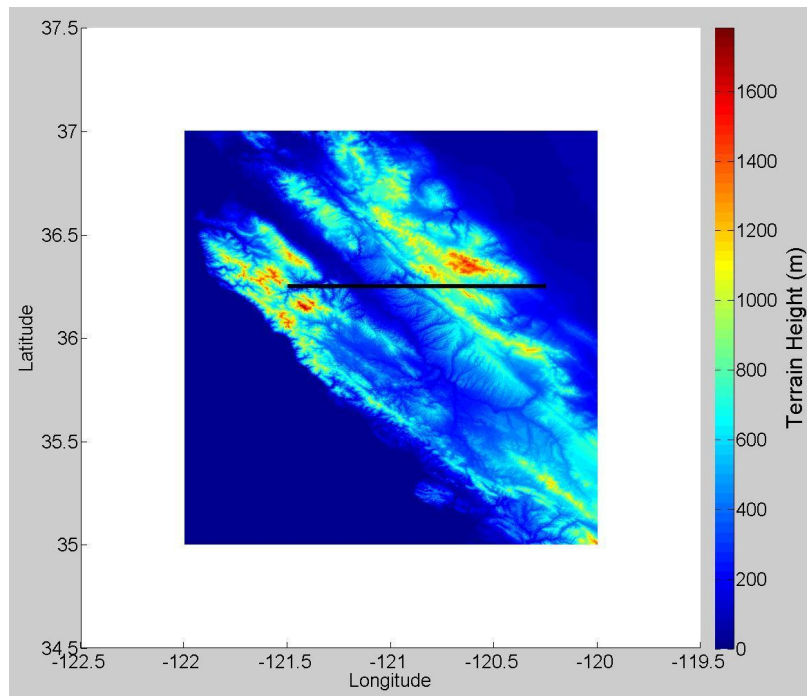
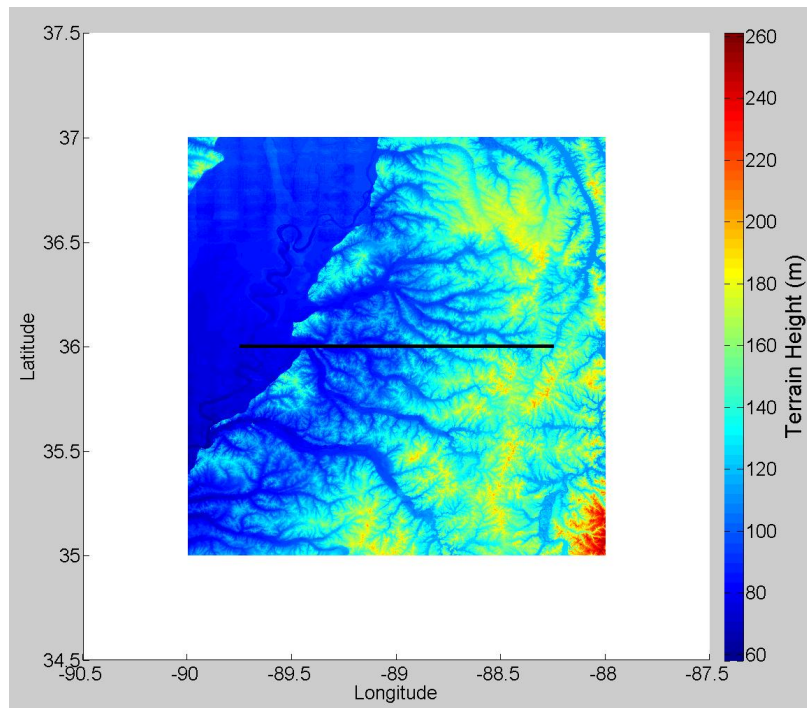


Figure 29: GGI-Aided Passive Navigation System Flowchart.

Test Conditions. Two track areas, one with with rapid terrain changes and one with relatively low levels of terrain changes (i.e. mountainous versus flat terrain) were selected for the navigation feasibility simulations. Track 1 (Figure 30a) is a west-east track beginning just southeast of Monterey, CA, ($36.25^{\circ}N$, $121.5^{\circ}W$) in a region of relatively mountainous terrain. This area was selected in part because Rice University contracted Bell Geospace to fly a gravity gradient survey in that area in 2004 [67]. As such, airborne gradiometer data is available for that area and may



(a) Track 1, rough terrain.



(b) Track 2, smooth terrain.

Figure 30: Test Tracks (note contour scale differences).

be valuable for future navigation research efforts given its vicinity to the Air Force Flight Test Center at Edwards Air Force Base, CA. Track 2 (Figure 30b) is also a west-east track located in western Tennessee beginning slightly north of Memphis. This track, starting at $36^{\circ}N$, $89.75^{\circ}W$, was selected as it represents one of the largest areas of relatively flat terrain in the United States. Note the different scales in Figure 30. The along-track terrain statistics for $\sim 135km$ tracks in each area are shown in Table 4. Should an area of smooth terrain be desired for flight test, the El Centro complex near the Salton sea could be useful as it contains relatively large stretches of flat terrain.

Table 4: Along-Track Terrain Statistics

Track	Min	Max	Mean	Std. Dev.
1, Rough	78m	1118m	403m	254m
2, Smooth	72m	146m	105m	24m

For each track, straight and level runs with altitudes ranging from 1000-20000m height above average terrain (HAAT) and velocities from 50-1200 m/s will be simulated for 100 seconds beginning once the filter has had time to produce meaningful results. These test points were chosen in order to map a wider range of the flight envelope than has been done in previous studies [44,51]. Note that most conventional military aircraft generally operate in the 5-10km altitude region at speeds of 100-300m/s. However, some surveillance aircraft operate at higher altitudes and loiter at slower velocities, hence the inclusion of 20km altitudes and velocities down to 50m/s. Additionally, the GGI signal sensed on board a theoretical high speed vehicle may be useful for future studies, thus 600-1200m/s velocities are also included. A time of 100s was chosen under the assumption that the map-matching algorithm will provide 1 second updates to the INS. Thus, general trends in the signal’s usefulness should be able to be seen over the course of 100s. Table 5 summarizes the planned test runs.

Table 5: Test Matrix.

Runs	Altitude (m HAAT)	Velocity (m/s)	Remarks
1 – 6	1000	50, 100, 150, 300, 600, 1200	GGI 1, Rough Terrain
7 – 12	1000	50, 100, 150, 300, 600, 1200	GGI 1, Smooth Terrain
13 – 18	1000	50, 100, 150, 300, 600, 1200	GGI 2, Rough Terrain
19 – 24	1000	50, 100, 150, 300, 600, 1200	GGI 2, Smooth Terrain
25 – 30	2500	50, 100, 150, 300, 600, 1200	GGI 1, Rough Terrain
31 – 36	2500	50, 100, 150, 300, 600, 1200	GGI 1, Smooth Terrain
37 – 42	2500	50, 100, 150, 300, 600, 1200	GGI 2, Rough Terrain
43 – 48	2500	50, 100, 150, 300, 600, 1200	GGI 2, Smooth Terrain
49 – 54	5000	50, 100, 150, 300, 600, 1200	GGI 1, Rough Terrain
55 – 60	5000	50, 100, 150, 300, 600, 1200	GGI 1, Smooth Terrain
61 – 66	5000	50, 100, 150, 300, 600, 1200	GGI 2, Rough Terrain
67 – 72	5000	50, 100, 150, 300, 600, 1200	GGI 2, Smooth Terrain
73 – 78	10000	50, 100, 150, 300, 600, 1200	GGI 1, Rough Terrain
79 – 84	10000	50, 100, 150, 300, 600, 1200	GGI 1, Smooth Terrain
85 – 90	10000	50, 100, 150, 300, 600, 1200	GGI 2, Rough Terrain
91 – 96	10000	50, 100, 150, 300, 600, 1200	GGI 2, Smooth Terrain
97 – 102	20000	50, 100, 150, 300, 600, 1200	GGI 1, Rough Terrain
103 – 108	20000	50, 100, 150, 300, 600, 1200	GGI 1, Smooth Terrain
109 – 114	20000	50, 100, 150, 300, 600, 1200	GGI 2, Rough Terrain
115 – 120	20000	50, 100, 150, 300, 600, 1200	GGI 2, Smooth Terrain
121	5000	150	GGI 1, Rough, Form w/KC-10
122	5000	150	GGI 1, Smooth, Form w/KC-10
123	5000	150	GGI 2, Rough, Form w/KC-10
124	5000	150	GGI 2, Smooth, Form w/KC-10
125	10000	150	GGI 1, Rough, Form w/KC-10
126	10000	150	GGI 1, Smooth, Form w/KC-10
127	10000	150	GGI 2, Rough, Form w/KC-10
128	10000	150	GGI 2, Smooth, Form w/KC-10

The Tanker Effect. Since aerial refueling (Figure 31) is an integral part of military force projection, it is desired to know if and by what amount the presence of a large tanker aircraft in the vicinity of the GGI carrying aircraft will corrupt the GGI signal. While it typically takes approximately five minutes to refuel a fighter size aircraft, these aircraft will often stay in formation with the tanker for extended periods of time, especially during transit to forward locations.



Figure 31: A KC-10 Offloading Fuel to an F-22 Raptor.

To model the gravitational gradient effects of a tanker aircraft, a simple rectangular prism model of a McDonnell Douglas KC-10 is created based on dimensions derived from Figure 32, taken from [68]. It should be noted that the volume calculation is only an approximation based on the relative dimensions of the KC-10. Once the approximate volume is known, a typical heavy weight for a KC-10 in flight is used to calculate the average density. Finally, to obtain a representative rectangular prism, the dimensions required to obtain the approximate volume were best fitted to the KC-10 as shown in Figure 33. All estimated properties are listed in Table 6. While a higher resolution model of the tanker could have been created via more rectangular prisms, the primary objective here is only to determine if a large object, located next to and flying at the same velocity as the sensor, having a density distribution and size that represents a large aircraft, will affect the signal. For this study, the GGI will nominally be located $30m$ laterally and co-altitude with respect to the center of the rectangular prism, but allowed to vary approximately $\pm 5m$ in all directions to sim-

Table 6: KC-10 Parameters

Parameter	Value
Total Mass	$240,000kg$
Approx. Volume	$1816m^3$
Approx. Density	$132\frac{kg}{m^3}$
Length of Equiv. Rect. Prism	$48.8m$
Width of Equiv. Rect. Prism	$6.1m$
Height of Equiv. Rect. Prism	$6.1m$

ulate relative motion between the two aircraft typically seen during formation flight. Gradients will be calculated at the 8 points which define the boundary of the GGI aircraft's deviation from the nominal position. The mean and standard deviation of these values will be computed and the "normrnd" command will be used to convert these gradients into effective white noise which will then be added to the gradient maps. Next, the filter will be applied as the maps are traversed. The filtered signals with and without the tanker effects will then be plotted for comparison. Additionally, these runs will only be accomplished at typical refueling/cruise altitudes and velocities (Table 5).

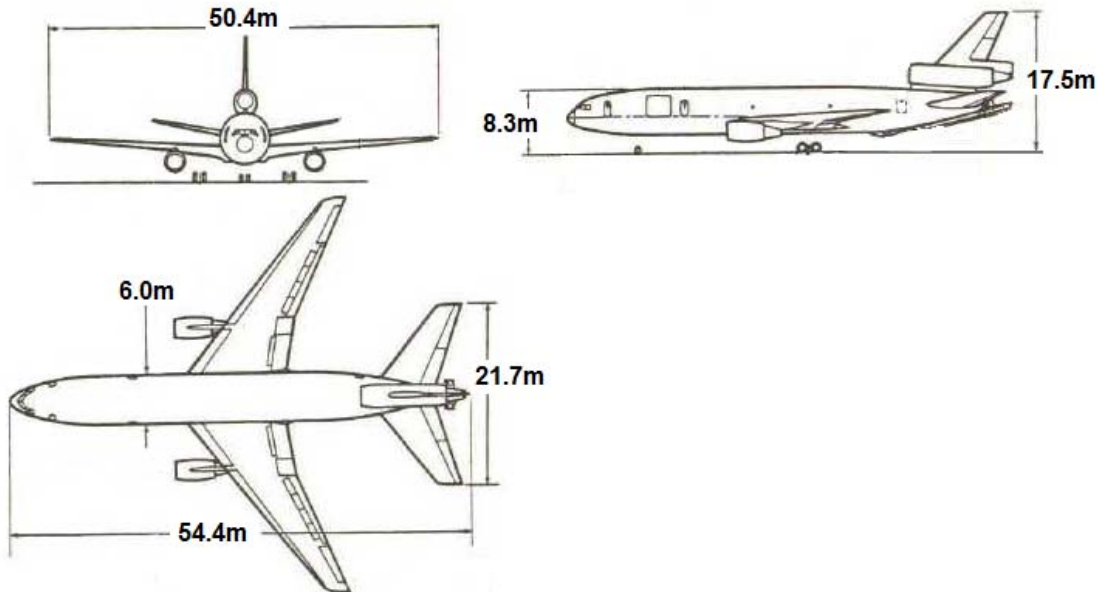


Figure 32: KC-10 Dimensions.

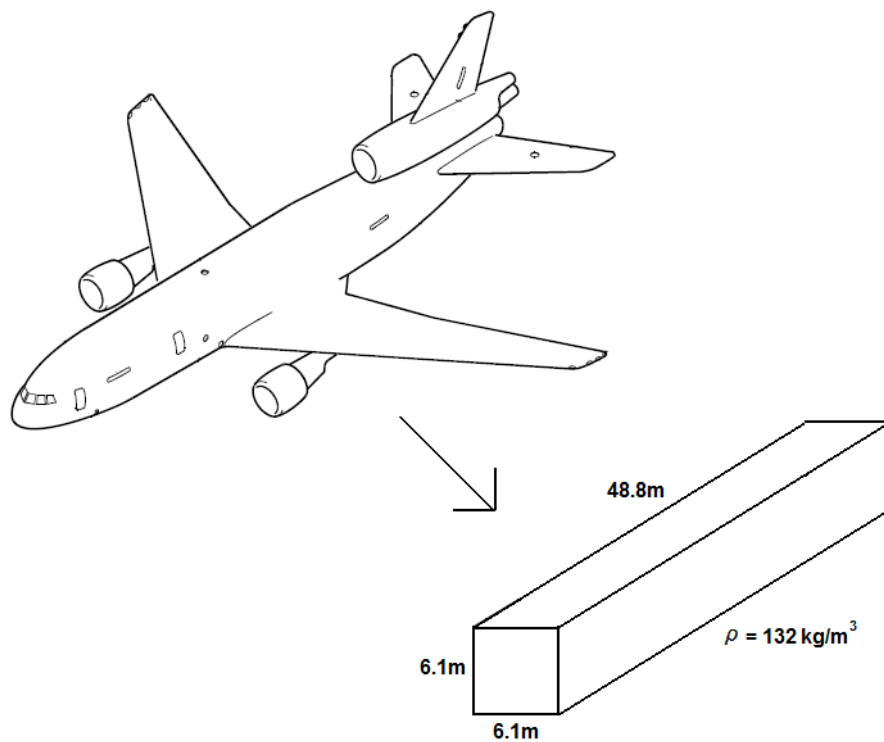


Figure 33: KC-10 Transformed into a Rectangular Prism.

Gradiometer Signal Metrics for Useful Navigation. For a signal to be usable in a map matching utility sense, it must vary in time at an adequate rate while maintaining good signal to noise characteristics. If the signal doesn't vary much with time, or there is excessive noise, matching it to a map would prove to be an exercise in futility and tell very little about relative position on the map. In order to determine if the simulated GGI signal is useful for navigation, several signal examination methods will be employed. First, the signal will be analyzed graphically to determine if the along-track signal changes are outside of the noise level from the gradiometer. To do this, the standard deviation of the noise will be plotted in relation to the mean value of the true gradient over the run time. Additionally, the overall uniqueness and clarity of the gradient contour outlined by the GGI will be examined. If less than approximately 5% of the signal is within the standard deviation of the noise and the contour is clearly defined, the signal is considered "excellent". That is, the signal defines the contour well *and* the contour varies in time to provide uniqueness. Should approximately 5-20% of the signal fall outside the noise standard deviation and the contour remain easily discernable, the signal will be deemed "useful". If approximately 20-50% of the signal is outside the standard deviation and contour uniqueness begins to drop but is still somewhat discernable, the signal is considered "marginally useful". Finally, if greater than 50% of the signal is within the noise standard deviation, the signal is considered "unusable". That is, the signal is too noisy to uniquely define the contour. These metrics bear no qualitative data as to expected navigation performance but are designed to give an idea of the relative map-matching usefulness of the signal at different flight conditions. While a signal to noise ratio (SNR) examination was considered, a strong SNR does not guarantee that the signal varies in time.

Next, a comparison of signal levels obtained from GGI1 will be measured against those previously proven useful for navigation by Richeson. GGI1 is chosen because Richeson found that a gradiometer with 1*Eo* of RMS error (i.e. GGI2) provided no gains over unaided navigation grade IMUs when used with his map-matching

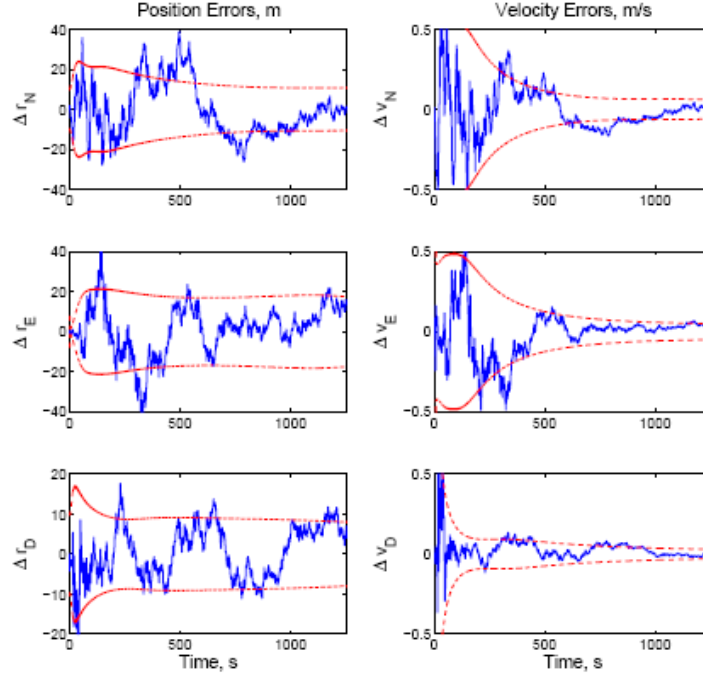
Table 7: Richeson’s “GGI Survey” simulation parameters

Parameter	Value
Track	45.0°N, 113.0° - 100.3°W
Velocity	40m/s
Altitude	100m
Gradient Model	EGM96 based
$dT_{ij}/dt(\text{RMS})$	0.05Eo/s

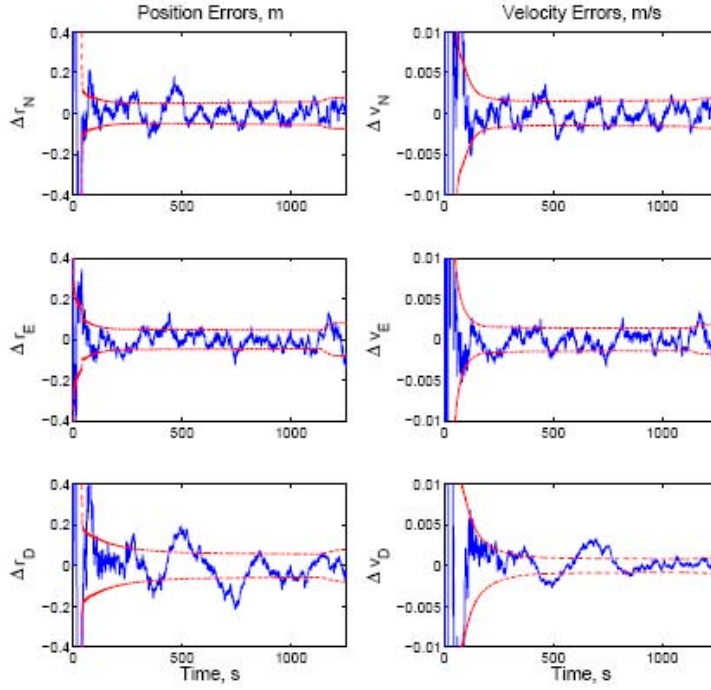
algorithm. However, a GGI with $0.1Eo$ of RMS noise did provide some benefit to the INS, though not to GPS levels. Though terrain effects were neglected and only EGM96 derived gradient maps were produced, Richeson’s research indirectly classified the signal threshold required for an improvement in navigation over an unaided navigation grade IMU, assuming a gradiometer with $0.1Eo$ of noise [51]. The metrics which define this threshold are obtained by examination of the average along track signal rate of change for each gradient, before noise is added.

Figure 34 shows the differences in navigation results from Richeson’s research using a $0.1Eo$ GGI and a GPS in combination with navigation grade IMUs. Given enough time, the GGI aided navigation system bounds the INS error to 10-20m in the north, east, and down directions whereas the GPS bounds the error of the system to approximately 0.01m. In other words, the GPS aided system provides results that are roughly 3 orders of magnitude better than the $0.1Eo$ GGI aided system. Since a gradiometer specific map-matching algorithm is still under development at AFIT, the assumption is made that order of magnitude differences in the noise free signal time rate of change will correspond to order of magnitude changes in navigation performance (i.e. the more unique the GGI signal is, the more likely it will be correctly correlated to a map and the better the navigation performance will be). Based on Richeson’s results, a signal having a $0.05Eo/s$ RMS rate of change and a GGI with $0.1Eo$ of noise will bound host-vehicle position error to roughly 10-20m. Using this metric, Table 8 was constructed.

It must be stressed that this only holds under the assumption that the gradient maps are truth. If the maps inherently have error in them (i.e. if GPS was used for



(a) Navigation results for a 0.1Eo GGI map-matching system providing 1Hz updates to the INS.



(b) Navigation results for a GPS providing 1Hz updates to the INS.

Figure 34: Richeson's Navigation Results: 0.1Eo GGI Map-Matching System vs GPS, taken from [51].

Table 8: 0.1Eo GGI Signal Classification Metrics

Navigation Usefulness (Anticipated Error Bounds)	Signal Time Rate of Change RMS, noise free
Unusable	$< 0.05Eo/s$
Marginally Useful (10^1m MRSE)	$0.05 - 0.5Eo/s$
Useful (10^0m MRSE)	$0.5 - 5Eo/s$
Excellent ($10^{-1}m$ MRSE)	$> 5Eo/s$

positioning during a survey), navigation performance, in a best case sense, will be limited to the amount of error present in the maps.

Terrain Avoidance

The use of a gravity gradiometer as a terrain avoidance warning enhancement is a distinct challenge. According to Gleason [23], the three parameters which dictate feasibility of the GGI in the role of terrain avoidance are the cutoff frequency of the filter used to suppress uncompensated error sources, the gradient production rate, and the final gradiometer noise level. This is compounded by the fact that many aircraft which maneuver at very low altitudes and could benefit from a passive terrain avoidance system typically fly at velocities often on the order of several hundred meters per second. Assuming the GGI bandwidth is fixed, the increase in speed serves to limit the shortest sensed wavelengths. Table 9 shows velocity versus minimum sensed wavelength with a gradiometer cutoff frequency of $0.2Hz$ using the relationship shown in Equation 55. Since the terrain makes up the higher frequency end of the overall

Table 9: Velocity vs. Minimum Wavelength, $f_c=0.2Hz$

Velocity (m/s)	Minimum Sensed Wavelength (m)
50	250
100	500
150	750
300	1500
600	3000
1200	6000

gradient spectrum, filtering high frequencies out in the name of noise reduction may prove devastating for terrain avoidance. Compounding the loss of spatial frequency

information is the fact that locating the mass anomaly corresponding to a gradient is an inverse problem. The following question must be posed: If a gradient change is sensed, is the change from a large mountain in the distance or from a small tower that the aircraft in question is about to impact?

Method 1. For this study, the assumption is made that no prior positional information is known and a GGI with a 1Hz gradient production rate and $0.2Hz$ cutoff is being used as the sole device in an attempt to provide a consistent terrain avoidance warning. In other words, besides GGI-provided information, the user has little situational awareness. Five runs, using a noise free version of the aforementioned gradiometer, will be flown from west to east over a perfectly flat surface on which obstacles of varying size will be placed. The obstacles will be cubic with dimensions of 25, 50, 100, 250, and 500m, all having a density of $2.67g/cm^3$. The aircraft will be flown straight and level at $50m/s$ on a plane 10m below the top of each object. The no noise, relatively slow velocity characteristics were chosen to make this a best-case scenario. If feasibility is not demonstrated for this case, then the addition of noise and higher velocities will only exacerbate the situation. Figure 35 shows the overall scenario setup. The geometry will make the T_{xx} gradient of utmost interest since it

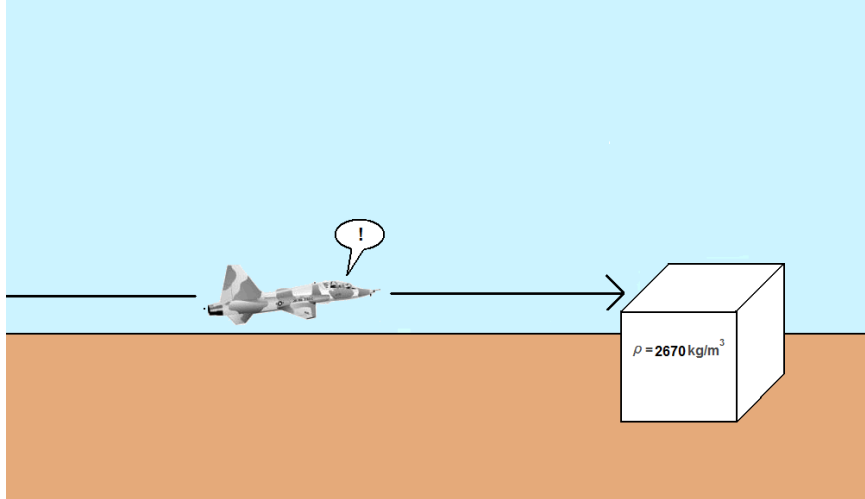


Figure 35: Terrain avoidance scenario.

defines the east-west edges of the anomaly. To potentially counter the inverse nature of determining the terrain distance from the gradient, the time rate of change of the T_{xx} gradient will also be examined. A threshold value of T_{zz} or $\frac{dT_{xx}}{dt}$ corresponding to imminent obstacle impact will be sought. For this study, imminent impact is defined as 1.5s to impact [13].

Method 2. The premise for this portion of the study is that the navigation system provides adequate latitude, longitude, and altitude information and that this position information is used to perform lookups on terrain elevation databases and gravity gradient maps stored onboard the aircraft. Thus, it is assumed that if a correct terrain elevation database is used, impact with the modeled terrain can be prevented (or at least predicted). The GGI's role then becomes to warn the navigation system, and ultimately the operator, of *unmodeled* terrain anomalies which may be encountered along the flight path. Some examples include communications towers, water tanks, and other "pop-up" structures that are often constructed before terrain databases can be updated. Though these structures should be listed in the NOTAMs, such information isn't always available in hostile areas. To investigate the feasibility of the GGI's ability to properly predict an potential impact with an un-modeled object, a simple case study using the world's tallest water tower, listed at 218 feet tall with approximately 500,000 gallons of water, will be executed (see Figure 36) [69]. Using



Figure 36: World's Tallest Water Tower

an assumed weight of 1 US Gallon of water of 3.785kg and $1\text{ USG water} = 3785.4\text{cm}^3$, the density of water was calculated to be approximately 1.0g/cm^3 . An average density of 3.9g/cm^3 (half that of mild steel) was used for the support prism. The water tower was chosen because it represents the larger end of the spectrum of un-modeled pop-up structures. If the gradiometer can predict an impact with it, smaller objects will be tested. The tower will be modeled with two rectangular prisms, one to simulate the support and one to simulate the tank. Before the simulation, a frequency domain analysis will be conducted on the anomaly to determine its signal structure. Then, runs will be flown from west to east over a perfectly flat surface (excluding the tower). This geometry will again make the T_{xx} gradient of utmost interest. As before, the time rate of change of the T_{xx} gradient will be examined. A threshold value of T_{zz} or $\frac{dT_{xx}}{dt}$ corresponding to imminent object impact (1.5s) will be sought. Figure 37 shows the overall test setup.

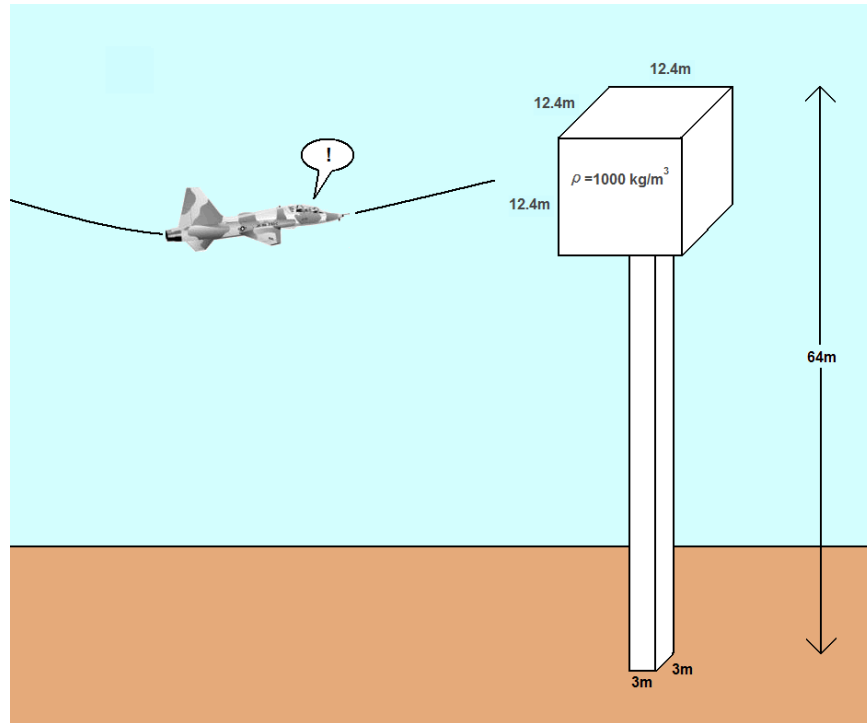


Figure 37: Modeling the Unmodeled

IV. Results and Analysis

Overview

This chapter presents the overall results and analysis obtained from the methods described in Chapter III. The overall goal is to present data that suggests or disproves the feasibility of using a gravity gradiometer in the roles of passive aircraft navigation and terrain avoidance. First, multi-step validation results will be presented to show that the gradiometer models used in this study are producing signals that represent real-time measurements of gravity gradients produced by the earth. Next, the signals' navigation usefulness over different terrain variety, altitude and velocity will be evaluated and summarized using metrics developed for this study. Additionally, the signal effects of flight in the vicinity of a large tanker aircraft will be examined. Finally, the results of several GGI-based terrain avoidance scenarios will be presented and discussed.

Model Validation

The model validation effort begins with an examination of results from the gravity gradient map making process. Figure 38 illustrates the differences between the gradients from the rigorous rectangular prism summation and from Parker's method. Clearly shown is the bias in the diagonal components of the gradient tensor (T_{xx} , T_{yy} , T_{zz}). While these biases are relatively large, they do not affect the overall shape, or *uniqueness*, of the diagonal gradients as a function of distance traveled. As such, these biases are deemed acceptable within the scope of this research. Also shown is the excellent correlation of off diagonal terms generated via the two methods. It should be noted that the first and last fifth of the original gradient grids were excluded due to edge effects that manifested during map generation. All gradient maps used in the simulations were corrected for edge effects.

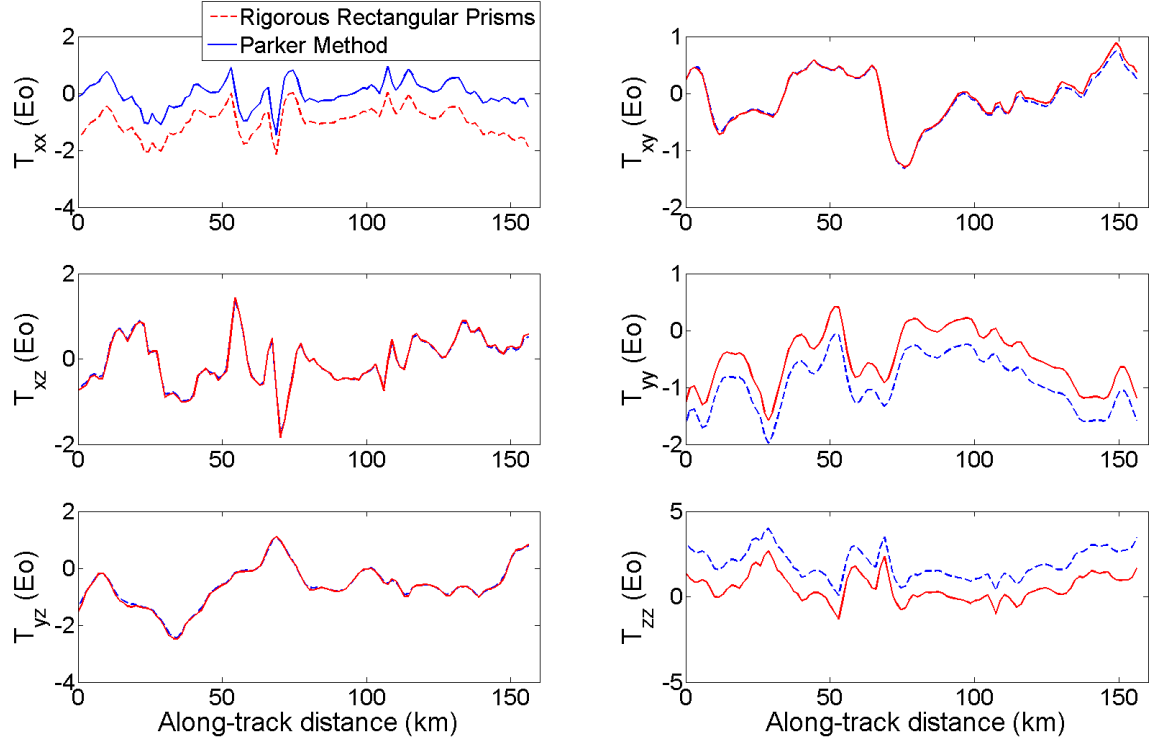


Figure 38: Model Validation - Parker's Method vs Rigorous Rectangular Prisms.

With a fast method of gradient calculation successfully implemented, a comparison of results from this technique are compared to those used by geophysicists. Figure 39 shows the final terrain generated gradient map verification. The data illustrates terrain implied gradients that were calculated along a track surveyed by an airborne gradiometer during a 2004 Bell Geospace flight. Note that Γ_{ij} is interchangeable with T_{ij} . It must be stressed that since data was superimposed onto a pre-existing plot, this is a qualitative comparison to ascertain if Parker's method is working properly. Based on the plots, is clear that Parker's method has been implemented successfully and that the terrain implied gradient maps generated in this study compare to those generated by geophysicists. Also evident are the biases present on the diagonal components of the gradient tensor. The slight mismatch in the off-diagonal components is likely due to the fact that the exact track coordinates were not known and were approximated by visual examination of a map.

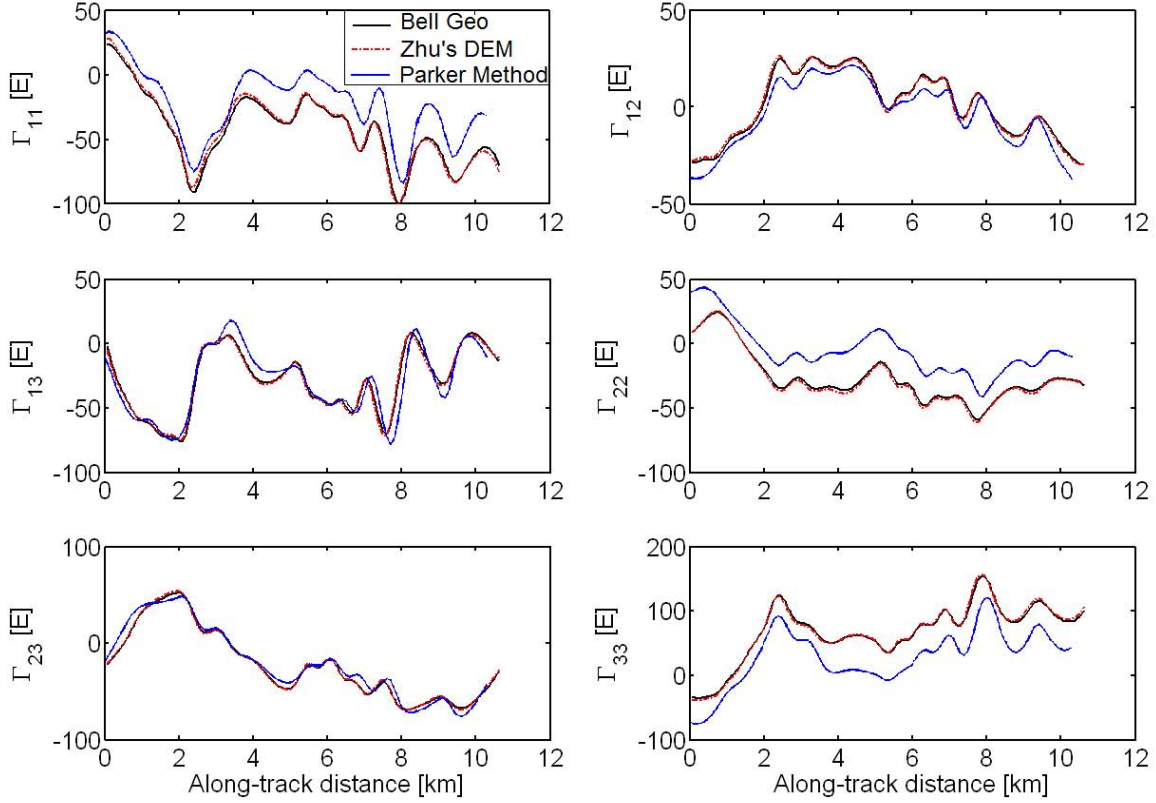


Figure 39: Terrain Effect Modeling verification: Bell Geospace vs. Zhu's Numerical Integration vs. Parker's Method, taken from [61] and modified.

Figure 40 compares the complete gravity gradient model to actual values obtained by a Bell Geospace Air-FTG gradiometer [61,67]. While the gradients are not an exact match, the trends are clearly predicted by the model. The larger differences in this figure are likely caused by the gradiometer sensing density anomalies within the terrain and geology which are not accounted for by the model. As before, the exact track coordinates were unknown - also likely contributing to the differences. It must be stressed that this figure illustrates units of 10^{-9} and any incorrect coding or other error is likely to skew modeled values considerably more than shown. Based on these results, it is concluded that the model is producing gradients that represent realistic values produced by the earth.

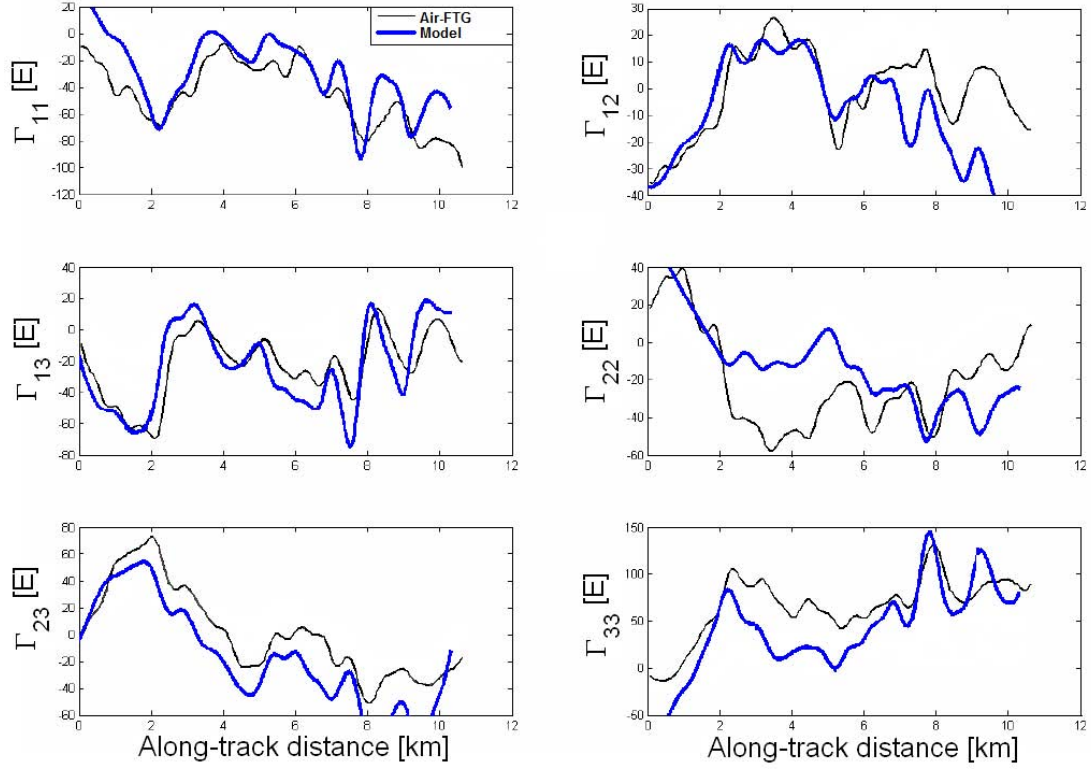


Figure 40: Model Validation - Modeled Gradients vs. Air-FTG Data, taken from [61] and modified.

Figure 41 shows the frequency response of the 7th order Butterworth filter used in this study. The gradiometers to which this filter was applied have a gradient production frequency of 1.0Hz, thus the Nyquist frequency is one-half that (0.5Hz). As stated in the gradiometer specifications (Table 3), the LPF cutoff frequency is 0.2Hz and, when normalized to the Nyquist frequency, becomes 0.4, as shown in the figure. Figure 42 shows the impulse response of the filter. As expected, the peak value is at 4 samples, which, with a sampling rate of 1Hz, corresponds to 4s. Also noted is the fact that the amplitude matches the predicted value of 0.4 as well. Based on this simple study, it is concluded that the filter used in this model was properly implemented.

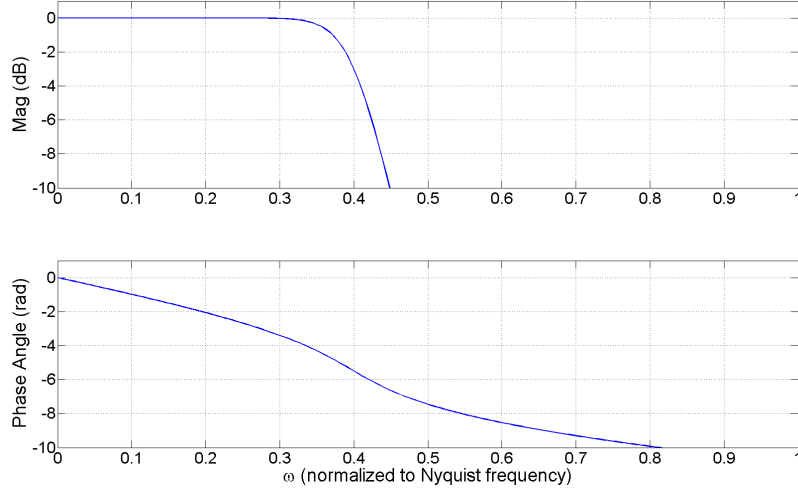


Figure 41: Filter validation - Frequency response of a 7th order Butterworth filter with $f_c=0.2\text{Hz}$ and $f_s=1\text{Hz}$.

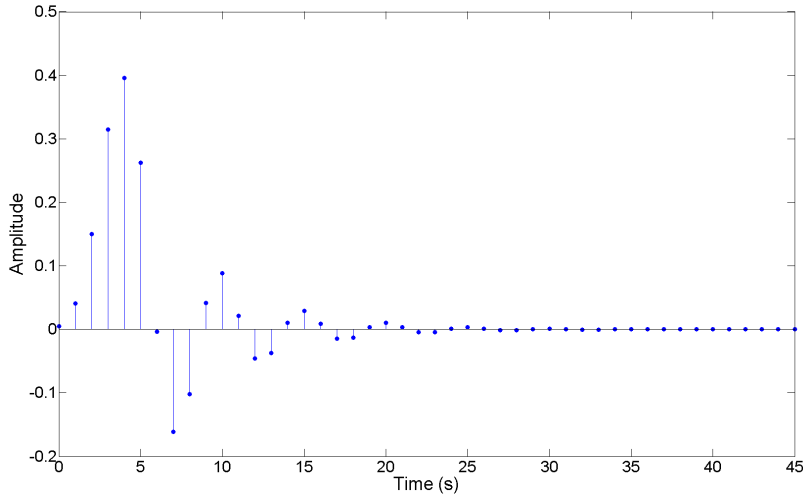
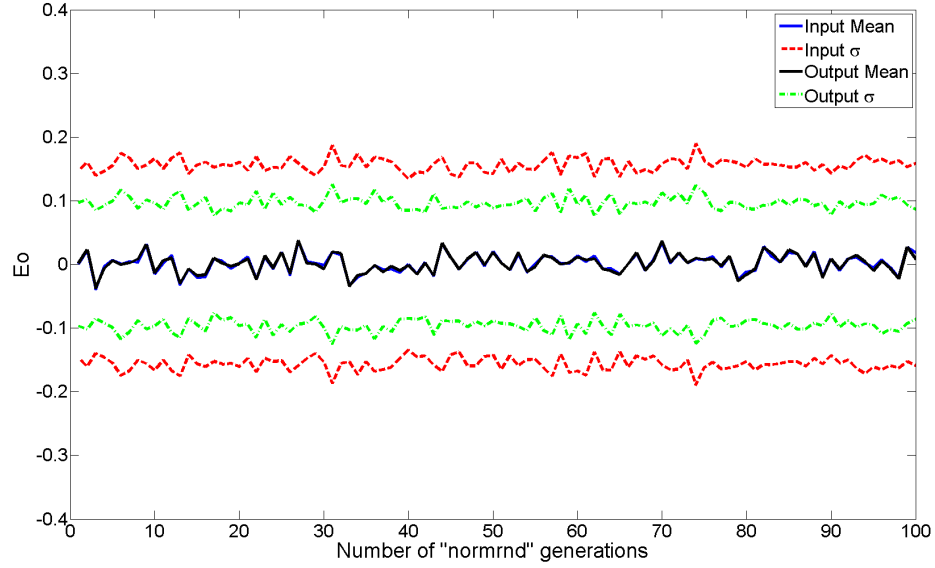


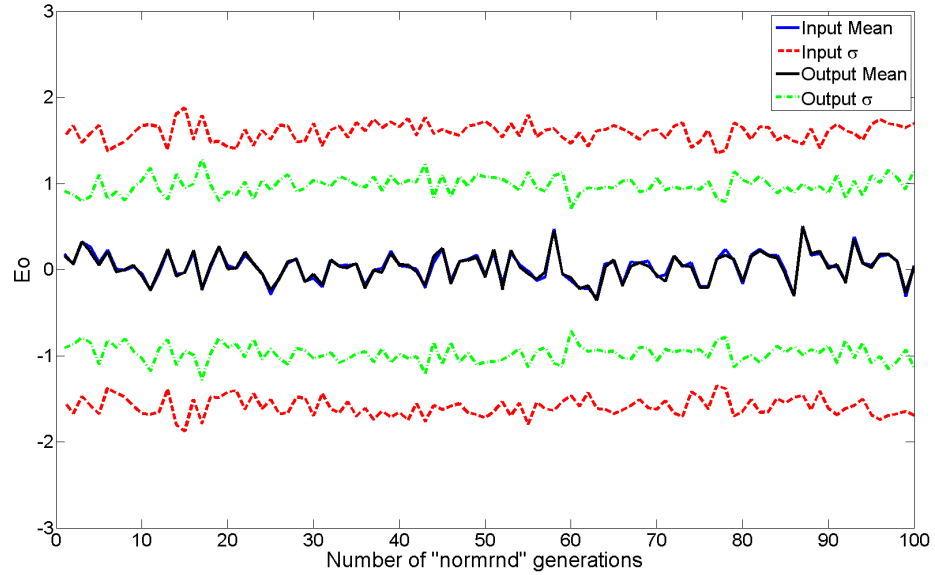
Figure 42: Filter Validation - Impulse Response of a 7th Order Digital Butterworth Filter with $f_c=0.2\text{Hz}$ and $f_s=1\text{Hz}$.

Figure 43 shows the mean and standard deviation of 100 samples of 100 random numbers generated using the “normrnd” command in an attempt to validate the simulated white noise before and after the filtering used for each GGI. Clearly, the mean noise of both GGIs’ pre and post-filtered signals are approximately zero, as anticipated. Recall that GGI1 represents a relatively low noise sensor projected to be available in 10 years and that GGI2 represent a more noisy sensor that is currently

in flight test. The standard deviation of GGI1's pre-filtered noise is approximately $0.158Eo$ while the output noise is approximately $0.1Eo$. Similarly, the standard deviation of GGI2's pre-filtered noise is approximately $1.58Eo$ while the output noise is approximately $1Eo$. All values are expected and indicate that the noise generation process and filter are working correctly.



(a) GGI 1 noise.



(b) GGI 2 noise.

Figure 43: GGI Noise Validation.

Aircraft Navigation Feasibility Results

In an effort to condense the results, only the “zz” (or down-down) component of the gravitational disturbance gradients will be examined in this section. This component was chosen because it is the most intuitive as it generally relates to the shape of the terrain. The remaining independent components (T_{xx} , T_{xy} , T_{yy} and T_{yz}) behave similarly and will offer additional uniqueness to the overall map-matching effort. Though they are omitted here, the data is available for future research. Plots of T_{zz} for all navigation runs (1-128) are located in Appendix C.

Navigation Feasibility via Qualitative Signal Analysis. Tables 10 and 11 summarize the signal characteristics derived from simulation results using GGI1, the lower noise gradiometer.

Table 10: GGI1 Signal Classification Results - Rough Terrain

	50m/s	100m/s	150m/s	300m/s	600m/s	1200m/s
1000m HAAT	E	E	E	E	U	X
2500m HAAT	E	E	E	E	E	U
5000m HAAT	E	E	E	E	E	E
10000m HAAT	E	E	E	E	E	E
20000m HAAT	U	E	E	E	E	E

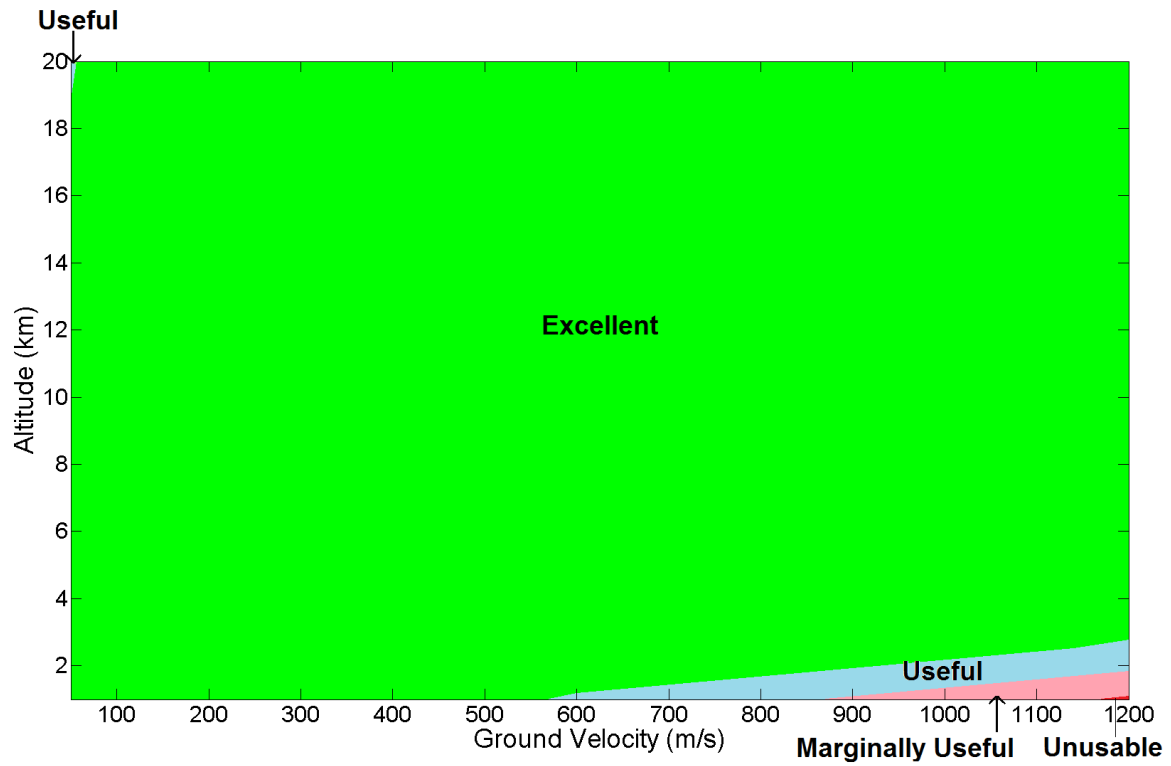
HAAT=Height Above Average Terrain

Table 11: GGI1 Signal Classification Results - Smooth Terrain

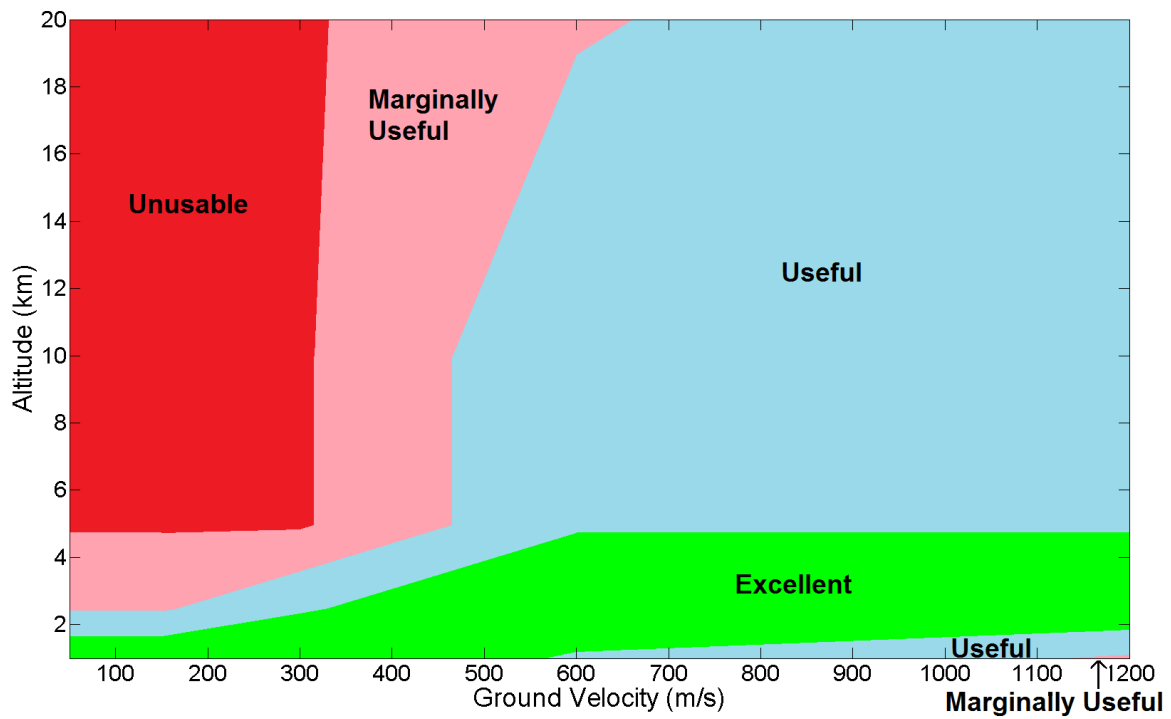
	50m/s	100m/s	150m/s	300m/s	600m/s	1200m/s
1000m HAAT	E	E	E	E	U	MU
2500m HAAT	MU	MU	U	E	E	E
5000m HAAT	X	X	X	X	U	U
10000m HAAT	X	X	X	X	U	U
20000m HAAT	X	X	X	X	MU	U

E=Excellent, U=Useful, MU=Marginally Useful, X=Unusable

Figure 44 graphically represents the data from Tables 10 and 11. Clearly shown is the excellent signal produced by GGI1 at nearly all tested flight conditions when it is flown over rough terrain (track 1). Note that the low altitude, high velocity signal degradation is caused by the LPF and will be later discussed. The signal quickly



(a) GGI1 signal classification results, rough terrain.



(b) GGI1 signal classification results, smooth terrain.

Figure 44: Low Noise GGI Signal Classification Summary (GGI1).

degrades when the instrument is flown over smooth terrain (track 2), as shown in Figure 44b. Note the detrimental effects of slower velocities and increasing altitude. To put these results into real-world terms, most conventional military aircraft would fall into the marginally useful to unusable regimes if using this GGI over smooth terrain. Though it can be argued that un-modeled density variations are certain to exist within and below the terrain and would help to give uniqueness to the signal, this case represents a worst case scenario where the aircraft may be flying over a deep ocean or other areas of sparse terrain and relatively constant subterranean density. Clearly, a more sensitive gradiometer will be required if accurate navigation is to be maintained in these conditions.

Tables 12 and 13 summarize the signal characteristics derived from simulation results using GGI2, the noisier gradiometer.

Table 12: GGI2 Signal Classification Results - Rough Terrain

	50m/s	100m/s	150m/s	300m/s	600m/s	1200m/s
1000m HAAT	E	E	E	E	U	X
2500m HAAT	E	E	E	E	E	U
5000m HAAT	U	U	U	U	E	E
10000m HAAT	X	MU	U	U	E	E
20000m HAAT	X	X	X	MU	MU	U

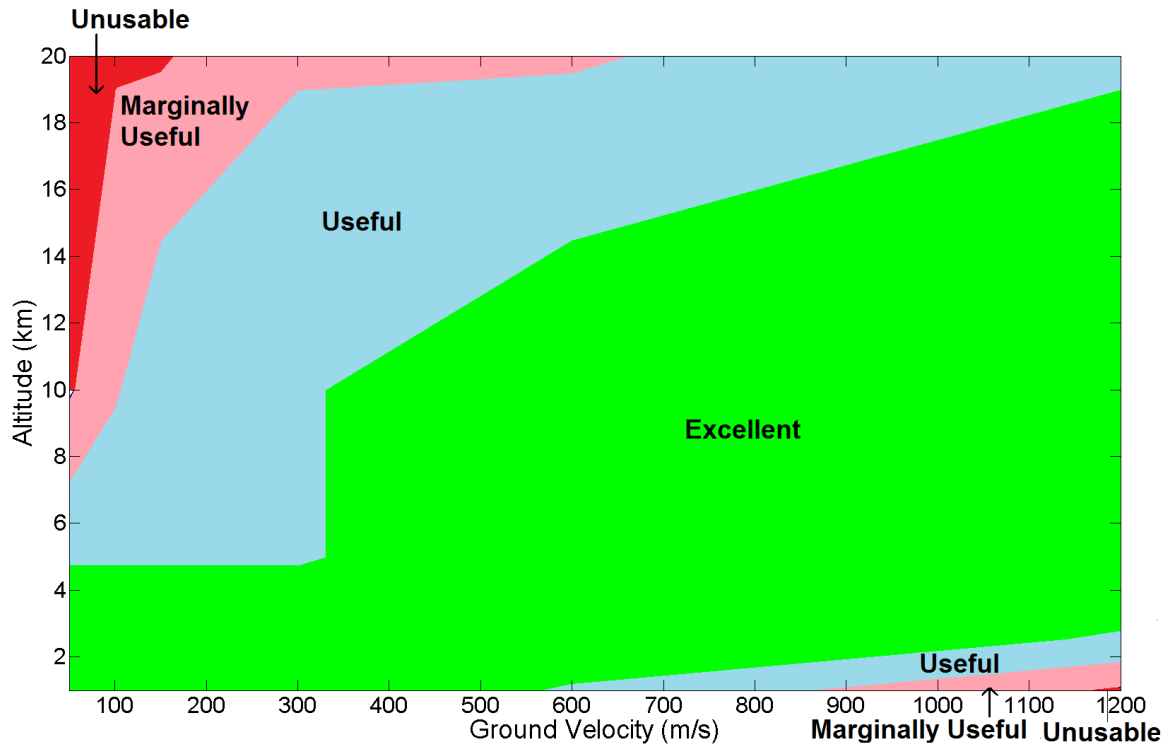
HAAT=Height Above Average Terrain

Table 13: GGI2 Signal Classification Results - Smooth Terrain

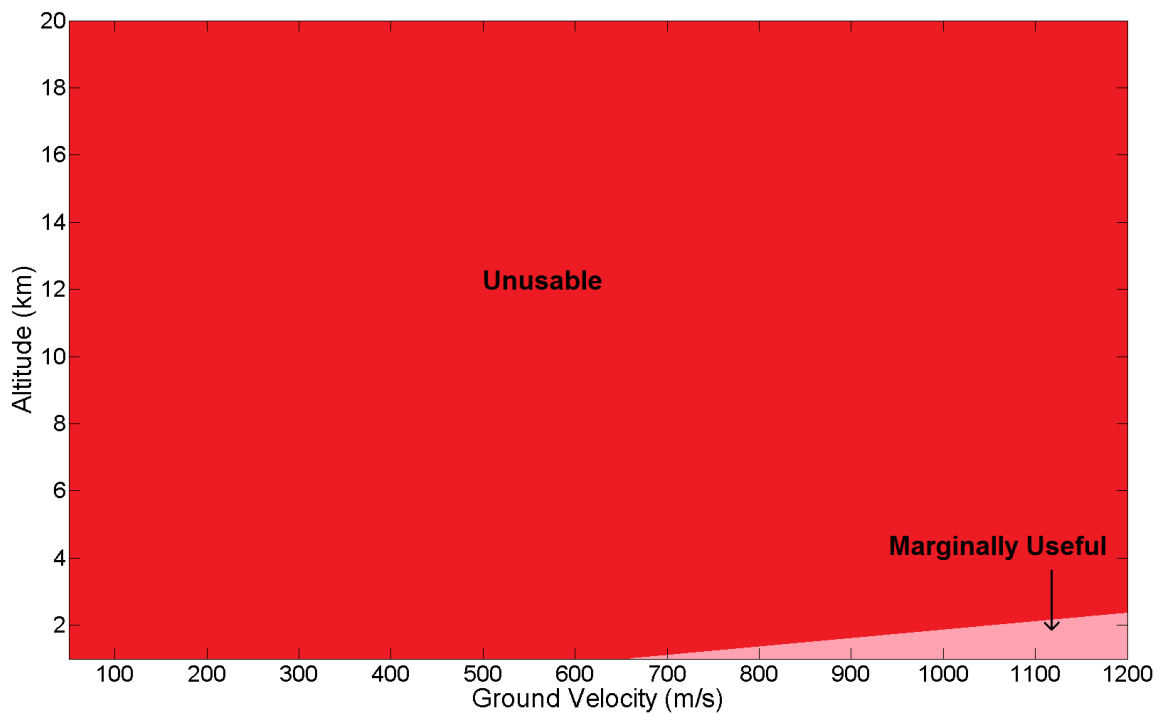
	50m/s	100m/s	150m/s	300m/s	600m/s	1200m/s
1000m HAAT	X	X	X	X	X	MU
2500m HAAT	X	X	X	X	X	X
5000m HAAT	X	X	X	X	X	X
10000m HAAT	X	X	X	X	X	X
20000m HAAT	X	X	X	X	X	X

E=Excellent, U=Useful, MU=Marginally Useful, X=Unusable

Figure 45 graphically represents the data from Tables 12 and 13. Clearly shown is the overall degradation of the signal produced by GGI2. Over rough terrain, the signal usefulness has some similarities to GGI1's performance over smooth terrain. As expected, the increase in GGI noise has the same effect as increasing altitude or



(a) GGI2 signal classification results, rough terrain.



(b) GGI2 signal classification results, smooth terrain.

Figure 45: Noisier GGI Signal Classification Summary (GGI2).

decreasing velocity. In real-world terms, most conventional military aircraft would fall into the useful to marginally useful regimes if using this GGI over rough terrain. When GGI2 is used over smooth terrain, the noise level causes a total loss in signal usefulness for all flight conditions except for a theoretical low altitude, hypersonic case. These results show that a GGI with $1.0Eo$ of noise will not be adequate for all flight and terrain conditions, in agreement with previous works [51]. For added physical insight, examples of the LPF effect and signals at each level of classification are now presented.

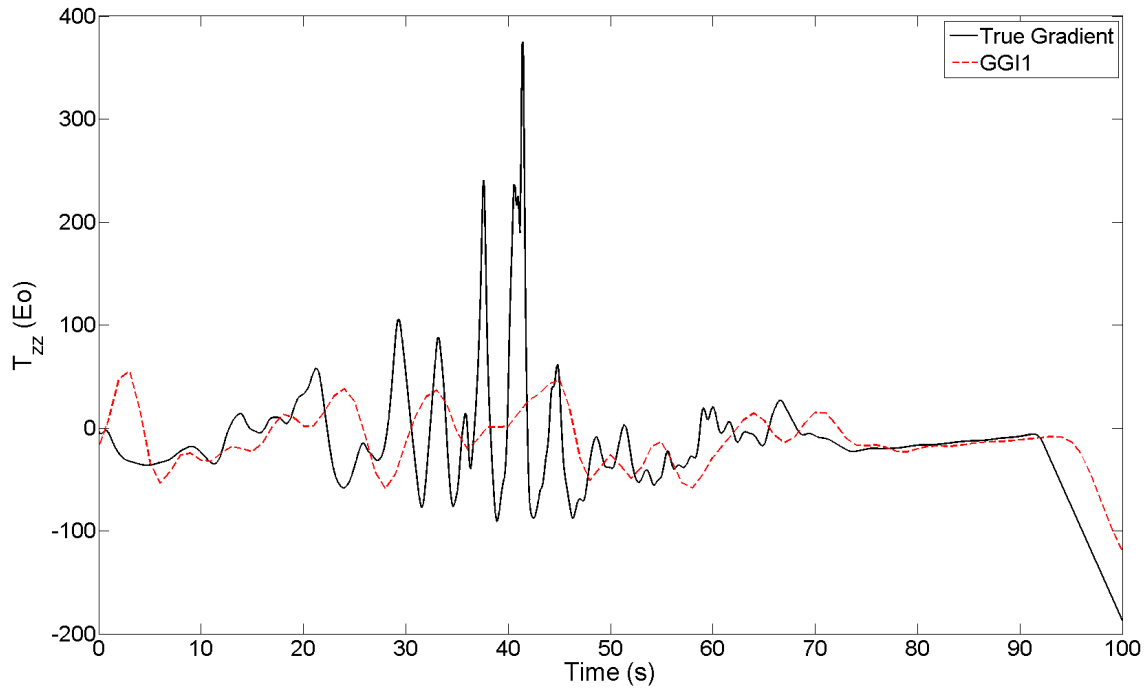


Figure 46: Low Pass Filter Effect, 1200m/s, 1000m, Rough Terrain.

Figure 46 shows the unique case where high velocity combined with rapid changes in gradient (high frequency) actually cause a loss in signal usefulness. This run was completed at 1000m HAAT and 1200m/s (run 6). While the signal may be able to be salvaged by filtering the true gradient as well, this illustrates the effects of the low pass filter at high velocities - significant loss of spatial frequency information in addition to time delay. While no conventional vehicles currently inhabit this flight regime, it is important to note the importance of including the moving average effect

that real time signal generation will require. Additionally, this behavior further serves to validate the overall modeling effort. Addressing these phenomena and optimizing the LPF for real-time signal generation will challenge future nav-grade gradiometer and map-matching algorithm designers.

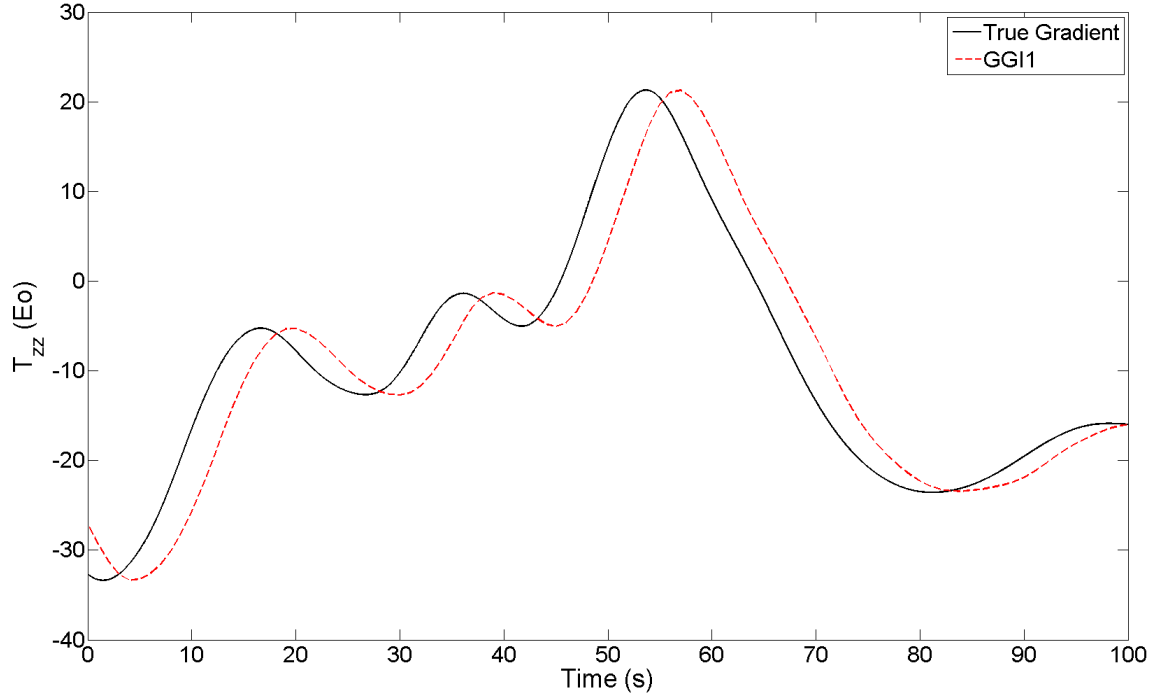


Figure 47: Signal Comparison: Excellent (GGI1) vs. Truth, 300m/s, 2500m, Rough Terrain.

Figure 47 presents a closer look at the behavior of an excellent signal when compared to the true gradient. This signal was generated by the lower noise GGI at 2500m HAAT, a velocity of 300m/s and over rough terrain (run 28). Note that while the time delay is still evident, the signal clearly outlines the overall gradient contour. Also note that the contour is unique yet is low enough in frequency content such that the LPF does not discard useful information. This gives foresight into the idea that a *contour* matching algorithm may be a good starting point for design of a gravity gradient map-matching scheme.

Figure 48 shows a useful signal produced by the lower noise GGI in comparison to the true gradient. This signal was generated at 10000m HAAT, a velocity of

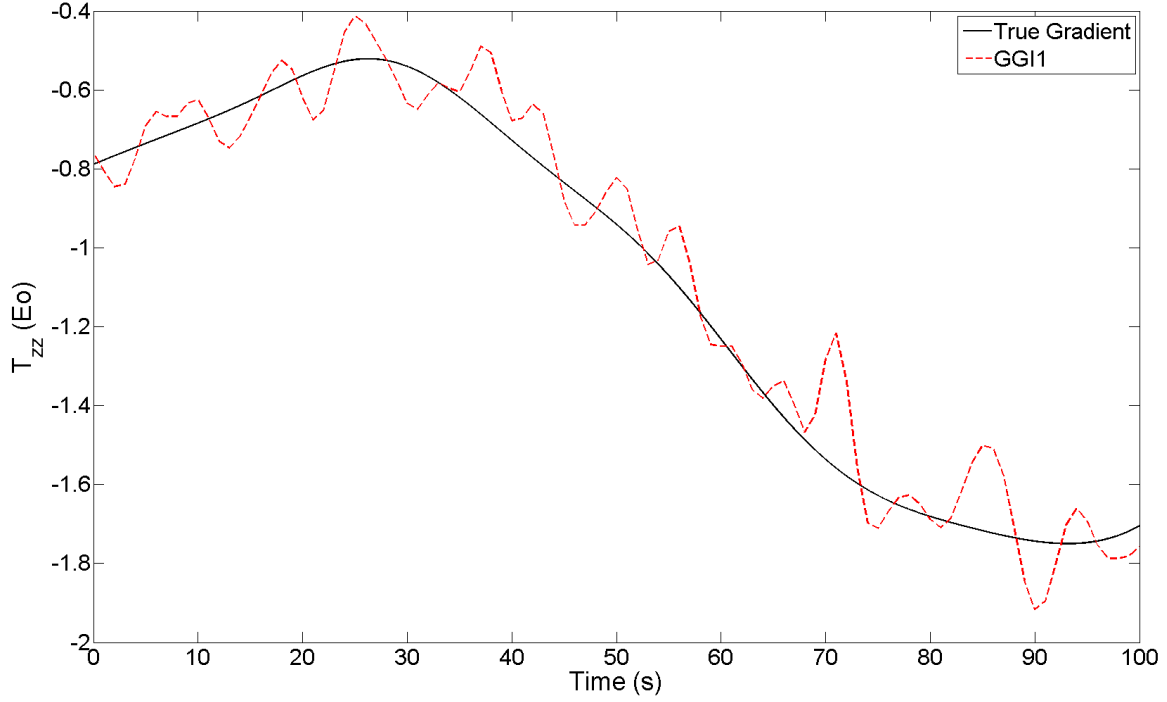


Figure 48: Signal Comparison: Useful (GGI1) vs. Truth, 600m/s, 10000m, Smooth Terrain.

600m/s and over smooth terrain (run 83). Note the overall flattening of the true gradient when compared to the previous case - this serves to reduce the uniqueness of the signal. As such, GGI1 produces a useful signal by doing a fair job of highlighting the true gradient contour. While changes changes aren't captured every second, the gradient contour is defined by the signal.

Figure 49 shows a marginally useful and unusable signal in comparison to the true gradient. These signals were generated at 10000m HAAT, a velocity of 300m/s and over smooth terrain (runs 82 and 94). Note that the true gradient has become relatively flat and doesn't change more than $0.5E_o$ over the entire run. This is a difficult case for either gradiometer. The lower noise gradiometer (GGI1) produces a marginally useful signal by doing a fair job of highlighting the true gradient contour. Even so, since the contour doesn't change very rapidly, it is more difficult to ascertain the exact shape of the contour. The noisier gradiometer (GGI2), however, produces a signal that gives no useful information about the contour shape. For scenarios with

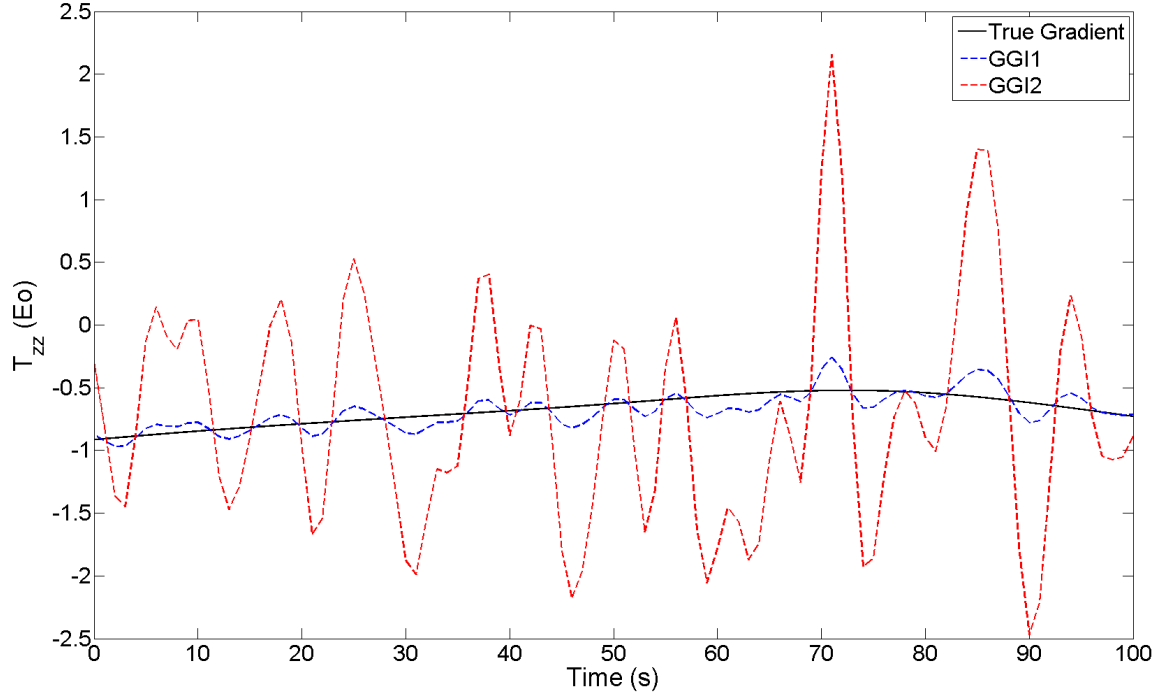


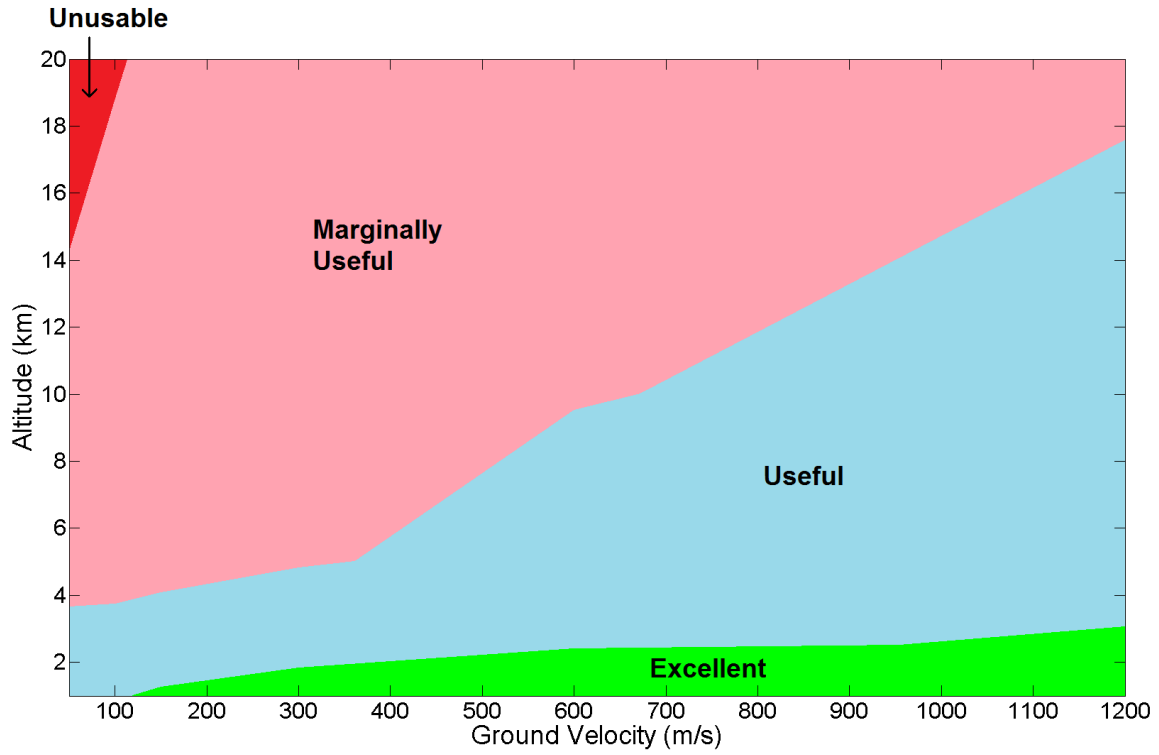
Figure 49: Signal Comparison: Marginally Useful(GGI1) vs. Unusable(GGI2) vs. Truth, 300m/s, 10000m, Smooth Terrain.

relatively sparse terrain (and relatively constant subterranean features), it is likely that the gradiometer must produce noise an order of magnitude lower than GGI1 (approx. $0.01E_o$ of error) for the signal to be excellent. This is consistent with results from Richeson's high altitude, hypersonic cases [51].

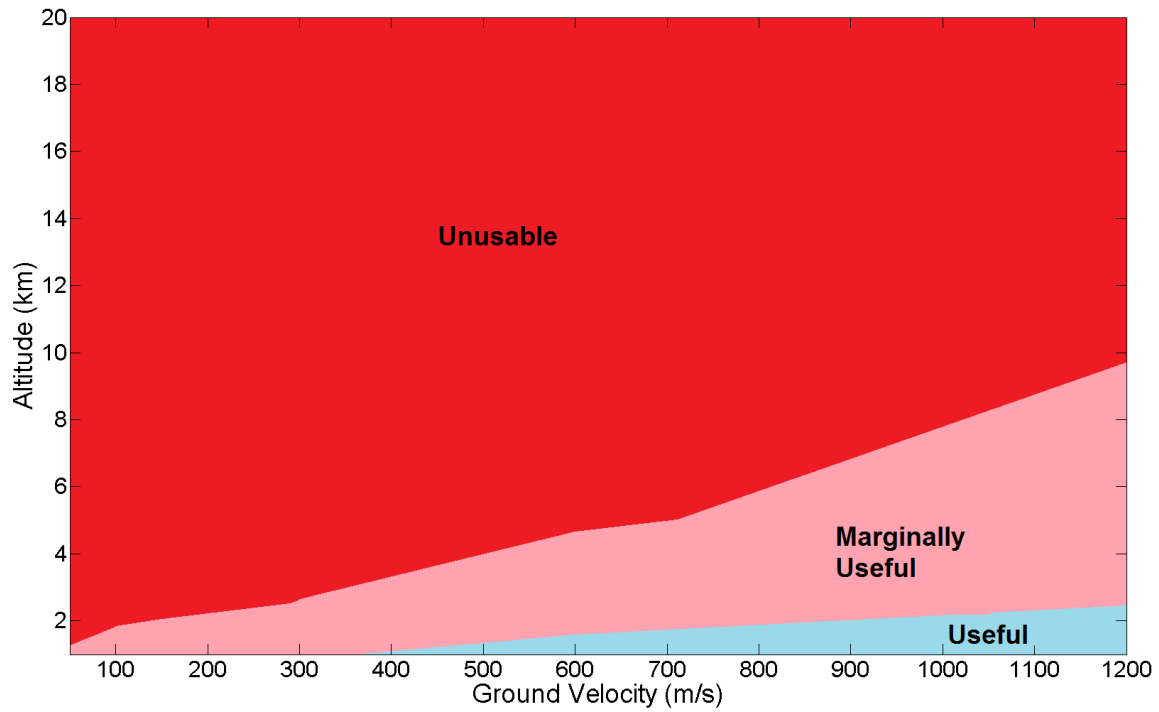
This concludes the qualitative gradiometer signal analysis which has shown that, as generally expected, higher altitudes, smooth terrain, slower velocities, and increased noise can significantly reduce the usefulness of the GGI signal. Additionally, the analysis has shown that LPF settings must be considered and carefully chosen so as not to exclude useful high frequency gradient information when traveling at low altitudes and high velocities. For a constant noise level, the largest contributor to signal degradation is the overflight of relatively flat terrain with constant subterranean density. The next largest contributor to signal loss is an increase in altitude, though slower velocities are nearly as detrimental. Unfortunately, the most difficult regimes to obtain a useful signal are also the regimes where most conventional military aircraft operate (50-

300m/s, 5-10km). In order to ensure an excellent to usable signal is present for all tested flight conditions, a gradiometer with 0.01Eo of RMS error will likely be required.

Navigation Feasibility via Signal Time Rate of Change Metrics. Figure 50 shows the signal usefulness envelope based on metrics obtained from Richeson's simulations and is a summary of the results shown in Figures C.11-C.15 located in Appendix C. Recall that these metrics only apply to GGI1 and that the amount of noise in GGI2 gave Richeson no improvement in navigation performance over an unaided INS. Immediately evident is the overall signal degradation when compared to the previous method (see Figure 44), particularly in areas with smooth terrain. As before, low terrain variance and increases in altitude are the main contributors to signal degradation. At 1000m over both terrain types, all velocities give signals that are at least marginally useful, with most being useful to excellent. However, the results quickly change as altitude increase. The signal at 2500m has already drastically dropped for the slower velocity cases. For the rough terrain, the signal is generally useful, whereas for the smooth terrain, the signal is only marginally useful for velocities greater than 300m/s. At 5000m, the signal has degraded significantly - only a marginally useful to useful signal is obtained for the rough terrain case and a largely unusable signal exists for smooth terrain overflight. Note that at 5000m, faster velocities (600m/s+) are critical in order to maintain signal usefulness over rough terrain due to the drop in gradient strength. The signal continues to degrade as the gradients further attenuate at 10000 and 20000m. The rough terrain signal becomes marginally useful while the smooth terrain signal is completely unusable. If it is again assumed that most military aircraft will be operating in the 50-300m/s and 5-10km region of the envelope, the sensed signal is marginally useful (rough terrain) to unusable (smooth terrain).



(a) GGI1 Signal Classification Results, Rough Terrain.



(b) GGI1 Signal Classification Results, Smooth Terrain.

Figure 50: GGI1 Signal Classification Summary - Signal Time Rate of Change Method.

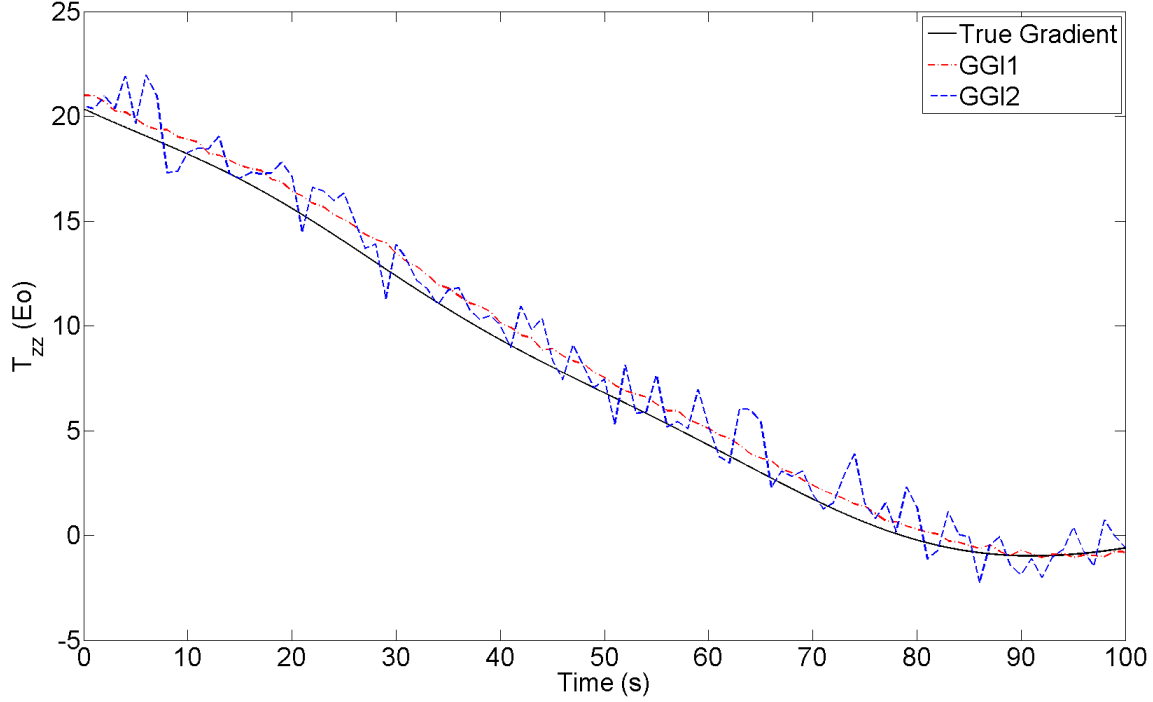


Figure 51: Signal Comparison: Marginally Useful (GGI1) vs. Unusable (GGI2) vs. Truth, 300m/s, 10000m, Rough Terrain, Signal Rate of Change Metrics.

For illustrative purposes, Figure 51 shows the signal required for the heart of the “marginally useful” envelope (300m/s ground velocity, 10000m altitude, rough terrain). This marginally useful signal, produced by GGI1, is shown in red. For comparative purposes, the signal from the noisier gradiometer (GGI2) is also shown. Note how close the GGI1 signal appears to the noise free signal, yet it still produces a “marginally useful” signal. Also note that GGI2 is able to capture the general shape of the contour, albeit not as well as GGI1. This gives rise to the question of whether a revised, gradiometer specific contour based map-matching algorithm could provide substantial benefits in navigation accuracy.

Figure 52 shows the signal from the gradiometers in the heart of the unusable portion of the envelope (300m/s ground velocity, 10000m altitude, smooth terrain). Recall that GGI1 produced a marginally useful signal in this same scenario when qualitative metrics were used (see Figure 49). Evident is the fact that the signal changes very little in time. While slight contour changes may be measured by GGI1, those

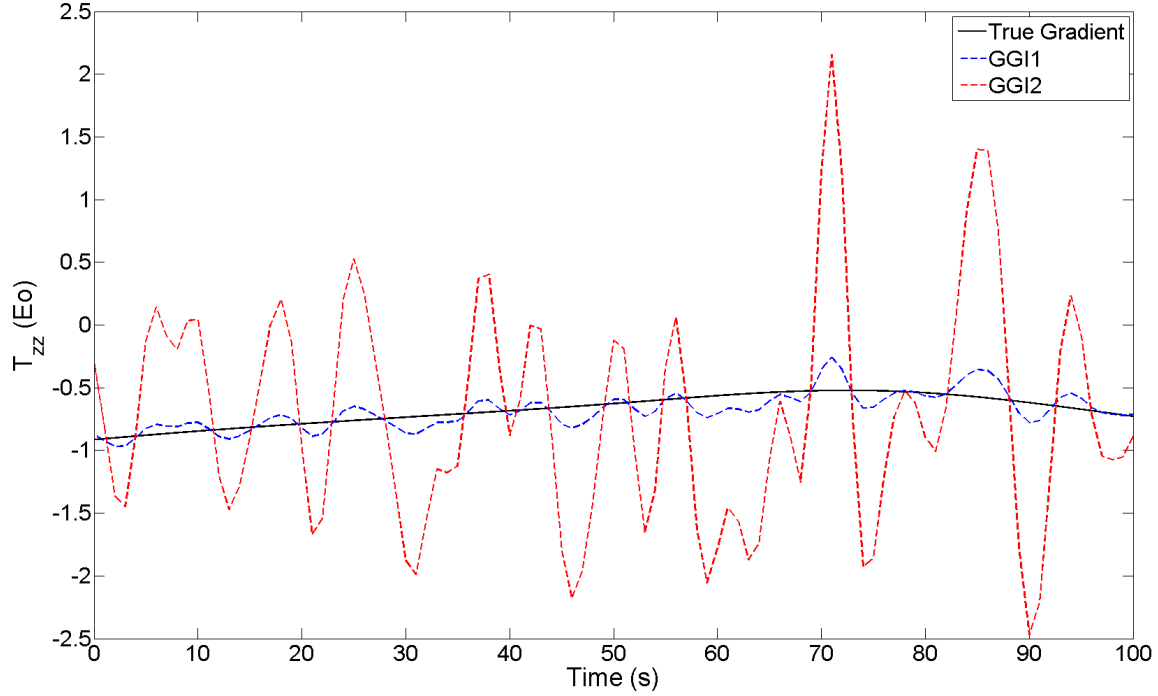


Figure 52: Signal Comparison: Unusable (GGI1 and 2) vs. Truth, 300m/s, 10000m, Smooth Terrain, Signal Rate of Change Metrics.

changes are likely to take several minutes to appear. Gradiometer accuracy would need to improve at least one order of magnitude over that of GGI1 (approximately $0.01E_o$ error) before a usable navigation signal could be obtained from this worst-case scenario. While these results differ slightly from the qualitative study, results from both cases suggest that a $0.01E_o$ gradiometer will be required to ensure a useful signal for all portions of the envelope, particularly for the conditions that most conventional military aircraft operate in. That stated, a gradiometer with performance similar to GGI1 could be used for an airborne navigation feasibility flight test or demonstration if flown at relatively low altitudes and over rough terrain.

To test the recommended gradiometer specification of $0.01E_o$, a run was flown at 20000m over smooth terrain at a velocity of 50m/s. The results, shown in Figure 53, show the signal produced by this gradiometer at the worst possible test conditions. The plot shows that signal is marginally useful as it is able to highlight the overall gravity gradient contour, but it does take time to do so. Also note the gradient scale

in the figure. Not only does the GGI have to provide a signal with $0.01E_o$ of error, but the gradient maps to which this signal will be matched must contain considerably less error. These are the challenges that must be met to ensure a useful signal in *all* flight conditions.

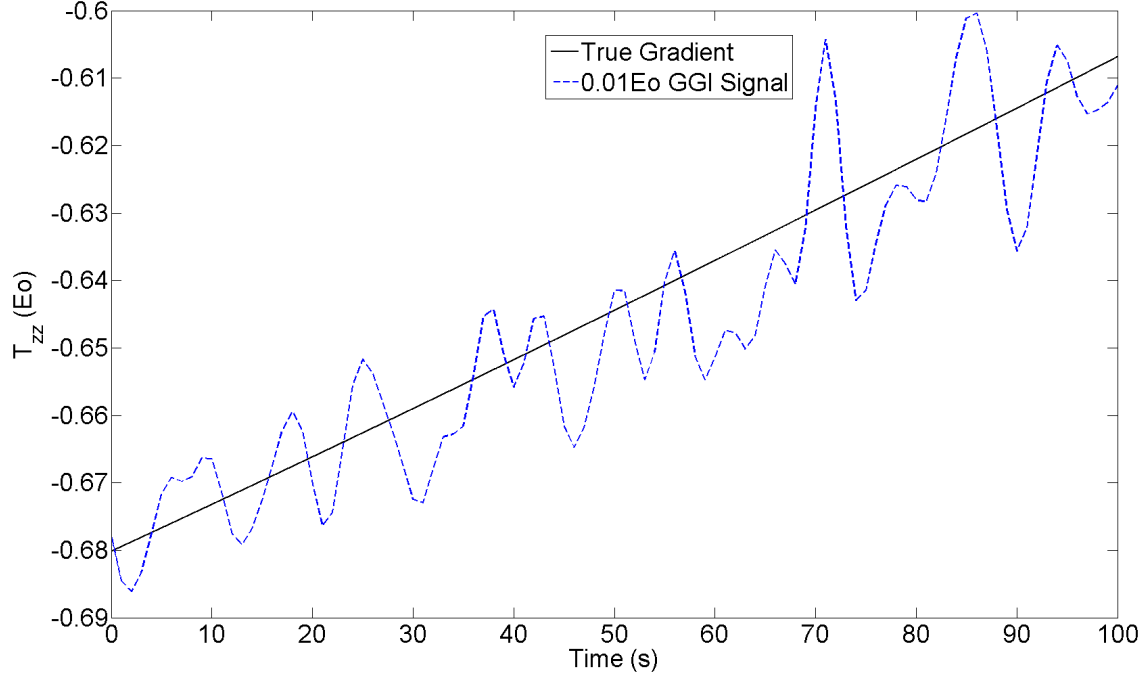
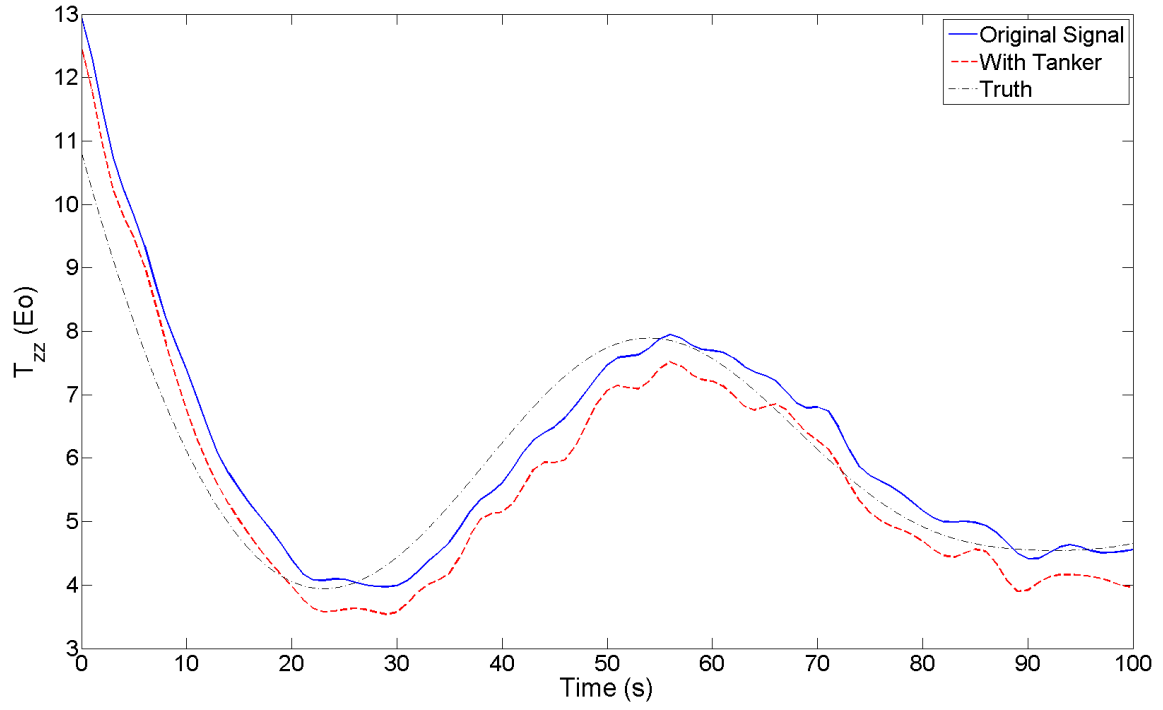


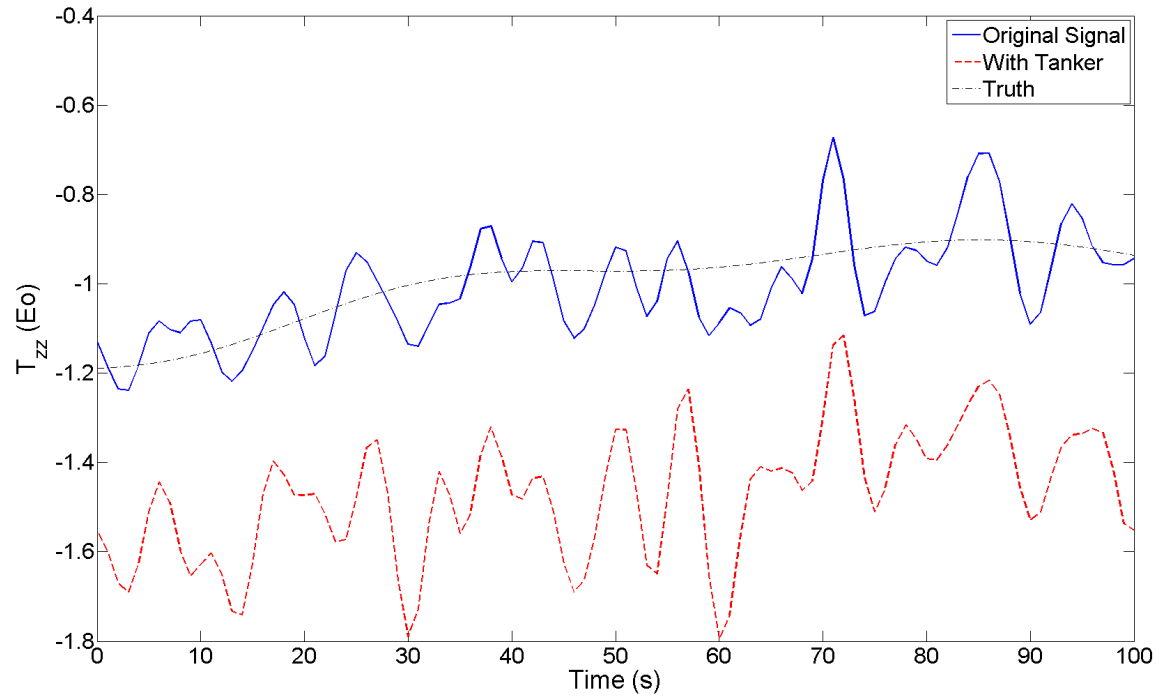
Figure 53: Signal Comparison: Ultra Low Noise GGI ($0.01E_o$) vs. Truth, Worst Case Scenario - 50m/s, 20000m, Smooth Terrain.

The Tanker Effect. Figure 54 captures the overall effect of a large tanker aircraft in the presence of the GGI-carrying aircraft flying at 150m/s and 5000m HAAT (runs 121-122). Only one figure is presented because the trends are the same for each run - the tanker essentially biases the signal by approximately $0.45E_o$ and adds a slight amount of white noise ($\sigma=0.18E_o$) corresponding to relative motion between the tanker and GGI-aircraft as the formation is maintained.

In no case does the tanker change the usefulness of the signal produced by the two GGIs. Should GGI performance improve an order of magnitude over GGI1 (i.e. a $0.01E_o$ GGI), the presence of the tanker may begin to hamper map-matching perfor-



(a) GGI1 tanker effect, rough terrain.



(b) GGI1 tanker effect, smooth terrain.

Figure 54: Tanker Effect, GGI1, 5000m, 150m/s.

mance, particularly over smooth terrain. That stated, a GGI specific map-matching algorithm should be inherently designed to reject biases. It could be argued that the presence of the tanker is akin to a self-gradient and could be removed similarly. However, without broadcasting an active signal, the exact position of the tanker is unknown. Plots of the remaining tanker test cases (runs 123-128) are shown in Figures C.16-C.18 located in Appendix C.

Aircraft Terrain Avoidance Feasibility Results

The results for the first terrain avoidance method will now be presented. Recall that no prior positional information is known and a GGI with a $1Hz$ gradient production rate and $0.2Hz$ cutoff is being used as the sole device in an attempt to provide a consistent terrain avoidance warning. It should be noted that much of the signal for the relatively small obstacles used in these simulations is in the higher frequency (shorter wavelength) portion of the spectrum. As such, the cutoff frequency of the LPF may present an issue when trying to detect the smaller obstacles. The aircraft is flying at $50m/s$ and is level on a plane located $10m$ below to the top of the obstacle (see Figure 35). Both the T_{xx} signal and signal time rate of change are examined in an attempt to determine a usable threshold that indicates imminent terrain collision.

Figure 55 summarizes the GGI signal and signal time rate of change for the 5 runs against obstacles of varying size. Results from the individual runs can be found in Appendix C, Figures C.19-C.23. The analysis begins by examination of the simulation using the smaller obstacles (25 and $50m$). Given the requirement for a warning $1.5s$ prior to impact and a gradient production rate of $1Hz$, the worst possible time for an update is approximately $2.49s$ prior to the impact. An update $2.49s$ prior to impact maximizes the time spent without an update by putting the next update at $1.49s$ until impact - too late given the threshold used for this study. In other words, the update at $2.49s$ prior to impact must contain enough information to trip a warning to the operator. The figure clearly illustrates that the filtered signal

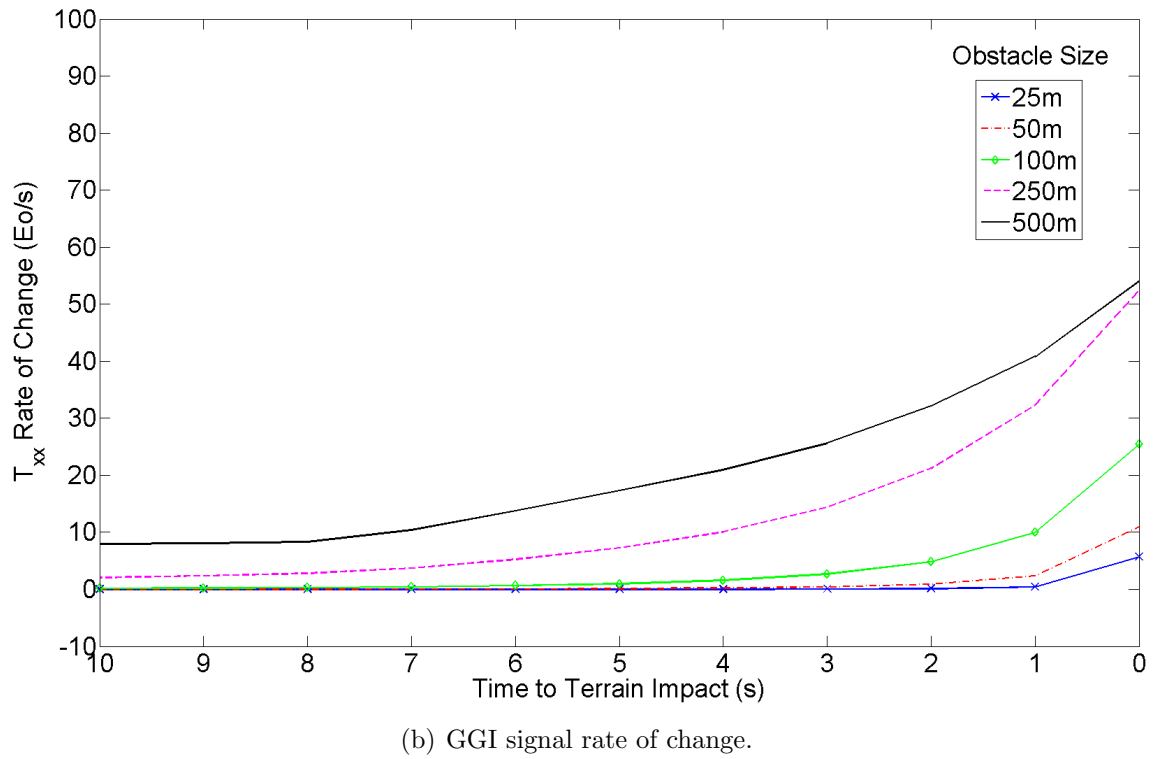
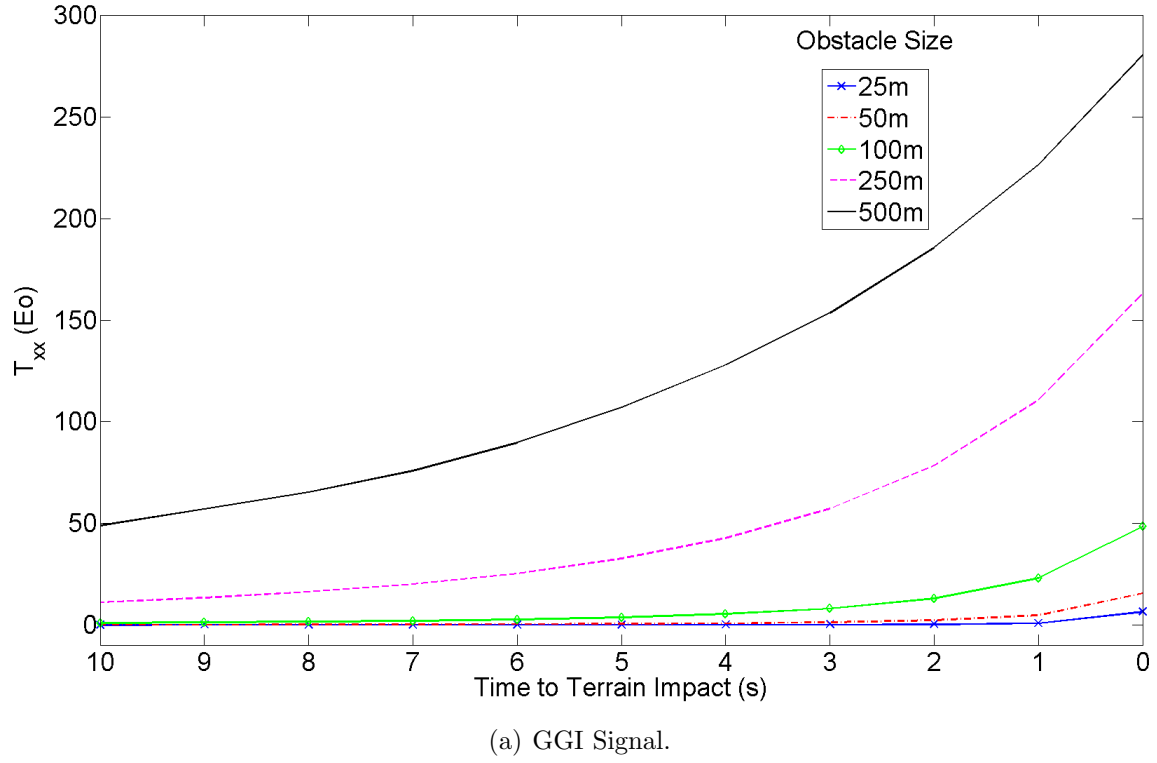
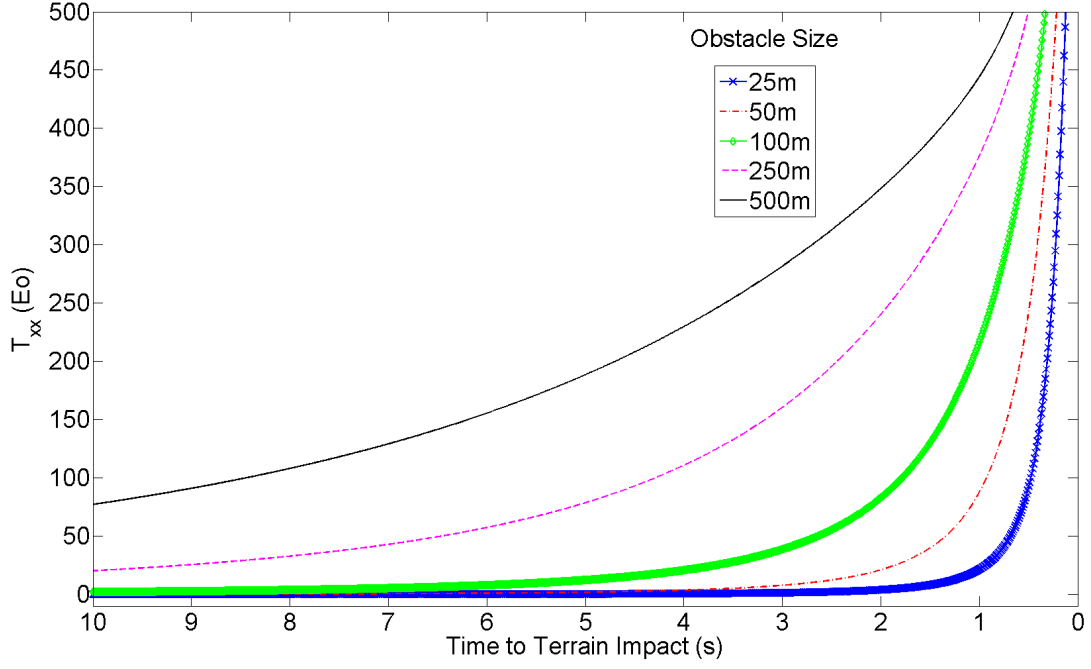


Figure 55: Terrain Avoidance Scenario Summary, GGI signals, 50 m/s, No Noise.

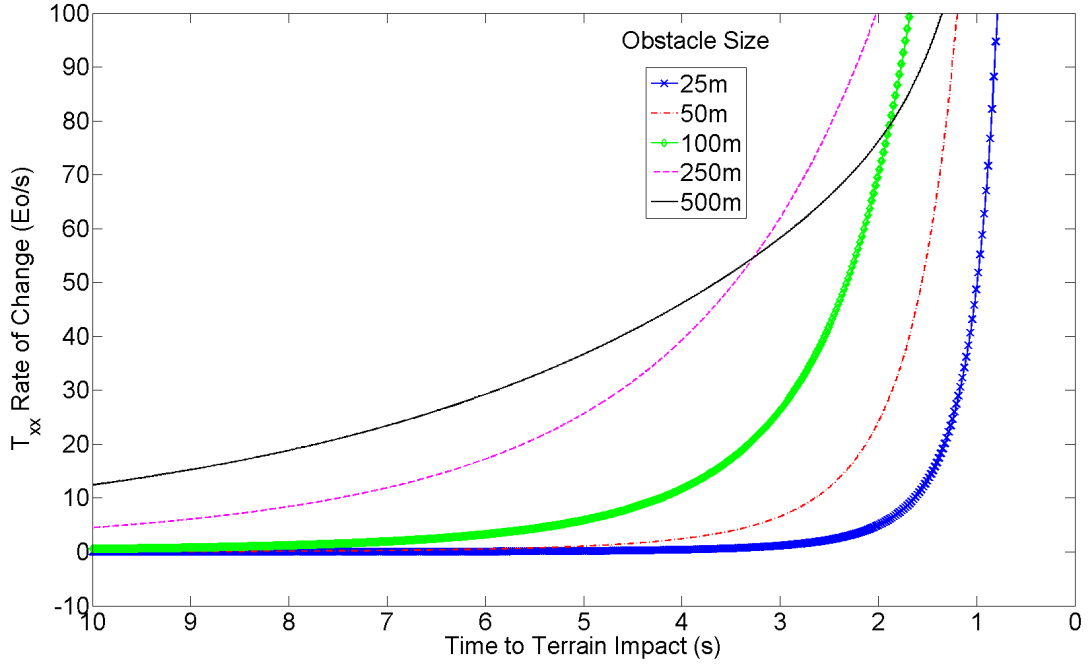
lags the true gradient considerably and that since most of the smaller obstacles' signal intensity is in the high frequency area of the spectrum, it is filtered out. Thus, there is no useful information about the obstacles at 2.49s. Examination of the results for the simulation using a 100m cubic obstacle shows that while there is a slight rise in the GGI signal at 2.49s, it is likely to be buried in signal noise. The results for the simulation using a 250m cubic obstacle show substantial improvements in gradient strength and time of detection over previous runs. Finally, as expected, the results for the simulation using a 500m cubic obstacle show even larger values and rates of change of the sensed gradient. Unfortunately, the plots also clearly show that there is no red flag signal or signal rate of change that signifies imminent terrain impact. The lag and loss of short wavelength information from the LPF are also evident. These results are not entirely unexpected due to the inverse nature of using gravity gradients for what is, in essence, ranging information. There are an infinite number of possible obstacles with different densities and locations that could provide the same signal. Also note that these runs were accomplished at only 50m/s, a relatively low velocity in comparison to many terrain following aircraft that routinely fly low-level routes at 200+m/s. At this point, the investigation moves to an examination of the actual gradients in order to determine, even if a perfect gradiometer existed, if there is some signal threshold that gives obstacle ranging information.

Figure 56 summarizes the true T_{xx} gradient and gradient rate of change produced by the 5 obstacles as the simulation grid is traversed. The plots clearly show that, even with a perfect gradiometer capable of measuring the true signal, there is no clear signal or signal rate of change threshold that signifies imminent terrain impact for these simple scenarios. While the measured gradient time rate of change contains more information earlier in time than the measured gradients, there is no uniqueness based on time to impact. If the threshold was arbitrarily set at some value, the user will get false alarms for larger obstacles and no alarm at all for small objects. Avoiding a big mountain does no good if the user subsequently impacts a small mound of dirt.

This is the crux of GGI-based terrain avoidance - without additional information, ranging information cannot easily be determined with only a gradiometer.



(a) True Gradient.



(b) True gradient rate of change.

Figure 56: Terrain Avoidance Scenario summary, True Gradients, 50 m/s.

Recall that the second method of terrain avoidance assumes that exact positional information is known and that gradient and terrain database maps are available. The role of the gradiometer then is to detect obstacles that were un-modeled on the gradient and terrain database maps. A large water tower was chosen to represent a best case un-modeled obstacle. That is, this object is the largest likely to be constructed quickly enough to avoid being included in NOTAMs or in intelligence reports. If the gradiometer cannot warn the user of the presence of an obstacle this size, scenarios with smaller objects such as communication towers will be even less successful. To better understand the signal structure of the obstacle, the analysis of this terrain avoidance method begins by examining the T_{xx} gradient produced by the water tower terrain anomaly in the spatial frequency domain.

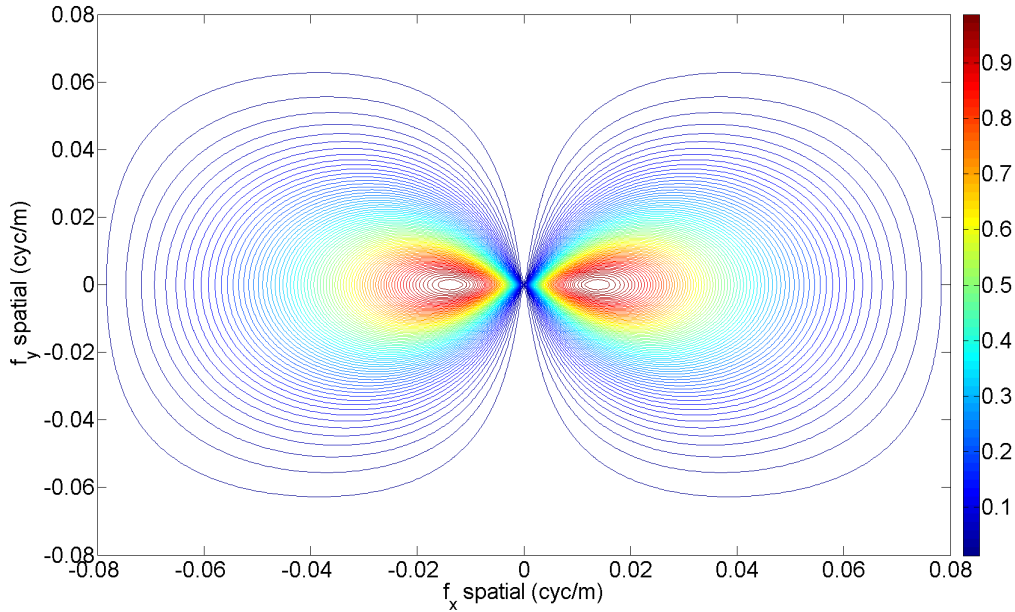
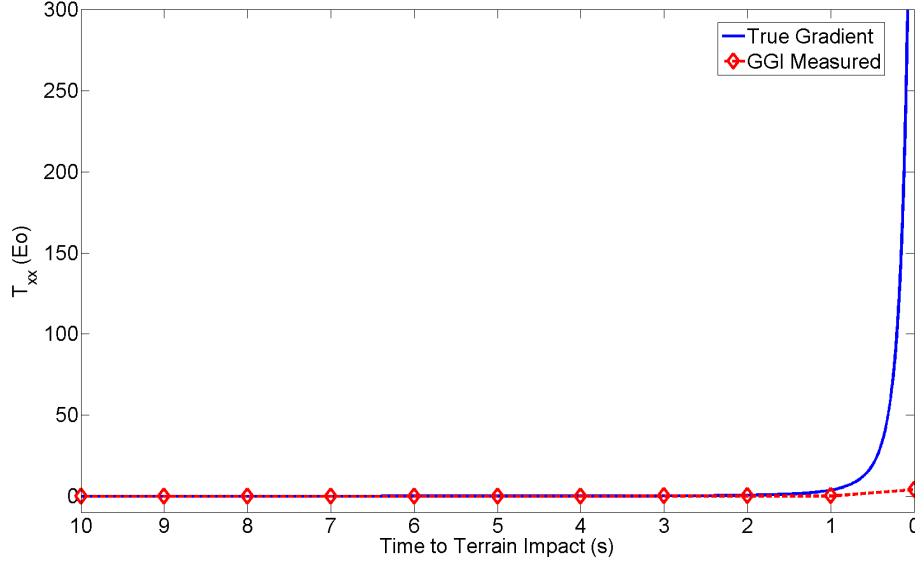


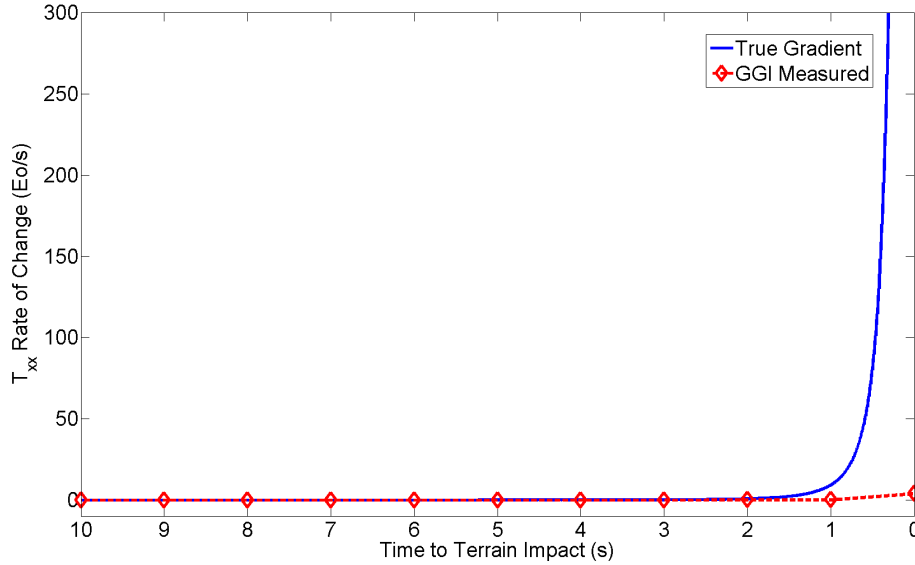
Figure 57: Water Tower Spectrum

Figure 57 shows the absolute amplitudes of the gradient as a function of spatial frequency (for continuity, this spectrum was calculated on a horizontal plane 5m above the top of the tower). The figure shows that most of the signal intensity is located in the 0.005-0.03cyc/m spatial frequency region (33-200m wavelengths). This

immediately raises concern because, even at relatively slow speeds ($\sim 50m/s$), the minimum wavelength allowed by a LPF with a $0.2Hz$ cutoff frequency is approximately $250m$ (see Table 9). This mirrors the phenomenon seen in the 25 and 50m obstacles from the previous analysis.



(a) Signal.



(b) Signal rate of change.

Figure 58: Water Tower Scenario, T_{xx} vs time, 50m/s, No Noise.

The results for the water tower run are shown in Figure 58. As in the 25 and 50m obstacle results, a gradiometer providing gradients at $1Hz$ and filtering the signal above $0.2Hz$ results in the water tower gravitational gradients never being sensed by the gradiometer until after impact. Also shown are the true gradients produced by the water tower. If the assumption of a perfect gradiometer is made, the water tower does produce a signal of approximately $1.0Eo$ at $1.5s$ to tower impact. Again the question arises: is the anomalous gradient from a small tower close-by or a larger un-modeled object in the distance (i.e. the inverse problem). Even if ranging information were able to be determined (perhaps by using the terrain avoidance method proposed by Jircetano [46]), the question of required gradiometer performance arises. To determine these values, the gradiometer requirements for sensing most of the example water tower's spectrum (down to 33m wavelengths) at different velocities are listed in Table 14.

Table 14: Gradiometer Requirements to sense Water Tower

Velocity(m/s)	Est. Gradient Production Rate(Hz)	Cutoff Frequency(Hz)
50	7.5	1.5
100	15	3.0
150	23	4.5
300	45	9.0
600	91	18
1200	182	36

To further support these estimated gradiometer requirements, it is assumed that additional information is supplied via a gravimeter in a scheme similar to the Lockheed Martin UGM. Under the assumption that the UGM provides adequate submarine terrain avoidance capability and that the gradiometer used within the UGM provides gradients at $1Hz$ with a cutoff frequency of $0.2Hz$ and is traveling at $20knots$ ($10m/s$), gradients are produced every 10m and wavelengths greater than 50m are sensed. By converting these metrics into equivalent airborne platform requirements based on velocities, Table 15 summarizes the equivalent gradiometer update rate and cutoff frequency requirements.

Table 15: Predicted Gradiometer Requirements for UGM Style Terrain Avoidance

Velocity (m/s)	Gradient Production Rate (Hz)	Cutoff Frequency (Hz)
50	5	1
100	10	2
150	15	3
300	30	6
600	60	12
1200	120	24

It must be stressed that these update rates and cutoff frequency specifications must be met without an increase in noise. That is, the gradiometer must have massive improvements in gradient production rate and LPF cutoff frequency, yet produce sub-Eotvos noise levels in the signal. In the $300m/s$ scenario, the necessary gradiometer noise spectral density for $0.1Eo$ of noise would be approximately $0.025Eo/\sqrt{Hz}$, valid up to half the sampling rate of $30Hz$. This is well beyond any estimated performance levels for future airborne gradiometers. These results highlight the significant challenge of using a gradiometer based system for aircraft terrain avoidance. Based on the results from both methods, it has been shown that gradiometer based airborne terrain avoidance is unfeasible in the near future.

Results Summary

It has been shown that if airborne GGIs can approach $0.01Eo$ standard deviation of noise, a signal strong and unique enough for map-matching exists for all tested flight conditions except for those involving extremely high velocities ($1200m/s$) and very low altitudes ($1000m$). This is provided that accurate gravity gradient databases exist. The necessity of such a gradiometer is driven by the fact that gradient uniqueness falls rapidly as the host vehicle traverses smooth terrain, increases altitude or decreases velocity. To adequately measure a gravity gradient contour in a worst case scenario, the noise level of the instrument must be an order of magnitude lower than those of gradiometers projected to be available within 10 years. Also, the assumption of the existence of accurate, high resolution gradient maps cannot go unchallenged.

While map availability is rapidly increasing through a variety of survey methods, worldwide coverage, particularly in remote or hostile areas, will likely remain a contingency for quite some time. While it is unlikely that this navigation method can be widely employed using a gradiometer available within 10 years, the signal analysis has also shown that a GGI with $0.1E_o$ of noise could be used in a ground or flight test demonstration of the technology. This assumes that relatively accurate gravity gradient maps of the area exist and the test is done at slow velocities, low altitudes, and over rough terrain. Success in such a test could open the door for more research and development funding.

The GGI-based terrain avoidance studies have painted a relatively bleak picture for the method as it pertains to conventional aircraft. Due to bandwidth, gradient production rate limitations and the inverse nature of the problem, a noise free gradiometer failed to provide any useful terrain avoidance information. These tests were designed as a best case approach to solving the problem and proved that no consistent signal threshold for imminent terrain impact exists. Should the inverse problem of ranging dangerous obstacles be solved via a novel method or increased observability, real world application of such a scheme would inevitably demand extremely high gradiometer performance - the likes of which have not been mentioned in open literature. That stated, research into methods of GGI-based or assisted terrain avoidance should not be abandoned as they could eventually be used in applications such as cave navigation or navigation through indoor environments. With the completion of the results and analysis of this study, the focus now turns to recommending the future steps needed to make this magnificent instrument the game changer it has the potential to be.

V. Discussion

Research Summary

This research represents the first step in a multi-phase approach towards development of a gravity gradiometer-based aircraft navigation and terrain avoidance system. By generating gravity gradient data from terrain and underlying geology, a realistic representation of gradients produced by the Earth was obtained. Next, using available gradiometer specifications, a signal processing approach was implemented to model the effects of real-time gradient measurement onboard an aircraft. The resulting signal was analyzed via metrics developed to rate signal strength and uniqueness at a variety of representative flight conditions. Based on this comparison between GGI signals and truth, map-matching and, in turn, aircraft navigation feasibility were demonstrated. Additionally, future gradiometer performance requirements necessary to produce a usable signal over the entire tested flight envelope were proposed and tested. Finally, several best case terrain avoidance scenarios were devised to determine feasibility of using a GGI in such a role. By using time to terrain impact metrics, an attempt to find a threshold gradiometer signal level was made for a variety of obstacles. While feasibility for GGI-based terrain avoidance was unable to be demonstrated, some alternative methods and corresponding gradiometer requirements were presented.

Challenges and Limitations

The two key obstacles which must be overcome in order to make gravity gradient map-matching aircraft navigation systems a reality are the performance of airborne gradiometers and the availability of accurate gravity gradient maps. In this research, it was assumed that with continued interest from the geophysical, mining, and defense industries, gravity gradiometers will eventually meet the proposed requirements for aircraft navigation feasibility. However, they must meet these requirements - making accurate measurements at the $10^{-11}s^{-2}$ level, yet still be small and light enough to fit within limited space inside an aircraft. Also, they must be robust enough to

survive the military flight environment - including rapid maneuvers, elevated g-forces and hostile environmental conditions often encountered at forward-deployed locations. Finally, increased gradiometer sensitivity does not come without drawbacks. Accounting for self gradients produced by the host vehicle is already a challenging prospect at the $1Eo$ sensitivity level. For this study, it was assumed that self gradients were always exactly known. Should a gradiometer able to sense changes at the $0.01Eo$ level be implemented, precise monitoring and correction of self gradients will be vital to ensure proper measurements. Fuel slosh, the release of stores, control surface and even pilot movement will all present gradient changes that must be accounted for.

It was also assumed that the generated gravity gradient maps represent truth - that is, each value was exactly correct in magnitude and position. Actual gravity gradient maps with enough resolution to be useful in a map-matching algorithm are very limited in quantity, generally proprietary and contain GPS level position errors. Obtaining accurate surveys over areas considered unfriendly or hostile presents an additional challenge. However, as more accurate ground, air, and space-based surveys take place and gradient calculation methods evolve, the resolution and availability (particularly in remote areas) of gravity gradient maps will significantly increase. In summary, there are significant challenges and limitations to overcome before GGI-based aircraft navigation can be a reality. Given continued research efforts, these issues are certainly solvable. Though unlikely to be completely addressed within 10 years, it is anticipated, based on previous trends, that these issues will largely be solved in 20-30 years time.

GGI-based airborne terrain avoidance is the more difficult problem due to the inverse nature of ranging hazardous terrain via gravity gradiometry. While methods have been proposed to solve this problem [46, 47], there is very little research published in open literature to back-up these ideas. Under the assumption that the inverse problem is solvable, the gradiometer requirements for sensing obstacles which threaten low flying aircraft are dramatically higher than any current or proposed GGI specifications. That is not to say that GGI-based (or assisted) airborne terrain avoid-

ance is impossible, but it is a distinctly greater challenge than aircraft navigation via gravity gradient map-matching.

Significant Contributions and Insights

In regards to gravity gradient modeling, this research has clearly implemented methods that were unable to be found in previous navigation via gravity gradiometry works. First, a user friendly interface to generate gravity gradient data representing realistic values produced by the Earth was developed. Next, it was proven that if a bias is acceptable, Parker's method can produce gravity gradient data much faster than more rigorous methods. Also, terrain and geology (high and low frequency) gravity effects were accounted for using a combination of modeling techniques. Finally, tanker aircraft and man-made ground obstacle gravitational gradient models were developed as well.

While relatively simple gravity gradiometer models have been presented in previous works, real time signal processing effects such as low pass filtering are rarely mentioned. In most previous studies, it was generally assumed that airborne gradiometers provide truth measurements plus white noise. This is not entirely true as the assumption fails to account for phase lag and time delay implications from the LPF. In other words, extensively processed post-flight data was assumed to be available instantly. For a more realistic approach, this research developed and validated two airborne gradiometer models required to provide real-time gravity gradient measurements for use in a map-matching navigation algorithm and terrain avoidance scenarios. Also, the effects of time-delay, phase distortion and loss of high frequency information caused by the low pass filter were examined and found to likely degrade map-matching performance - especially at extremely low altitudes and high velocities. Finally, future navigation-specific gradiometer design targets were proposed and validated.

Significant contributions to the study of passive aircraft navigation via a GGI-based map-matching system are now presented. This research developed two methods of GGI signal usefulness classification and demonstrated that unique gravity gradient signals do exist and can be measured by an airborne gradiometer. The study also investigated the GGI signal in regimes previously not examined and found that signal levels are highly dependent on terrain uniqueness and host-vehicle altitude and velocity. As such, low terrain variance, high altitude, and low velocities are detrimental to the signal. Unfortunately, legacy military aircraft flight regimes generally provide the weakest signal. Additionally, this study was the first to examine the effects of formation flight on the GGI signal. It was shown that placing the GGI aircraft next to a large tanker aircraft gave a bias and small amount of noise to the GGI signal. While it did not significantly hamper the signal's usefulness for the tested GGIs, formation flight may reduce map-matching performance if a more sensitive gradiometer is used, particularly in areas with smooth terrain. Also, it was shown that future GGIs will need to achieve error levels on the order of $0.01E_o$ for navigation usefulness over most of the tested flight envelopes (50-1200m/s velocity, 1-20km altitude, rough and smooth terrain). However, should a ground or flight test demonstration of the navigation technology be desired, gradiometers currently in flight test for mining industries can provide a useful navigation signal for lower flying vehicles traversing rough terrain.

While previous works involving GGI-based terrain avoidance are few in number, this research sheds some insight as to why. After development of a GGI-based terrain avoidance test methodology by modeling a variety of obstacles which are hazardous to low flying aircraft, it was demonstrated that obstacle range calculation is an inverse problem - no imminent terrain impact signal threshold exists. It was also shown that, should the inverse problem be solved, major GGI improvements are needed for terrain avoidance feasibility. For example, a 45x improvement over current GGI gradient production rate and LPF cutoff frequency is needed for an aircraft traveling 300m/s to sense small obstacles. Additionally, the GGI must meet these specifications

with *no additional* noise. The key driver for these steep gradiometer requirements is the fact that obstacles most dangerous to low flying aircraft, such as towers and water tanks, have a high frequency signal easily filtered out, buried in noise, or masked in the signal from surrounding terrain.

Recommendations for Future Research

With the initial feasibility investigation complete, this section highlights future research recommendations. While these recommendations are not ordered by priority (all must eventually be addressed), the next logical step for researchers is the development of a gravity gradiometer specific map-matching algorithm. Once developed, the effort to integrate the algorithm into a navigation system can begin. This is critical as it will ultimately provide *quantitative* navigation performance results that can be used to validate and refine the feasibility metrics used in this research. Future research recommendations are as follows:

- Continue development of a contour based gravity gradient map-matching algorithm.
- Integrate map-matching algorithm into an aircraft navigation system and determine qualitative navigation performance.
- Investigate the navigation performance of an INS using a GGI for gravity compensation *and* position updates provided via a map-matching scheme.
- Refine gradiometer model and examine effects of different filter types.
- Further validate and refine the signal usefulness metrics proposed in this research.
- Further validate navigation grade gradiometer requirements proposed in this research.
- Analyze navigation performance when position and measurement errors are embedded within gravity gradient maps used as truth sources.

- Generate gravity gradient maps using methods that include density anomalies within the terrain and geology.
- Model low frequency gravitational effects via the higher resolution EGM2008 model (in lieu of EGM96).
- Pursue methods to solve the inverse problem of terrain avoidance.

Conclusion

While this research has shown that major improvements in GGI gradient production rate and bandwidth are needed before GGI assisted terrain avoidance can be realistically considered, it has also proven that the fundamentals of using a modern gravity gradiometer as the foundation of a completely passive, precision aircraft navigation system are sound and that the method is entirely feasible. By modeling sensors that provide real-time measurement of gravity gradients and then analyzing the resulting signals via several metrics, it was determined that a specialized GGI can provide a signal strong and unique enough for map-matching utility. While the limiting factors have been mentioned, they are certainly conquerable given more time. With the results of this study and the efforts of previous researchers, along with the contributions from the gravity gradiometer development community, the foundation for a passive, essentially unjammable, precision aircraft navigation system has been laid. Forty years ago, airborne gravity gradient surveys would never work. Today, these once impossible surveys can be flown daily. Forty years from now, gravity gradiometers may very well form the backbone of aircraft navigation systems.

Appendix A. Matlab[®] Code

Listing A.1:

```
1 %*****%
% Gravity Gradient Signal and "Truth" Calculation %
% based on Parker methods and EGM96. %
% %
% Marshall Rogers 2008 %
6 % %
%*****%

close all
clear all
11 clc

G=6.67E-11; %Universal Gravity Const.
p=2670; %Average terrain density

16 Eotvos=1E-9; %use to convert units to Eotvos

M=input('Rough or Smooth Terrain [R/S]?','s');
% pulling in elevation data, use/add different areas if desired
if ((M=='R')|(M=='r'))
21 lat=[35 37]; %NS Geodetic coordinates (WGS84 reference ...
    ellipsoid) of grid
    long=[-122 -120]; %EW Geodetic coordinates (WGS84 reference ...
        ellipsoid)of grid
    [Z, refvec] = dted('CA_elev2', 1,lat,long); % read in rough ...
        area dted data, Z is referenced to MSL (the geoid)
    elseif ((M=='S')|(M=='s'))
        lat=[35 37]; %NS Geodetic coordinates (WGS84 ...
            reference ellipsoid) of grid
26 long=[-90 -88]; %EWGeodetic coordinates (WGS84 ...
        reference ellipsoid) of grid
```

```

        [Z, refvec] = dted('AK_elev', 1,lat,long); % read in ...
            smooth dted data, Z is referenced to MSL (the geoid...
        )

        else
            fprintf('Wrong Answer!');
            break;
31 end

figure % plot the terrain contour map
geoshow(Z,refvec,'DisplayType','texturemap'), colorbar
xlabel('Longitude','FontSize',20), ylabel('Latitude','FontSize'...
    ,20)
36 set(gca,'FontSize',20);
vcb = colorbar;
set(get(vcb,'Ylabel'),'String','Terrain Height (m)','FontSize',24)
set(vcb,'FontSize',20)

41 alt=input('Input altitude (meters height above average terrain) = ...
    ');
track_start=input('Track Start [lat long] = ');
track_end=input('Track End [lat long] = ');
vel=input('Input Velocity (meters/sec) = ');
update_rate=input('Enter GGI Update Rate (sec) = ');
46 filter_cutoff=input('Enter GGI Low Pass Filter Cutoff Frequency (...
    Hz) = ');
bandwidth=filter_cutoff;
NSD=input('Enter GGI Noise Spectral Density (E/(Hz^1/2)) = ');
filename1=input('Input Filename for GGI Signals (use .mat ...
    extension): ','s');
filename3=input('Input Filename for True Map (use .mat extension):...
    ','s');
51 alt=mean2(Z)+alt; % Height above average terrain calc
alt_EGM96=alt+mean2(Z);

%% Computer Earth's Radius at central grid point

```

```

a = 6378137.0; % earth semimajor axis in meters
56 f = 1/298.257223563; % reciprocal flattening
e2 = 2*f-f^2; % eccentricity squared

lat_middle=(min(lat)+max(lat))/2;
lat_middle2=atand((1-e2)*tand(lat_middle)); %convert geodetic lat ...
    to geocentric lat
61 long_middle=(min(long)+max(long))/2;
N=a/sqrt(1-e2*sin(lat_middle2)^2);
X_ECEF=N*cosd(lat_middle2)*cos(long_middle);
Y_ECEF=N*cos(lat_middle2)*sin(long_middle);
Z_ECEF=(N*(1-e2))*sin(lat_middle2);
66 R1=sqrt(X_ECEF^2+Y_ECEF^2+Z_ECEF^2); % Earth's radius at grid ...
    midpoint

dlong=max(abs(long))-min(abs(long)); %distance longitude
dlat=max(lat)-min(lat); % distance latitude
x_dist=R1*(pi/180)*dlong*cosd(lat_middle);
71 y_dist=R1*(pi/180)*dlat;
y_int=R1*(pi/180)*(3/3600); %3 arc sec spacing (DTED Level 1) ...
    3/3600
x_int=cosd(lat_middle)*y_int;
Y1=[0:y_int:y_dist];
X1=[0:x_int:x_dist];
76 [X2,Y2]=meshgrid(X1,Y1);

x_track=-R1*(pi/180)*(abs(track_end(2))-abs(track_start(2)))*cosd(...
    lat_middle);
y_track=R1*(pi/180)*(abs(track_end(1))-abs(track_start(1)));
track_angle=(180/pi)*atan2(y_track,x_track);
81
% setup initial position and velocity for simulink
x_vel=vel*cosd(track_angle);
y_vel=vel*sind(track_angle);
vi=[x_vel y_vel 0];

```

```

86 speed=norm(vi);
   sim_time=floor(sqrt(x_track^2+y_track^2)/vel);
   ipos=[x_dist-R1*(pi/180)*(abs(track_start(2))-min(abs(long)))*cosd...
        (lat_middle) y_dist-R1*(pi/180)*abs(max(lat)-track_start(1)) ...
        0]; % initial position based on input

   figure % plot the track onto the terrain contour map
91 geoshow(Z,refvec,'DisplayType','texturemap'), colorbar
   xlabel('Longitude','FontSize',20), ylabel('Latitude','FontSize'...
        ,20)
   set(gca,'FontSize',20);
   vcb = colorbar;
   set(get(vcb,'Ylabel'),'String','Terrain Height (m)','FontSize',24)
96 set(vcb,'FontSize',20)
   hold on
   plot([track_start(2) track_end(2)],[track_start(1) track_end(1)],'...
        k','Linewidth',4)

   %% Gradients by Parker's Methods (Terrain)
101 del_x1=x_int; % x interval
   del_x2=y_int; % y interval
   m1=length(X1);
   m2=length(Y1);
   p1=[0:1:m1-1];
106 p2=[0:1:m2-1];

   for ctr=1:m1
       if p1(ctr)≤(m1/2)-1
           f1_p(ctr)=p1(ctr)/(del_x1*m1); % spatial frequency x
111 f2_p(ctr)=p2(ctr)/(del_x2*m2); % spatial frequency y
       else
           f1_p(ctr)=(p1(ctr)-m1)/(del_x1*m1); % spatial frequency x
           f2_p(ctr)=(p2(ctr)-m2)/(del_x2*m2); % spatial frequency y
       end
116 end

```

```

[f1m_p,f2m_p]=meshgrid(f1_p,f2_p); % gridded spatial freq data
f_p=sqrt(f1m_p.^2+f2m_p.^2);

121 sig=0;
    for ctr=1:20
        sig=sig+((1./factorial(ctr)).*(2*pi.*f_p).^(ctr-2).*fft2((Z.^...
            ctr)))); % perform FFT (see Jekeli & Zhu)
    end

126 sig(1)=1E15; %prevent infinite value
    mu_xx=-((2*pi)^2).*f1m_p.^2;
    mu_xy=-((2*pi)^2).*f1m_p.*f2m_p;
    mu_xz=i*((2*pi)^2).*f1m_p.*f_p;
    mu_yy=-((2*pi)^2).*f2m_p.^2;
131 mu_yz=i*((2*pi)^2).*f2m_p.*f_p;
    mu_zz=((2*pi)^2).*f_p.^2;

    Txx_parker=(2*pi*p*G.*ifft2(mu_xx.*exp(-2*pi*alt.*f_p).*sig));
    Txy_parker=(2*pi*p*G.*ifft2(mu_xy.*exp(-2*pi*alt.*f_p).*sig));
136 Txz_parker=(2*pi*p*G.*ifft2(mu_xz.*exp(-2*pi*alt.*f_p).*sig));
    Tyy_parker=(2*pi*p*G.*ifft2(mu_yy.*exp(-2*pi*alt.*f_p).*sig));
    Tyz_parker=(2*pi*p*G.*ifft2(mu_yz.*exp(-2*pi*alt.*f_p).*sig));
    Tzz_parker=(2*pi*p*G.*ifft2(mu_zz.*exp(-2*pi*alt.*f_p).*sig));

141 Txx_parker=real(Txx_parker)./Eotvos;
    Txy_parker=real(Txy_parker)./Eotvos;
    Txz_parker=real(Txz_parker)./Eotvos;
    Tyy_parker=real(Tyy_parker)./Eotvos;
    Tyz_parker=real(Tyz_parker)./Eotvos;
146 Tzz_parker=real(Tzz_parker)./Eotvos;

%% Gradients from EGM96 (Long wavelength subterranean effects)
% Taken from Kiamehr & Eshagh and Modified
% Could also use geopot97.v0.4e.f code

```



```

151 phi_south=min(lat);
    phi_north=max(lat);
    lambda_west=min(long);
    lambda_east=max(long);
    phi_step=30/60; %EGM96 provides a 30 arcmin resolution
156 lambda_step=30/60; %EGM96 provides a 30 arcmin resolution
    X_EGM96=lambda_west:3/3600:lambda_east; %setup 3 arcsec array for ...
        griddata function
    Y_EGM96=phi_south:3/3600:phi_north; %setup 3 arcsec array for ...
        griddata function
    [X2_EGM96,Y2_EGM96]=meshgrid(X_EGM96,Y_EGM96);

161 filename='EGM96Gradients';
    [Nmax,Ae,GM,C,S,dC,dS]=Modelread('egm_coef.ascii'); % Read ...
        spherical harmonic model
    [a,b,c,d,g,h,beta,psi,mu,eta]=coefficients(Nmax+3); % calculate ...
        Legendre coeffs.

    CN=Normal(GM,Ae,Nmax);
166 C(3:11,1)=C(3:11,1)-CN(3:11)'; % Generation of the Potetial ...
        Anomaly
    fid=fopen(filename,'w'); % Opening a file for the EGM96 Gradients

    for phi=phi_south:phi_step:phi_north
        phigeodetic=phi;
171     phi=phi*pi/180;

        % Compute the Geocentric latitude via geodetic latitude
        e2=.00669437999013; %1st eccentricity squared
        phi=atan((1-e2)*tan(phi));

176     % Compute the Associated Legendre functions
        [pnm,dP]=Pnm(phi*180/pi,Nmax+3,Nmax+3);

        for lambda=lambda_west:lambda_step:lambda_east

```

```

181         lambda=lambda*pi/180;

sum=0; % Initialize summations
sum1=0;
sum2=0;
186 sum3=0;
sum4=0;
sum5=0;
sumN=0;
sumdg=0;
191 sumeta=0;
sumpsi=0;

% Computation of geocentric distance
N=Ae/sqrt(1-e2*sin(phi)^2);
196 X_ECEF=(N+alt_EGM96)*cos(phi)*cos(lambda);
Y_ECEF=(N+alt_EGM96)*cos(phi)*sin(lambda);
Z_ECEF=((N+alt_EGM96)*(1-e2))*sin(phi);
r=sqrt(X_ECEF^2+Y_ECEF^2+Z_ECEF^2);

201 for n=3:Nmax+1
    for m=1:n

        CS=(C(n,m)*cos((m-1)*lambda)+S(n,m)*sin((m-1)*...
            lambda));
        AA=(Ae/r)^(n+2);
        AA1=(Ae/r)^n;
206 CS1=(-S(n,m)*cos((m-1)*lambda)+C(n,m)*sin((m-1)*...
            *lambda));
        PNM=pnm(n,m);

        if (abs(m)-2) ≤ 0

211         PP=(-1)^(abs(m-4)-1)*pnm(n,abs((m)-4));
        PP1=(-1)^(abs(m-4)-1)*pnm(n-1,abs((m)-4));

```

```

else

216         PP=pnm(n,abs(m)-2);
           PP1=pnm(n-1,abs(m)-2);

end

221     if (abs(m)-1) ≤ 0

           QQ=(-1)^(abs(m-3)-1)*pnm(n,abs(abs(m)-3));
           QQ1=(-1)^(abs(m-3)-1)*pnm(n-1,abs(abs(m)...
               -3));

226     else

           QQ=pnm(n,abs(m)-1);
           QQ1=pnm(n-1,abs(m)-1);
       end

231     % Computing the Txx summation
       sum1=sum1+AA*CS*(a(n,abs(m))*PP+b(n,abs(m))*pnm...
           (n,abs(m))+...
           c(n,abs(m))*pnm(n,abs(m)+2));

       % Computing the Txy summation

236     sum3=sum3+AA*CS1*(d(n,m)*PP1+g(n,m)*pnm(n-1,(m)...
           )+h(n,m)*pnm(n-1,(m)+2));

       % Computing the Txz summation

       sum4=sum4+AA*CS*(beta(n,m)*QQ+psi(n,m)*pnm(n,(m...
           )+1));

241     % Computing the Tyz summation
       sum5=sum5+AA*CS1*(mu(n,m)*QQ1+eta(n,m)*pnm(n...
           -1,(m)+1));

```

```

        % Computing the Tzz summation
        sum2=sum2+(n*(n+1))*AA*CS*PNM;

246
        end % of m
        end % of n

        %The gravity gradient tensor components

251
        Txx=-GM/Ae^3*sum1/Eotvos;
        Tzz= GM/Ae^3*sum2/Eotvos;
        Txy= (-GM/Ae^3*sum3/Eotvos)/10;
        Tyz= -GM/Ae^3*sum4/Eotvos;

256
        Txz= GM/Ae^3*sum5/Eotvos;

        fprintf(fid,'%g %g %e %e %e %e %e %e \n',phigeodetic,...
                lambda*180/pi,...
                Txx,-(Txx+Tzz),Tzz,Txy,Txz,Tyz);

261        end % of lambda
        end % of phi

        fclose(fid);
        U=load(filename);

266
        % interpolate EGM96 gradients from 30arcmin res to 3arcsec res
        Txx_EGM96=griddata(U(:,2),U(:,1),U(:,3),X2_EGM96,Y2_EGM96,'v4');
        Tyy_EGM96=griddata(U(:,2),U(:,1),U(:,4),X2_EGM96,Y2_EGM96,'v4');
        Tzz_EGM96=griddata(U(:,2),U(:,1),U(:,5),X2_EGM96,Y2_EGM96,'v4');
271 Txy_EGM96=griddata(U(:,2),U(:,1),U(:,6),X2_EGM96,Y2_EGM96,'v4');
        Txz_EGM96=griddata(U(:,2),U(:,1),U(:,7),X2_EGM96,Y2_EGM96,'v4');
        Tyz_EGM96=griddata(U(:,2),U(:,1),U(:,8),X2_EGM96,Y2_EGM96,'v4');

        %% The Gradients!

276 Txx=Txx_parker+Txx_EGM96;
        Txy=Txy_parker+Txy_EGM96;

```

```

Txz=Txz_parker+Txz_EGM96;
Tyy=Tyy_parker+Tyy_EGM96;
Tyz=Tyz_parker+Tyz_EGM96;
281 Tzz=Tzz_parker+Tzz_EGM96;

%% Run Simulink Model
sim('GGI', 0:sim_time); % used 120s in thesis runs
movefile('filename2.mat',filename1)
286 movefile('filename4.mat',filename3)

```

Listing A.2:

```

% This function reads the spherical harmonic model

3 function [Nmax,Ae,GM,C,S,dC,dS]=Modelread(filename)

fid=fopen(filename,'r');

A1=fscanf(fid,'%g %g %g \n',6);
8
Nmax=A1(1);
Ae=A1(2);
GM=A1(3);

13 while (~feof(fid))

    B=fscanf(fid,'%d %d %g %g %g %g \n',6);
    n=B(1);m=B(2);
    C(n+1,m+1)=B(3);S(n+1,m+1)=B(4);
18    dC(n+1,m+1)=B(5);dS(n+1,m+1)=B(6);
end

fclose(fid);

```

Listing A.3:

```

%*****%
%
% This function computes the coefficients of the Legendre
4 % functions
%
% INPUT
% the maximum desired degree of geopotential model to be used%
% plus 2 -it is suggested to introduce higher values than the%
9 % maximum degree of the model.
%
% OUTPUT
%
% all of the coefficients of Legendre functions needed for
14 % computing the gravity gradients
%
% REFERENCE
% Petrovskaya, M.S. and A.N. Vershkov (2006), Non/Singular
% expressions for the gravity gradients in the local
19 % north-oriented and orbital reference frames. Journal of
% Geodesy, Vol 80, 117-127%
%
%
% by
24 % Mehdi Eshagh and Ramin Kiamehr 2006
% Division of Geodesy
% Royal Institute of Technology
% Stockholm, Sweden
% Email:eshagh@kth.se
29 %
% Modified by Marshall Rogers 2008
%
%*****%
34

```

```

function [a,b,c,d,g,h,beta,psi,mu,eta]=coefficients(N)
for n=1:N
    for m=1:n
        if ((abs(m-1)==0) | abs(m-1)==1)
39
            a(n,abs(m))=70;

            b(n,abs(m))=(n-1+abs(m-1)+1)*(n-1+abs(m-1)+2)/(2*abs(m...
                -1)+1);

44
            c(n,abs(m))=sqrt(1+Δ(abs(m-1),0))*sqrt((n-1)^2-(abs(m...
                -1)+1)^2)*...
                sqrt((n-1)-abs(m-1))*sqrt(n-1+abs(m-1)+2)/4;

            elseif (2 ≤ abs(m-1) ≤ n-1)
                a(n,abs(m))=sqrt(1+Δ(abs(m-1),2))*sqrt((n-1)^2-(abs(m...
                    -1)-1)^2)*...
49
                    sqrt((n-1)+abs(m-1))*sqrt(n-1-abs(m-1)+2)/4;

                b(n,abs(m))=((n-1)^2+(m-1)^2+3*(n-1)+2)/2;

                c(n,abs(m))=sqrt((n-1)^2-(abs(m-1)+1)^2)*sqrt((n-1)-...
                    abs(m-1))*...
54
                    sqrt((n-1)+abs(m-1)+2)/4;

                d(n,m)=-(m-1)/4/abs(m-1)*sqrt((2*(n-1)+1)/(2*(n-1)-1))...
                    *sqrt(1+kron(m-1,2))*...
                    sqrt((n-1)^2-(abs(m-1)-1)^2)*sqrt(n-1+abs(m-1))...
                    *sqrt(n-1+abs(m-1)-2);

59
                g(n,m)=(m-1)/2*sqrt((2*(n-1)+1)/(2*(n-1)-1))*sqrt(n-1+...
                    abs(m-1))*...
                    sqrt(n-1-abs(m-1));

```

```

64      h(n,m)=(m-1)/4/abs(m-1)*sqrt((2*(n-1)+1)/(2*(n-1)-1))*...
        sqrt((n-1)^2-(abs(m-1)+1)^2)*...
        sqrt(n-1-abs(m-1))*sqrt(n-1-abs(m-1)-2);

end

69      if (abs(m-1)==1)

        d(n,m)=0;

        g(n,m)=(m-1)/4/abs(m-1)*sqrt((2*(n-1)+1)/(2*(n-1)-1))*...
        sqrt(n)*sqrt(n-2)*(n+1);

74      h(n,m)=(m-1)/4/abs(m-1)*sqrt((2*(n-1)+1)/(2*(n-1)-1))*...
        sqrt(n-4)*sqrt(n-3)*...
        sqrt(n-2)*sqrt(n+1);

end

79      if (abs(m-1)==0)

        beta(n,m)=0;
        psi(n,m)=-(n+1)*sqrt((n-1)*n/2);

84      elseif (1 ≤ abs(m-1) ≤ (n-1))

        beta(n,m)=(n+1)/2*sqrt(1+Δ(abs(m-1),1))*sqrt(n-1+abs(m...
        -1))*sqrt(n-1-abs(m-1)+1);
        psi(n,m)=-(n+1)/2*sqrt(n-1-abs(m-1))*sqrt(n-1+abs(m-1)...
        +1);

89      end

      if (abs(m-1)> 0)

```



```

mu(n,m)=- (m-1)/abs(m-1)*(n+1)/2*sqrt((2*(n-1)+1)/(2*(n...
-1)-1))*sqrt(1+Δ(abs(m-1),1))*...
94      sqrt(n-1+abs(m-1))*sqrt(n-1+abs(m-1)-1);

eta(n,m)=- (m-1)/abs(m-1)*(n+1)/2*sqrt((2*(n-1)+1)/(2*(...
n-1)-1))*...
      sqrt(n-1-abs(m-1))*sqrt(n-1-abs(m-1)-1);

end

99
end

end

```

Listing A.4:

```

% This function computes the normal field potential coefficients
function [J]=Normal(GM,AX,Nmax)
    GMS=0.3986005e15;
4    AXS=6378137.0;
    JJ=0.108262982131e-2;
    FINV=298.257;
    FLTN=1.0/FINV;
    E2=FLTN*(2.0-FLTN);
9
    J(1)=GMS/GM;
    J(3) =-0.484169650276e-3;
    J(5) = 0.790314704521e-6;
    J(7) =-0.168729437964e-8;
14   J(9) = 0.346071647263e-11;
    J(11)=-0.265086254269e-14;

```

Listing A.5:

```

%*****%
%
% This function computes the Legendre function and its%
% first order derivatives using recursive formulae %
5 %
% INPUT %
%     phi=latitude of the desired point %
%     Nmax=maximum desired degree %
%     Mmax=maximum desired order %
10 %
% OUTPUT %
%
%     pnm=Normalized associated Legendre function %
%     dP=first order derivative of the Normalized %
15 %     associated Legendre function %
%
% REFERENCES %
%     Hwang, C. and M.J. Lin, (1998), Fast Integration%
%     of low orbiter's trajctory perturbed by the %
20 %     Earth non-sphericity, Journal of Geodesy, %
%     vol 72:578-585 %
%
%     Borre, Kai (2004), Geoid Undulations computed by%
%     EGM96, report, Aalborg University %
25 %
%
%     By Mehdi Eshagh and Ramin Kiamehr 2006 %
%     Division of Geodesy %
%     Royal Institute of Technology %
30 %     Stckholm, Sweden %
%     Email:eshagh@kth.se %
%
%*****%

```

```

35 function [pnm,dP]=Pnm(phi,Nmax,Mmax)

    nrow=Nmax+1;np1=Mmax+1;
    phii=phi*pi/180;

40    x=sin(phii);
    y=cos(phii);

    pnm(1,1)=1.0;
    pnm(2,1)=sqrt(3.0)*x;
45    pnm(2,2)=sqrt(3.0)*y;
    pnm(3,2)=sqrt(5.0)*pnm(2,2)*x;

    for i=3:np1
        n=i-1;
50        pnm(i,i)=sqrt((n+0.5)/n)*pnm(i-1,i-1)*y;
    end
    k=np1-1;
    for i=3:k
        n=i-1;
55        pnm(i+1,i)=sqrt(2.0*n+3)*pnm(i,i)*x;
    end
    nm1=np1-2;
    for j=1:nm1
        m=j-1;
60        k=j+2;
        for i=k:np1
            n=i-1;
            c=(2.0*n+1.0)/(n-m)/(n+m);
            c1=c*(2.0*n-1.0);
65            c2=c*(n+m-1)/(2*n-3)*(n-m-1);
            c1=sqrt(c1);
            c2=sqrt(c2);
            pnm(i,j)=c1*x*pnm(i-1,j)-c2*pnm(i-2,j);
        end
    end

```

```

70     end

    for n=1:Nmax-1
        for m=1:n
            dP(n,m)=sqrt(((n-1)-(m-1))*((n-1)+(m-1)+1)*(1+Δ(m-1,m-1))*...
                pnm(n,m+1)-(m-1)*...
75         tan(phi)*pnm(n,m));
        end
    end
end

```

Listing A.6:

```

%*****%
2 % Gradients due to KC-10 Tanker %
% (used to generate white noise)%
%*****%

close all
7 clear all
clc

% z positive "downward"

12 G=6.67E-11;
p=132; %density contrast for tanker
Eotvos=1E-9; %Eotvos conversion

a=[-3.05+25 3.05+25]; % Point 1, Permuted for 7 remaining points
17 b=[-5-24.4 -5+24.4]; % Point 1, Permuted for 7 remaining points
c=[-5-3.05 -5+3.05]; % Point 1, Permuted for 7 remaining points
alt=0;
Ng=0;
Eg=0;
22

```

```

sumTxx=0;
for ctr1=1:2
    for ctr2=1:2
        for ctr3=1:2
27         sumTxx=sumTxx+((-1)^(ctr1)*(-1)^(ctr2)*(-1)^(ctr3)).*...
            atan2(((Ng-b(ctr2)).*(alt-c(ctr3))),((Eg-a(ctr1))...
                .*((Eg-a(ctr1)).^2+(Ng-b(ctr2)).^2+(alt-c(ctr3))...
                    .^2).^(.5))));
        end
    end
end

32 Txx=G*p*sumTxx/Eotvos

sumTxy=0;
for ctr1=1:2
37     for ctr2=1:2
        for ctr3=1:2
            sumTxy=sumTxy+((-1)^(ctr1+ctr2+ctr3)).*log(((alt-c(...
                ctr3))+((Eg-a(ctr1)).^2+(Ng-b(ctr2)).^2+(alt-c(ctr3...
                    )).^2).^(.5))));
        end
    end
42 end

Txy=-G*p*sumTxy;

47 sumTxz=0;
for ctr1=1:2
    for ctr2=1:2
        for ctr3=1:2

```

```

sumTxz=sumTxz+((-1)^(ctr1)*(-1)^(ctr2)*(-1)^(ctr3)).*...
    log(((Ng-b(ctr2))+((Eg-a(ctr1)).^2+(Ng-b(ctr2))...
        .^2+(c(ctr3)-alt).^2).^(.5)));
52     end
    end
end

Txz=-G*p*sumTxz/Eotvos;
57

sumTyy=0;
for ctr1=1:2
    for ctr2=1:2
62     for ctr3=1:2
        sumTyy=sumTyy+((-1)^(ctr1)*(-1)^(ctr2)*(-1)^(ctr3)).*...
            atan2(((Eg-a(ctr1)).*(alt-c(ctr3))),((Ng-b(ctr2))...
                .*((Eg-a(ctr1)).^2+(Ng-b(ctr2)).^2+(c(ctr3)-alt)...
                    .^2).^(.5)));
            end
        end
    end
end
67
Tyy=G*p*sumTyy/Eotvos

sumTyz=0;
72 for ctr1=1:2
    for ctr2=1:2
        for ctr3=1:2
            sumTyz=sumTyz+((-1)^(ctr1)*(-1)^(ctr2)*(-1)^(ctr3)).*...
                log(((Eg-a(ctr1))+((Eg-a(ctr1)).^2+(Ng-b(ctr2))...
                    .^2+(c(ctr3)-alt).^2).^(.5)));
            end
        end
    end
77 end
end

```

```
Tyz=-G*p*sumTyz/Eotvos;
```

```
82 Tzz=-(Tyy+Txx)
```

Listing A.7:

```
%*****%
% Terrain Avoidance Scenario %
3 %*****%
close all
clear all
clc

8 vi=[50 0 0];
speed=norm(vi);
G=6.67E-11;
p=2670; %density contrast ground
% p=1000; % density contrast water tower
13 spacing=1;
N=[0:spacing:1550]; % setup grid
E=[0:spacing:1550]; % setup grid

Eotvos=1E-9; %Eotvos conversion
18 update_rate=1;
filter_cutoff=.2;

%% 25m Cubic Object - dimensions permuted for each obstacle size, ...
    water tower gradients calculated similarly
length1=25; % object base (assumes square)
23 c=[0 25]; % obstacle height

t1=0:spacing/speed:(round(length(N)/2)-(length1/spacing)/2-1)/...
    speed; % Truth signal time array
```

```

t2=0:1/update_rate:(round(length(N)/2)-length1/2-1)/speed; % time ...
    array for sensor with 1Hz sampling rate

28 a=[1000 1000+length1]; % putting obstacle on grid
    b=[round(length(N)/2)-length1/2 round(length(N)/2)+length1/2]; % ...
        putting obstacle on grid
        %obstacle height

    alt=15; % 10m below obstacle top
33 ipos=[0 length(N)/2 alt];

[Eg,Ng]=meshgrid(E,N);

    %Txx
38 sumTxx=0;

    for ctr1=1:2
        for ctr2=1:2
            for ctr3=1:2
43         sumTxx=sumTxx+((-1)^(ctr1)*(-1)^(ctr2)*(-1)^(ctr3)).*...
                atan2(((Ng-b(ctr2)).*(alt-c(ctr3))),((Eg-a(ctr1))...
                    .*((Eg-a(ctr1)).^2+(Ng-b(ctr2)).^2+(alt-c(ctr3))...
                        .^2).^(.5)))));
            end
        end
    end

48 Txx=G*p*sumTxx/Eotvos;

    % Txy
    sumTxy=0;
    for ctr1=1:2
53         for ctr2=1:2
            for ctr3=1:2

```



```

        sumTxy=sumTxy+((-1)^(ctr1+ctr2+ctr3)).*log(((alt-c(...
            ctr3))+((Eg-a(ctr1)).^2+(Ng-b(ctr2)).^2+(alt-c(ctr3...
            )).^2).^(.5)));
    end
end
58 end

Txy=-G*p*sumTxy;
Txy(727,1051)=-0.000001; % Prevent infinite values
Txy(727,1001)=0.000001; % Prevent infinite values
63 Txy(777,1051)=0.000001; % Prevent infinite values
Txy(777,1001)=-0.000001; % Prevent infinite values
Txy=Txy/Eotvos;

% Txz
68 sumTxz=0;
for ctr1=1:2
    for ctr2=1:2
        for ctr3=1:2
            sumTxz=sumTxz+((-1)^(ctr1)*(-1)^(ctr2)*(-1)^(ctr3)).*...
                log(((Ng-b(ctr2))+((Eg-a(ctr1)).^2+(Ng-b(ctr2))...
                .^2+(c(ctr3)-alt).^2).^(.5)));
73         end
    end
end

Txz=G*p*sumTxz/Eotvos;
78

% Tyy
sumTyy=0;
for ctr1=1:2
    for ctr2=1:2
83         for ctr3=1:2
            sumTyy=sumTyy+((-1)^(ctr1)*(-1)^(ctr2)*(-1)^(ctr3)).*...
                atan2(((Eg-a(ctr1)).*(alt-c(ctr3))),((Ng-b(ctr2))...

```

```

        .*((Eg-a(ctr1)).^2+(Ng-b(ctr2)).^2+(c(ctr3)-alt)...
        .^2).^(.5)));

    end

end

end

88 Tyy=G*p*sumTyy/Eotvos;

% Tyz
sumTyz=0;
93 for ctr1=1:2
    for ctr2=1:2
        for ctr3=1:2
            sumTyz=sumTyz+((-1)^(ctr1)*(-1)^(ctr2)*(-1)^(ctr3)).*...
            log(((Eg-a(ctr1))+((Eg-a(ctr1)).^2+(Ng-b(ctr2))...
            .^2+(c(ctr3)-alt).^2).^(.5)));
        end
    end
98 end

end

Tyz=G*p*sumTyz/Eotvos;

103 % Tzz
Tzz=-(Tyy+Txx);

% Simulation
sim('terrain_avoidance_sim', 0:.01:30); %run sim for 30s

```

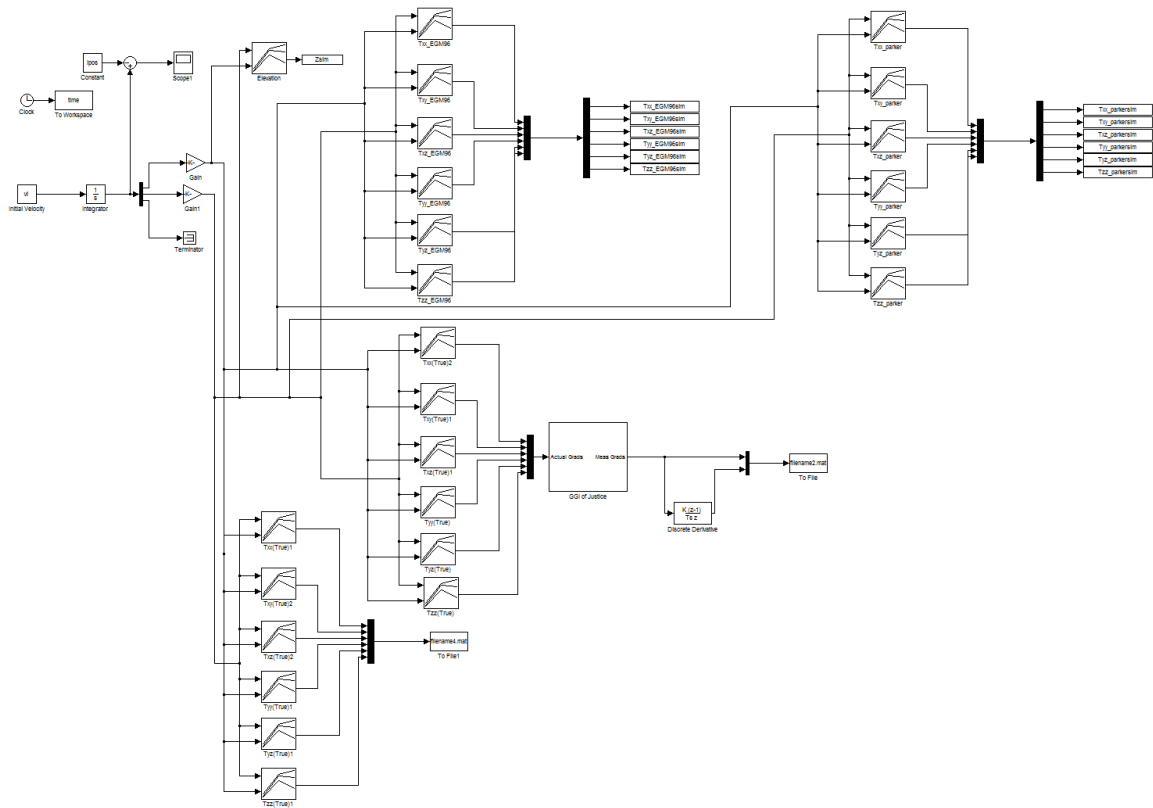


Figure A.1: GGI Simulink Block Diagram.

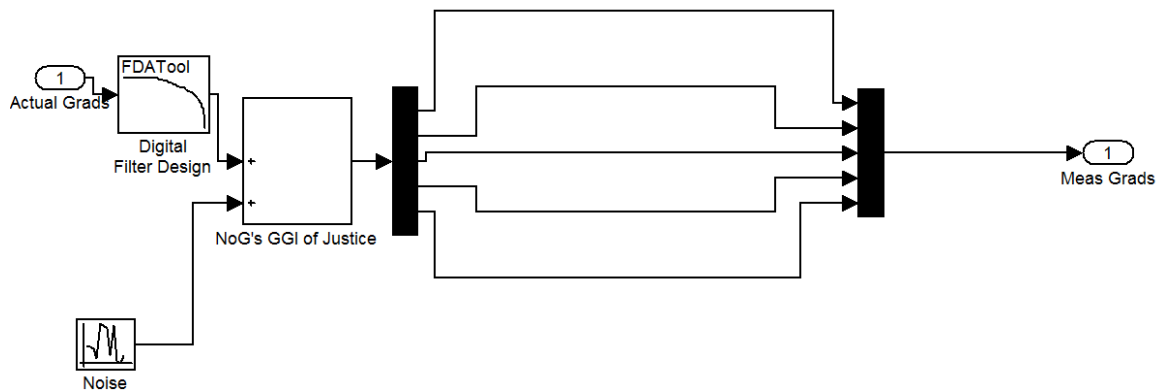


Figure A.2: GGI of Justice Simulink Block Diagram.

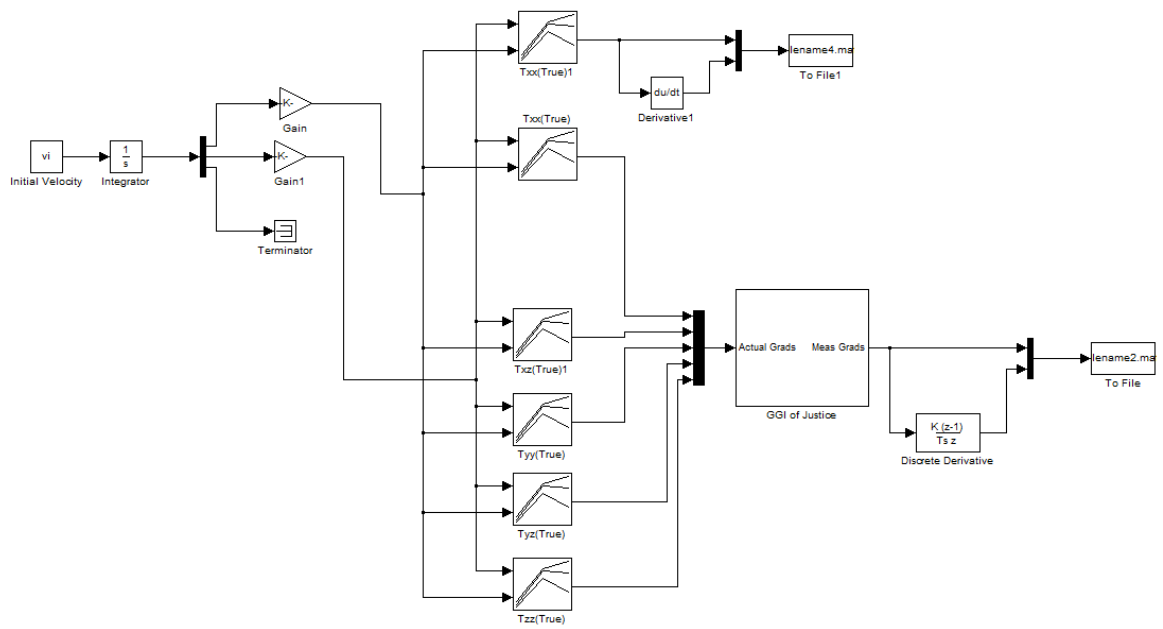


Figure A.3: Terrain Avoidance Simulink Block Diagram.

Appendix B. Legendre Function Coefficients used for EGM96

Gradient Calculations

$$a_{n,m} = 70, \quad m = 0, 1$$

$$a_{n,m} = \frac{\sqrt{1 + \delta_{m,2}}}{4} \sqrt{n^2 - (m-1)^2} \sqrt{n+m} \sqrt{n-m+2}, \quad 2 \leq m \leq n$$

$$b_{n,m} = \frac{(n+m+1)(n+m+2)}{2(m+1)}, \quad m = 0, 1$$

$$b_{n,m} = \frac{n^2 + m^2 + 3n + 2}{2}, \quad 2 \leq m \leq n$$

$$c_{n,m} = \frac{\sqrt{1 + \delta_{m,0}}}{4} \sqrt{n^2 - (m+1)^2} \sqrt{n-m} \sqrt{n+m+2}, \quad m = 0, 1$$

$$c_{n,m} = \frac{1}{4} \sqrt{n^2 - (m+1)^2} \times \sqrt{n-m} \sqrt{n+m+2}, \quad 2 \leq m \leq n$$

$$d_{n,m} = 0, \quad m = 1$$

$$d_{n,m} = -\frac{m}{4m} \sqrt{\frac{2n+1}{2n-1}} \sqrt{1 + \delta_{m,2}} \sqrt{n^2 - (m-1)^2} \sqrt{n+m} \sqrt{n+m-2}, \quad 2 \leq m \leq n$$

$$g_{n,m} = \frac{m}{4m} \sqrt{\frac{2n+1}{2n-1}} \sqrt{n+1} \sqrt{n-1} (n+2), \quad m = 1$$

$$g_{n,m} = \frac{m}{2} \sqrt{\frac{2n+1}{2n-1}} \sqrt{n+m} \sqrt{n-m}, \quad 2 \leq m \leq n$$

$$h_{n,m} = \frac{m}{4m} \sqrt{\frac{2n+1}{2n-1}} \sqrt{n-3} \sqrt{n-2} \sqrt{n-1} \sqrt{n+2}, \quad m = 1$$

$$h_{n,m} = \frac{m}{4m} \sqrt{\frac{2n+1}{2n-1}} \sqrt{n^2 - (m+1)^2} \sqrt{n-m} \sqrt{n-m-2}, \quad 2 \leq m \leq n$$

$$\beta_{n,m} = 0, \quad m = 0$$

$$\beta_{n,m} = \frac{n+2}{2} \sqrt{1 + \delta_{m,1}} \sqrt{n+m} \sqrt{n-m+1}, \quad 1 \leq m \leq n$$

$$\psi_{n,m} = -(n+2)\sqrt{\frac{n(n+1)}{2}}, \quad m = 0$$

$$\psi_{n,m} = -\frac{n+2}{2}\sqrt{n-m}\sqrt{n+m+1}, \quad 1 \leq m \leq n$$

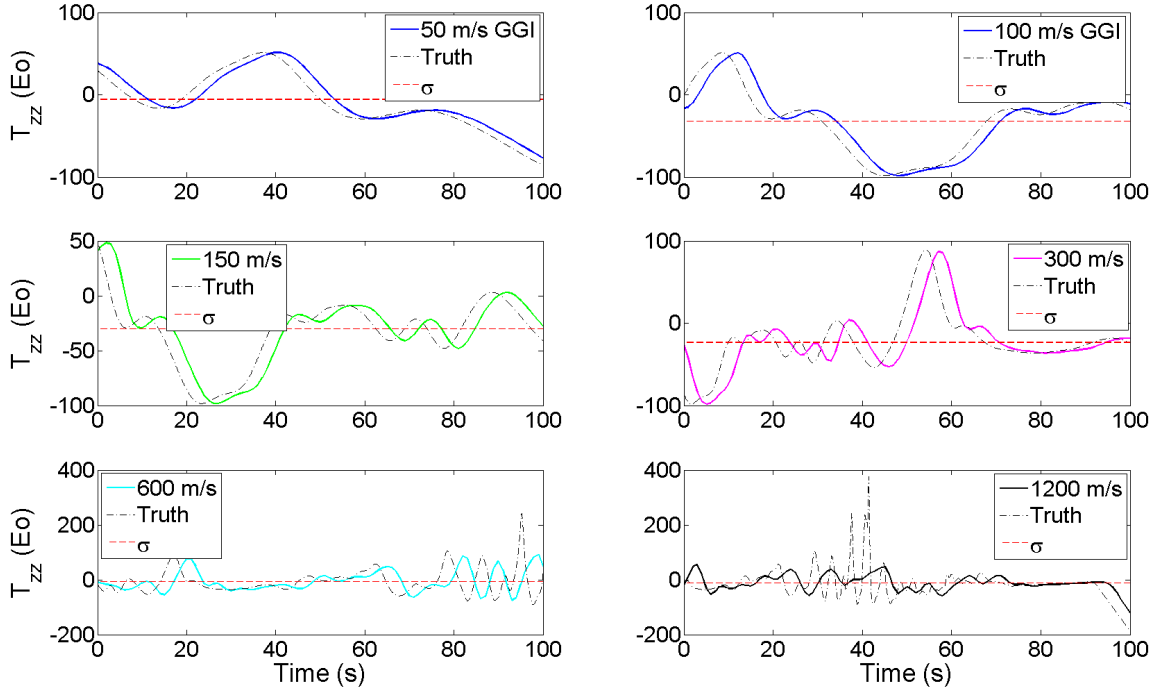
$$\mu_{n,m} = -\frac{nm+2m}{2m}\sqrt{\frac{2n+1}{2n-1}}\sqrt{1+\delta_{m,1}}\sqrt{n+m}\sqrt{n+m-1}, \quad 0 \leq m \leq n$$

$$\eta_{n,m} = -\frac{nm+2m}{2m}\sqrt{\frac{2n+1}{2n-1}}\sqrt{n-m}\sqrt{n-m-1}, \quad 0 \leq m \leq n$$

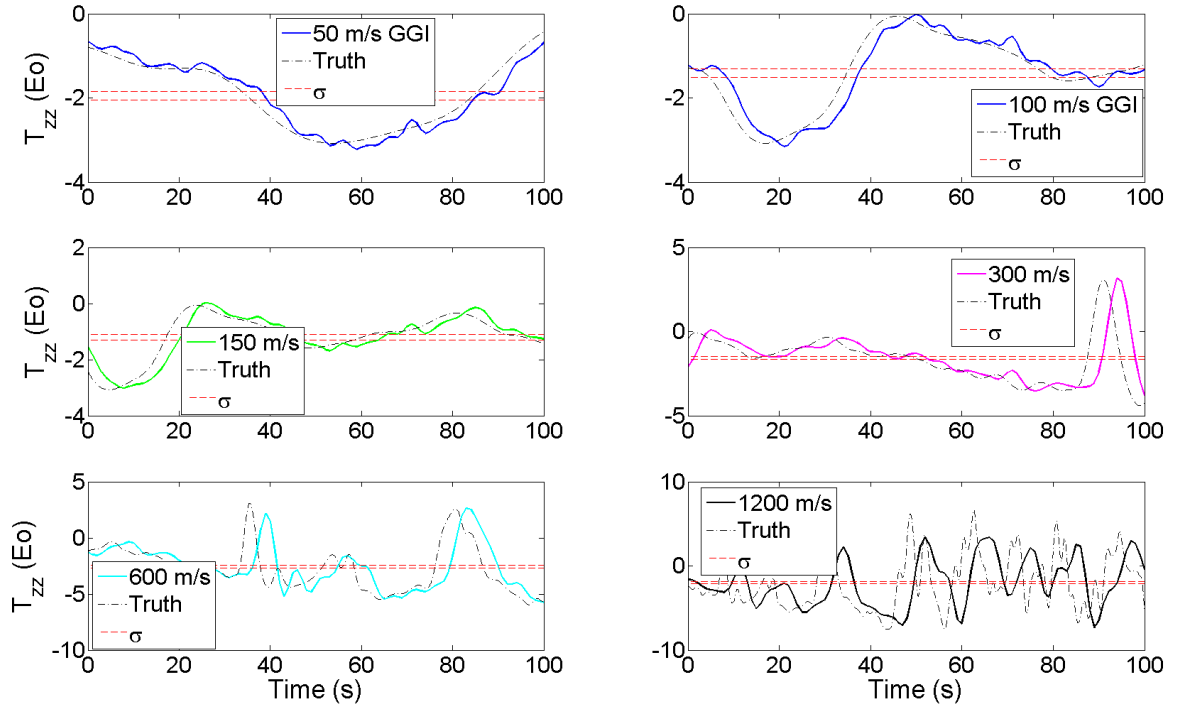
$$\delta_{p,q} = 1, \quad p = q$$

$$\delta_{p,q} = 0, \quad p \neq q$$

Appendix C. Supplementary Figures

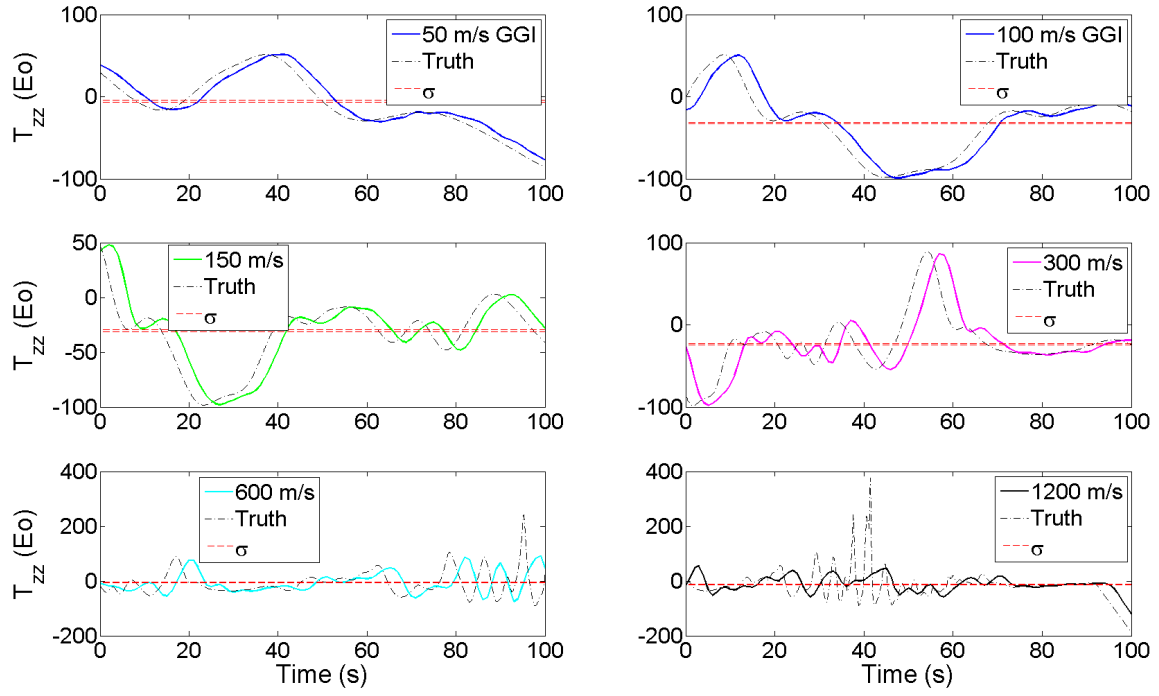


(a) Runs 1-6, 1000m, GGI 1, Rough Terrain.

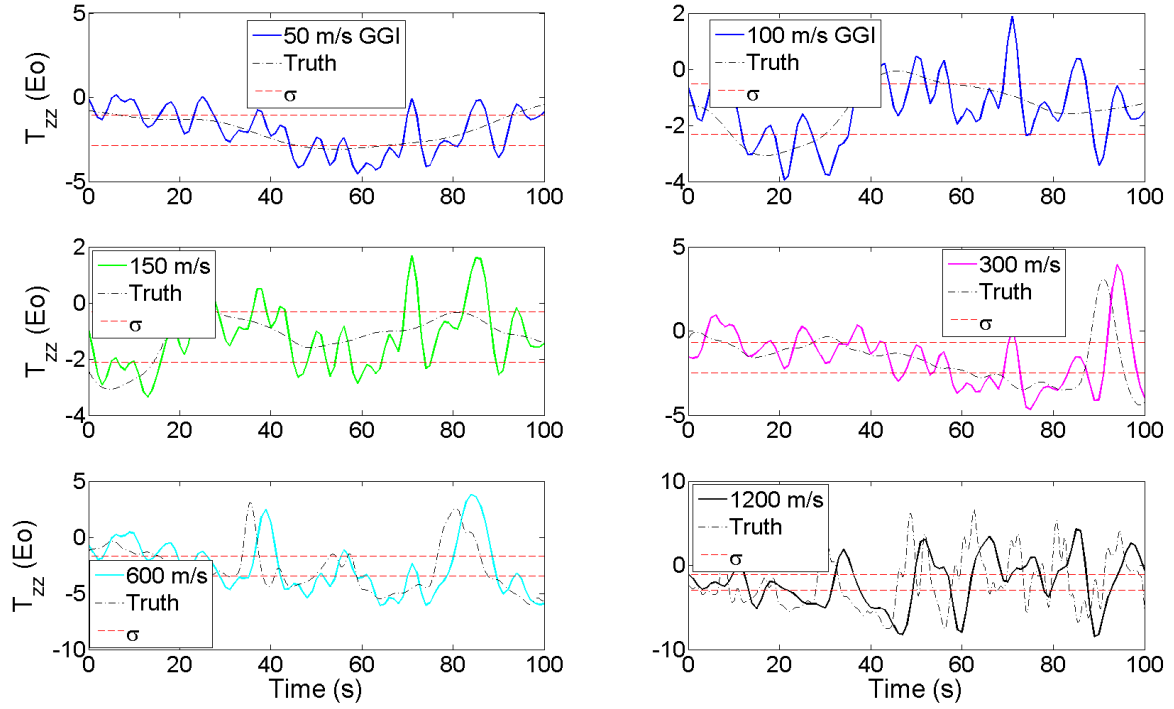


(b) Runs 7-12, 1000m, GGI 1, Smooth Terrain.

Figure C.1: Runs 1-12, 1000m, GGI 1.

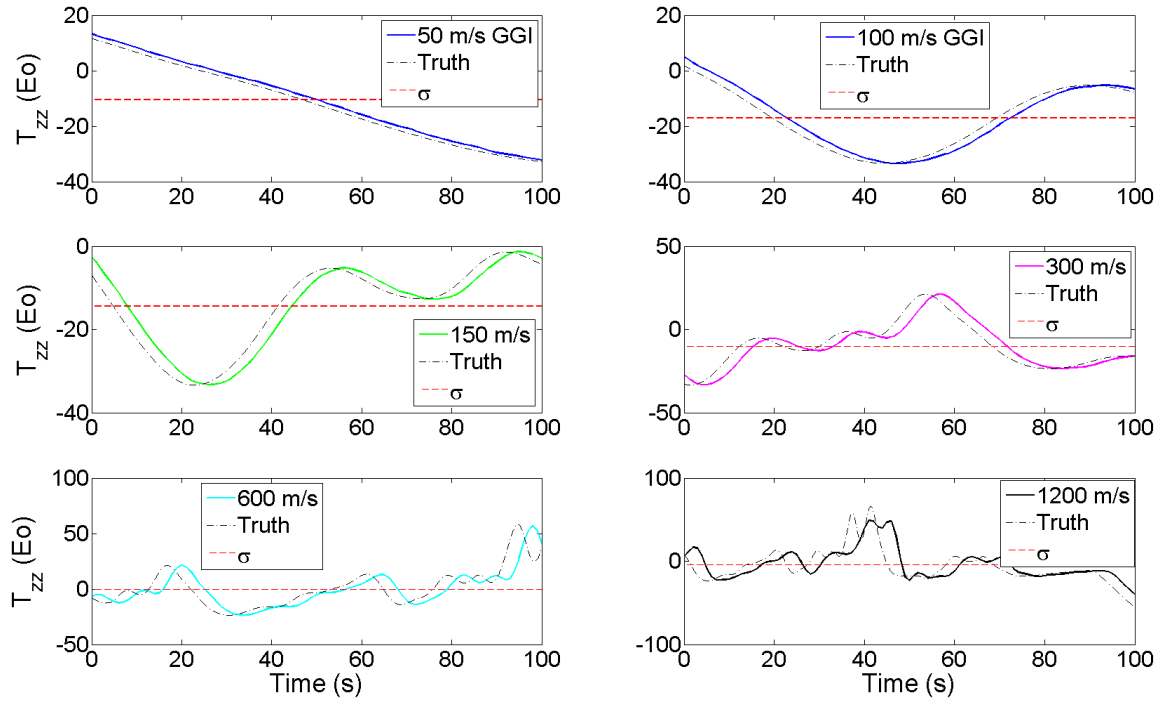


(a) Runs 13-18, 1000m, GGI 2, Rough Terrain.

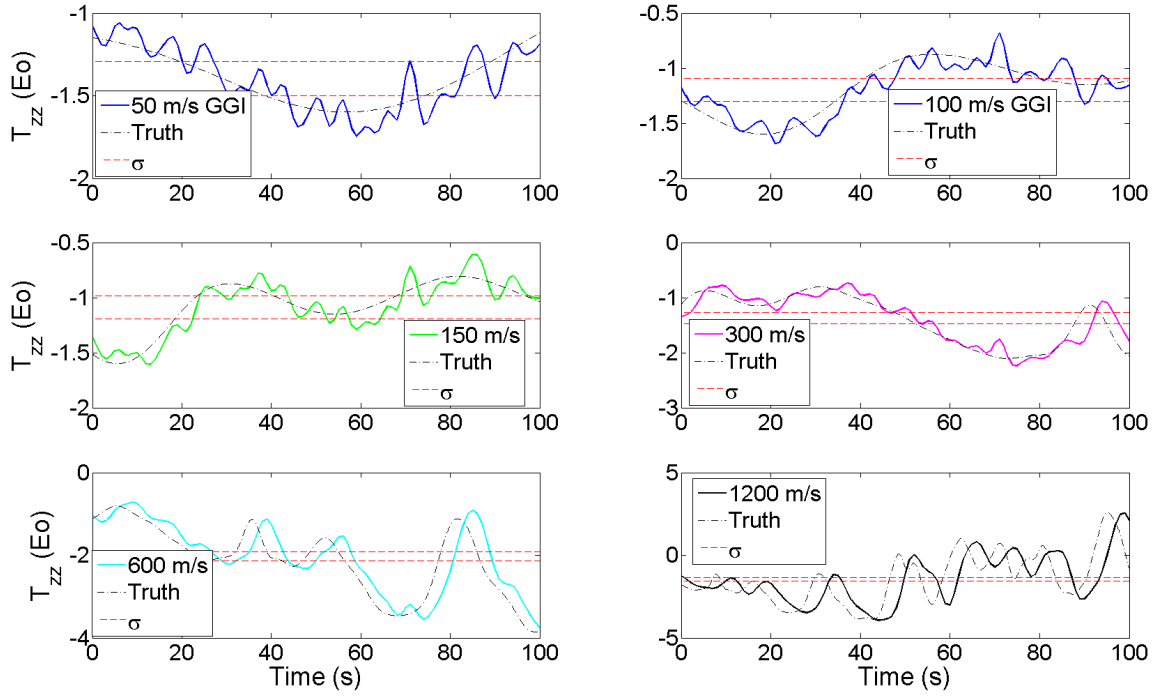


(b) Runs 19-24, 1000m, GGI 2, Smooth Terrain.

Figure C.2: Runs 13-24, 1000m, GGI 2.

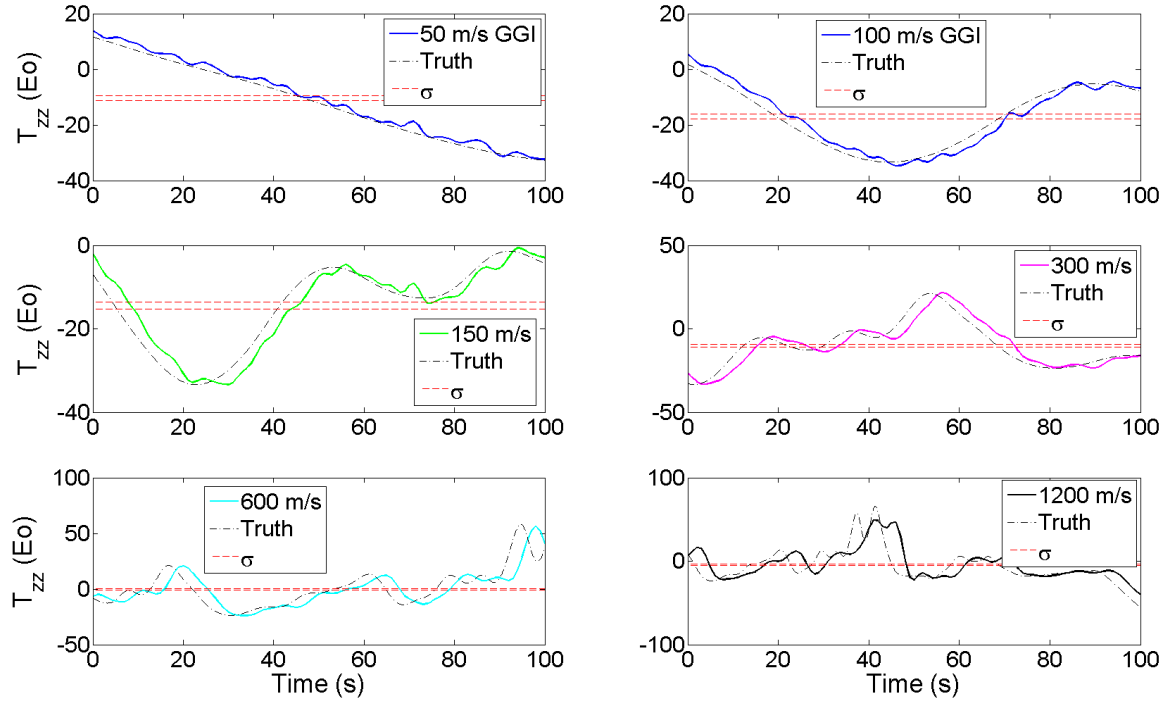


(a) Runs 25-30, 2500m, GGI 1, Rough Terrain.

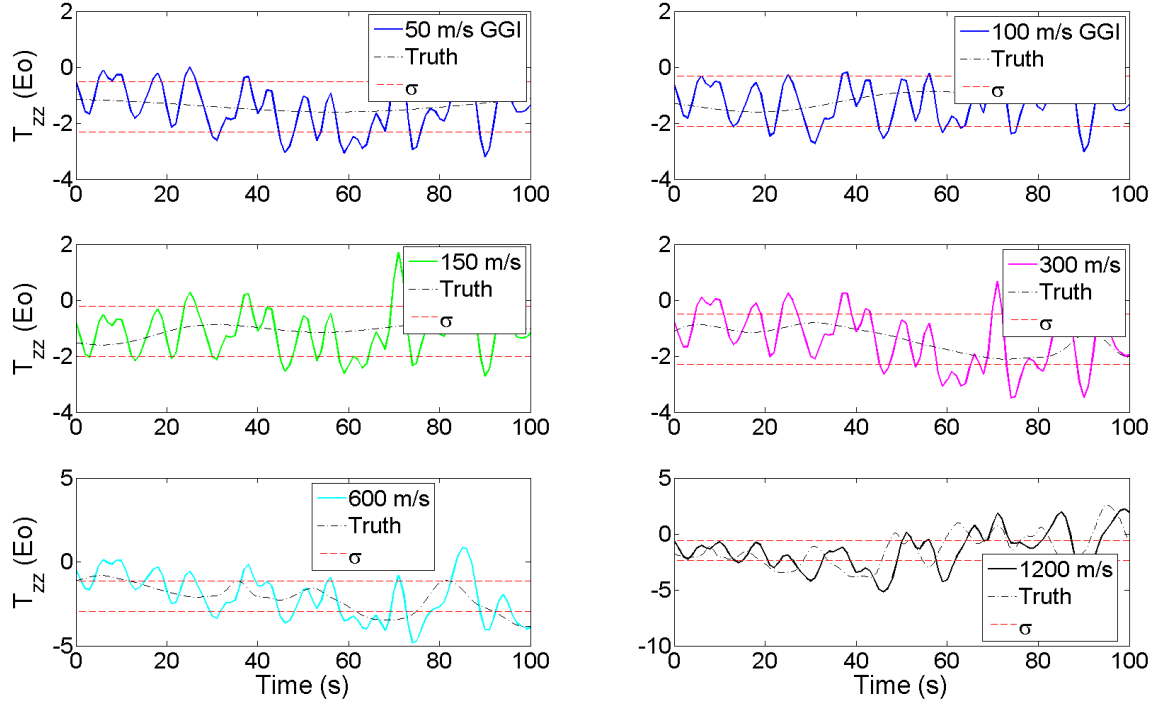


(b) Runs 31-36, 2500m, GGI 1, Smooth Terrain.

Figure C.3: Runs 25-36, 2500m, GGI 1.

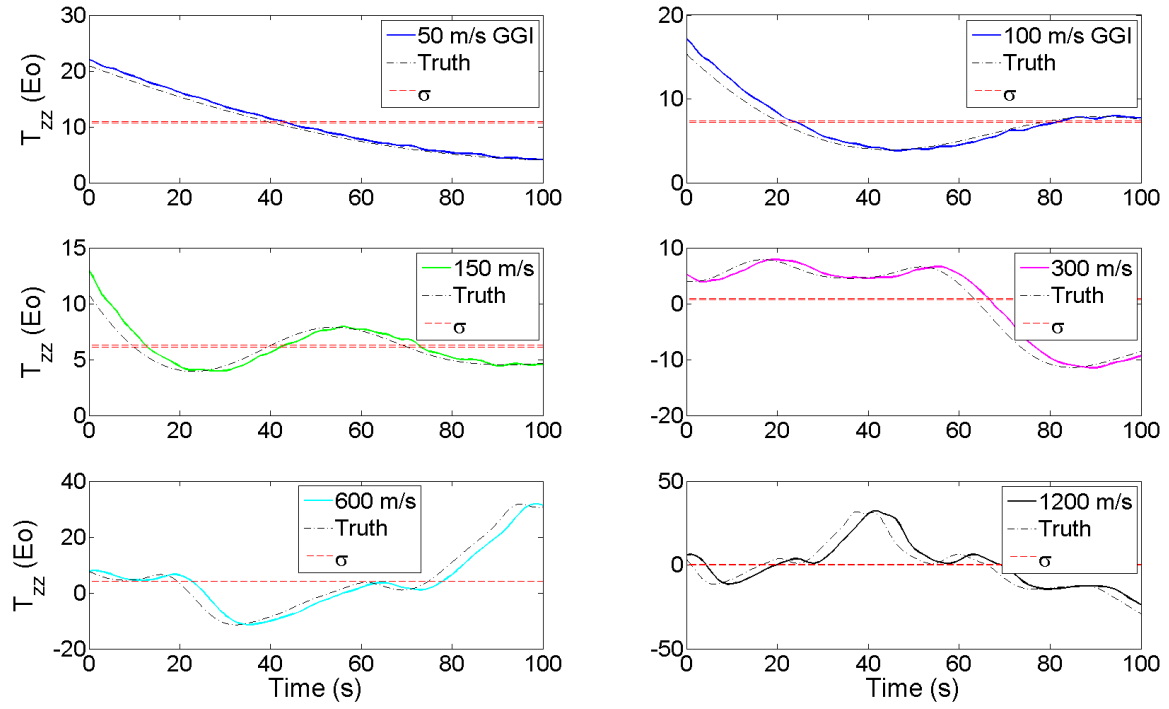


(a) Runs 37-42, 2500m, GGI 2, Rough Terrain.

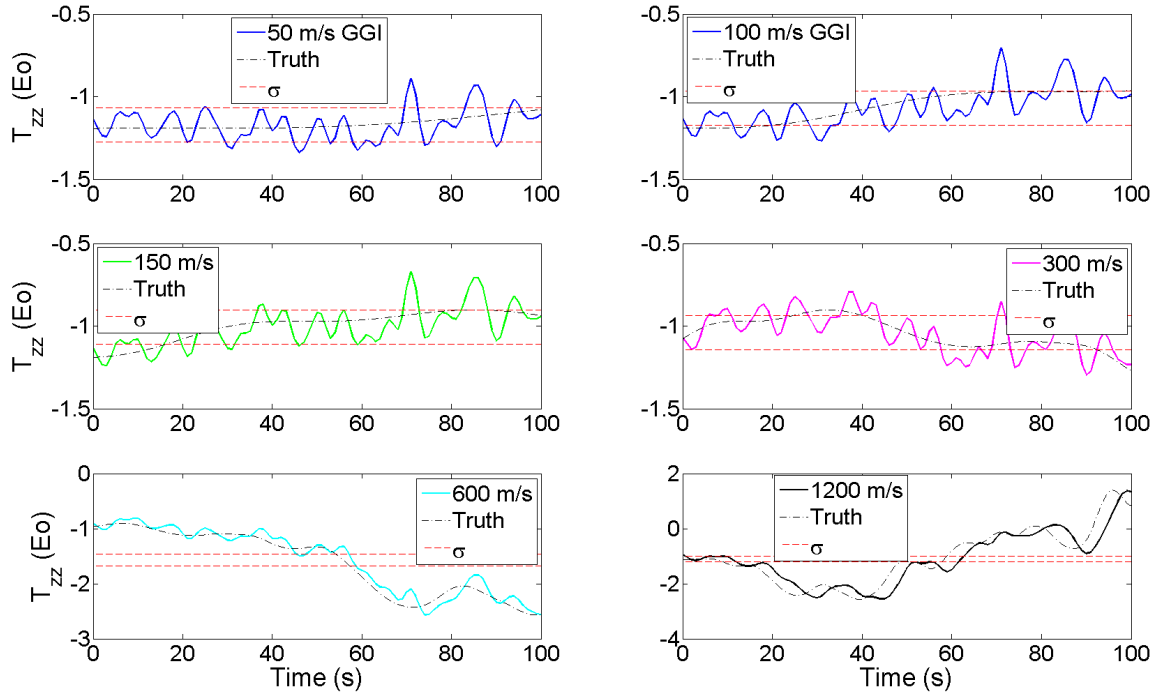


(b) Runs 43-48, 2500m, GGI 2, Smooth Terrain.

Figure C.4: Runs 37-48, 2500m, GGI 2.

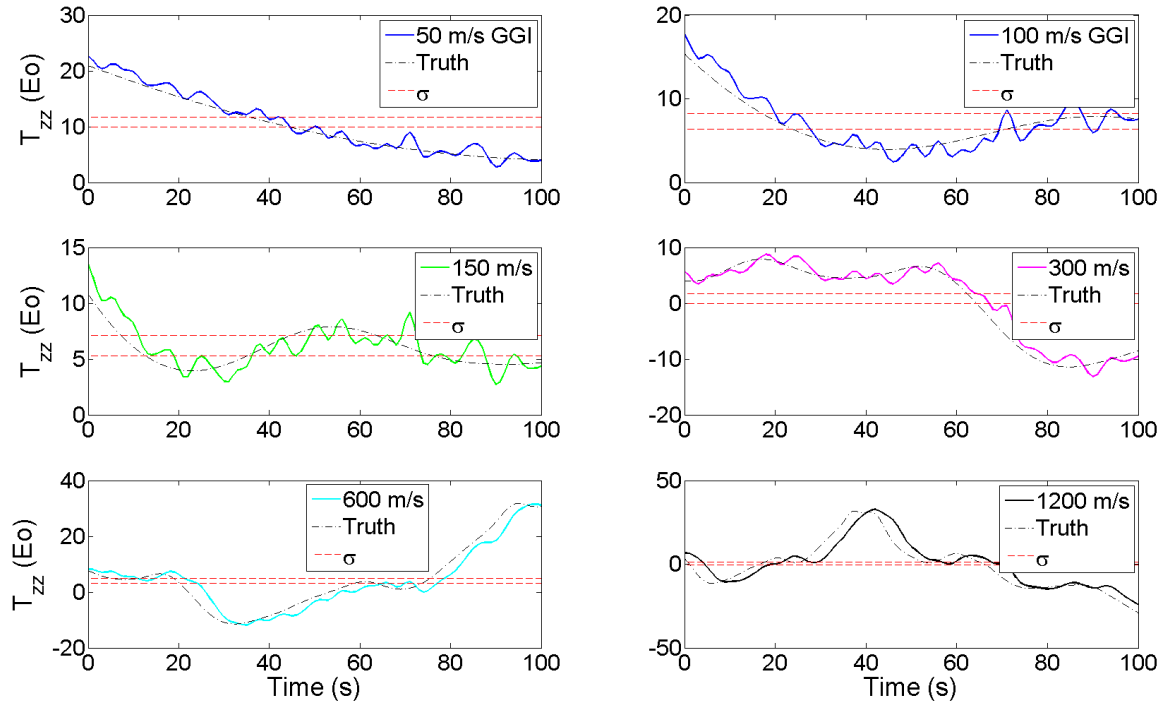


(a) Runs 49-54, 5000m, GGI 1, Rough Terrain.

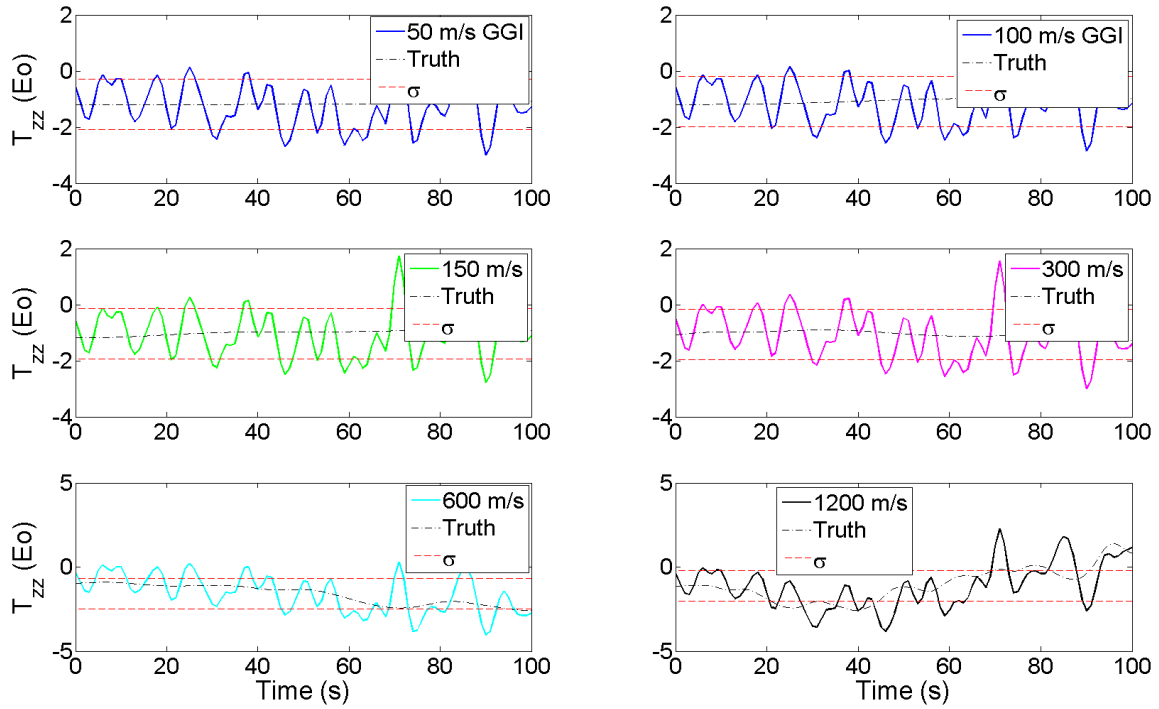


(b) Runs 55-60, 5000m, GGI 1, Smooth Terrain.

Figure C.5: Runs 49-60, 5000m, GGI 1.

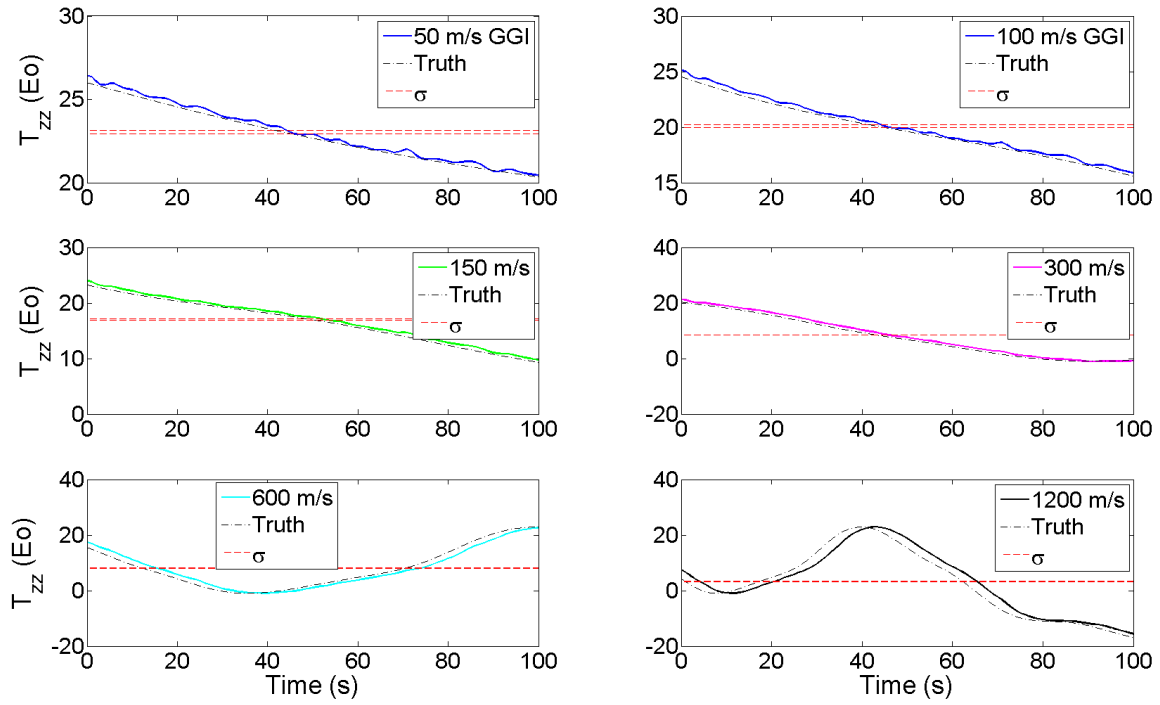


(a) Runs 61-66, 5000m, GGI 2, Rough Terrain.

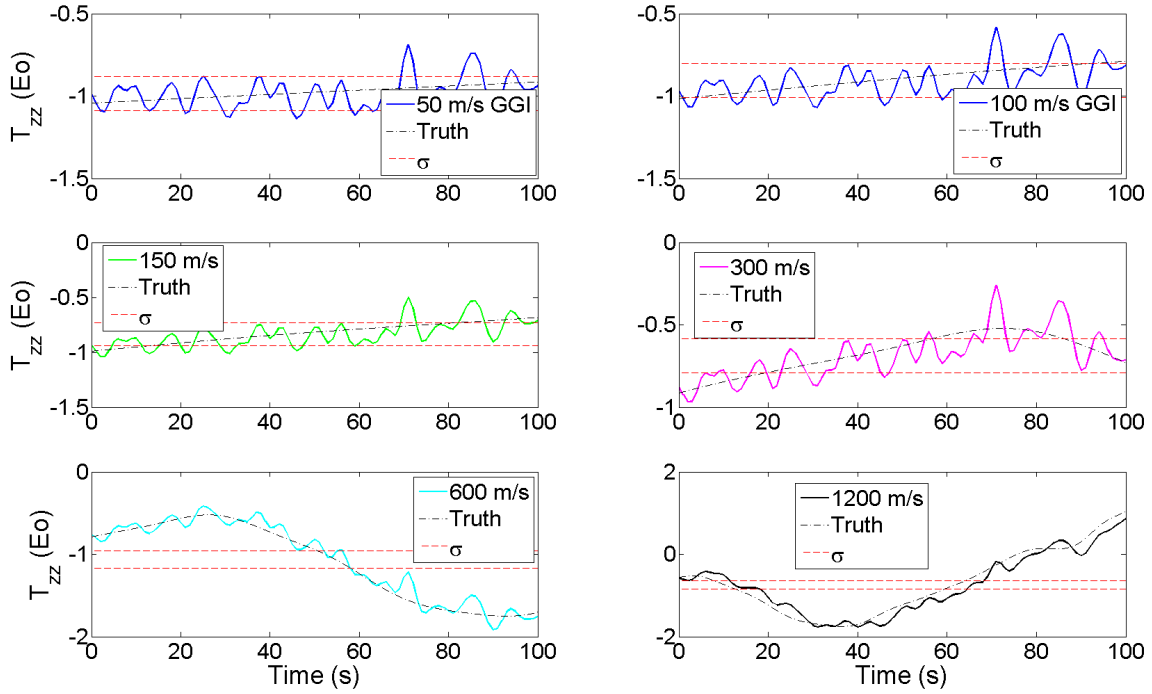


(b) Runs 67-72, 5000m, GGI 2, Smooth Terrain.

Figure C.6: Runs 61-72, 5000m, GGI 2.

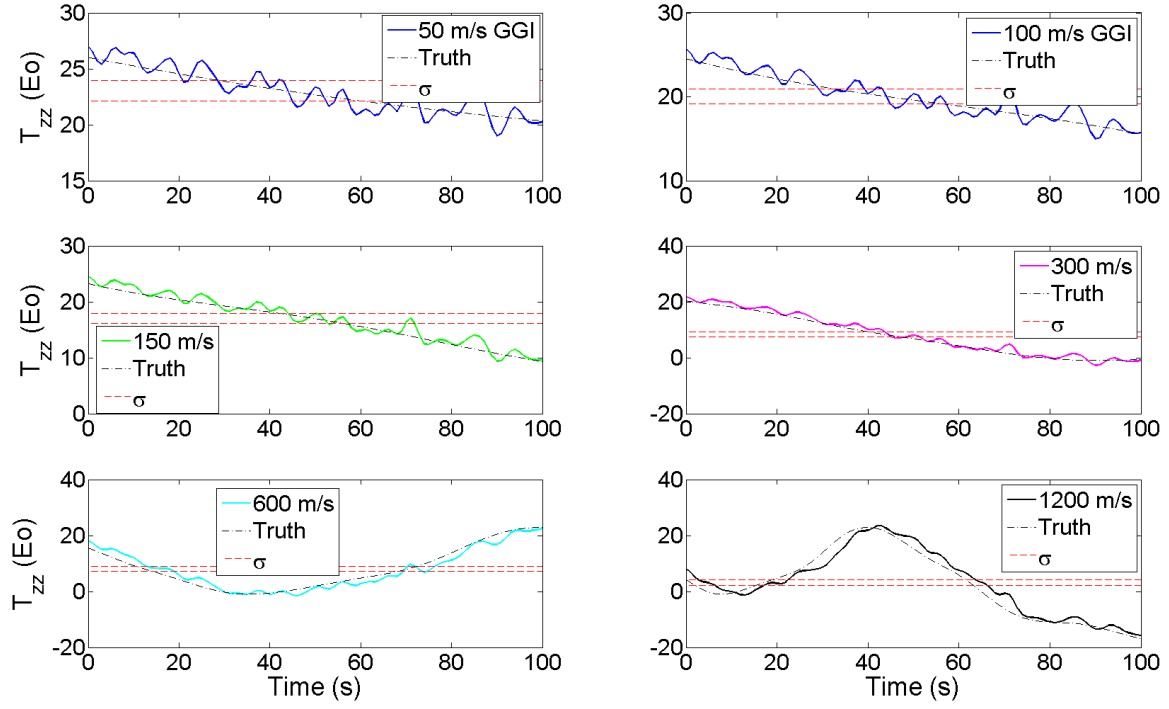


(a) Runs 73-78, 10000m, GGI 1, Rough Terrain.

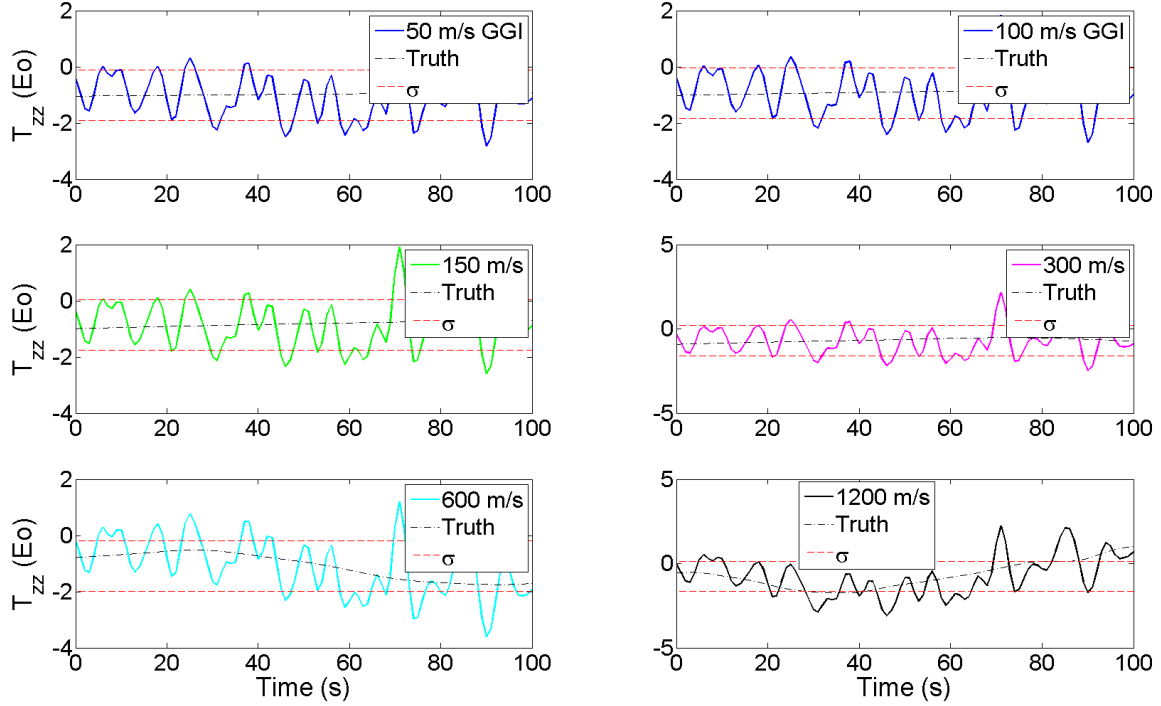


(b) Runs 79-84, 10000m, GGI 1, Smooth Terrain.

Figure C.7: Runs 73-84, 10000m, GGI 1.

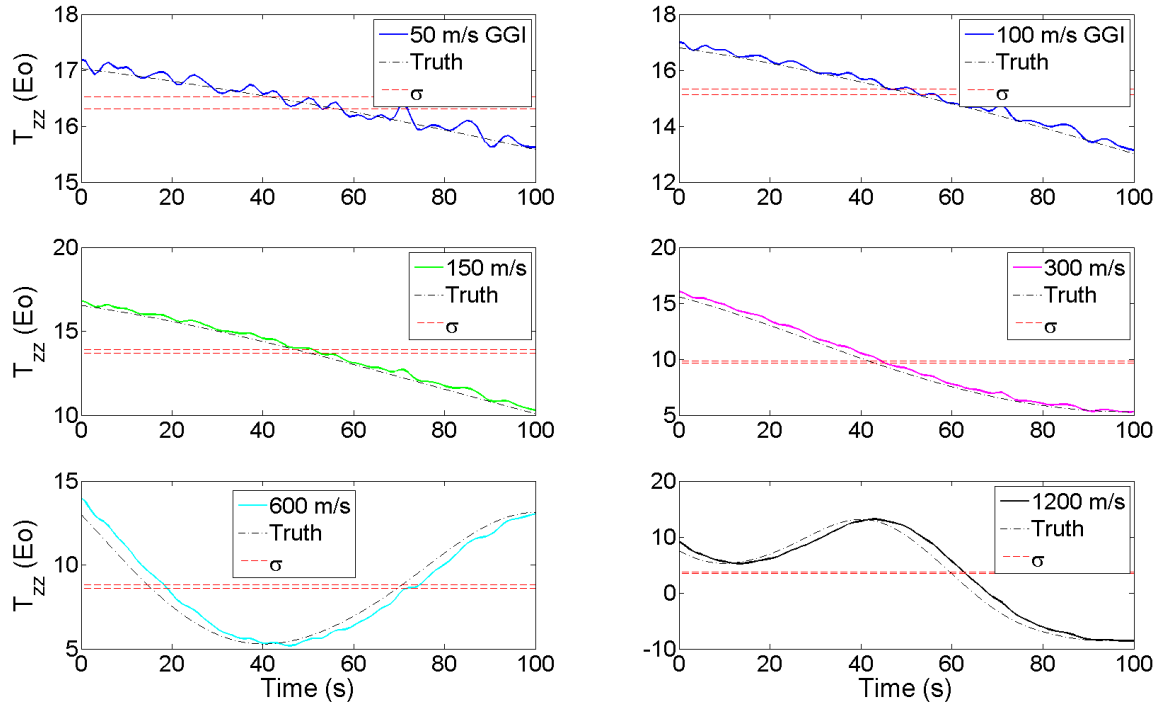


(a) Runs 85-90, 10000m, GGI 2, Rough Terrain.

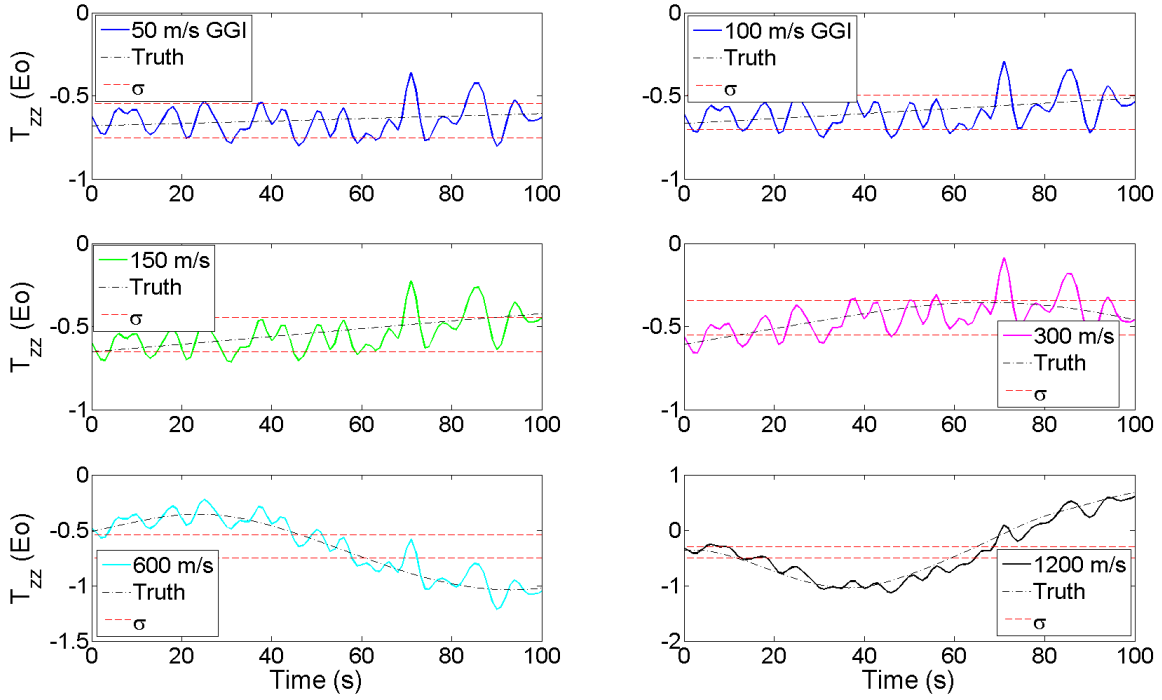


(b) Runs 91-96, 10000m, GGI 2, Smooth Terrain.

Figure C.8: Runs 85-96, 10000m, GGI 2.

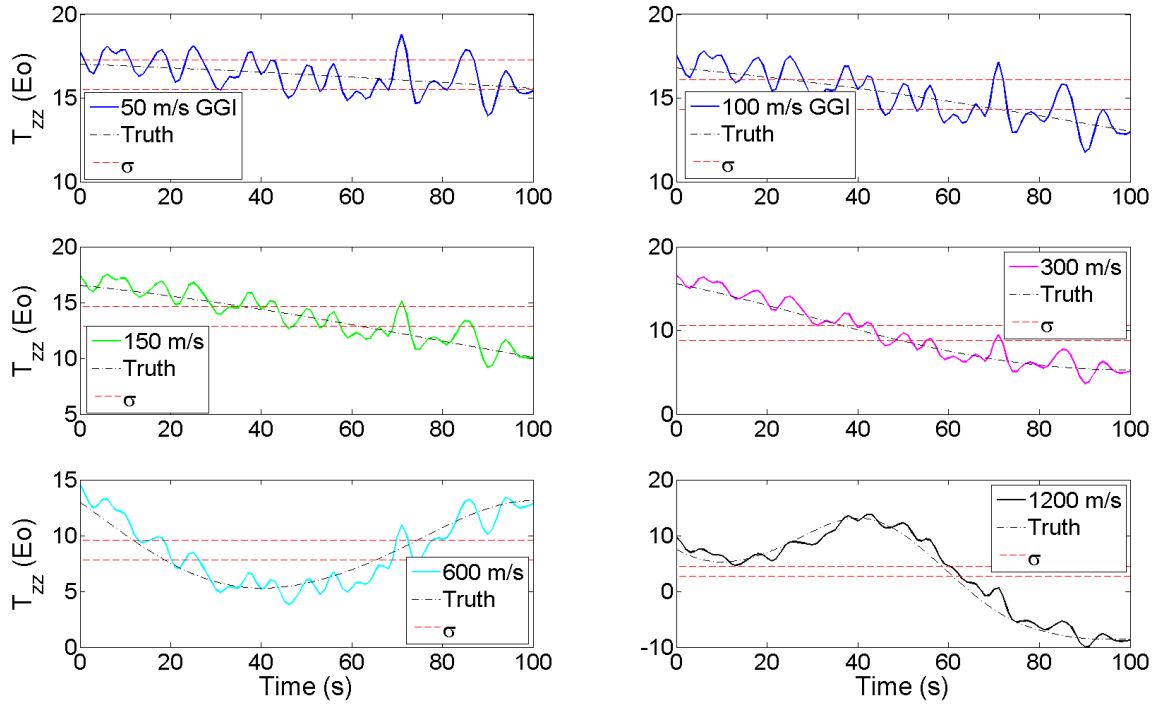


(a) Runs 97-102, 20000m, GGI 1, Rough Terrain.

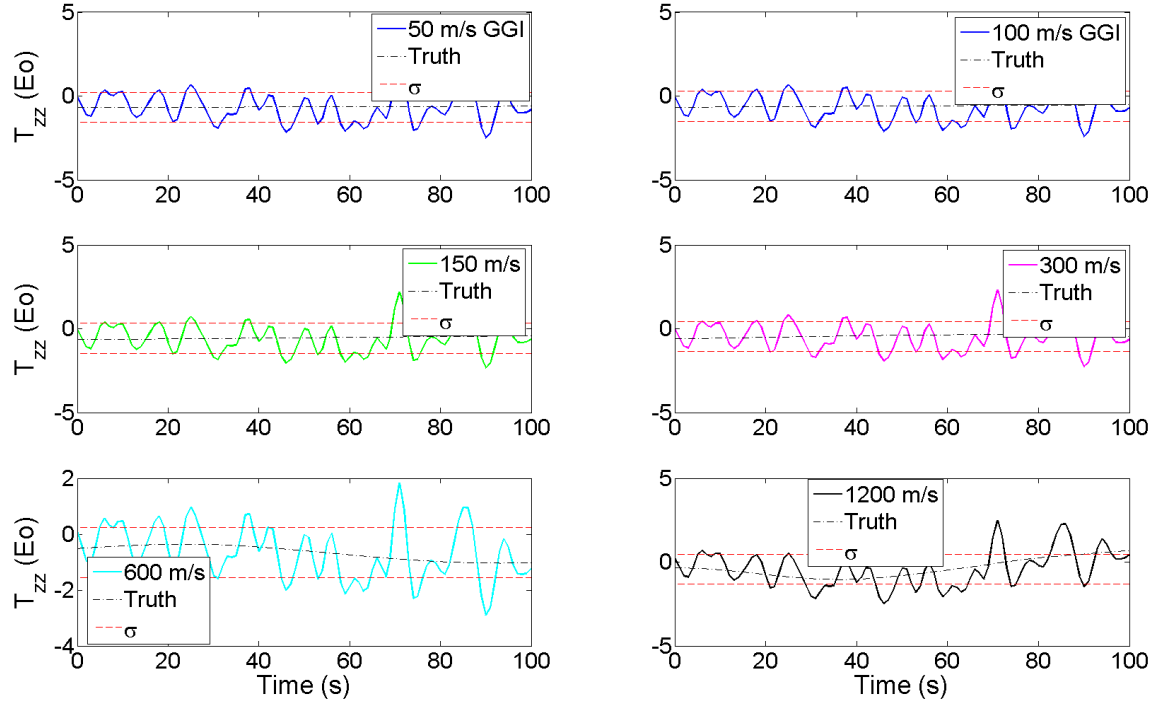


(b) Runs 103-108, 20000m, GGI 1, Smooth Terrain.

Figure C.9: Runs 97-108, 20000m, GGI 1.

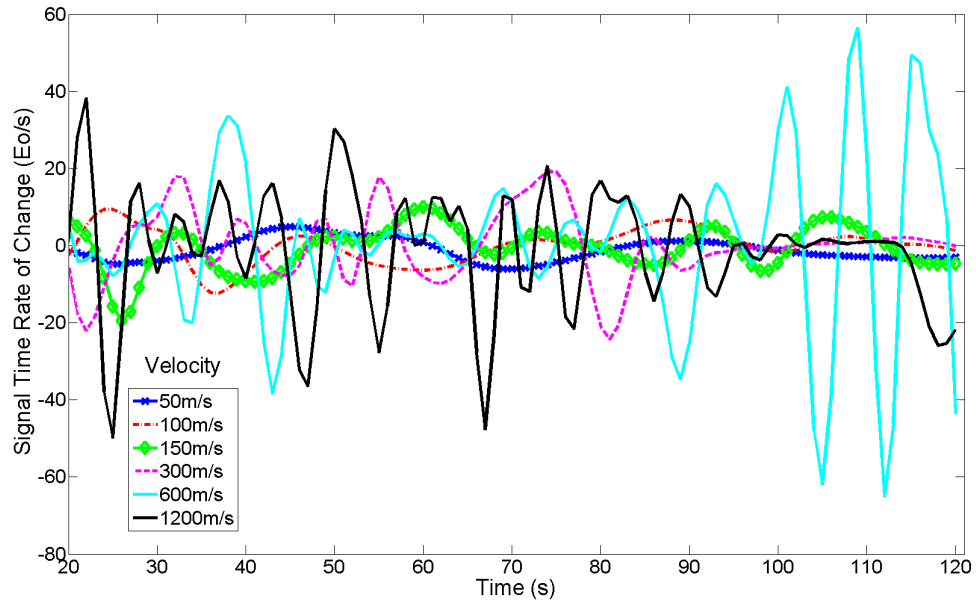


(a) Runs 109-114, 20000m, GGI 2, Rough Terrain.

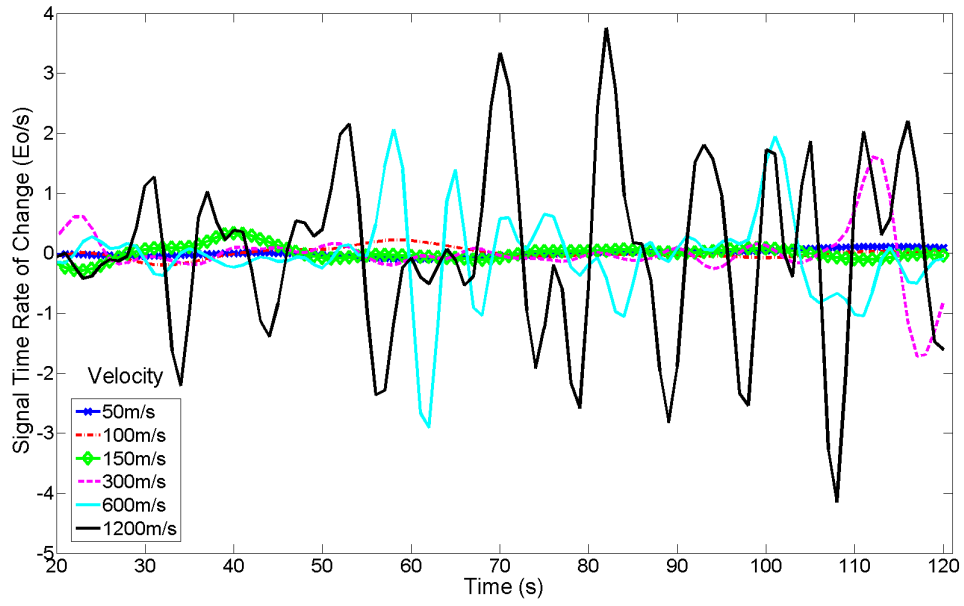


(b) Runs 115-120, 20000m, GGI 2, Smooth Terrain.

Figure C.10: Runs 109-120, 20000m, GGI 2.

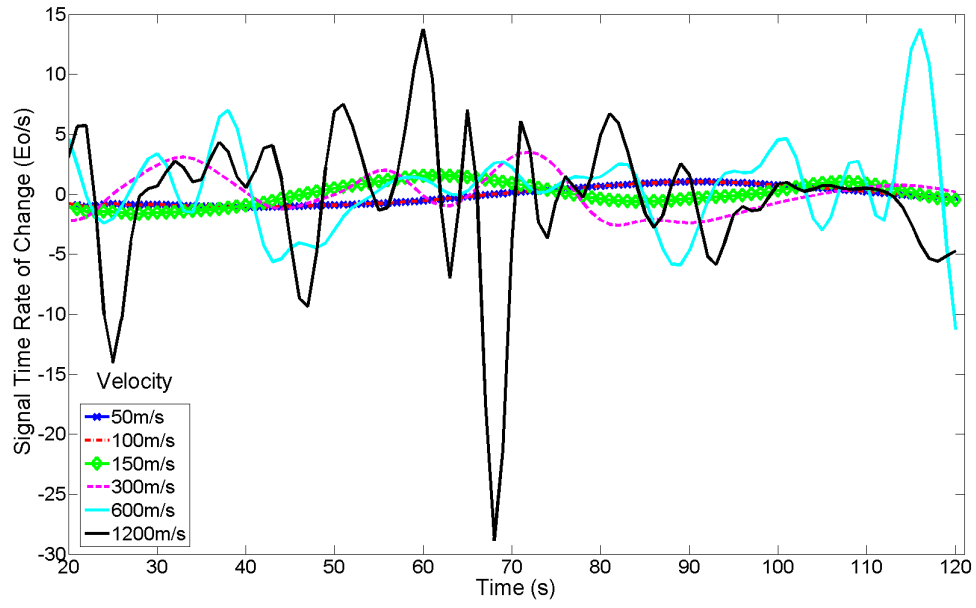


(a) Signal time rate of change, noise free, rough terrain.

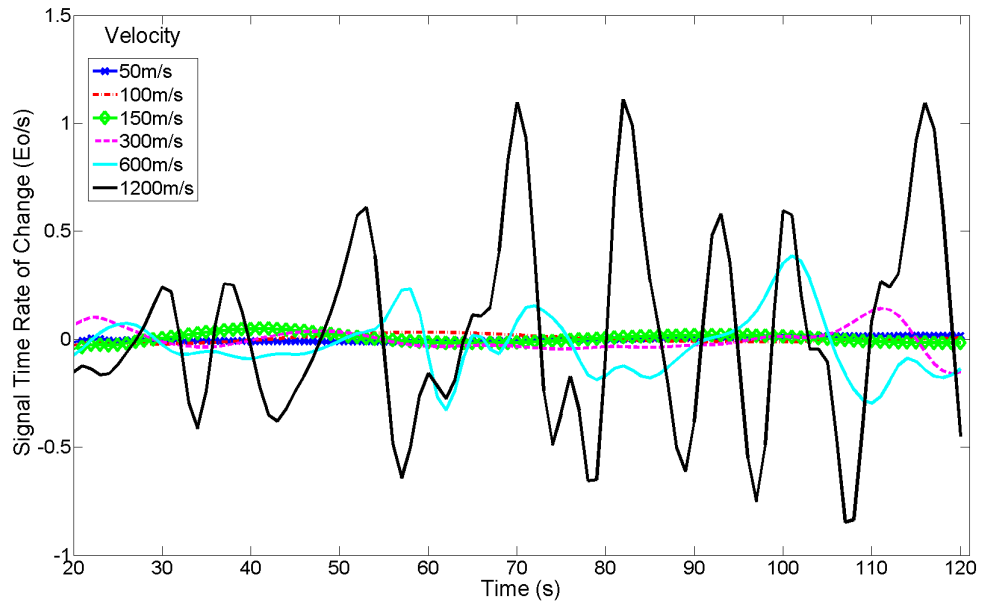


(b) Signal time rate of change, noise free, smooth terrain.

Figure C.11: Signal Time Rate of Change, 1000m.

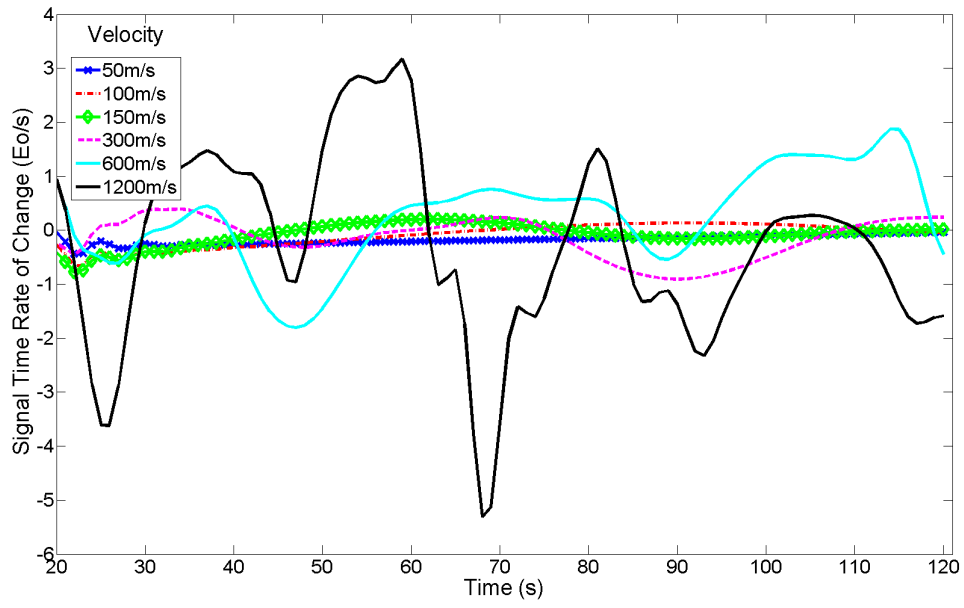


(a) Signal time rate of change, noise free, rough terrain.

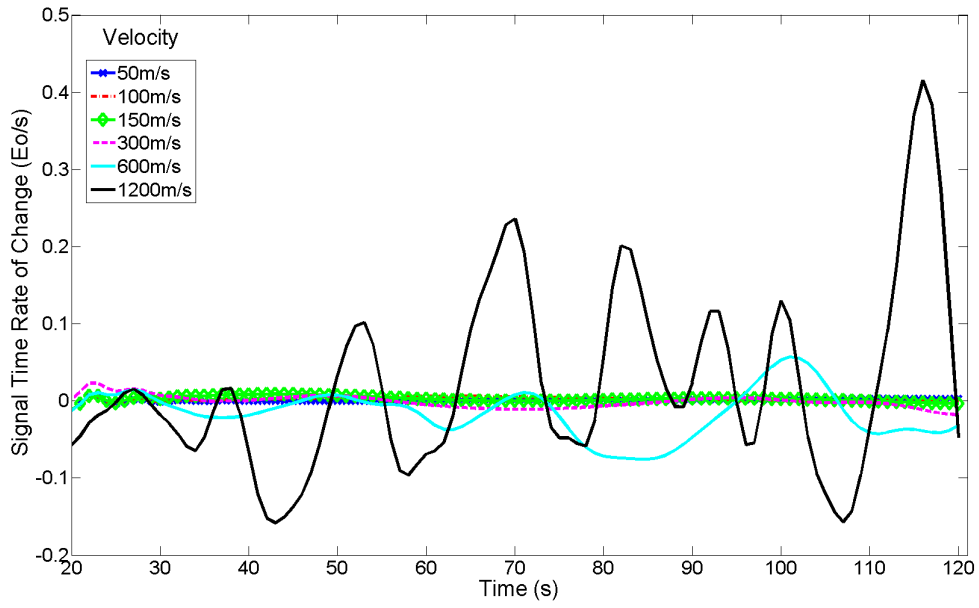


(b) Signal time rate of change, noise free, smooth terrain.

Figure C.12: Signal Time Rate of Change, 2500m.

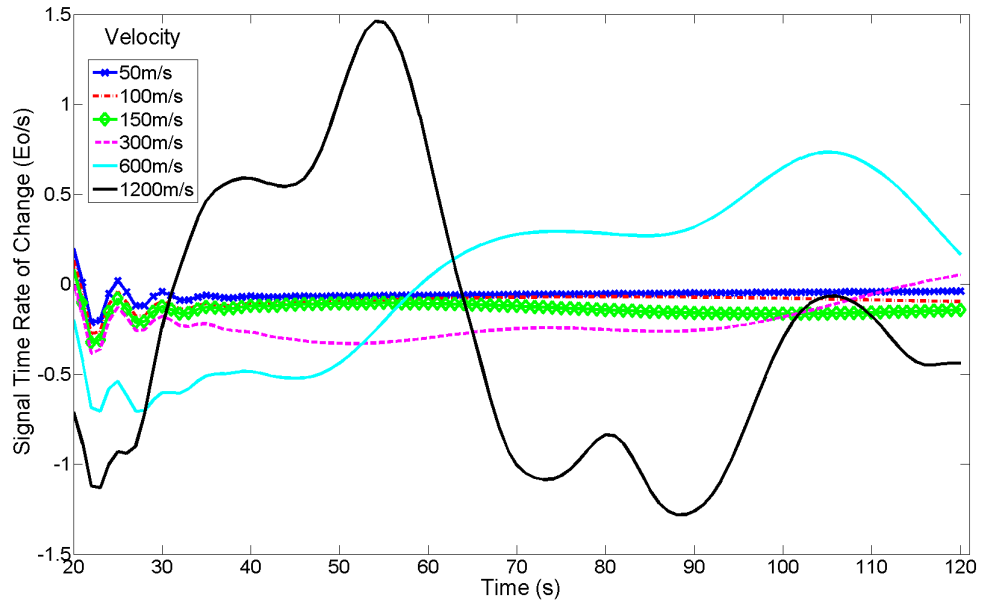


(a) Signal time rate of change, noise free, rough terrain.

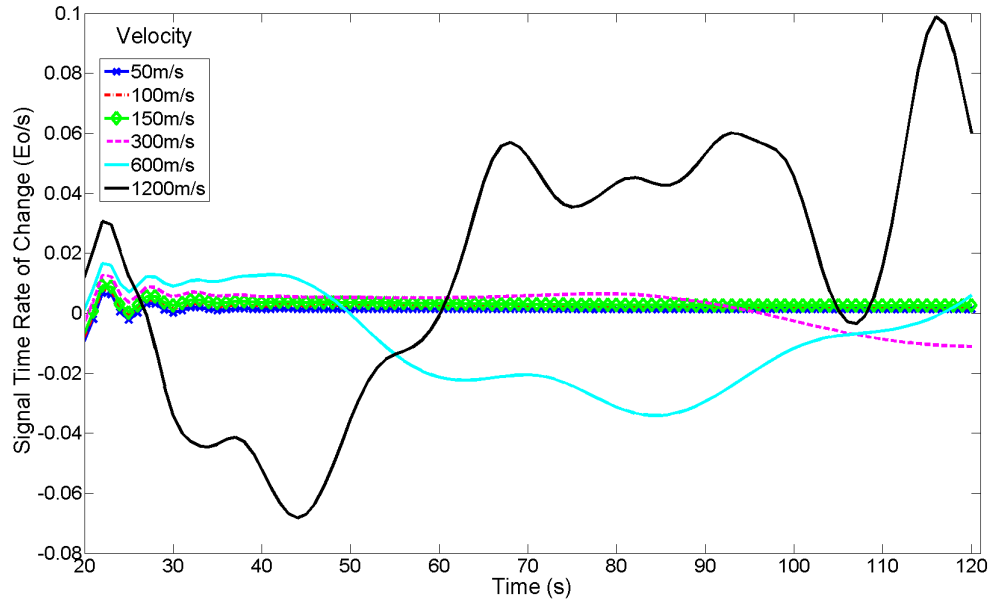


(b) Signal time rate of change, noise free, smooth terrain.

Figure C.13: Signal Time Rate of Change, 5000m.

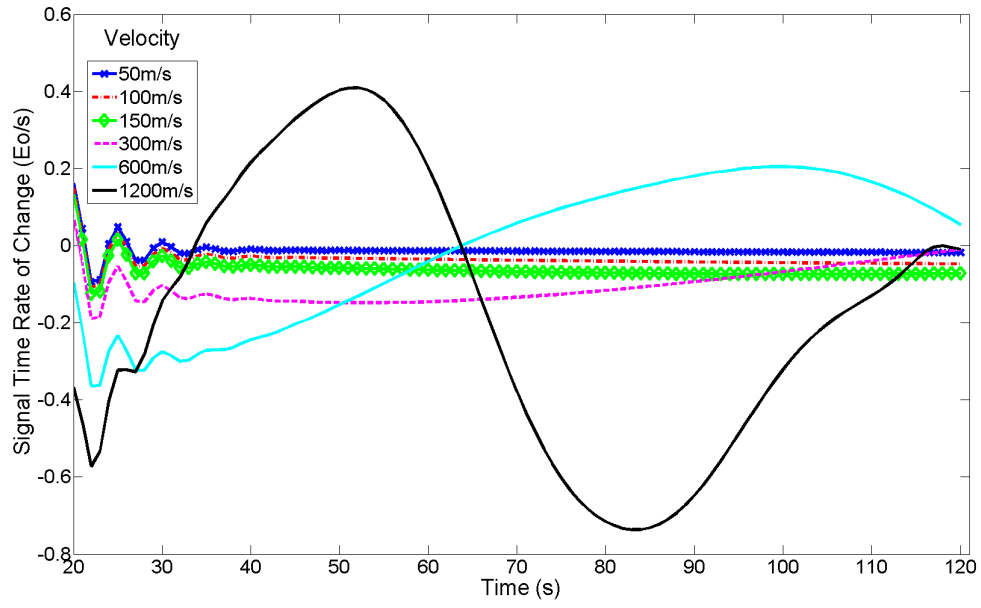


(a) Signal time rate of change, noise free, rough terrain.

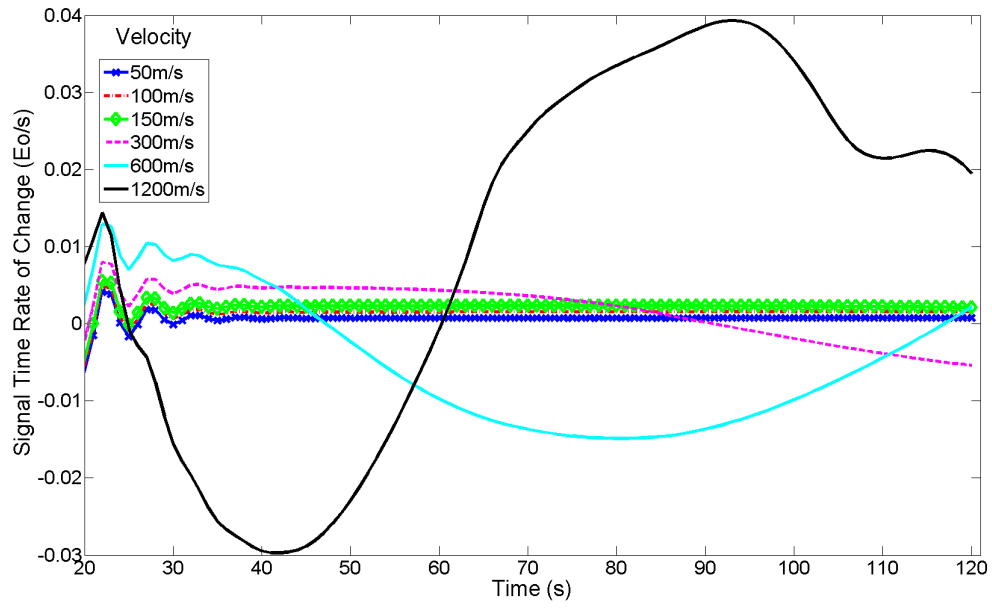


(b) Signal time rate of change, noise free, smooth terrain.

Figure C.14: Signal Time Rate of Change, 10000m.

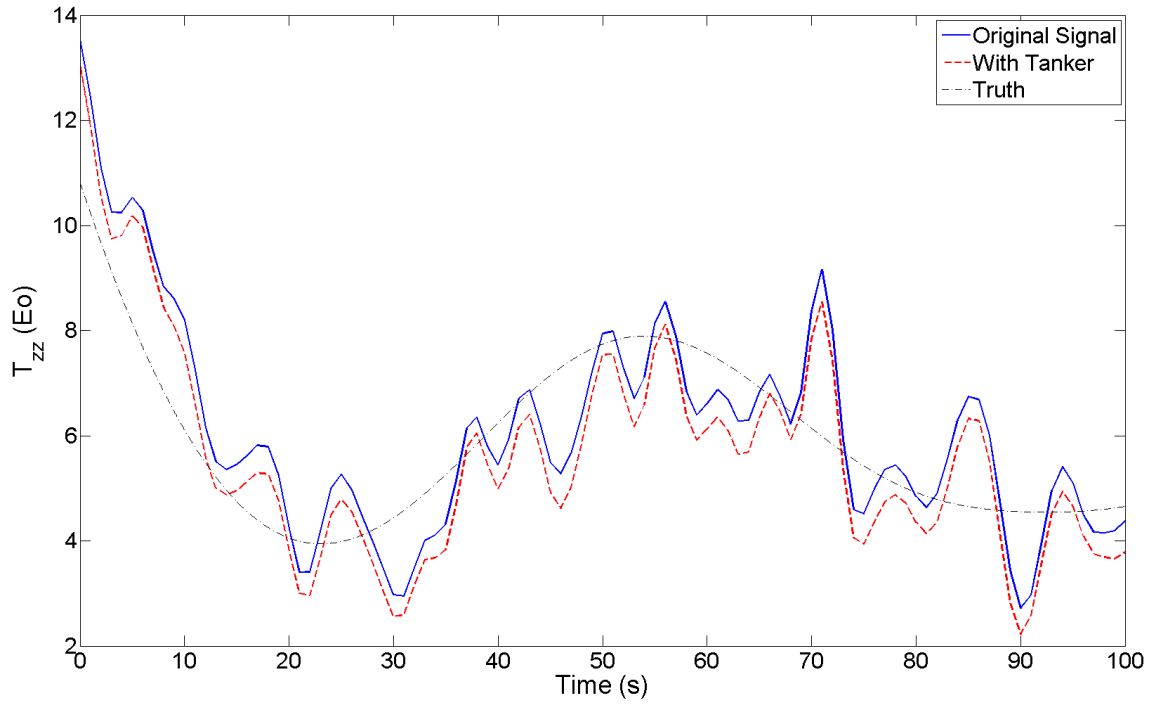


(a) Signal time rate of change, noise free, rough terrain.

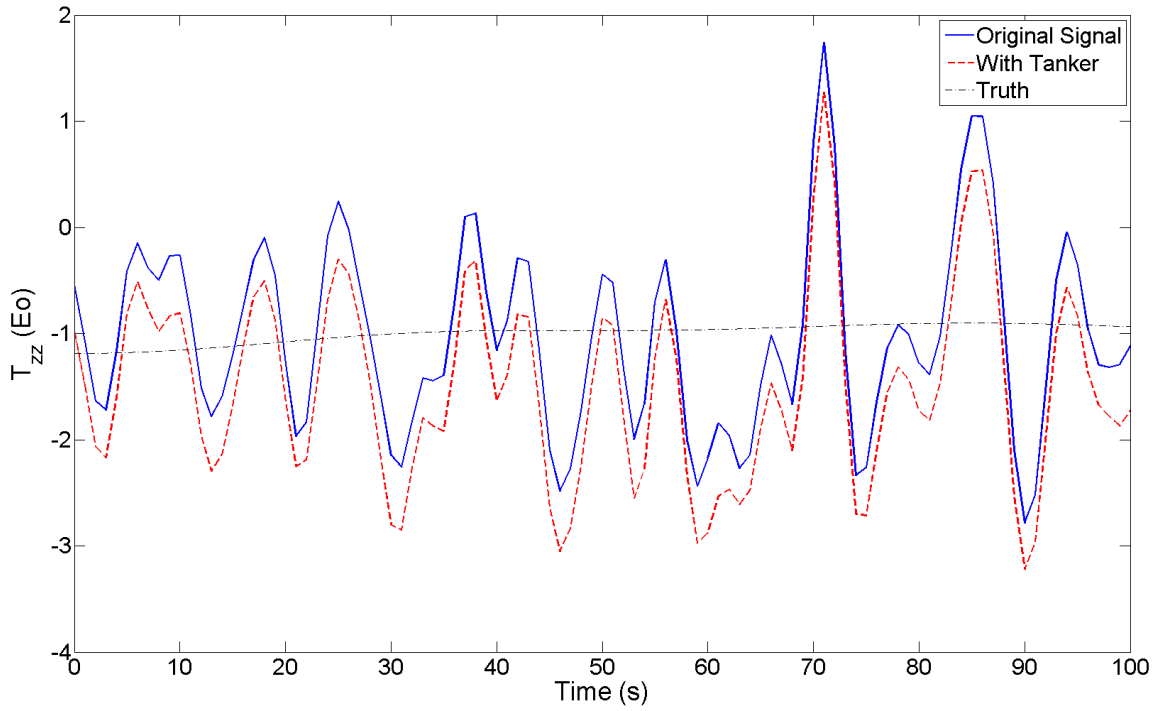


(b) Signal time rate of change, noise free, smooth terrain.

Figure C.15: Signal Time Rate of Change, 20000m.

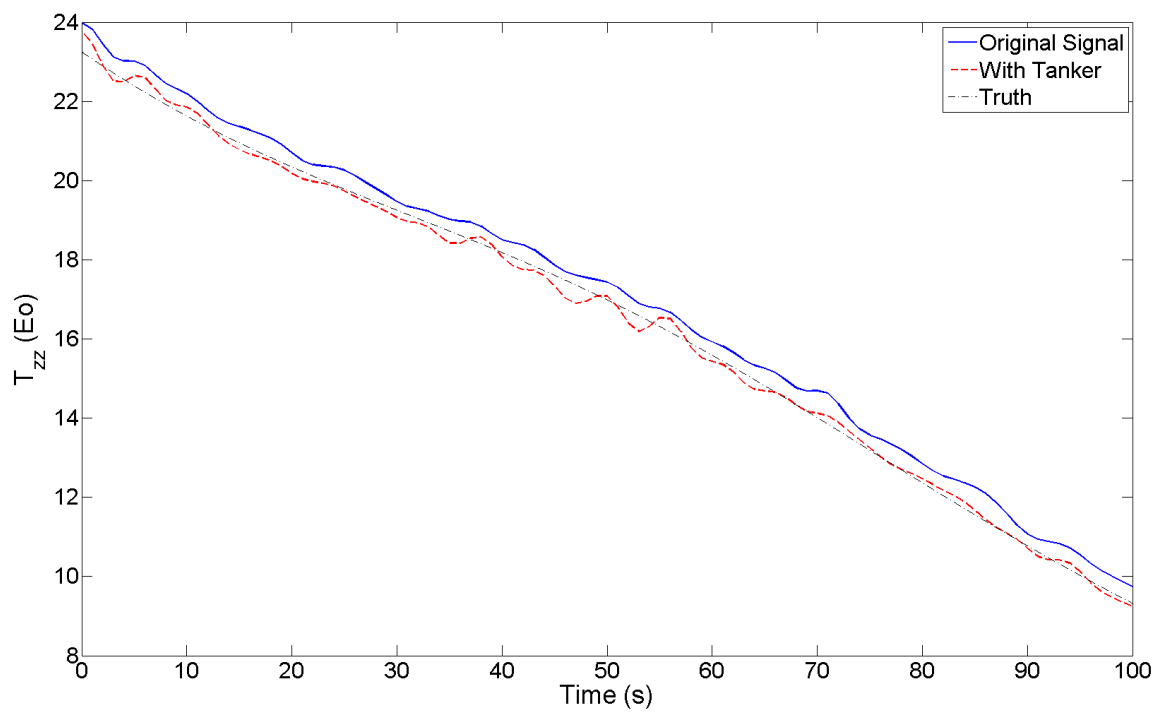


(a) GGI2 Tanker Effect, Rough Terrain.

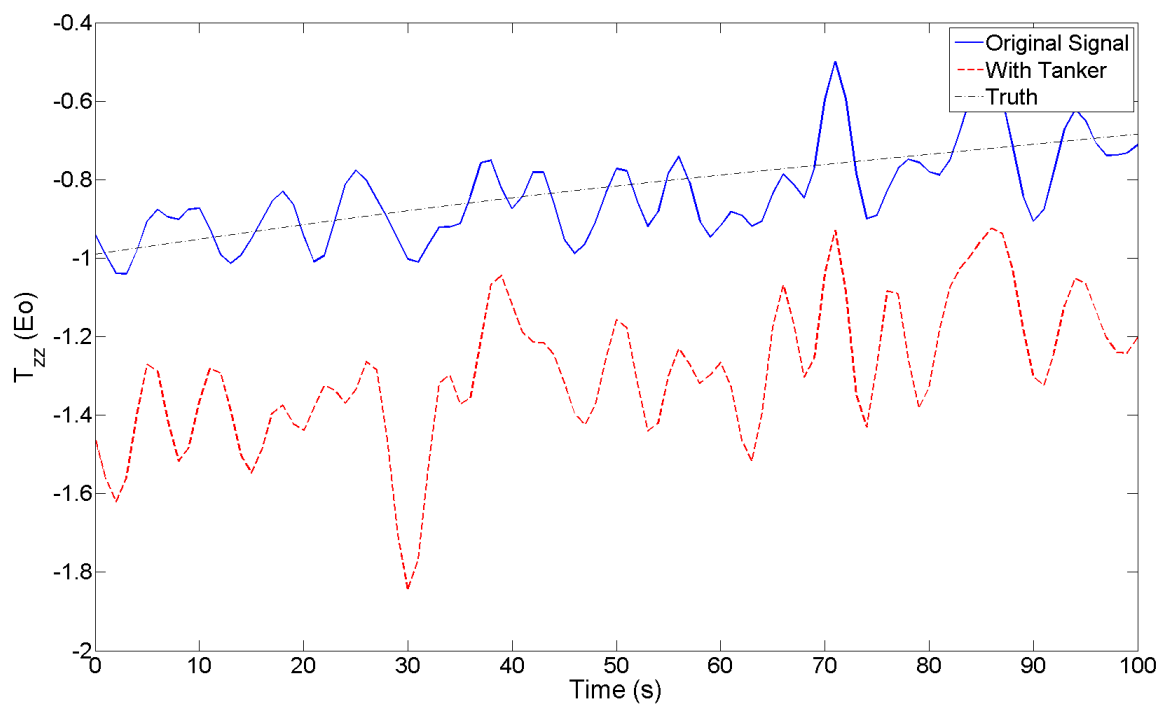


(b) GGI2 Tanker Effect, Smooth Terrain.

Figure C.16: Runs 123-124, GGI2 Tanker Effect, 5000m, 150m/s.

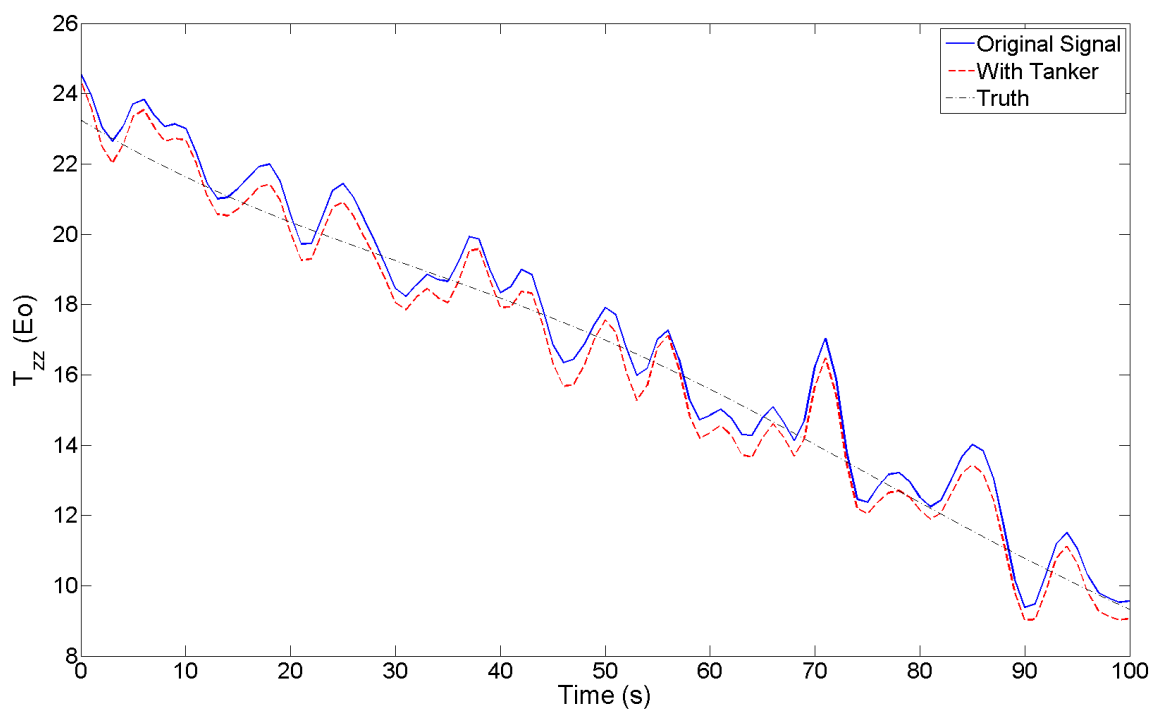


(a) GGI1 Tanker Effect, Rough Terrain.

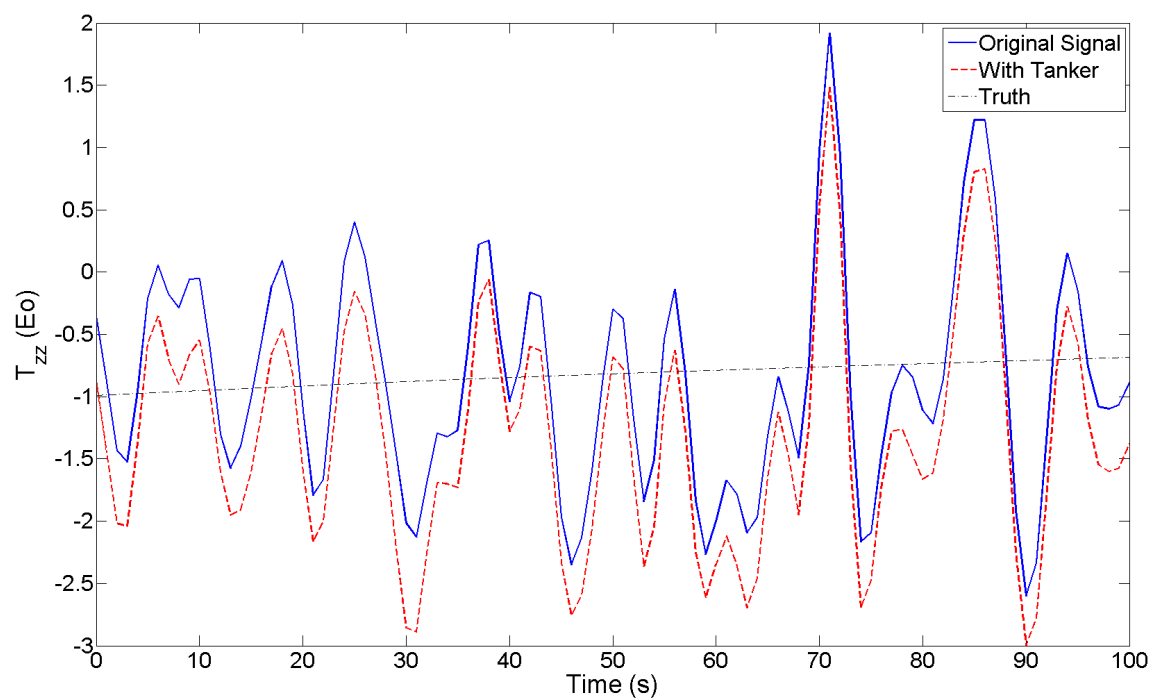


(b) GGI1 Tanker Effect, Smooth Terrain.

Figure C.17: Runs 125-126, GGI1 Tanker Effect, 10000m, 150m/s.

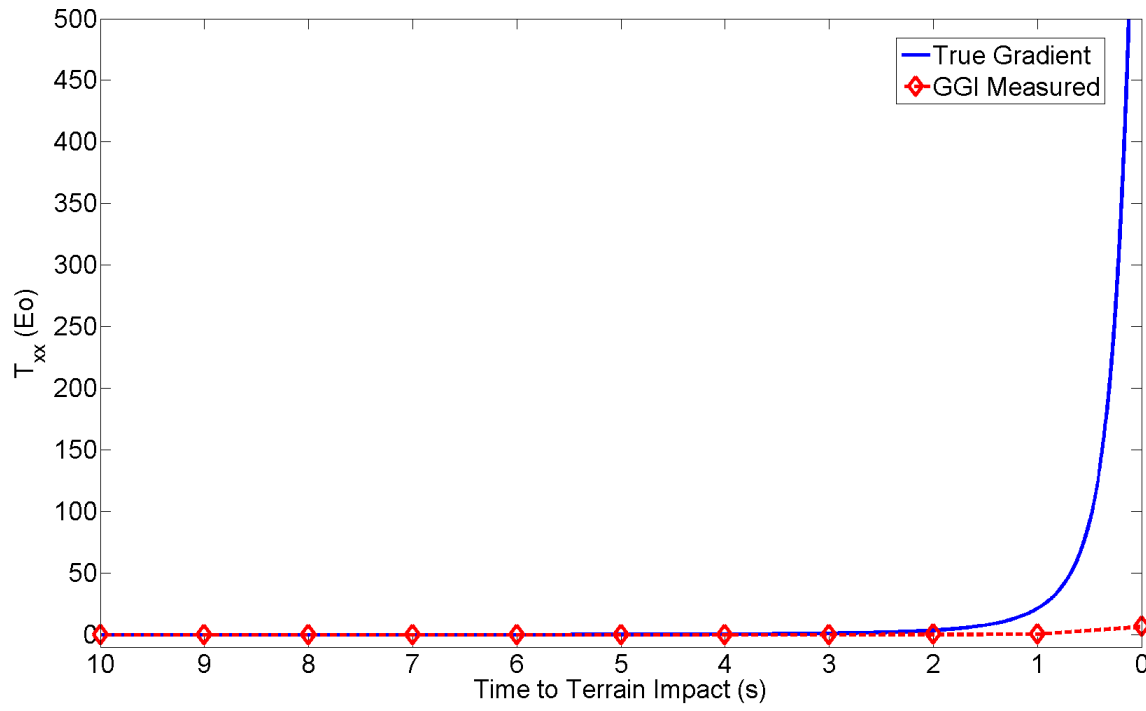


(a) GGI2 Tanker Effect, Rough Terrain.

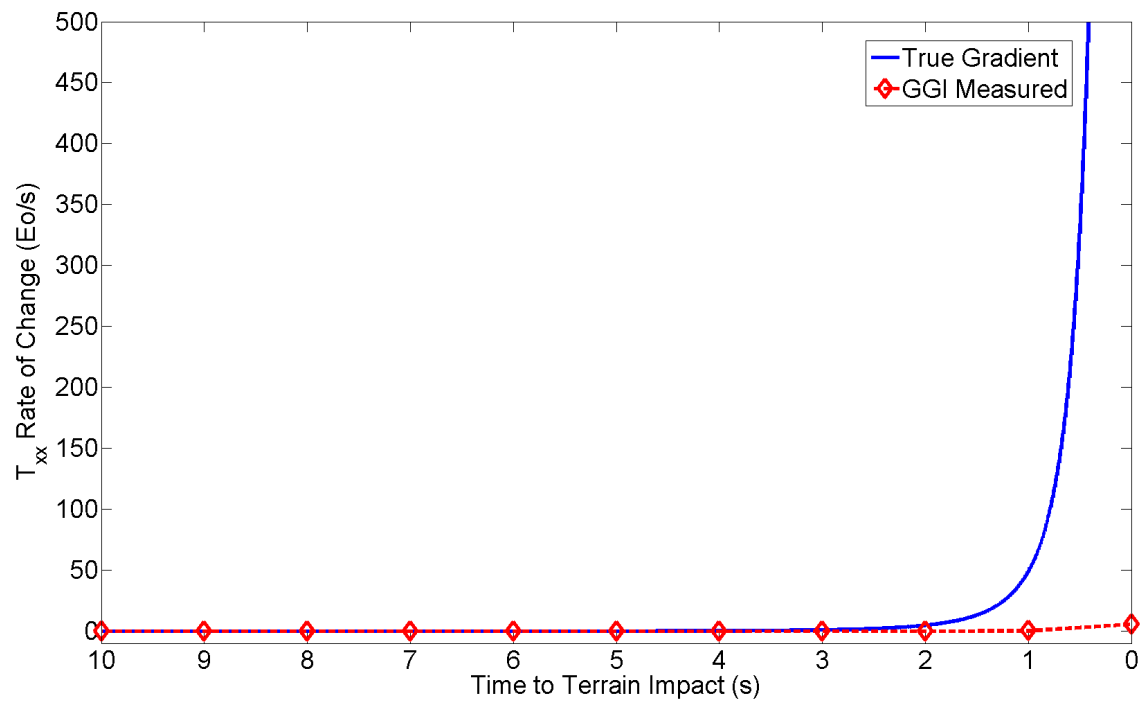


(b) GGI2 Tanker Effect, Smooth Terrain.

Figure C.18: Runs 127-128, GGI2 Tanker Effect, 10000m, 150m/s.

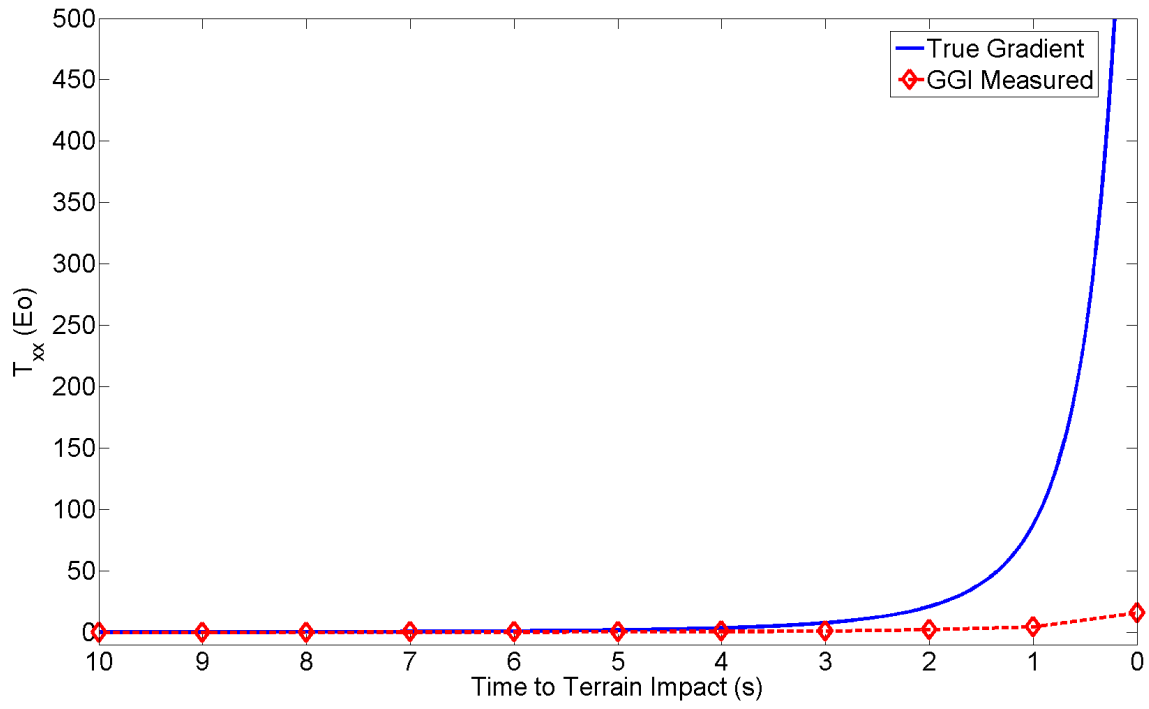


(a) Signal.

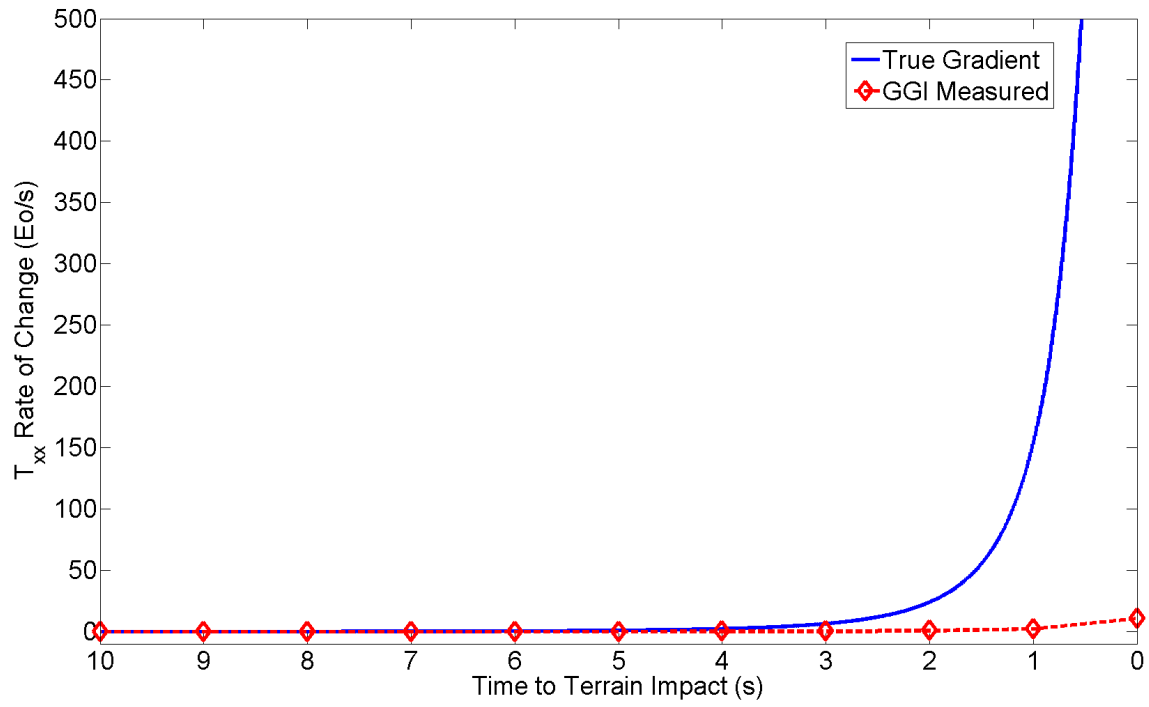


(b) Signal rate of change.

Figure C.19: Terrain Avoidance Scenario, 50 m/s, 25x25x25m Block.

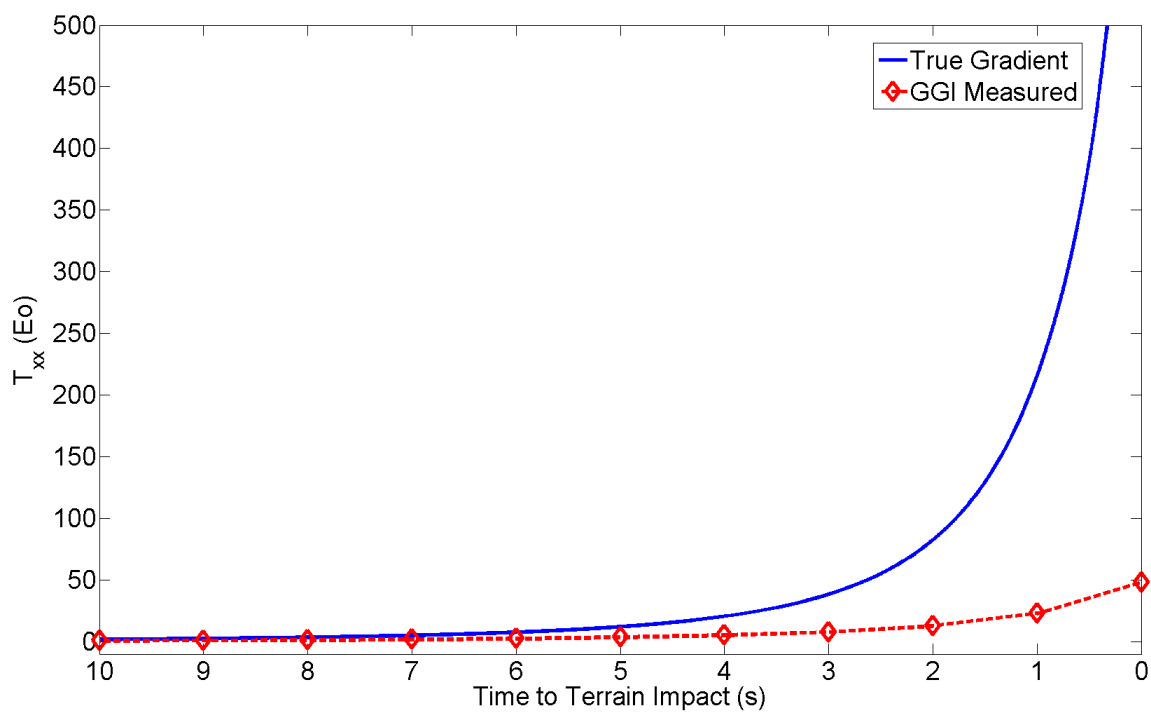


(a) Signal.

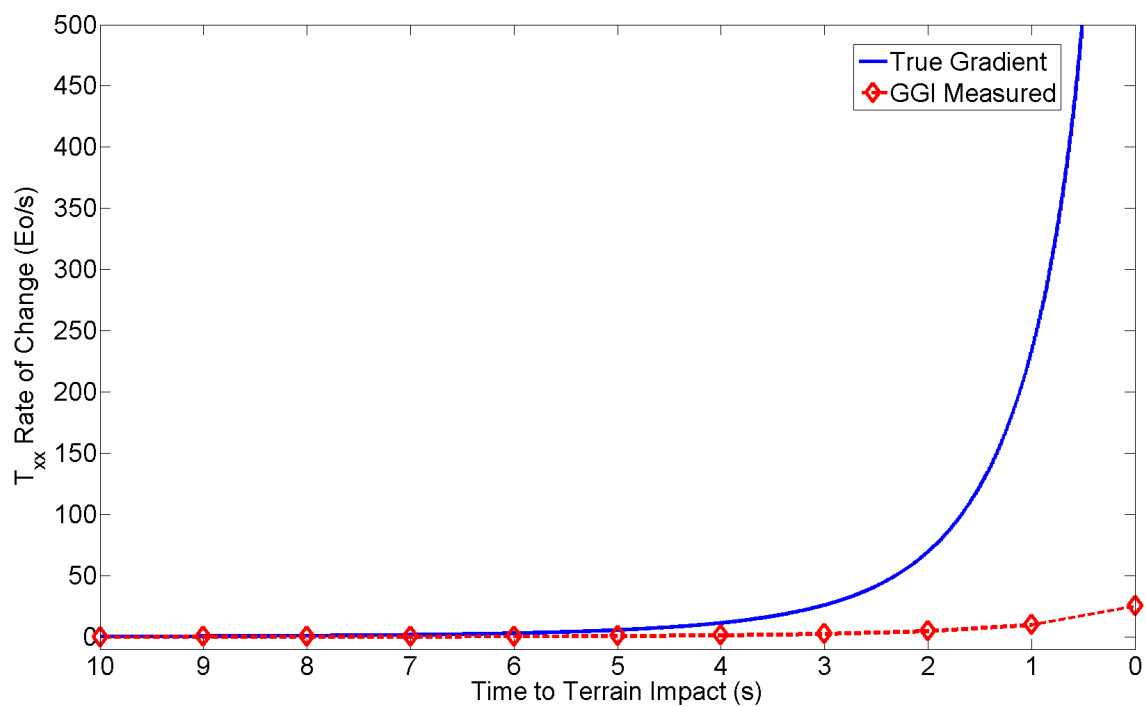


(b) Signal rate of change.

Figure C.20: Terrain Avoidance Scenario, 50 m/s, 50x50x50m Block.

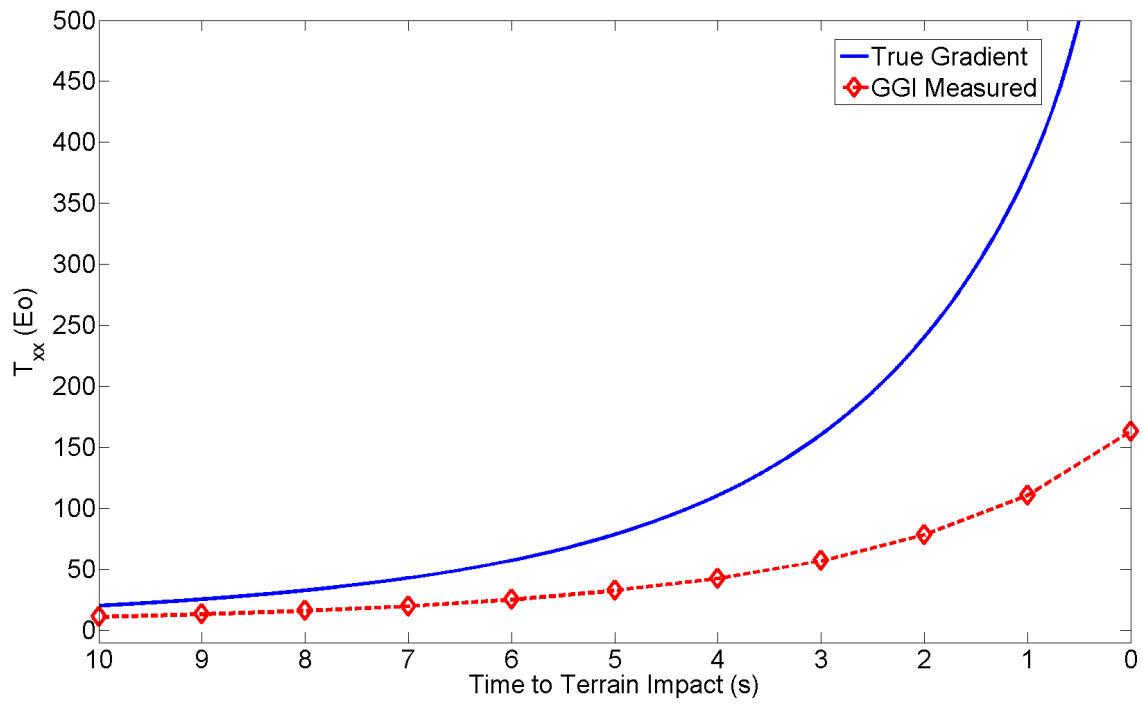


(a) Signal.

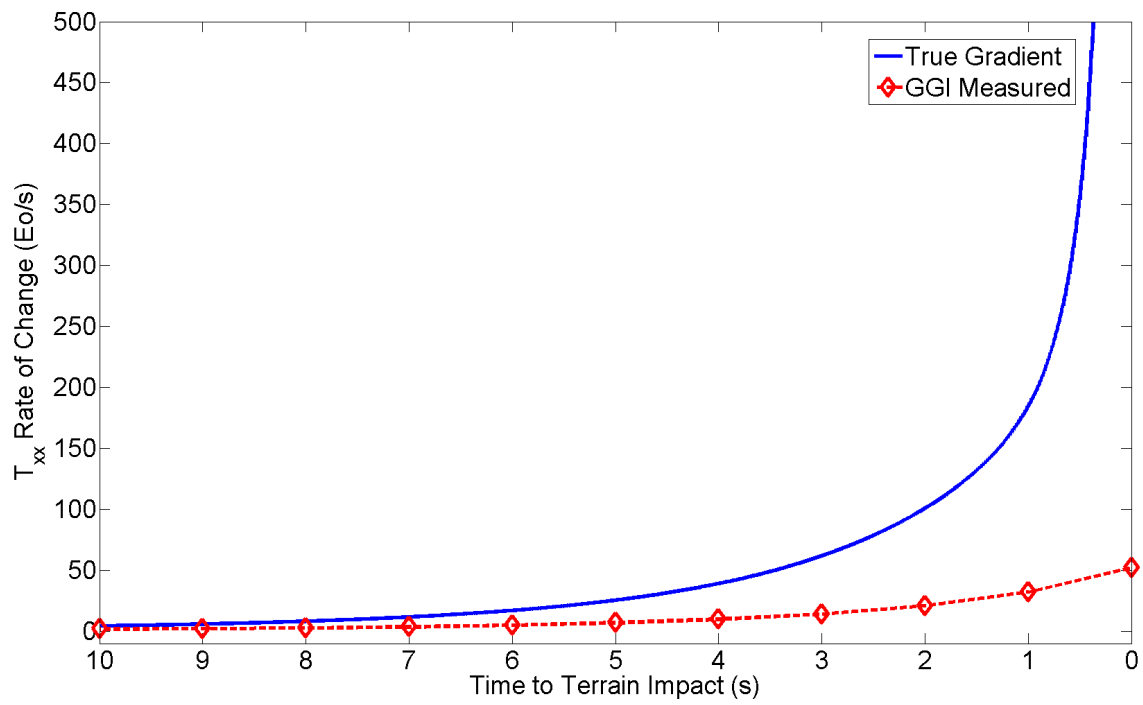


(b) Signal rate of change.

Figure C.21: Terrain Avoidance Scenario, 50 m/s, 100x100x100m Block.

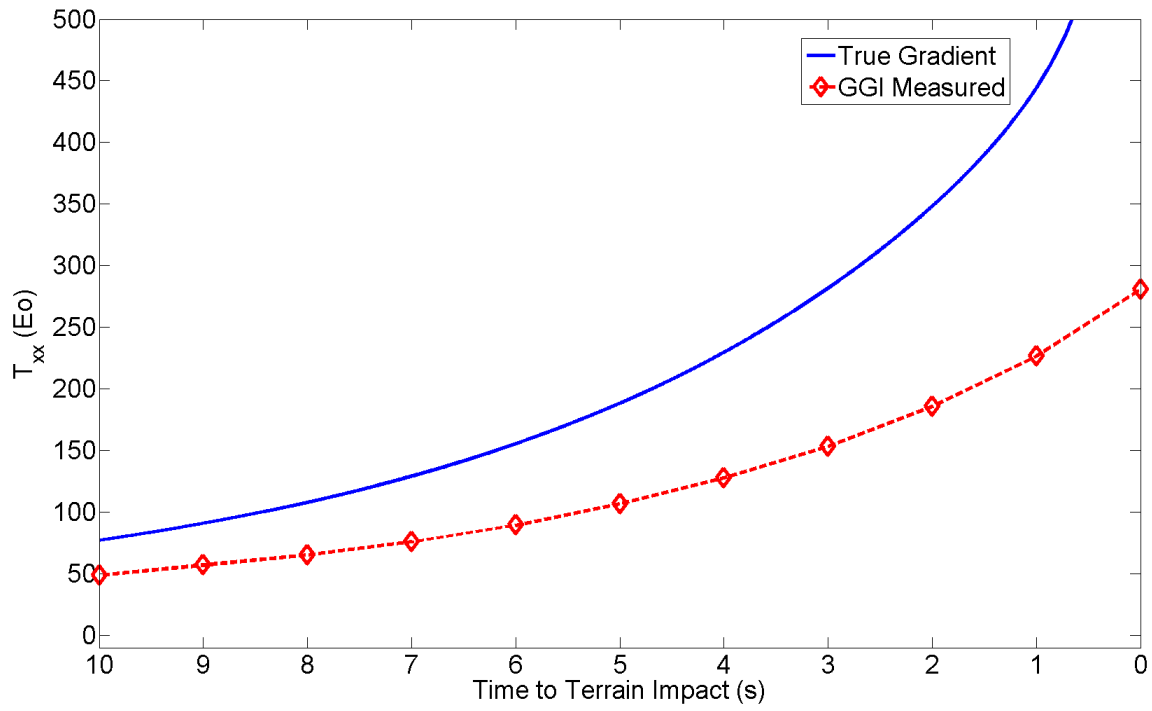


(a) Signal.

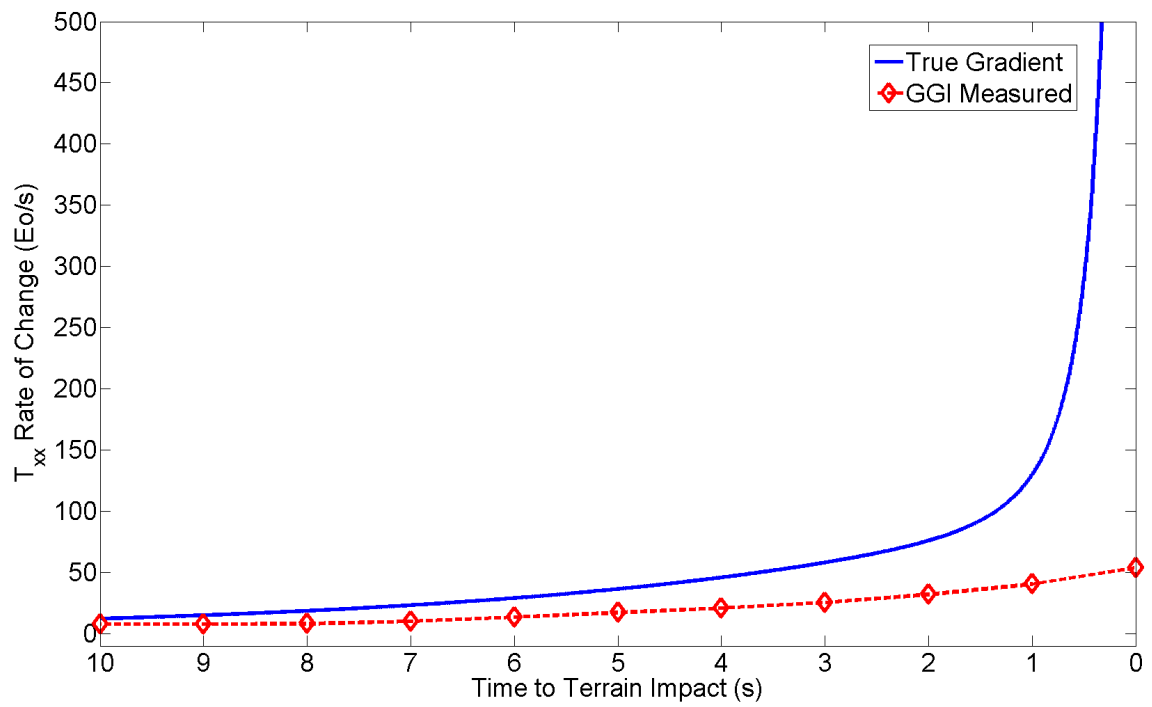


(b) Signal rate of change.

Figure C.22: Terrain Avoidance Scenario, 50 m/s, 250x250x250m Block.



(a) Signal.



(b) Signal rate of change.

Figure C.23: Terrain Avoidance Scenario, 50 m/s, 500x500x500m Block.

Bibliography

1. O. K. Hagen. (2008, Sep.) Terrain navigation principals and application. [Online]. Available: http://www.navlab.net/Publications/Terrain_Navigation_Principles_Application.pdf
2. J. P. Golden, "Terrain contour matching (TERCOM): A cruise missile guidance aid," *SPIE: Image Processing for Missile Guidance*, vol. 238, pp. 10–18, 1980.
3. C. A. Murphy, "The Air-FTG airborne gravity gradiometer system," in *Abstracts from the ASEG-PESA Airborne Gravity Workshop: Geoscience Australia Record*, 2004, pp. 7–14.
4. E. H. van Leeuwen, "Airborne gravity gradiometry," *ATSE Focus*, no. 119, pp. 1–5, 2001.
5. J. Brett. (2008, Dec.) Norden bombsight webpage. [Online]. Available: http://www.twinbeech.com/norden_bombsight.htm
6. B. Hofmann-Wellenhoff and H. Moritz, *Physical Geodesy*. New York, NY: SpringerWeinNewYork, 2005.
7. N. Domenico, "The SEG museum's torsional balance," *The Leading Edge*, vol. 13, pp. 683–686, 1994.
8. J. Parmentola, "The gravity gradiometer as a verification tool," *Science and Global Security*, vol. 2, pp. 43–57, 1990.
9. D. Nagy, G. Papp, and J. Benedek, "The gravitational potential and its derivatives for the prism," *Journal of Geodesy*, vol. 74, pp. 552–560, 2000.
10. C. Jekeli, *Inertial Navigation Systems with Geodetic Applications*. New York, NY: de Gruyter, 2001.
11. D. E. Dosch and D. Sieracki, "Gravity gradiometer and method for calculating a gravity tensor with increase accuracy," U.S. Patent 0 209 070, Nov. 13, 2003.
12. D. Difrancesco, "Advances and challenges in the development and deployment of gravity gradiometer systems," *EGM 2007 International Workshop*, Apr. 2007.
13. R. E. Huffman, M. D. Cawood, M. Ferm, and M. A. Skoog, "Determination of nuisance criteria for ground collision avoidance systems," presented at the 4th Saint Petersburg International Conference on Integrated Navigation Systems, 1997.
14. R. E. Bell, "Gravity gradiometry," *Scientific American*, vol. 278, no. 6, 1998.
15. C. Jekeli, "The gravity gradiometer survey system (GGSS)," *Eos*, vol. 69, no. 8, pp. 105, 116–117, 1988.
16. G. R. Mumaw. (2008, Apr.) Marine 3D full tensor gravity gradiometry. [Online]. Available: http://www.bellgeo.com/doc/Hydro_09_04_F_Mumaw.pdf

17. (2008, Apr.) GRACE Gravity Recovery and Climate Experiment. [Online]. Available: <http://www.csr.utexas.edu/grace>
18. (2008, Apr.) GOCE Gravity field and steady-state Ocean Circulation Explorer. [Online]. Available: <http://www.esa.int/SPECIALS/GOCE/index.html>
19. G. M. Hofmeyer and C. A. Affleck, "Rotating accelerometer gradiometer," U.S. Patent 5 357 802, Oct. 25, 1994.
20. D. Hatch, C. Murphy, G. Mumaw, and J. Brewster, "Performance of the Air-FTG aboard an airship platform," presented at the Australian Earth Science Convention, 2006.
21. J. Brett. (2008, Jun.) Theory of FTG measurements. [Online]. Available: http://www.bellgeo.com/tech/technology_theory_of_FTG.html
22. (2008, Dec.). [Online]. Available: http://www.bellgeospace.com/tech/technology_system.html
23. D. M. Gleason, "Passive airborne navigation and terrain avoidance using gravity gradiometry," *Journal of Guidance, Control, and Dynamics*, vol. 18, no. 6, pp. 1450–1458, 1995.
24. M. Dransfield, A. Christensen, M. Rose, P. Stone, and P. Diorio, "FALCON test results from Bathurst mining camp," *Exploration Geophysics*, vol. 32, pp. 243–246, 2001.
25. R. J. L. Lane, "Integrating ground and airborne data into regional gravity compilations," in *Abstracts from the ASEG-PESA Airborne Gravity Workshop: Geoscience Australia Record*, 2004, pp. 81–97.
26. (2008, Jun.) Bluecube technical case. [Online]. Available: <http://www.arkex.com/bq-tour-technical-4.php>
27. H. J. Paik, "Three-axis superconducting gravity gradiometer," U.S. Patent 4 841 772, Jun. 27, 1989.
28. (2008, Jun.). [Online]. Available: <http://www.superconductors.org/INdex.htm>
29. (2008, Jun.). [Online]. Available: <http://www.superconductors.org/History.htm>
30. (2008, Apr.). [Online]. Available: http://en.wikipedia.org/wiki/Meissner_effect
31. (2008, Jun.). [Online]. Available: <http://www.superconductors.org/Type2.htm>
32. J. M. Lumley, J. P. White, G. Barnes, D. Huang, and H. J. Paik, "A superconducting gravity gradiometer tool for exploration," presented at the Gradiometry workshop SEG 2001, 2001.
33. (2008, Jun.). [Online]. Available: <http://www.superconductors.org/Uses.htm>
34. P. Shirron. (2008, Jun.) Superconducting gravity gradiometer (SGG). [Online]. Available: http://cryo.gsfc.nasa.gov/other_hardware/SGG/SGG.html

35. H. V. Moody and H. J. Paik, "A superconducting gravity gradiometer for inertial navigation," in *Proceedings of IEEE's Position Location and Navigation Symposium (PLANS)*, Apr. 2004, pp. 775–781.
36. "Airborne gravity surveying," *Supplement to the Northern Miner*, vol. 93, no. 52, p. 16, 2008.
37. M. Smith, "Exploration with gravitas, improved airborne gravity gradiometry to aid hunt for hydrocarbons," *New Technology Magazine*, pp. 7–8, Feb. 2007.
38. B. Main, "The Gedex HD-AGG: Impact of 1 Eotvos $\text{Hz}^{-1/2}$, overview of system, development and testing update," in *Abstracts from KEGS Recent Developments in Passive Geophysical Methods*, Mar. 2008.
39. (2008, Jun.) High definition airborne gravity gradiometer Gedex HD-AGG. [Online]. Available: <http://www.gedex.ca/pdf/tech2.pdf>
40. (2008, Apr.) Gravity gradiometer development. [Online]. Available: <http://www.oil-itf.com/index/cms-filesystem-action/casestudies/gravitygradiometer.pdf>
41. N. Yu, J. M. Kohel, L. Romans, and L. Maleki. (2008, Jun.) Quantum gravity gradiometer sensor for earth science applications. [Online]. Available: <http://trs-new.jpl.nasa.gov/dspace/bitstream/2014/8684/1/02-1235.pdf>
42. M. Kasevich. (2008, Apr.) Atom interferometry. [Online]. Available: http://vmsstreamer1.fnal.gov/VMS_Site_03/Lectures/Colloquium/presentations/080507Kasevich.PPT
43. E. H. Metzger and A. Jircitano, "Inertial navigation performance improvement using gravity gradient matching techniques," *Journal of Spacecraft and Rockets*, vol. 13, no. 6, 1975.
44. C. A. Affleck and A. Jircitano, "A passive gravity gradiometer navigation system," in *Proceedings of IEEE's Position Location and Navigation Symposium (PLANS)*, Las Vegas, NV, 1990, pp. 60–66.
45. A. Jircitano and D. E. Dosch, "Gravity aided inertial navigation system," U.S. Patent 5 339 684, Aug. 12, 1994.
46. J. S. White and A. Jircitano, "Gradiometer based terrain estimation," U.S. Patent 5 402 340, Mar. 28, 1995.
47. J. Moryl, H. Rice, and S. Shinnars, "The Universal Gravity Module for enhanced submarine navigation," in *Proceedings of IEEE's Position Location and Navigation Symposium (PLANS)*, Palm Springs, CA, Apr. 1998, pp. 324–331.
48. J. B. Archibald, "Two novel approaches to navigation using the earth's gravity and magnetic fields," Ph.D. dissertation, Univ. of New York at Buffalo, Amherst, NY, 1993.
49. J. G. Blaylock, D. E. Swihart, and A. F. Barfield, "Feasibility of gravity gradient technology for fighter aircraft," *ICAS*, pp. 562–557, 1996.

50. C. Jekeli, "Precision free-inertial navigation with gravity compensation by an onboard gradiometer," *Journal of Guidance, Control, and Dynamics*, vol. 29, no. 3, pp. 704–713, 2006.
51. J. A. Richeson, "Gravity gradiometer aided inertial navigation within non-GNSS environments," Ph.D. dissertation, Univ. of Maryland, College Park, MD, 2008.
52. D. A. Smith, "There is no such thing as 'The' EGM96 geoid: Subtle points on the use of a global geopotential model," *IgeS Bulletin No. 8*, pp. 17–28, 1998.
53. R. Kiamehr and M. Eshagh, "Egmlab, a scientific software for determining the gravity and gradient components from global geopotential models," *Journal of Earth Science Informatics*, vol. 1, no. 2, pp. 93–103, 2008.
54. X. Li and H. J. Gotze, "Tutorial: Ellipsoid, geoid, gravity, geodesy, and geophysics," *Geophysics*, vol. 66, pp. 1660–1668, 2001.
55. F. G. Lemoine, S. C. Kenyon, J. K. Factor, R. G. Trimmer, N. K. Pavlis, D. S. Chinn, C. M. Cox, S. M. Klosko, S. B. Luthcke, M. H. Torrence, Y. M. Wang, R. G. Williamson, E. C. Pavlis, R. H. Rapp, and T. R. Olsen, "The development of the joint NASA GSFC and the National Imagery and Mapping Agency (NIMA) geopotential model EGM96," NASA, Goddard Space Flight Center, Greenbelt, Tech. Rep. NASA/TP-1998-206861, 1998.
56. M. Petrovskaya and A. Vershkov, "Non-singular expressions for the gravity gradients in the local north-oriented and orbital reference frames," *Journal of Geodesy*, vol. 80, pp. 117–127, 2006.
57. (2008, Sep.). [Online]. Available: <http://earth-info.nga.mil/GandG/wgs84/gravitymod/egm2008/index.html>
58. R. L. Parker, "The rapid calculation of potential anomalies," *The Geophysical Journal of the Royal Astronomical Society*, vol. 31, no. 4, pp. 447–455, 1972.
59. C. Jekeli and L. Zhu, "Comparison of methods to model the gravitational gradients from topographic data bases," *Geopys. J. Int.*, vol. 166, pp. 999–1014, 2006.
60. C. Jekeli, "Statistical analysis of moving-base gravimetry and gravity gradiometry," The Ohio State University, Columbus, OH, Tech. Rep. 466, 2003.
61. L. Zhu, "Gradient modeling with gravity and DEM," Ph.D. dissertation, The Ohio State University, Columbus, OH, 2007.
62. D. M. Gleason, "Obtaining Earth surface and spatial deflections of the vertical from free-air gravity anomaly and elevation data without density assumptions," *Journal of Geophysical Research*, vol. 95, no. B5.
63. D. T. Sandwell, "Biharmonic spline interpolation of GEOS-3 and SEASAT altimeter data," *Geophysical Research Letters*, vol. 14, no. 2, pp. 139–142, 1978.

64. P. Dumrongchai, "Small anomalous mass detection from airborne gradiometry," Ph.D. dissertation, The Ohio State University, Columbus, OH, 2007.
65. J. R. Cogdell, *Foundations of Electrical Engineering*. NJ: Prentice Hall, 1996.
66. C. B. Rorabaugh, *DSP Primer*. New York: McGraw-Hill Professional, 1999.
67. M. Talwani, "Airborne gradiometer survey over the San Andreas fault drill site," presented at the EGM2007 International Workshop, Capri, Italy, Apr. 2007.
68. (2008, Dec.). [Online]. Available: <http://www.kc-10.net/kc10/dimensions.htm>
69. P. Genovese, *New Jersey Curiosities*. Guilford, CT: Globe Pequot, 2007.

Vita

Marshall Rogers is a Captain serving in the United States Air Force. He was raised in Marietta, GA and graduated with a BS in Aerospace Engineering from the Georgia Institute of Technology in 2002. Prior to his assignment at the Air Force Institute of Technology, he was assigned as a flight test engineer on the F-22 Raptor at Edwards Air Force Base, California. His follow-on assignment is to AFRL at Kirtland AFB, NM, where he will be performing laser effectiveness research.

Permanent address: 2950 Hobson Way
Air Force Institute of Technology
Wright-Patterson AFB, OH 45433

REPORT DOCUMENTATION PAGE			Form Approved OMB No. 0704-0188	
The public reporting burden for this collection of information is estimated to average 1 hour per response, including the time for reviewing instructions, searching existing data sources, gathering and maintaining the data needed, and completing and reviewing the collection of information. Send comments regarding this burden estimate or any other aspect of this collection of information, including suggestions for reducing this burden to Department of Defense, Washington Headquarters Services, Directorate for Information Operations and Reports (0704-0188), 1215 Jefferson Davis Highway, Suite 1204, Arlington, VA 22202-4302. Respondents should be aware that notwithstanding any other provision of law, no person shall be subject to any penalty for failing to comply with a collection of information if it does not display a currently valid OMB control number. PLEASE DO NOT RETURN YOUR FORM TO THE ABOVE ADDRESS.				
1. REPORT DATE (DD-MM-YYYY) 26-03-09		2. REPORT TYPE Master's Thesis		3. DATES COVERED (From — To) 1 Jan 2008 – 26 Mar 2009
4. TITLE AND SUBTITLE An Investigation Into the Feasibility of Using a Modern Gravity Gradient Instrument for Passive Aircraft Navigation and Terrain Avoidance AFIT/GAE/ENY/09-M16			5a. CONTRACT NUMBER	
			5b. GRANT NUMBER	
			5c. PROGRAM ELEMENT NUMBER	
6. AUTHOR(S) Rogers, Marshall M, Captain, USAF			5d. PROJECT NUMBER 09ENY313	
			5e. TASK NUMBER	
			5f. WORK UNIT NUMBER	
7. PERFORMING ORGANIZATION NAME(S) AND ADDRESS(ES) Air Force Institute of Technology Graduate School of Engineering and Management (AFIT/ENY) 2950 Hobson Way WPAFB OH 45433-7765			8. PERFORMING ORGANIZATION REPORT NUMBER AFIT/GAE/ENY/09-M16	
9. SPONSORING / MONITORING AGENCY NAME(S) AND ADDRESS(ES) Air Force Research Lab , RF Sensor Technology Division, Reference Systems Branch Dr. Stewart DeVilbiss 2241 Avionics Circle Bldg 620, WPAFB OH 45433-7765 (937) 255-6127 x 4274, stewart.devilbiss@wpafb.af.mil Air Force Research Lab, Munitions Directorate, Advanced Guidance Division Dr. Mikel Miller 101 West Eglin Blvd, Bldg13 AFRL Eglin, FL 32542 (850) 882-4033, mikel.miller@eglin.af.mil			10. SPONSOR/MONITOR'S ACRONYM(S) AFRL/RYRN, AFRL/RWG	
			11. SPONSOR/MONITOR'S REPORT	
12. DISTRIBUTION / AVAILABILITY STATEMENT APPROVED FOR PUBLIC RELEASE; DISTRIBUTION UNLIMITED				
13. SUPPLEMENTARY NOTES This material is declared a work of the U.S. Government and is not subject to copyright protection in the United States.				
14. ABSTRACT Recently, Gravity Gradient Instruments (GGIs) - devices which measure the spatial derivatives of gravity, have improved remarkably due to development of accelerometer technologies. Specialized GGIs are currently flown on aircraft for geological purposes in the mining industries. As such, gravity gradient data is recorded in flight and detailed gradient maps are created after post mission processing. These maps, if stored in a database onboard an aircraft and combined with a GGI, form the basis for a covert navigation system using a map matching process. This system is completely passive and essentially unjammable. To determine feasibility of this method, a GGI sensor model was developed to investigate signal levels at representative flight conditions. Aircraft trajectories were simulated over modeled gravity gradient maps to determine the utility of flying modern GGIs in the roles of navigation and terrain avoidance. It was shown that the GGI based map-matching navigation system can likely provide a marked improvement over a non-aided INS but is limited by decreasing gravity gradient strength at higher altitudes, particularly over smooth terrain. Additionally, GGI output rate and bandwidth limitations, along with the inverse nature of the terrain avoidance problem, rendered GGI aided terrain avoidance unfeasible for the time being.				
15. SUBJECT TERMS gradiometer, gravity, navigation, passive, gradient, terrain				
16. SECURITY CLASSIFICATION OF:			17. LIMITATION OF ABSTRACT UU	18. NUMBER OF PAGES 180
a. REPORT U	b. ABSTRACT U	c. THIS PAGE U		
			19a. NAME OF RESPONSIBLE PERSON Maj Richard E. Huffman AFIT/ENY	
			19b. TELEPHONE NUMBER (Include Area Code) (937) 255-3636 x 7490 richard.huffman@afit.edu	